Searching for Gravitational Waves from Pulsars

Colin D. Gill, B.Sc, M.Sc.

Submitted in fulfilment of the requirements
for the degree of Ph.D.

School of Physics and Astronomy
University of Glasgow
2012

Abstract

The work presented here looks at several aspects of searching for continuous gravitational waves from pulsars, often referred to simply as continuous waves or CWs. This begins with an examination of noise in the current generation of laser interferometer gravitational wave detectors in the region below 100 Hz. This frequency region is of particular interest with regards to CW detection as two prime sources for a first CW detection, the Crab and Vela pulsars, are expected to emit CWs in this frequency range. The Crab pulsar's frequency lies very close to a strong noise line due to the 60 Hz mains electricity in the LIGO detectors. The types of noise generally present in this region are discussed. Also presented are investigations into the noise features present in the LIGO S6 data and the Virgo VSR2 data using a program called Fscan. A particular noise feature present during VSR2 was discovered with the use of Fscan, which I report on and show how it degrades the sensitivity of searches for CWs from the Vela pulsar using this data.

I next present search results for CWs from the Vela pulsar using VSR2 and VSR4 data. Whilst these searches did not find any evidence for gravitational waves being present in the data, they were able to place upper limits on the strength of gravitational wave emission from Vela lower than the upper limit set by the pulsars spin-down, making it only the second pulsar for which this milestone has been achieved. The lowest upper limit derived from these searches confines the spin-down energy lost from Vela due to gravitational waves as just 9 % of Vela's total spin-down energy. The data from VSR2 and VSR4 are also examined, analysis of hardware injections in these datasets verify the calibration of the data and the search method. Similar results are also presented for a search for CWs from the Crab pulsar, where data from VSR2, VSR3, VSR4, S5 and S6 are combined to produce an upper limit on the GW amplitude lower than has been previously possible, representing 0.5 % of the energy lost by the pulsar as seen through its spin-down.

The same search method is also applied to analyse data for another 110 known pulsars, with five of these being γ-ray pulsars that have been timed by the Fermi satellite. GWs from the pulsars timed by Fermi are expected at frequencies below 40 Hz, the LIGO detectors are not calibrated below these frequencies but the Virgo detector is. Hence the data used to search for GWs from these pulsars is the Virgo

VSR4 data. The other 105 pulsars were analysed using out of date ephemerides obtained for the LIGO S5 run and the data analysed was from the LIGO S6 run, hence the results obtained for these pulsars are presented as an indication of what results can be expected with updated ephemerides only. For these 110 pulsars the spin-down limits were not able to be beaten, although there are a few pulsars for which this may be able to be achieved with an analysis combining all the possible datasets, in particular J1913+1011.

The final part of this thesis reports extensions to the search method used for the analyses previously described. The first way in which this search method is extended is the use of a nested sampling algorithm to perform the parameter estimation stage of the analysis which was previously preformed using a MCMC. The nested sampling code also allows for model selection through the computation of the Bayesian evidence, I present results from characterisation tests of this nested sampling search code that demonstrate the equivalence of its results to those from the MCMC and grid based codes. The other extension to the search method looks at a new CW emission mechanism from a neutron star with a pinned superfluid core that is misaligned from the star's principle axes. This emission model predicts CWs at both the stars spin frequency f_{rot} and twice its spin frequency $2f_{rot}$, providing an extra data channel with which to perform a search when compared to the triaxial rotator model which only emits at $2f_{rot}$. I present the development of a search for the emission from this new model, tests of the algorithm developed using simulated data, and results from a search using actual data from the VSR4 run for CWs from the Crab pulsar. The testing of the search algorithm shows that the posterior for the model is sufficiently complex to inhibit useful parameter estimation, but that the computation of the Bayesian evidence allows one to distinguish between this model and the triaxial rotator given a low SNR signal in the f_{rot} data channel.

Declaration

In this thesis I report on an investigation into laser interferometer gravitational wave detector noise and on a number of searches for gravitational waves in the data from the LIGO and Virgo interferometers. This would not be possible without the many members of the LIGO Virgo collaboration and their work to create, develop and maintain both the detector infrastructure and also the data analysis hardware and software infrastructures. Here I provide an account of what work described in this thesis is not my own.

Chapter one consists of introductory material only, and as such this information is taken form the literature and is presented with references where appropriate.

The work presented in Chapter two uses a program called Fscan, which as part of the LALsuite repository relies on many other pieces of software to function. Fscan was initially developed by Greg Mendell and Rejean Dupuis. My work on this software was to develop certain aspects of it related to the display of results in general, and to show the expected frequency for gravitational waves for a given source in these results. In this chapter I clearly point out the specific development work I carried out.

Chapter three presents the search for gravitational waves from the Vela pulsar. The search algorithms used for this form part of the LALSuite repository and rely on a number of other LALSuite programs to perform basic functions. The search algorithms themselves, lalapps_heterodyne_pulsar and lalapps_pulsar_parameter_estimation were developed by Matt Pitkin, Graham Woan and Rejean Dupuis (Pitkin & Woan 2004; Dupuis & Woan 2005). The timing solution used for the Vela analyses were derived by Matt Pitkin using software called Tempo2. This software was developed by Hobbs et al. (2006). The timing information used to create the timing solution was obtained from Sarah Bruckner from the Hartesbessthoek Radio Astronomy Observatory and by Aiden Hotan and Jim Palfreyman of the Mt. Pleasant Observatory. The data used for the analyses are from the Virgo detector, and as such the data run and calibration of the data are the work of the Virgo team.

Chapter four presents analyses of Virgo and LIGO data for gravitational waves from the Crab pulsar. The timing solution used for this is obtained from Andrew Lyne (2011). The method of using this data to account for the timing noise of the Crab pulsar was the work of Pitkin & Woan (2004).

The results presented in chapter five again use the search algorithms lalapps_heterodyne_pulsar and lalapps_pulsar_parameter_estimation. The ephemerides used to perform these searches were created by the Fermi LAT team, and by radio astronomers at the Green Bank Telescope, the Jodrell Bank Telescope and the Parkes Radio Telescope.

Chapter six begins with characterisation of the search algorithm lalapps_pulsar_parameter_estimation_nested, this was developed by Matt Pitkin (Pitkin et al. 2012), and as well as using a number of the LALSuite sub-routines as normal, uses a nested sampling algorithm from LALSuite developed by Veitch & Vecchio (2010) which itself was based on the work of Skilling (2004). The latter portions of this chapter present the development of a search method for gravitational waves from the model of Jones (2010), this development was the work of Graham Woan, Matthew Pitkin and I and in collaboration with Ian Jones.

Acknowledgements

I feel extremely privileged to have been able to do a PhD in gravitational wave astronomy, and will be forever indebted to the people that made it possible. In chronological order these start with John Brown and Lyndsay Fletcher - for offering me a MSc project, which I enjoyed immensely and without which I would not have been in the position to undertake a PhD. Next is Matt Pitkin, for suggesting I might like to do a PhD in gravitational waves, and to Graham Woan and Jim Hough for offering me a studentship with the IGR. Thanks to Graham again, for his supervision and support, and to Matt again for his constant help over the years with so many different things. Thank you also to Greg Mendell for his collaboration and help with Fscan, this work would not have been possible without his help. Thanks to Ian Jones, for the many teleconferences and explanations of his pinned superfluid neutron star model, these were invaluable.

I would also like to thank my wife Laura, for her support and understanding of this abrupt career change, I definitely would not have been able to do this without it. I also want to thank my family their unwavering support, in particular my mum for proof reading this thesis.

Finally I would like to thank my examiners, Martin Hendry and Stephen Fairhurst whose comments and corrections have improved this thesis.

Contents

List of Figures

List of Tables

Chapter 1

Introduction

1.1 Introduction

The aim of this chapter is to introduce the reader to the field of gravitational wave (GW) astronomy. This begins with a brief discussion on the role of gravitational wave astronomy within the wider discipline of general astronomy in §1.2, where it will be shown that GW astronomy has the potential to provide a view on the Universe in a way that is not possible through conventional astronomical observations. I discuss the theory of GWs in §1.3, and the way in which GWs can be detected including a review of the current detectors in §1.4. In §1.5 I outline some of the potential astrophysical sources of gravitational waves. How to search for continuous GWs is the final topic of interest for this chapter in §1.6, with a brief overview of some of the current search methods.

1.2 Gravitational wave research motivation

When Galileo first looked through his telescope he revolutionised astronomy, previously astronomy had been carried out by eye. Though this did not preclude earlier astronomers from building observatories and gaining some understanding of the cosmos, their view was limited. The telescope was able to push back these limits. As telescope technology improved, these limits were pushed further and astronomers were able to look at increasingly distant and dim objects with ever improving resolution. The introduction of photometry and spectroscopy were the next step changes in astronomy but the fundamentals of what one could see remained the same. This changed in 1930s with the observation of radio waves from the milky way by Karl Jansky. The advent of radio astronomy opened up an entirely new view of the cosmos by looking outside of the optical spectrum. For the first time astronomers were able to see phenomena which they were previously blind to, such as pulsars and

quasars, and also to see familiar objects in a new way. The next major milestone in the journey toward multi-wavelength astronomy was Infra-red (IR) astronomy. It could be argued that IR astronomy was born with William Herschel's measurement of IR radiation from the sun in 1800. Despite this discovery and subsequent observations of other stars, the field did not really get going until the 1960s. The view of the universe expanded rapidly from here and observations were no longer consigned to a small part of the electro-magnetic (EM) spectrum, but sample it across a wide range of wavelengths including Ultraviolet, X-ray and γ-ray. With each new wavelength of radiation astronomers have been able to view, they have been rewarded by unexpected discoveries. The term "multi-wavelength astronomy" is used to describe the approach where objects are studied in a number of different wavelengths, which is now considered essential for current astrophysics. The next and most recent paradigm shift has been towards the inclusion of non-EM observations, for example cosmic rays and neutrinos, in the move towards what has been termed multi-messenger astronomy. It is hoped in the near future that GWs will be able to contribute to multi-messenger astronomy, as again the limits on what astronomers can see will be pushed back, and a new view will open on the universe that is complementary to the existing view gained mostly through EM observations. EM radiation interacts strongly with small portions of matter, and so provides information about small scale phenomenon. It is also easily absorbed or scattered and so conveys information about its last interaction rather than its source, for example a photon radiated from the centre of a supernova will undergo many interactions before making its way past the enshrouding stellar material so that when it is observed at Earth it no longer carries information about the SN explosion itself but rather the intervening matter. Gravitational waves on the other hand are produced by large scale bulk motion of matter, and interact very weakly with matter. This means that they travel unaltered from source to observer, for example observations of GWs from the Big Bang will be from just 10^{-30} s into the lifetime of the Universe (Sathyaprakash & Schutz 2009), which is long before the time at which the universe became EM transparent ($\sim 379\,000$ yr), from which we observe the cosmic microwave background (CMBR).

1.3 General relativity and gravitational waves

In 1905 Albert Einstein published his paper "On the electrodynamics of moving bodies" (Einstein 1905), introducing the world to his special theory of relativity (SR). The motivation for the development of SR was to provide a theory in which the laws of physics hold for any observer irrespective of their motion. SR has the important caveat that it only applies for inertial observers, i.e. observers that are

not accelerating. SR has at its core two principles, the principle of relativity and the principle of the constancy of the speed of light. The principle of relativity states that the laws of physics are the same for all inertial frames of reference. The principle of the constancy of the speed of light states the speed of light in a vacuum is the same for all inertial frames of reference. From these simple principles Einstein showed that the concepts of absolute space and time were no longer valid, but that instead the measurements of space and time depend on the motion of the observer, leading to counter-intuitive phenomenon such as time dilation and length contraction. The fundamental quantity of SR that different observers can agree on is the spacetime interval, given as $ds^2 = -c^2dt^2 + dx^2 + dy^2 + dz^2$. The idea of the constancy of the speed of light was in the minds of many physicists at the time, as a result of the Michaelson Morley experiment. Notable contributions in this area were made by Poincare, Fitzgerald and Lorentz.

Shortly after the publication of this paper on SR, Minkowski introduced a geometrical view of SR, which describes (t, x, y, z) as coordinates in a four dimensional space and was fundamental in the development of general relativity (GR), which Einstein published in 1915 (Einstein 1915). General relativity took the concepts of special relativity and generalised it for all observers, which meant those observers which were not inertial. The crucial step in the development of GR was Einstein's realisation that gravity is equivalent to an acceleration. This idea is referred to as the equivalence principle and is often split into the strong and weak equivalence principles. The equivalence principle led Einstein to think of gravity as a manifestation of spacetime curvature, rather than a force in the conventional sense.

An important construct in GR is that of the geodesic. The geodesic is the GR equivalent of the straight line, in that Newtonian physics says that an object which is not acted upon by an external force will continue in a straight line. This concept is replaced in GR by the geodesic. The geodesic is a curved path that an object will follow when it is not acted upon by a non-gravitational external force. The amount by which two geodesics diverge is important, as this is a measure of the curvature of spacetime. Geodesics only diverge in a non-uniform gravitational field.

Previous to general relativity the accepted theory of gravity was that of Newtonian gravity, which had been the accepted theory of gravity for hundreds of years as it was successful in describing the observed effects of gravity - i.e. the motion of the celestial bodies, and of the attraction between the Earth and objects on it (apples!). However Newtonian gravity acts instantaneously, something which did not fit in with SR that placed the limit on the speed of any information at the speed of light. This important revision to the description of gravity can be shown to predict gravitational waves based on otherwise Newtonian gravity alone (Schutz 2009).

GR was famously summarised by John Wheeler as "matter tells space how to

curve. Space tells matter how to move", this simple statement is useful, but can be improved by replacing "matter" with "matter and energy", and replacing "space" with "spacetime". How mass and energy curves spacetime is expressed in the Einstein field equations, where natural units are used ($G = c = 1$),

$$G^{\alpha\beta} = R^{\alpha\beta} - \frac{1}{2}g^{\alpha\beta}R = 8\pi T^{\alpha\beta}. \tag{1.1}$$

The term $T^{\alpha\beta}$ is the energy momentum tensor, which is also known as the stress-energy tensor, it describes the density and flow of energy and momentum due to the distribution and motion of matter and radiation. The terms R and $R^{\alpha\beta}$ are the Ricci scalar or the curvature scalar and Ricci tensor respectively, together with the metric $g^{\alpha\beta}$, they describe the curvature of spacetime. The Ricci scalar is a scalar measure of the curvature of spacetime. The term $G^{\alpha\beta}$ is known as the Einstein tensor and describes the curvature of spacetime. The Einstein field equations are non-linear partial differential equations.

A weak field approximation to GR can be arrived at through the use of linearised theory. Such an approximation is valid in regions of space remote from strong concentrations of matter and radiation, where spacetime is close to being flat. In this weak field approximation the metric tensor can be thought of as the combination of flat spacetime plus a small perturbation, this is written as

$$g_{\alpha\beta} = \eta_{\alpha\beta} + h_{\alpha\beta}, \tag{1.2}$$

where $\eta_{\alpha\beta}$ is the Minkowski metric and represents flat spacetime, and $h_{\alpha\beta}$ describes small perturbations from that flat spacetime. The result is that, provided $|h_{\alpha\beta}| << 1$, one can ignore the non-linear terms in $h_{\alpha\beta}$ and so write linearised versions of the Einstein field equations

$$\Box\bar{h}^{\mu\nu} = -16\pi T^{\mu\nu}, \tag{1.3}$$

where the $\Box$ is known as the wave operator, or the four dimensional Laplacian, and $\bar{h}^{\mu\nu}$ is the trace reversed form of $h^{\mu\nu}$. From Equation 1.3, we can write the Einstein equations for a region of spacetime in a vacuum (i.e. $T^{\mu\nu} = 0$) far away from a rapidly changing relativistic source. This is

$$\Big(-\frac{\partial^2}{\partial t^2} + \nabla^2\Big)\bar{h}^{\alpha\beta} = 0. \tag{1.4}$$

This is known as the three dimensional wave equation, and describes metric perturbations i.e. waves in spacetime, which travel at speed c, i.e. GWs. A solution of Equation 1.4 is

$$\bar{h}^{\alpha\beta} = A^{\alpha\beta} exp(ik_\alpha x^\alpha), \tag{1.5}$$

which describes a plane wave with amplitude $A^{\alpha\beta}$, and wave vector k_α. If we then perform a gauge transformation into the Transverse traceless gauge, we can show that

$$A^{TT}_{\alpha\beta} = \begin{pmatrix} 0 & 0 & 0 & 0 \\ 0 & A_{xx} & A_{xy} & 0 \\ 0 & A_{xy} & -A_{xx} & 0 \\ 0 & 0 & 0 & 0 \end{pmatrix} \tag{1.6}$$

The effect of the passing of a GW on free test particles is not immediately obvious. In Schutz (2009), we are shown that the effect of a GW on two free test particles at rest is to change the *proper distance* between them, despite the fact that in the TT gauge the coordinates of the two free test particles remain unaffected by the GW. The proper distance is shown to be

$$\delta l = [1 + \frac{1}{2} h^{TT}_{xx}(x = 0)]\epsilon, \tag{1.7}$$

where ϵ is the separation between the two particles in the x coordinate, and with $y = z = 0$ for both particles. This tells us that the change in the proper distance between the particles is proportional to their initial separation, something which has a direct consequence for the design of interferometer GW detectors. It is also possible to look at the question of the affect of a GW on free test particles by considering tidal effects of the GW in a local inertial frame centred on one of the particles. Where test particles are not free but have another force acting upon them, the effect of GWs can be thought of as imparting a tidal force which acts to alternately stretch and contract the separation of the particles. The degree to which the proper distance is stretched and contracted due to the GW wave then depends on the strength of the GW induced tidal force in comparison to the other force. If the particles being considered are bound in some material the forces binding the particles will far outweigh the small tidal force due to the GW.

From Equation 1.6 we can infer the polarisation states of GWs. These polar-

isations are referred to as the + and × polarisations, and correspond to the two independent terms in h, i.e. h_{xx}^{TT} and h_{xy}^{TT} respectively. The effect due to these different polarisations is best demonstrated diagrammatically with a ring of free test particles, as in Figure 1.1.

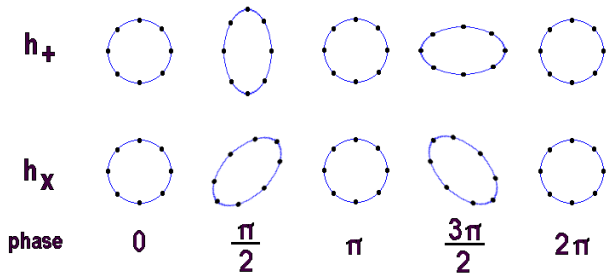

Figure 1.1: The effect of plus and cross polarised GWs on a ring of free test particles.

To consider the situation where $T^{\mu\nu} \neq 0$, i.e. the region of space containing a GW source, we again take the results from Schutz (2009), starting with Equation 1.4, but with $T^{\mu\nu} \neq 0$, we have

$$\Big(-\frac{\partial^2}{\partial t^2} + \nabla^2 \Big) \bar{h}^{\mu\nu} = 16\pi T^{\mu\nu}, \tag{1.8}$$

which, given certain assumptions, can be solved to give Equation 1.9, the quadrupolar approximation. The assumptions that need to be made to arrive at this solution are: first that the time-varying part of $T^{\mu\nu}$ is sinusoidal, and second that the velocity of the source is much less than c. This is known as the slow motion approximation, and holds valid for all but the most relativistic sources of GWs. In Equation 1.9, r is the spherical polar radial coordinate, Ω is the frequency of the sinusoidal variation in $T^{\mu\nu}$, and t is time.

$$h_{jk} = -2\Omega^2 D_{jk} e^{i\Omega(r-t)}/r. \tag{1.9}$$

This equation is often referred to as the quadrupole approximation, as D_{jk} is derived from the quadrupole moment of the mass distribution. Lower order mass moments do not contribute to GWs. A monopole mass moment represents the mass, so a changing mass monopole would violate the conservation of mass/energy, and similarly a changing mass dipole would violate the conservation of momentum.

1.4 Gravitational wave detection

This section provides a brief overview of gravitational wave detection. For a more in depth review see Pitkin et al. (2011).

The very first GW detectors took the form of large aluminium bars and the so called bar detector approach was pioneered by the founder of GW research, Joseph Weber (Weber 1961). The principle behind this type of detector is that the aluminium bar behaves as a damped harmonic oscillator, a GW passing through it acts as a force to drive the oscillations (Schutz 2009). If a GW, of frequency at or near the bar's resonant frequency, passes through the bar then the GW would cause the excitation of the bar. The excitation of the bar at its resonant frequency is measured using piezoelectric transducers. Developments of the bar detector saw an effort to cool them and hence minimise thermal noise, however their fundamental drawback is that they are only sensitive in a small band around the bars resonant frequency. Bar detectors fell out of favour when laser interferometer detectors were able to achieve better sensitivities across a much broader frequency range.

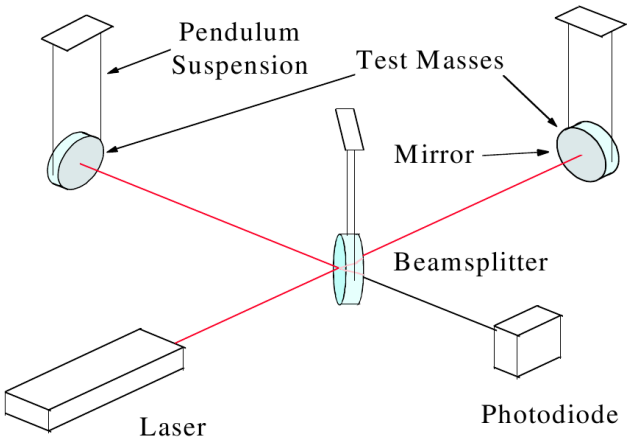

Figure 1.2: The basic layout of a Michelson interferometer GW detector.

The use of laser interferometers as GW detectors was pioneered by several research groups from around the world during the late 1980s and throughout the 1990s (Shoemaker et al. 1988; Robertson et al. 1995; Mizuno & et al. 1998; Fritschel et al. 1998; Araya et al. 1997; Abramovici et al. 1996). Current interferometer detectors are based on the Michelson interferometer design, with the beam splitter and the end mirrors as the free test masses (or particles), as they were referred to as in §1.3, whose separation is altered by a passing GW. The basic layout of such an interferometer is shown in Figure 1.2, although it should be noted that in reality these detectors are extraordinarily complex with many subsystems. The basic operation of these detectors sees a stable laser sent to the beam-splitter, here half of the beam is sent down one arm and half down the other, the laser is reflected back down the

arms by the test mass mirrors at the end of each arm to the beam splitter, where they are combined and sent to the photo-detector. The recombined beams produce an interference pattern which the photo-detector senses. If the proper distance of one arm changes relative to the other then the interference pattern is changed and the photo-detector senses the change in the differential arm length. One of the reasons that a Michelson interferometer design is used, is that the effect of a GW passing through the detector along the z-axis of a particular polarisation, would decrease the length of one arm whilst increasing the length of the other by the same amount, meaning that the change in the differential arm length, which is what such a detector is measuring, is twice that of the fractional change in length of one arm. This is shown by the characteristic strength of a GW wave h, where

$$h = 2\frac{\Delta L}{L}, \tag{1.10}$$

ΔL is the fractional change in length between two test masses - in this simple case the mirrors and the beam splitter, and L is the length between the two test masses. For different combinations of the direction of propagation and the polarisation of GWs an interferometer will have differing sensitivities, as described by the detector beam pattern. Figure 1.3, shows just such a beam pattern for a Michelson interferometer GW detector. As we have seen from Equations 1.7 and 1.10, for a given strength of GW the fractional change in proper length/arm length is proportional to its length, hence one way to make a interferometer detector more sensitive is to make the arm lengths longer. This has led to the construction of the large scale interferometers that make up the current detector network, including GEO600 (Lück & the GEO600 Team 1997), LIGO (Abbott et al. 2009b), and Virgo (Acernese et al. 2008). The largest of these are the two LIGO detectors, which each have arm lengths of 4 km. Next in terms of size is the Virgo detector with 3 km long arms, and finally GEO600 with 600 m long arms. The scientists that operate and analyse data from these detectors work together in a large international collaboration known as the LIGO Virgo collaboration.

These detectors achieve high sensitivity measurements across a broad frequency range, from ~ 40 Hz to ~ 10 kHz, this can be seen in Figure 1.4, which shows the sensitivity curves for the LIGO and Virgo detectors from their most recent science runs. Below these frequencies seismic noise degrades the sensitivity excessively. Seismic noise is the movement of the test mass mirrors due to vibrations of the ground the detector sits on. This effect is mitigated by suspending the mirrors from pendulum and cantilever spring assemblies, see §2.3.2 for a more detailed discussion. At high frequencies photon shot noise limits the sensitivity. Photon shot noise is

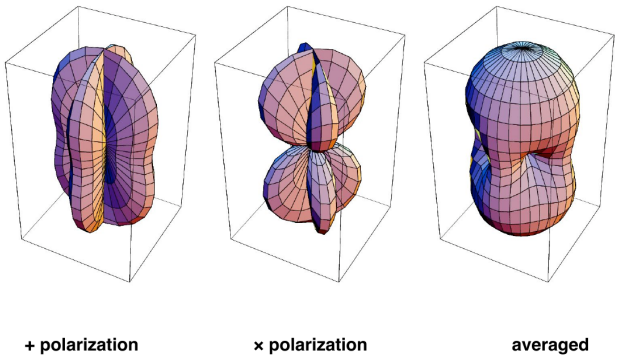

Figure 1.3: The beam pattern for a Michelson interferometer GW detector.

the noise introduced into the measurements at the photo-detector where there are low numbers of incident photons and is proportional to the square root of the laser power of the interferometer. Other important sources of noise in these detectors is thermal noise in the test masses and their suspensions, and gravity gradient noise. Thermal noise and gravity gradient noise are expected to become limiting sources of noise to the detector sensitivity in the advanced detector era, which is forecast to start in 2014.

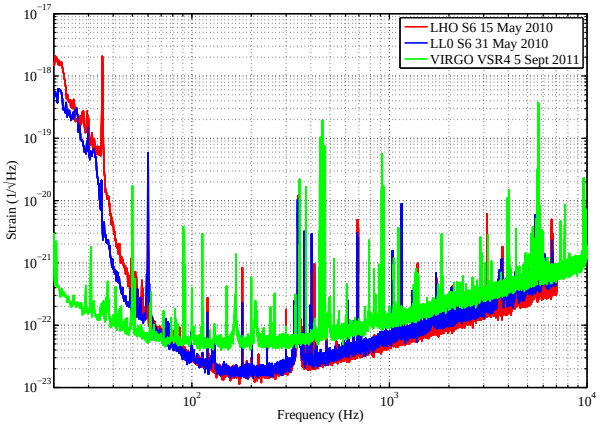

Figure 1.4: Sensitivity curves for the most recent science runs of the LIGO and Virgo detectors. (The Virgo Collaboration 2010; The LIGO Scientific Collaboration 2010).

There are a number of refinements to the basic Michelson interferometer are employed in current detectors to achieve a greater sensitivity. These include the use of Fabry-Pérot resonant cavities and the techniques of power and signal recycling, which I will give a brief and simplistic description of here. Increasing the laser power in the interferometer is important as a means of reducing the shot noise. One simple way to increase the laser power in the interferometer is to add an extra mirror into each arm of the interferometer and and reflect the laser light back between these

extra intermediate mirrors and the end mirrors. This can be achieved by making the cavity between the intermediate mirrors and the end mirrors optically resonant Fabry-Pérot cavities. The placing of the intermediate mirrors can be seen in Figure 1.5, where they are labelled ITM, for intermediate mirror. Power recycling is also employed as a means of reducing the shot noise of an interferometer. Power recycling increases the power of the laser in the interferometer by aligning the interferometer such that the light reflected back from the end mirrors combine destructively at the photodiode. This results in the majority of the laser power being reflected back towards the laser source. The introduction of a power recycling mirror between the laser source and the beam splitter recycles this laser power by reflecting it back towards the beam splitter and down the two arms of the interferometer. The positioning of the power recycling mirror is shown in Figure 1.5. Signal recycling is employed by placing a mirror at the output of the interferometer, as shown in Figure 1.5, the aim being to reflect back into the interferometer side-bands on the light created by the presence of a GW signal. The side-bands resonate within interferometer and so enhance the signal. In order to operate an interferometer with these systems in place the mirrors must be precisely positioned and aligned and the laser must be stable in frequency and power. The mirrors in the interferometer are controlled to achieve and maintain the necessary positioning and alignment, this is commonly known as locking the interferometer.

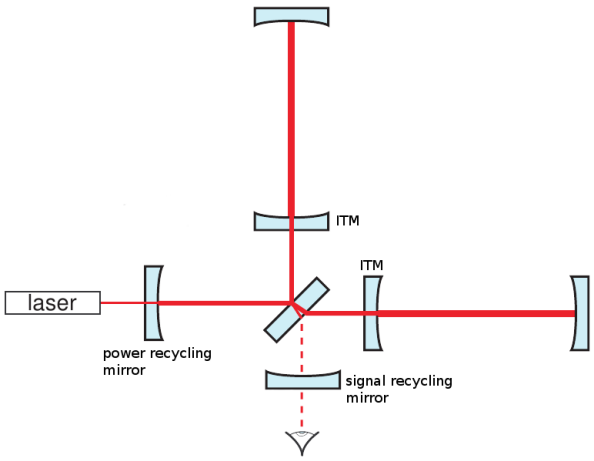

Figure 1.5: A diagramatic representation of a Michelson interferometer with Fabry-Pérot resonant cavities and power and signal recycling.

As well as purpose built GW detectors, there are other attempts afoot to detect GWs. One method that is currently undergoing a coordinated global development is the use of pulsar timing arrays (Hobbs et al. 2010a). This method relies on the extraordinary regularity with which pulsars spin. Pulsars are regularly monitored by astronomers. A timing model is constructed for each monitored pulsar, against

which the observed pulsar signal can be compared. The residuals between the observations and the model are studied closely as these relate to phenomenon which have not been modelled. One such un-modelled phenomena is GWs, the effect of a GW passing through space is predicted to alter the observed pulsar signals timing (Sazhin 1978; Detweiler 1979). By careful study of these residuals in multiple pulsars, astronomers expect to be able to see a particular correlation in the residuals due to GWs. The effect of GWs are predicted to be so small that a particular subset of the pulsar population, known as millisecond pulsars, are needed to perform this type of analysis. Millisecond pulsars are even more regular than normal pulsars, and so the precision of their timing is much better with residuals as low as 30 ns achievable. This compares to GW induced residuals which are expected to be ~ 100 ns (Hobbs et al. 2010a). Groups of pulsar astronomers from radio observatories around the globe are coordinating global collaborations (the European pulsar timing array (Janssen et al. 2008), the north American nanohertz observatory for GWs (Jenet et al. 2009), the Parkes pulsar timing array (Manchester 2008), and the international pulsar timing array (Hobbs et al. 2010b)) to achieve the observations necessary for GW detection with pulsar timing arrays. Searches for GWs using this method has already yielded results by placing upper limits on the stochastic background of GWs (Jenet et al. 2006; van Haasteren et al. 2011).

1.5 Sources of gravitational waves and their generation

1.5.1 Introduction to sources of gravitational waves

It is common practice to categorise GW sources based on the types of signal that they produce. The signals can be categorised by their duration and whether the waveform of the signal is thought to be well or poorly modelled. A transient signal is one whose duration is limited to a period of time shorter than a typical period of observation (as a guide a typical observation run for the LIGO interferometers is of the order of one year). The non-transient signals are those whose duration is longer than a typical period of observation. The non-transient signals are subdivided into stochastic signals, and continuous wave signals. The stochastic signal is not well modelled as it is made up by the superposition of many GW signals from different sources, that are too weak to stand out on their own, that contribute to create a stochastic background signal. Continuous wave gravitational wave (CW) signals are non-transient signals for which the emission mechanism is thought to be understood well.

This section will give a brief overview of astrophysical sources capable of pro-

ducing these different types of signal, as my work is concentrated on the detection of CWs I will spend more time and go into greater detail discussing the sources capable of producing this category of GWs in §2.2.9. For a more complete review of the expected GW sources and their associated astrophysics see Sathyaprakash & Schutz (2009).

1.5.2 Transient sources

Transient sources of GWs can be further subdivided into categories based on those where it is possible to predict the waveform and those where it is not. The possession of good models and so accurate predictions of waveforms for GW signals enables a search method known as matched filtering, where the waveform is looked for in the data and can be found buried beneath the noise. Where no reliable predictions of the waveform exists, searches become a little harder, and must rely on the signal being strong enough to stand out above the background noise. In such cases coincident detections in multiple detectors are essential for verifying the presence of a signal.

The signals where there are no predicted waveforms are often referred to as burst GWs. These are perhaps the most exciting category of GWs as they may be from previously un-imagined astrophysical objects and processes. Burst GWs are expected from Supernova (SN), which are thought to be the result of a star collapsing in on itself due to gravity. SN are expected to produce GWs if the explosion is not spherically symmetric (Sathyaprakash & Schutz 2009). Simulating SN is a notoriously difficult task, but one that has seen significant development over the last decade. Current models are used to predict GW signal waveforms, although different types of model predict very different waveforms (Andersson et al. 2011), meaning a detection of GWs from a SN could provide some much needed validation and rejection for these models. SN that happen in our galaxy are expected to produce GWs detectable by the current generation of interferometric detectors (Andersson et al. 2011).

The work of Hulse & Taylor (1975) has shown that binary NS systems produce GWs, and that in doing so their orbit is caused to shrink due to the loss of energy and angular momentum from the system. Of course the same can be said for non NS binary systems, although the more compact the objects are the stronger the GW emission will be, so any combination of White dwarves, NS and BHs are interesting in terms of GWs. Binaries containing more compact objects can produce stronger GW emission as their compactness allows them to get closer before they begin to coalesce. Such systems are expected to produce transient signals during the latter stages of the binary's evolution, as well as CW signals when the binary orbit is close to being fixed over time. The transient GWs are produced in the later stages of

the evolution of the binary system, once the stars being to *inspiral*. As the binary's orbit shrinks due to the emission of GWs, the energy lost due to the emission of GWs also increases due to the orbit shrinking, a runaway event results ending in the coalescence of the two stars. The GW signal produced has a distinct waveform called a *chirp*, it is so called due to its distinctive increase in frequency and amplitude. As GW frequencies happen to be audible frequencies it is possible to hear chirp examples, I point the reader to Einstein online for examples. The binary inspiral and merger are well modelled using post-Newtonian approximation to Einstein's field equations, e.g. (Buonanno et al. 2007), and so predicted waveforms are produced to enable matched filter searches. Models are also constructed using numerical relativity (Aylott et al. 2009). As the newly formed object vibrates in what is known as the ring-down phase, GWs are again emitted.

Another possible source of transient GWs is from NS glitch. The nature of a NS glitch is discussed in more detail in §2.2.4 and for now it is sufficient to say that a glitch is a sudden change in the spin-down of a NS thought to be caused by some reconfiguration of the stars crust and interior. It is thought a glitch could excite the star causing it to oscillate in a number of quasi-normal modes which would produce GWs (Clark et al. 2007). Work into this area concentrates predominantly on f-modes and r-modes, earlier work favoured p-modes, also considered are g-modes.

1.5.3 The stochastic background

The stochastic background of GWs is thought to be the combination of GWs from cosmological and astrophysical sources combining incoherently to produce a randomly fluctuating background GW field, which is analogous to the cosmic microwave background (Abbott et al. 2004). These individual astrophysical sources can be any that produce GWs that are sufficiently weak at the point of observation to blend into this stochastic background and one example could be a local binary star. As well as discrete sources some fundamental processes in the universe are also thought to contribute to the stochastic background, and one process that is of particular interest to GW astronomers is the Big Bang. Observation of these GWs will enable the study of a time period further back in time than is possible with EM astronomy.

1.5.4 Continuous Wave Sources

Continuous waves (CW) sources are those that emit a signal over a long period of time. There is not an exact universally agreed upon duration for classification as a CW signal, however signals that last longer than a data taking run from the detectors are normally considered CWs. The major advantages of analysing this type of signal is that it is possible to add together observations over a long period of

time and so increase the signal-to-noise ratio (SNR). It is also possible to re-examine old data or examine new data if a detection candidate is found, negating the need to check with data from a different detector. Continuous wave sources include rapidly rotating NSs and binary star systems. The favoured type of source for detection is the rapidly rotating NS, as the emission from binary star systems are thought to be either too weak by the time they reach earth or at frequencies outside the sensitive band of current detectors (Sathyaprakash & Schutz 2009).

A rapidly rotating NS will emit GWs if it has some mass asymmetry about its axis of rotation. This asymmetry is possible through precession of the axis of rotation, if the NS is deformed from a simple spheroid such that it is triaxial in shape, or through oscillatory modes in the fluid part of the NS. Each of these topics is discussed in detail in Section 2.2.9, and as such I will not repeat that material here.

1.6 Search methods for CW sources

1.6.1 Types of search

Searches for CWs can be placed into three main categories: blind, directed and targeted. These categories describe what is known about the source of GWs. Blind searches know nothing about the sources, so they necessarily search over a very large parameter space with many dimensions, unknown parameters of the signal include the location of the source on the sky, the signal amplitude, the polarisation of the signal, and the frequency and frequency evolution. Directed searches are where the location of the source is known, and possibly something about its frequency may also be known. The parameter space that directed searches must look over is much smaller compared to that of blind searches, however the task is still computationally demanding. The final category of search is the targeted search. Here the location and frequency evolution of the source is known, hence the parameter space that must be searched is much smaller with fewer dimensions. Pulsars make good sources for targeted searches, as their sky location and frequency evolutions are known, also as they are rapidly rotating NSs, they are sources from which we expect CWs. With smaller parameter space comes increasing sensitivity, due to the decreased likelihood of finding noise that appears as a signal over a smaller parameter space. Each of these types of search are essentially looking for the presence of a Cw signal in a dataset. Unlike transient signals, CW signals should be present over through an entire dataset, this enables the searches to build up the signal power by summing the signal over the data run. The different types of searches do this in different ways.

1.6.2 Blind searches

Powerflux is a semi-coherent all sky search (Abbott et al. 2009a). I will use it as an example of an all sky search (or blind search) as other search methods such as the Hough and Stackslide methods are similar in principle (Abbott et al. 2008a). Powerflux is a semi-coherent search method that works by summing a measure of the GW strain power together over many Fourier transforms of 30 minute segments of detector data. These short Fourier transforms (SFTs) are so called as they are Fourier transforms of 30 minutes of detector data and many of these would make up the dataset with which a search is performed. The discrete SFT bins that would contain a signal from a particular source at a certain sky location and with a certain frequency and frequency derivative will be offset from one another due to the sidereal modulation of the signal and its intrinsic frequency evolution. This search method calculates which bins would contain the signal, for a set of given parameters. The bins are then summed with a weighting dependant on the noise level to provide a detection statistic referred to as the *powerflux signal estimator* given a particular set of source parameters. Once a blind search is performed, it is important to examine the resulting candidates and apply some rejection criteria to weed out those likely to have been caused by instrumental noise artefacts. One way to do this is to compare the results between different detectors. It is also important with this type of search to carefully choose the parameter space, such that realistic and likely values of parameters are searched over, but that the parameter space is chosen is not too large to perform the search within a reasonable time.

There are a number of search pipelines producing results in the LIGO Virgo collaboration for each type of search. For blind all sky searches the most notable is Einstein@Home, which uses distributed computing to enable a timely search over the large parameter space (Prix 2006). Einstein@Home, as all searches for GWs, has yet to detect a GW signal, however it has achieved success through the discovery of a number of pulsars (Deneva et al. 2011). Einstein@Home currently employs the $\mathcal{F}$ statistic of Jaranowski et al. (1998) as its detection statistic.

1.6.3 Directed searches

Directed searches are used when something is known about a particular source, but the full picture is not known. For example, if we know a NS exits in a particular location but are unable to see it as a pulsar. The central compact object in the SN remnant Cassiopeia A, is just this type of source. For ease the central compact object is simply referred to as Cas A. Cas A has been observed through X-rays and is believed to be a NS (Pavlov & Luna 2009). Searches for radio pulses from Cas A have yielded no evidence of their existence (McLaughlin et al. 2001). Similar

searches for periodicity in its X-ray emission have fared slightly better, but still do not see statistically significant evidence for pulses (Pavlov & Luna 2009). Cas A is also thought to be very young, possibly as young as ~ 300 yr, meaning it is likely to be a strong GW emitter. As a result a directed search for GWs from Cas A was carried out in (Abadie et al. 2010b). The search was over a range of frequency and frequency derivatives thought astrophysically likely for a NS of Cas A's age with the sky position determined by X-ray observations. The search again used the $\mathcal{F}$ statistic of Jaranowski et al. (1998), but unlike the all sky searches where a semi-coherent method is normally employed, this search used a fully coherent method, which was possible due to the decreased parameter space, and hence computational demand, that comes from knowing the position of the source.

1.6.4 Targeted searches

Targeted searches are used where the location of the source and the frequency evolution of the signal is known precisely. This enables these searches to be fully coherent. There are three separate pipelines for targeted searches. These are the time domain Bayesian pipeline, the $\mathcal{F}$ and $\mathcal{G}$ statistic search, and the matched filter on Fourier components search. The time domain Bayesian search was developed in Dupuis & Woan (2005), it uses a two-stage time domain heterodyne to drastically down sample the detector data and remove the phase evolution from the signal. The resulting data set is then used for Bayesian parameter estimation using a Markov Chain Monte Carlo method. This search method is described in more detail in next section, §1.6.5, as it is used for a large portion of the work in subsequent chapters. The $\mathcal{F}$ statistic was developed in Jaranowski et al. (1998), with its extension to include known information about the orientation of the source, the $\mathcal{G}$ statistic, being developed later in Jaranowski & Królak (2010). The $\mathcal{F}$ and $\mathcal{G}$ statistic search is a time domain matched filter search, that uses the aforementioned statistics to calculate the maximum likelihood values of the unknown parameters. The matched filter on Fourier components search, developed in Astone et al. (2010), operates in the frequency domain. It uses a database of Fourier transforms of segments of the detector data, and against this matches Fourier components of the signal produced by the Earth's sidereal motion. These three search methods are described in more detail along side a comparison of their results from a search in data from the Virgo detector in Abadie et al. (2011a).

1.6.5 TDS isolated code

The method employed in the time domain Bayesian search pipeline was initially developed by Rejean Dupuis and Graham Woan (Dupuis & Woan 2005), and has

since been developed by Matt Pitkin and Graham Woan (Pitkin & Woan 2004). This method has been used to search for GWs from a number of known pulsars in data from the previous LIGO science runs (Abbott et al. 2007, 2008b, 2010; Abadie et al. 2011a).

The search pipeline consists of two distinct stages. The first stage performs a precise complex heterodyne to remove the known spin phase evolution from the data and drastically down-samples the data in the process (from 16 384 Hz to 1/60 Hz). In order to remove the phase evolution from the signal it is assumed that the GW signal is phase-locked to its radio signal. The heterodyne is performed by taking the data, assumed to contain the GW signal plus noise, and multiplying it with $e^{-i[\Phi(t)-\Phi_0]}$. This splits the signal into a fast varying part and a zero frequency part. The data is low-pass filtered to remove the fast varying part of the signal leaving a complex dataset with the GW signal shifted to zero frequency. The down-sampling is necessary in order to make the process computationally efficient. The Bayesian parameter estimation is the second stage of the pipeline, and uses a Markov Chain Monte Carlo (MCMC) algorithm to explore the posterior probability volume and produce marginalised posteriors for the unknown signal parameters $h_0, \phi_0, \psi, \cos\iota$, defined below.

The heterodyned data undergoes a process aimed at removing any particularly large outliers, by simply removing data points whose absolute value is greater than five times the standard deviation of the data. This test is run on the heterodyned data twice, to account for any extreme outliers that might skew the standard deviation of the data and so render the process useless.

The heterodyned GW signal $h'(t)$ for the triaxial rotator model has the form

$$\begin{aligned} h'(t) &= h_0\left(\frac{1}{4}F_+(1+\cos^2\iota)\cos\phi_0 + \frac{1}{2}F_\times\cos\iota\sin\phi_0\right) + \\ &\quad ih_0\left(\frac{1}{4}F_+(1+\cos^2\iota)\sin\phi_0 - \frac{1}{2}F_\times\cos\iota\cos\phi_0\right), \end{aligned} \tag{1.11}$$

where F_+ and $F_\times$ are the antenna beam patterns of the interferometer to plus and cross polarisations, h_0 is the GW amplitude, ψ is the GW polarisation angle, ι is the inclination of the pulsar's rotation axis with respect to the line of sight, and ϕ_0 is the initial phase of the signal (Dupuis & Woan 2005). The triaxial rotator model is discussed in more detail in §2.2.9.

The parameter estimation assumes the data is Gaussian and stationary over 30-minute segments of contiguous data, and divides the data into as many 30-minute sections as possible. If there is a section of data of 5 minutes or longer on the end of a longer contiguous section of data already included, then these smaller segments are also included.

One advantage of performing a Bayesian parameter estimation, is that if something is known about any of the four signal parameters, this information can be easily fed into the search through the priors on the parameters. The priors are an important part of the Bayesian approach to statistics, they encode what is already known about the problem being considered, even when one is in complete ignorance. For example, where we are in complete ignorance of the parameters prior to the analysis, the search would use uniform priors on all parameters. Where as if, as in the case for some pulsars, we know something about the orientation of the pulsar through independent observations, then we can place priors on $\cos\iota$ and ψ that reflect this.

The output of the time domain Bayesian pipeline is posterior probability distribution functions (PDFs) for each of the signal parameters. The PDFs convey the calculated degree of belief for values of the parameter considered, given the available information (such as the orientation of the pulsar), the data used and the model used for the GW signal. Each PDF is calculated by marginalising over the other signal parameters, meaning that at each value of the parameter for which the PDF has been calculated, the posterior probability is calculated considering all plausible combinations of values for the other signal parameters. The PDF of most interest is the amplitude parameter h_0, as this is the strength of the GW signal. Where the h_0 PDF indicates there is no signal present, e.g. the PDF peaks at a h_0 value of zero, we find the h_0 value that bounds 95% of the probability density. This value is a 95% credible upper limit on h_0.

1.7 Summary

This chapter has provided an introduction to GW astronomy and this started with a broad introduction to the motivation for GW searches, including the context that GW astronomy inhabits. I have explored the theory behind GWs - general relativity (GR), looking at what GR tells us that can guide us in the design of GW detectors as well as looking at the generation of GWs. The current detector network was also described, and an overview of the types of searches performed to look for GWs. In the next chapter I will provide more introductory material about neutron stars (NS) as sources of GWs, and look at GW detector noise and its characterisation.

Chapter 2

10–100 Hz gravitational waves

2.1 Introduction

The range of frequencies from $\sim 10\,\mathrm{Hz}$ to $\sim 100\,\mathrm{Hz}$ pertains to the lower portion of the frequency band to which current ground-based interferometers are sensitive. However there are many noise artifacts in the data in this frequency range, and many of the sources of these noise artifacts are related to human activity, for example mains electricity produces a noise line at the AC frequency of 50 Hz in Europe and 60 Hz in the USA. I refer to this frequency range as "low-frequency" from here on. This term should not be confused with reference to millihertz frequencies which GWs are expected from super massive binary black hole black hole (BH-BH) systems and the space based GW detector eLISA/NGO is designed to be sensitive to (Amaro-Seoane et al. 2012). When considering CW sources the low frequency region stands out as it contains two famous young pulsars, the Crab and Vela pulsars.

In this chapter I investigate this region, looking at both the detector data and the CW sources whose emission is expected to lie at these frequencies. The part of this chapter looking at the detector data is mainly concerned with a program called Fscan. This program was used to help find problematic noise in LIGO and Virgo data during recent science runs. Characterising the noise in the detector data is of vital importance when the SNR of any signal is likely to be low.

Understanding the sources of noise present in observations is of vital importance in all areas of astronomy where the signal is weak in comparison to the noise, for example in radio astronomy - where interference from radio communications can drown out the weak signals from distant astronomical radio sources, or perhaps even more analogous, in neutrino astronomy - where neutrinos interact very rarely with the detectors and incident cosmic rays are a problematic source of noise. GW astronomy is similar in this respect, except that the need to understand the noise is even greater when considering a first detection.

The section on low-frequency CW sources will look at rapidly rotating NSs, in particular pulsars, as they provide a promising opportunity to search for GWs from NSs due to their known positions and frequency evolution.

2.2 Neutron stars as GW sources

2.2.1 Introduction to neutron stars and pulsars

In 1934, just two years after the discovery of the neutron by James Chadwick, Walter Baade and Fritz Zwicky suggested that stars could exist that were comprised entirely of tightly packed neutrons (Baade & Zwicky 1934b). This type of star was unsurprisingly dubbed the neutron star (NS). Baade and Zwicky went on to suggest that a normal star transitioned into a NS through a supernova (SN) (Baade & Zwicky 1934a). It was many years later in the late 1960s that observational evidence was found for the existence of NSs and this evidence came in the form radio pulsars. The first radio pulsar was discovered by Antony Hewish and Jocelyn Bell Burnell in 1967 as a surprisingly regular series of pulses in the output from their radio antenna array. In their paper announcing the discovery they concluded that the source of the pulses lay outside the solar system and suggested it could be a pulsating white dwarf or NS. Subsequent to the publication of the discovery paper different theories were put forward to explain the nature of pulsars. The favoured theory explained pulsars as rotating NSs (Pacini 1968; Gold 1969) with a dipole magnetic field whose axis is offset from the star's axis of rotation. This explained the pulses as beamed emission from a region near the magnetic poles and along the magnetic axis. When the magnetic axis sweeps through the line of sight to the Earth as the star rotates we see a pulse. This is often referred to as the lighthouse model, see Figure 2.1. This model agreed with some key observational properties of pulsars, such as the extraordinary regularity and narrow width of the pulses due to the large angular momentum of the rotating NS. The discovery of pulsars near the centre of the Crab and Vela nebulae (both are SN remnants) was taken as direct observational confirmation that pulsars were in fact rotating NS (Gold 1969), not only because NS should be found in SN remnants, but significantly also because their periods were sufficiently small to rule out the competing models.

Pulsar astronomy has grown considerably since the late 1960s, the Australia Telescope National Facility (ATNF) catalogue (Manchester et al. 2005) lists nearly 2000 pulsars as of July 2010, and more are still being discovered at a rate of ~ 100 yr^{-1} (Lorimer 2010). Whilst the majority of pulsars are still studied by one or more of the many radio telescopes on Earth, they have also been observed in the optical, X-ray and gamma-ray parts of the EM spectrum, and have been observed

This figure has been removed for copyright reasons.

Figure 2.1: A schematic of the pulsar lighthouse model. The pulsar is a highly magnetised star where the magnetic axis is offset from the spin axis. The beamed emission travels along the magnetic axis and originates above the surface of the star. (Lorimer & Kramer 2005).

by satellites such as Fermi, RXTE and Chandra (Abdo et al. 2010; Gavriil & Kaspi 2002; Heinke & Ho 2010). If and when we are able to observe gravitational emission from pulsars, these observations will combine with EM observations to provide a true multi-messenger window on one of the Universe's most interesting and extreme astronomical objects.

2.2.2 Radio pulses

The observed pulses that give pulsars their name are not confined only to the radio part of the EM spectrum, but can span right across the spectrum through optical and right up to gamma rays. The number of pulsars discovered and studied through higher energy emission is increasing, but the number of such pulsars remain a small fraction of the number observed through radio only.

Despite 40 years of study, the mechanism responsible for producing the beamed radio emission we observe from pulsars is still not known in detail, however there is a consensus on the basic idea. Charged particles are pulled out of the star's surface by a strong electric field and form a dense plasma that is forced to co-rotate with the pulsar by the magnetic field. This dense rotating plasma atmosphere is known as the magnetosphere. At some distance from the pulsar the rotating magnetosphere reaches the speed of light. This is the extent of the pulsar's *light cylinder*, see Figure 2.1. Magnetic field lines inside the light cylinder are closed and those outside are open. The beamed radio emission is created by the acceleration of charged particles from the magnetosphere along the open magnetic field lines (Gold 1969; Pacini 1968). For astronomers studying pulsars, gaining an understanding of this mechanism is

interesting in its own right, but it is also important for GW astronomers. Targeted searches for GWs from known pulsars, which were discussed in §1.6.4, assume that the GW emission is phase locked with the radio pulses and so infer the GW phase evolution from radio observations. This assumption stems from the belief that the radio and GW emission are fixed in relation to the solid crust of the NS, which fits in with current understanding. Without knowledge of the radio emission mechanism of pulsars providing justification of this assumption, such a search strategy would not be be considered as plausible.

This figure has been removed for copyright reasons.

Figure 2.2: The individual pulse profiles from B1919+21 (Ostriker 1971).

Typically pulses are very weak, meaning that it is usually necessary to integrate several hundreds or, for weaker pulsars, several thousands of individual pulses before a signal is detectable. Where single pulses are strong enough to be detected they have shown a large degree of variability in both their profile and strength. An example of this variability can be seen in Figure 2.2, which shows a series of individual pulse profiles from B1919+21. Hence, even where individual pulses are strong enough to be seen, to perform accurate timing an integrated pulse profile is constructed. It is this integrated pulse profile that is extremely stable over time, acting as a finger print of the pulsar and enabling the extraordinary precision timing pulsars are famed for. This practice enables more pulsars to be observed and in more accurate timing of pulsars in general, thus resulting in more known pulsars being viable targets for GW searches.

2.2.3 High-energy and optical pulses

Of the many known pulsars, high energy and optical pulses have only been observed from a small proportion. The most well known of these is the Crab pulsar, whose pulsed emission is unusually strong across the EM spectrum. The strength of the emission from the Crab pulsar enables the study of single pulses. Studies of single optical pulses suggest that the emission is produced by a incoherent non-thermal

process. The similarity of the single pulse profiles of optical, X-ray and γ-ray pulses is possibly an indication that they are produced in the same region. Some X-ray pulsars have not yet been observed to have radio pulses. This may be because the radio pulses are too weak, or because their beams do not point at Earth. Increasing numbers of pulsars are being discovered in X-rays and γ-rays, helping to expand the catalogue of known pulsars and therefore the number of targets for GW searches. With the discovery of each new pulsar comes the chance that its location will be close enough to Earth and that it possesses the physical attributes such that it will produce GWs detectable by the current GW detector network.

2.2.4 Spindowns, glitches and timing noise

One of the most studied properties of pulsars is the pulse period, and through this the rotation period of the pulsar. As already discussed, in general the pulse period is extraordinarily regular due to the large moment of inertia ($\sim 10^{38}\,\mathrm{kg\,m^2}$) of the pulsar, however this is far from the whole story. Over time the period is seen to steadily increase. This is a result of the rotational energy being radiated away from the pulsar by the magnetic dipole radiation, i.e. the beamed emission. This so called spin-down is generally very stable, enabling a period derivative to be calculated from observations based over a number of years. A search for GWs from a pulsar uses a model of the pulsar's spin over time, often referred to as the timing model. Where this model does not match the actual rotation of the pulsar over the time spanned by the data, signal power is lost from the search. Therefore it is essential to take into account the spin-down of a pulsar in order to conduct a meaningful search for GWs.

This steady spin-down is occasionally seen to suddenly reverse and the star spins up before an exponential recovery to the previous spin-down rate. This behaviour is known as a glitch. An example is shown in Figure 2.3 for the Vela pulsar and the glitch is seen as a step down in the period where it otherwise shows a steady increase.

Glitches are thought be the result of one of two mechanisms. The first of these to be proposed is the star quake model; as the pulsar's spin slows down the oblate crust will naturally tend to a more spherical shape. When the internal stress exceeds that which the crust can sustain, it cracks and forms a more spherical shape. A decrease in the moment of inertia and the conservation of angular momentum result in an increase in spin (Baym et al. 1969). The other proposed mechanism envisages a superfluid interior to the pulsar, the magnetic dipole braking is applied to the star's crust slowing the spin of the crust, but not the superfluid interior. As time progresses, the lag between the crust and the superfluid interior builds up until

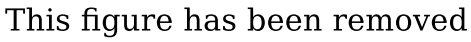

Figure 2.3: A glitch in the vela pulsar(McCulloch et al. 1987).

suddenly they couple and angular momentum is transferred from the interior to the crust spinning it up (Anderson & Itoh 1975). This superfluid core model is the currently favoured mechanism for producing the majority of glitches. The star-quake model struggles to explain the energies involved in the larger of observed glitches, such as those seen in Vela, however it could still be responsible for producing smaller glitches, and may also play a role in triggering the larger glitches (Espinoza et al. 2011). Glitches present a difficulty for GW searches, as the effect of a glitch on the GW emission is unknown. Glitches could cause a change in the strength and/or the phase GWs emitted by a pulsar.

Timing noise is a random variation in the timing of the pulses in comparison to a steady spin-down. It is strongly correlated with spin-down, and so usually seen in young pulsars, most notably the Crab. The recently observed correlation between pulse profiles and timing noise has led (Lyne et al. 2010) to suggest that the cause of timing noise is a change in the pulsar magnetosphere. Previous explanations for timing noise have included many very small "micro-glitches". Searches for GWs from pulsars that have strong timing noise, such as the Crab, must use a timing model that takes the timing noise into account in order to prevent the loss of signal power from the search. A detailed investigation into the effect of Crab pulsar's timing noise on targeted GW searches is presented in Pitkin & Woan (2004).

2.2.5 The magnetic field

One of the defining properties of a pulsar is that it has a strong magnetic field; typical pulsars have magnetic fields of 10^{12} G, whilst millisecond pulsars (MSPs)

have weaker fields of around 10^8 G. These estimates come from assuming that a pulsar's spin-down is completely due to magnetic dipole breaking. Whilst this may not be entirely true it is generally accepted that it is the dominant factor affecting a pulsar's spin-down. These estimates also agree with independent estimates based on the observations of cyclotron radiation in the X-ray spectra of an isolated NS (Bignami et al. 2003). The creation of such strong magnetic fields is attributed to flux conservation and the collapse of the progenitor star.

2.2.6 Neutron star mass, radii, and equations of state

The basic properties of NSs, i.e. their mass, radius, and the *equation of state* (EOS) that relates the two, are not well confined. The mass of NSs is the most well constrained of these properties. There have been a number of masses that have been determined through observations of pulsars in binary systems, examples of these have measured masses from $1.35 \pm 0.04\,\mathrm{M}_\odot$ (Thorsett & Chakrabarty 1999), all the way up to $1.97 \pm 0.04\,\mathrm{M}_\odot$ (Demorest et al. 2010). The maximum possible mass for a NS is determined by the EOS, typical EOS constrain this at $\sim 2\,\mathrm{M}_\odot$. It is more difficult to measure the radius of a NS. Low mass X-ray binaries have enabled estimates, for example Özel et al. (2009) and Güver et al. (2010), although the interpretation of the observations is somewhat contentious (Steiner et al. 2010). Typical values for the radius are in the range $\sim 9 - 11\,\mathrm{km}$. Accurate and reliable observations of mass and radii of NSs is critical to determining the EOS, although efforts have been made to use laboratory based experiments to help constrain EOS (Li & Steiner 2006). The main input into NS EOS are currently theoretical and more observations are needed to determine which of the many current EOS theories are valid and which are not. This is an area that GW observations can add some much needed observational constraints.

The basic idea of the structure of a NS has a crystalline solid crust composed of iron nuclei, a transition region between the solid crust and the fluid interior, a super-fluid interior consisting almost entirely neutrons which increases in density with decreasing distance from the core. The composition of NS cores is pretty much unknown. Cross sectional diagrams of NS typically label the core with a question mark, some predictions suggest a core made of quarks (Klähn et al. 2007). The internal structure depends very strongly on the EOS.

The equatorial ellipticity of a NS is highly relevant to GW searches, as rotating non-axisymmetric NSs are expected to produce GWs, and the equatorial ellipticity is one of the factors governing the strength of the GW emission. It is not currently possible to measure the equatorial ellipticity of a NS, so it is difficult to get an idea of what emission we can expect from NSs. With this lack of observational evidence, we

look to theoretical predictions to gain an idea of the ellipticities we can expect. The maximum sustainable equatorial ellipticity depends on the NS EOS, which I have already stated is not well known, hence the estimates for the maximum sustainable ellipticity are varied. More exotic EOS predict ellipticities of up to 10^{-4}, where as more conventional EOS predict ellipticity of $\sim 10^{-7}$ to 10^{-8} (Owen 2005; Haskell et al. 2007; Lin 2007; Knippel & Sedrakian 2009). I will discuss this topic in more detail when discussing NS as GW emitters.

2.2.7 The distribution and velocity of pulsars

Pulsar velocities are typically high in comparison to the stellar population and in comparison to their progenitor stars (Hobbs et al. 2005; Lyne & Lorimer 1994). The high velocities are explained by the violent birth of NSs in SN. Although the precise mechanism for providing the strong "kick" which accelerates the NSs is still not clear, the basic idea invokes some small asymmetry in the SN explosion (Shklovskii 1970).

The majority of the known pulsars reside within our Galaxy, and these are concentrated about the galactic plane, this can be seen in Figure 2.4. The current sample of known pulsars consists only those that are close enough or bright enough to be seen, therefore the sample is strongly biased.

As pulsars are moving fast, and the datasets used for CW searches are typically long, knowing the velocity of pulsars is vital for performing searches for CWs from pulsars. Studies of pulsar distributions are also helpful for making predictions about pulsars that are currently unknown but may be emitting GWs that will be detectable with future GW observatories.

2.2.8 Populations

It is common to split pulsars into two distinct populations based on their period; MSPs and normal pulsars. Generally pulsars with a a period less than $\sim 20\,\mathrm{ms}$ are considered MSPs. These two populations appear very distinct from one another on a plot commonly know as the p vs $\dot{p}$ plot. This plot shows the population of known pulsars as a function of their period and period derivative, a p vs $\dot{p}$ plot is shown in Figure 2.5. Of the normal population of pulsars, of particular interest as emitters of GWs are the "young" pulsars. Young pulsars, such as the Crab and Vela, have relatively short periods and high period derivatives, and occupy the top right of Figure 2.5. As a pulsar ages it moves diagonally down and right on the plot until its rotation drops below a critical point at which it no longer produces observable pulses and passes beyond the pulsar death line. If the pulsar is in a binary system it can spin-up by accreting matter and angular momentum from its binary companion.

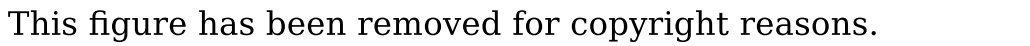

Figure 2.4: The galactic distribution of known pulsars, with millisecond pulsars shown in red, and the binary pulsars are indicated by the open circles. The fact that the binary and millisecond pulsars are not so strongly clustered towards the galactic plane is due to selection effects. Image taken from (Lorimer 2005).

If a dead pulsar accretes enough matter and angular momentum then it once again starts to emit beamed radiation. Such pulsars are recycled as MSPs. This idea of MSPs as recycled normal pulsars is supported by the fact that most MSPs are found in binary systems, whereas only one percent of normal pulsars are.

Understanding how the population of pulsars are distributed in the p vs $\dot{p}$ space aids predictions of GW detections of pulsars which are not seen with EM observations with future GW observatories. Such predictions can inform the design process of future GW observatories to ensure that these observatories are sensitive in the frequency bands which are most likely to contain pulsars which are strong GW candidates and so provide the best chance of yielding detections.

2.2.9 As GW emitters

There are a number of different mechanisms through which NSs can emit GWs, these can be classified into those that produce long lasting GWs (CWs) and those that produce short lasting (or *burst*) GWs. As the focus of this thesis is on CWs, I will not describe in much detail those mechanisms thought to be responsible for producing burst GWs. Such mechanisms include glitch-induced oscillations, the birth of NSs in SNe, or the inspiral and merger of a NS with a binary companion such as another NS, a BH or white dwarf. The mechanisms responsible for producing the longer duration CWs require some form of non-axisymmetry in the NS mass about its

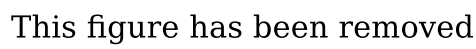

Figure 2.5: A P vs $\dot{P}$ diagram of the known pulsar population

rotation axis. This can be caused by the non-axisymmetry in the rigid shape of the NS, oscillatory modes in the fluid component of the star, and free-precession.

Free precession

Free-precession of a pulsar would produce GW emission at $f_{\rm rot}$ and $2f_{\rm rot}$, as proposed in Jaranowski et al. (1998), but whether NSs actually undergo free-precession is not clear. A freely precessing pulsar would exhibit evidence for the precession in the time of arrivals (TOAs) of the radio pulses, and there is some debate as to whether such a signature has been observed (Staubert et al. 2011; Jones 2011). There is also work to suggest that free-precession in NSs would be damped on short timescales (Jones & Andersson 2002), making it likely that, at any point in time, the majority of the NS population would not be freely precessing. This short damping time-scale makes freely precessing pulsars poor targets for GW searches.

Oscillations

There are a number of different oscillatory modes possible in NSs, for an in-depth review of the different types of modes and the associated physics see Andersson (2003) and Stergioulas (2003). The nature of oscillation modes in NSs depends on the unknown EOS. If GW observations were made from these oscillations it would reveal information about NS interiors and their EOS, which in turn would lead to better models of oscillation modes. The more important modes for GWs are thought to be r-modes, f-modes and bar modes. A phenomenon important for instability modes, is the Chandrasekhar-Friedman-Schutz or CFS instability (Chandrasekhar

1970; Friedman & Schutz 1978). This instability is caused by the emission of GWs. The CFS instability is particularly important for r-modes, as it has been shown that r-modes are unstable to GW emission due to the CFS instability at low rotation frequencies of the star. F-modes are only unstable in this way for unrealistically high rotation frequencies. It is for this reason that r-modes are often considered the most likely oscillation mode for producing detectable GWs. The most likely scenario for r-modes is in newly formed NS, or in NS that are accreting matter in a LMXB (Andersson 1998; Owen et al. 1998). Depending on the properties of NSs, r-modes could last for short periods of time or up to thousands of years.

Non-axisymmetric rigid shape

Non-axisymmetry of the rigid structure of NSs has been the favoured mechanism for several CW searches in recent years (Abbott et al. 2007, 2008b, 2010; Abadie et al. 2011a). It was proposed in Jaranowski et al. (1998). This emission mechanism requires a rigid rotating NS with a non-zero equatorial ellipticity, i.e a triaxial NS, and was introduced in §1.6.4. This model is often referred to as the triaxial rotator model, and simply describes a triaxial NS rotating about its principal axis, emitting GWs at twice its rotation frequency. There is no direct observational evidence to suggest that NSs with significant equatorial ellipticities appear in nature. In light of the lack of observational evidence there has been much theoretical work to provide a prediction of the equatorial ellipticities of NS.

One approach is to estimate the maximum deformation that the crust of a NS is capable of sustaining and this of course depends on the NS EOS discussed in Section 2.2.6. Estimates place these maximum equatorial ellipticities in a range from 10^{-7} for more conventional EOS, up to 10^{-4} for the more exotic EOS invoking quark cores (Owen 2005; Haskell et al. 2007; Lin 2007; Knippel & Sedrakian 2009).

Strong internal magnetic fields with a toroidal component could sustain a significant equatorial ellipticity in NSs. That stars with strong magnetic fields can deform their shape from a perfect sphere was suggested by Chandrasekhar & Fermi (1953), and if, as is the case for pulsars, the magnetic axis is offset from the rotation axis, then the deformation would be asymmetric about the rotation axis and so produce GWs (Cutler 2002; Haskell et al. 2008).

Horowitz (2010) suggests that low-mass NSs would support large equatorial ellipticities owing to the weaker gravitational field of the star, in fact ellipticities of 0.005 could be maintained for a minimal mass NS. It is not suggested that such small NS are formed directly in SN, but rather that they are a result of a normal mass NS fragmenting during its formation or as the result of a subsequent collision.

Low mass X-ray binaries

Low mass X-ray binaries (LMXBs) are thought to contain accreting NS. As the NS accretes matter and angular momentum from its binary companion, it spins up. This scenario was described as the rebirth mechanism for MSPs in Section 2.2.8. NSs in LMXBs are observed to have very similar rotation rates which are well below the rotation rate at which they are expected to break apart. This observation has led to the belief that there is some torque balancing process preventing the NS from spinning up further. The process responsible proposed in Bildsten (1998), is that the accreting matter causes mass asymmetry in the NS which therefore emits gravitational waves, with the angular momentum lost as a result of GW emission balancing with that gained through accretion (Ushomirsky et al. 2000).

2.3 Monitoring noise and detector characterisation

2.3.1 Introduction to detector characterisation and noise

As already stated, the current goal of GW research is to make a first detection, a task which is inherently difficult owing to the weakness of the GW signal with respect to the noise in the detector data. This scenario means that the importance of being able to distinguish between a signal and noise is impossible to understate, and as such a large effort is made by the GW research community to characterise and understand the noise present in the detector data. This point should be emphasized, as particular noise artifacts can appear very similar to GWs from particular types of astrophysical source. CWs from pulsars are expected to be quasi-monochromatic, as they are emitted at a multiple of the pulsars spin frequency and are then modulated by the Earth's rotation and orbit around the Sun. Noise lines in the detector data mirror this type of signal. Instrument glitches are short duration increases in the detector noise and are a frequent occurrence in current detectors. These noise features could be confused with a GW burst signal or even an GW inspiral signal. Given that both glitches and noise lines are present in the detector data in large numbers, there is some probability that they will randomly appear to be coincident in LIGO and VIRGO detector data in the same way a GW signal would be expected to.

As well as characterising the noise present in the detector data, it is also important to be able to spot any new noise artifacts and if possible mitigate their impact on the data. This may be possible by decoupling the noise source from the interferometer mirrors, or where this is not possible, by changing the frequency of

the noise to a frequency where it is less of a problem.

In this Section I will take a look at the noise sources in the low frequency region of the current detectors, discuss a program called Fscan used to study this noise, and present results from the use of Fscan to analyse recent science run data.

2.3.2 Low frequency noise

Sensitivity curves for GW detectors show the strain noise floor across the range of frequencies for which the detector is calibrated. These curves show the lowest noise floor, and so greatest sensitivity, in the central portion of the frequency range with lower sensitivities at high and low frequencies. A plot showing the sensitivity curves for recent science runs for LIGO and VIRGO is shown in Figure 2.6. The noise that limits the sensitivity in the low frequency region for the LIGO interferometers is primarily seismic noise. In the VIRGO interferometer, the mitigation of seismic noise has been achieved to a high degree due to multi-stage suspension system combining pendulums and cantilever springs known as the *superattenuator* (Braccini et al. 2005). Seismic noise is only expected to be the dominant noise source at very low frequencies for Virgo, i.e. below $\sim 10\,\mathrm{Hz}$. The dominant noise in the low frequency region is noise from the control systems (Acernese et al. 2008; Tournefier 2007), whose purpose is to keep the interferometer locked as discussed in §1.4. This noise is caused by the control of mirrors at low frequencies in order to hold the interferometer in resonance (Tournefier 2007).

Seismic noise in the detectors is caused by the movement of the ground that the detector is sitting on, and this coupling into the test masses through their suspensions. Seismic noise can be due to small earth-quakes, human activity such as cars travelling along a near-by road, the wind coupling into the ground by shaking buildings or trees, and even ocean waves (Abbott et al. 2009b). In order to combat seismic noise the test masses can be hung from multiple stage suspensions, as discussed above with reference to the VIRGO detector.

Electrical equipment can introduce noise into the detector data - most notably the mains electricity supply in the country the interferometer resides in couples into the interferometer and creates a noise line at its frequency and harmonics of its frequency. This coupling primarily occurs through the magnetic field of the electricity supply influencing the magnets attached to the interferometer mirrors (Abbott et al. 2009b). The mains electricity noise lines can be seen in Figure 2.6, at 50 Hz for Virgo and at 60 Hz for LIGO, where they clearly stand out far above the background noise floor. The 60 Hz line is of particular interest as the frequency that we expect GWs from the Crab pulsar, a prime target for GW searches, is very close to 60 Hz.

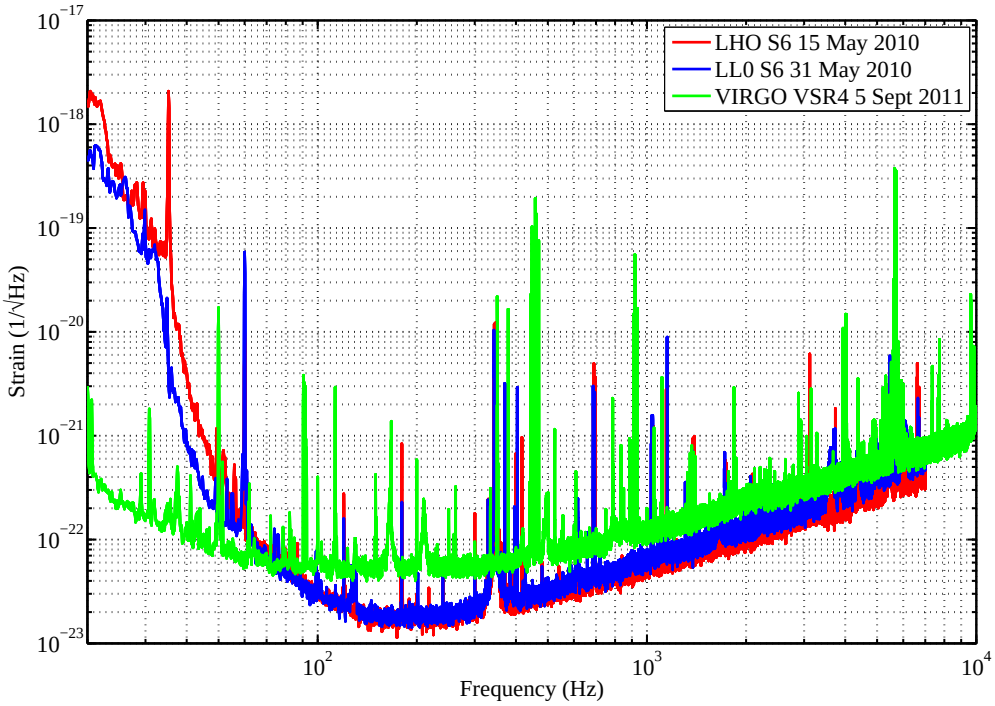

Figure 2.6: The strain/$\sqrt{}$Hz sensitivity noise curves for the LIGO and Virgo interferometers in S6 and VSR4 respectively (The Virgo Collaboration 2010; The LIGO Scientific Collaboration 2010).

Other noise sources are of importance in this frequency region, such as thermal noise and gravity gradient noise, but do not dominate in current detectors. In future detectors where the seismic isolation may be improved, or the location chosen for a quieter seismic environment, these noise sources could become the limiting factor for the sensitivity of the interferometer, and hence much research is currently being carried out to discover ways of limiting their effect on the detectors (Hild et al. 2011).

2.4 Fscan

2.4.1 Introduction to Fscan

In this section I give an introduction to the Fscan software suite. Fscan is a noise monitoring program that I have helped to develop for use with LIGO S6 data, it forms part of LALAPPS (applications built out of the LIGO Algorithm Library (LAL)) and is used for the monitoring and analysis of GW detector noise artifacts.

I have made modifications to Fscan in collaboration with Greg Mendell of LIGO Hanford. These modifications can be split into two distinct areas. The first area

I worked on was the graphical outputs from Fscan. As an on-line quick analysis tool these outputs are essential to the effective utilisation of Fscan for spotting new and troublesome noise artifacts in the detector data. The other area I focussed my development work on was in creating new functionality to enable monitoring of important frequency bands where GWs from certain promising CW sources, such as the Crab and Vela pulsars, are expected. In the rest of this section I provide background introductory material on Fscan, both on how the software works and also the context in which a tool such as Fscan becomes important. I then provide detail of the developments I made to the Fscan software in §2.4.2. In §2.4.3, I show some examples of certain noise features that show up in the outputs from Fscan. I conclude §2.4 by showing some examples where Fscan has been successfully used to identify problematic noise lines in the LIGO S6 and VIRGO VSR2 runs in §2.4.4.

Fscan was created by Rejean Dupuis and Greg Mendell. Its main function is to take as an input the detector data frame files and produce on-line spectrograms and SNR spectra over specified frequency bands of specified interferometer channels. The detector frame files are the output from the detector and give the raw output from many data channels from the interferometer, in particular the differential arm length data which would contain the GW signal. These spectrograms and spectra are used as a visual aid for finding, and helping diagnose the cause of noise artifacts in the interferometer data.

The LIGO detectors' lifetimes consist of time when they are being upgraded and refined, and times when they are being run with a view to taking as much good quality data as possible. The periods of data acquisition are known as science runs, and are referred to by an integer number referring to its place in the sequence of science runs prefixed with a capital S for science (i.e S1, S2 etc). The LIGO science runs aim to coincide with similar periods of operation at other GW observatories around the world, such as GEO 600 and VIRGO, in order to provide a means of verifying results and triangulating sources in the event of a detection. During a science run at LIGO the interferometers are operated and maintained by full-time staff working in shifts known as operators. Also working in shifts are science monitors (SciMons), who are usually GW research scientists. Their job is to monitor the detector data, including a large number of auxiliary channels containing data from a range of physical environment monitor (PEM) sensors, during the science run for any new or problematic sources of noise. Fscan is designed to aid the SciMons in this task.

During a science run noise artifacts will appear in the detector data. When this noise artifact is present for a sustained period of time and exhibits a lot of power confined to a small frequency band it is dubbed a noise line, or simply a line. The origin of such lines may be due to some instrumental or environmental

noise source, or the line could actually be a GW signal. When a line is identified as noise, efforts can be made to track down the source and remove or mitigate its effects on the detector data. It can also be added to a list of known instrumental and environmental lines which can then be used to rule out GW detection candidates produced by all-sky searches for CWs. The visual outputs from Fscan, i.e. the spectrograms and the spectra, make it easy and quick to spot the appearance of new noise artifacts and this is aided by the output plots being shown next to reference plots. These reference plots can be used to compare current results against the same channel at a time when the interferometer was thought to be in a good state. Any increase in noise at a particular frequency, or the appearance of a new line will be easily identifiable through a visual comparison of these plots. This referencing feature can also be used to compare a PEM auxiliary channel against the GW signal channel over the same time period. The PEM auxiliary channels record data from instruments such as magnetometers and accelerometers which are placed at a number of positions around each interferometer. By checking for coherence between one of these auxiliary channels and the GW channel, it is possible to track down the location and the type of source that is causing the noise.

Fscan is designed to be run on the LSC computing clusters using Condor. Condor is a *workload management system* for managing multiple computationally intensive jobs from multiple users on computer clusters (The Condor team 2009). There are three separate codes that make up Fscan, these are spec_avg.c, plotSpecAvgOutput.m and FscanDriver.py. FscanDriver.py generates a Condor *SuperDag*, which determines how Condor should run the other *dags* (jobs), the number of which depends on the options passed to FscanDriver.py. If the user decides to create short time Fourier transforms (SFTs) specifically for the purpose of running Fscan an optional extra *dag* is created that calls the program MakeSFTs, which will create SFTs for the specified interferometer channels and time period. The alternative to this option is to pass the program existing SFTs. The spec_avg.c reads in the SFTs, computes the spectral power for discrete frequency bins for each SFT and writes this to a file. The plotSpecAvgOutput.m code reads in the file output from spec_avg.c and plots the data to produce a spectrogram and spectra. It is also possible to specify a set of reference plots against which the newly created plots are compared and any spectral lines coincident with the reference are flagged.

An example spectrogram and SNR spectra produced by Fscan is shown in Figure 2.7. In this particular spectrogram it is possible to see a strong spectral line that wanders in frequency at $\sim 58.7\,\mathrm{Hz}$. This shows the strength of this kind of visual analysis as such "wandering lines" can be very quickly and easily be identified by eye whereas automated tracking of such features is more involved. It is also possible to see the edge of the 60 Hz line and how this varies over time. It appears, that

for this time period at least, the 60 Hz line has little effect on the data at the Crab frequency (which is at 59.54 Hz).

2.4.2 Developing Fscan

I have made a number of changes to the output of Fscans, these are:

- To enable the user to specify the frequency resolution of the plots. Being able to choose the frequency resolution used in the plots is important, as some lines may be sufficiently small to not appear in Fscans that use a coarse resolution. This was particularly helpful for the studies I completed of small frequency bands around frequencies at which we expect GWs from important CW sources, which is discussed later in Section 2.4.4.

- To show time in days along the x-axis, this was previously the SFT number. This change to the labelling of the plots was made to improve the speed at which Fscan outputs can be compared against other information relevant to the detector and its data. In a tool such as Fscan, that is primarily there to perform quick intuitive analyses, the speed and ease at which such rough analyses can be carried out is critical in it being of benefit to the user.

- To show any gaps in time that occur between the SFTs in the spectrogram. This alteration was needed for the same reasons as the modifications to the labelling of the x-axis, that is to make possible the comparison of Fscan outputs with other sources of information relevant to the detector.

- To change the start and end times from GPS seconds to UTC time, once more to improve the ease at which Fscan's outputs can be compared against other information relevant to the detector, for example the time that a truck was making a delivery to the site.

- To flag new spectral lines that show up against the reference Fscan or any that have disappeared since the reference. The flagging of new spectral lines, and lines that have disappeared, is primarily used by people looking to perform more in depth detector characterisation studies, such as Coughlin et al. (2010). The line flagging algorithm in Fscan already existed, my contribution here was to compare the lists of the flagged lines in the new data and the reference data.

- To Kurtosis test each 0.25 Hz band of data and print the results to a text file. The kurtosis testing is also designed for those wishing to make further studies. The kurtosis test is used to measure the Gaussianity of data, it reflects how outlier prone the data is, with a larger number showing that the distribution

has more outliers than a smaller number. The idea of using this in Fscan was that it could be used to identify frequency regions which were regularly prone to large outliers.

As well as the changes listed above, I have developed Fscan so that it can be used to monitor the noise in the frequency band at which we expect GWs from known pulsars. This new feature simply plots the frequency at which GWs are expected from the specified pulsar onto the spectrogram that serves as the main output from Fscan. This feature was designed with the Crab and Vela pulsars in mind but can be run for any pulsar given the relevant information. This information is passed to the Fscan code in the form of a ".par" file. This is a standard file type in pulsar astronomy but can contain different information depending on what is known about the pulsar. For example if the pulsar is in binary system, the .par file will contain the parameters of the binary orbit. The essential information needed for Fscan about the pulsar include the position of the pulsar and its frequency and frequency derivative. For the Crab pulsar, where accurate timing of its spin evolution needs to account for timing noise (Pitkin & Woan 2004), a monthly ephemeris produced by Jodrell bank is an optional extra input for Fscan. For the Crab pulsar this monitoring was thought to be particularly relevant, due to the presence of a 60 Hz noise line in the LIGO detectors' data close to the Crab GW frequency band and the status of the Crab pulsar as a prime target for GW searches. The 60 Hz line is produced as a result of the AC frequency of the mains electricity in America coupling to the interferometer mirrors. The line wanders around in frequency and produces noise features within an area 2 mHz wide around the central frequency (Lazzarini et al. 2009). The pulsar ephemeris data is read into the spec_avg.c code. The code calculates the Doppler modulation of the GWs due to the Earth's rotation and by its orbit around the sun. This Doppler modulation is computed for the time centred at each SFT, enabling the calculation of the frequency of GWs from the source observed at Earth (simply referred to as the source's GW frequency from here onwards). The doppler modulation of the signal is not sufficiently large to show up on an average Fscan plot. Also produced is a plot of the spectral power density in a 1/60 Hz band centred on the source's GW frequency. Together these outputs enable a qualitative assessment of how the instrumental noise affects analyses looking for CW from known pulsars.

2.4.3 Using Fscan to identify types of noise artifact

Using Fscan, primarily the spectrogram output from Fscan, it is possible to catalogue some of the types of noise artifacts. One such noise artifact is the spectral line, as already discussed in Section 2.4.1. These appear as horizontal lines in an

Fscan spectrogram. A line is characterised by large amounts of power confined to a small frequency range. Such lines can be wandering lines, i.e. the frequency of the line is seen to change over time, an example of such a line is shown in Figure 2.7 at ~ 58.7 Hz. Lines can also be very stable over time and an example of a static line is shown in Figure 2.8 there are a few such lines in this plot, but there is one that stands out very strongly from the background at ~ 720 Hz. Lines can vary in thickness from the relatively thin, as in Figure 2.8, to the very broad, as the lines at ~ 690 and ~ 695 Hz in Figure 2.9 demonstrates.

An entirely different noise artifact is that of the glitch, a glitch is characterised by an increase in the noise across a wide frequency band, up to 1000 s of Hz, over a short period of time, typically of the order of seconds (Blackburn et al. 2008). The primary tool for looking at glitches is a piece of software called Omega scans, which was previously known as Qscans (Blackburn et al. 2008; Isogai et al. 2010). This produces spectrograms as Fscan does, but with much higher time resolution and for much shorter periods of time. A noise feature lasting such a short time may not appear in Fscan, as each bin in time is representative of half an hour of detector data. If they were to appear in Fscan spectrograms they would likely appear only in one time bin as a vertical line of increased power. Such features appear regularly in Fscan, and examples are shown in Figures 2.10 to 2.12, where the glitch, if indeed I can classify it as such, appears at roughly at time ~ 0.16 days. It can be seen at frequencies ranging from 50 Hz up to around 500 Hz where it begins to fade into the background noise. Figures 2.10 to 2.12 shows Fscans of three frequency bands spanning the total range that the glitch is visible at. It is not practical to include more here, however the interested reader can see the full set of Fscans across all frequency ranges at https://ldas-jobs.ligo-wa.caltech.edu/ pulsar/fscan/hoftS6/fscanNavigation.html.

A different noise artifact that appears in Fscan is shown in Figure 2.13. This feature does not have a name, but it does have a very distinctive appearance. I have only observed it in the Virgo detector, and it only appears after the interferometer has regained lock, suggesting some link with the locking process. It appears as if these features are in fact static noise lines that undergo a broadening shortly after the interferometer has regained lock, the breadth of the line then rapidly shrinks.

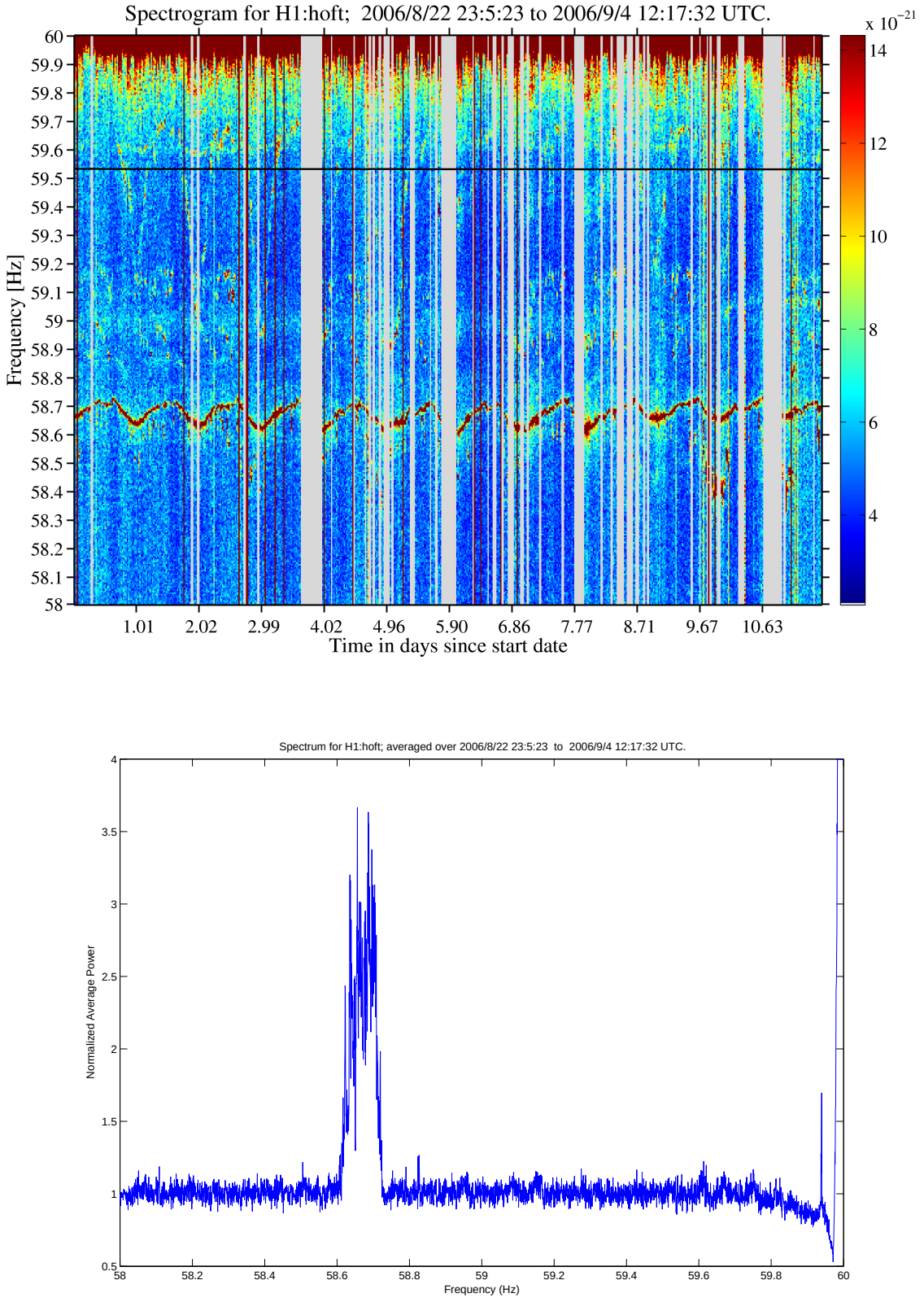

Figure 2.7: An example spectrogram and spectra output from the Fscan program for the 4km interferometer at LIGO Hanford. There is a spectral noise line present in the data which clearly shows up on both plots at $\sim 58.7\,\mathrm{Hz}$. The frequency of GWs as they would be observed at Earth from the Crab pulsar is plotted over the spectrogram as a dashed black line at $59.5\,\mathrm{Hz}$.

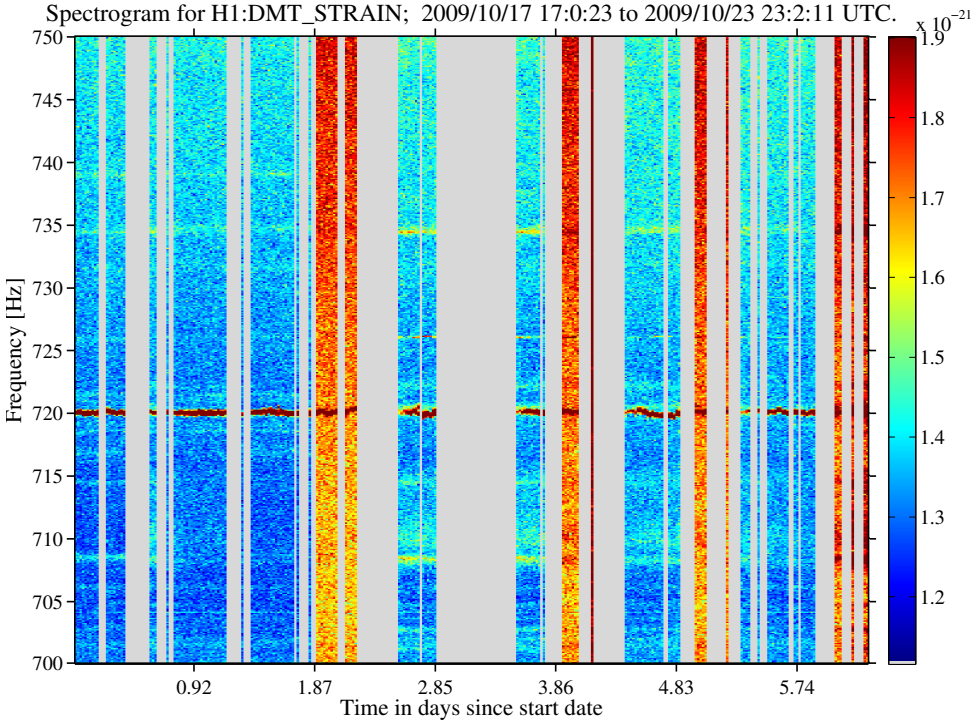

Figure 2.8: A Fscan spectrogram demonstrating the existence of a stationary spectral line, although there is more than one line in this spectrogram, it is very clear to see one in particular at $\sim 720\,\mathrm{Hz}$.

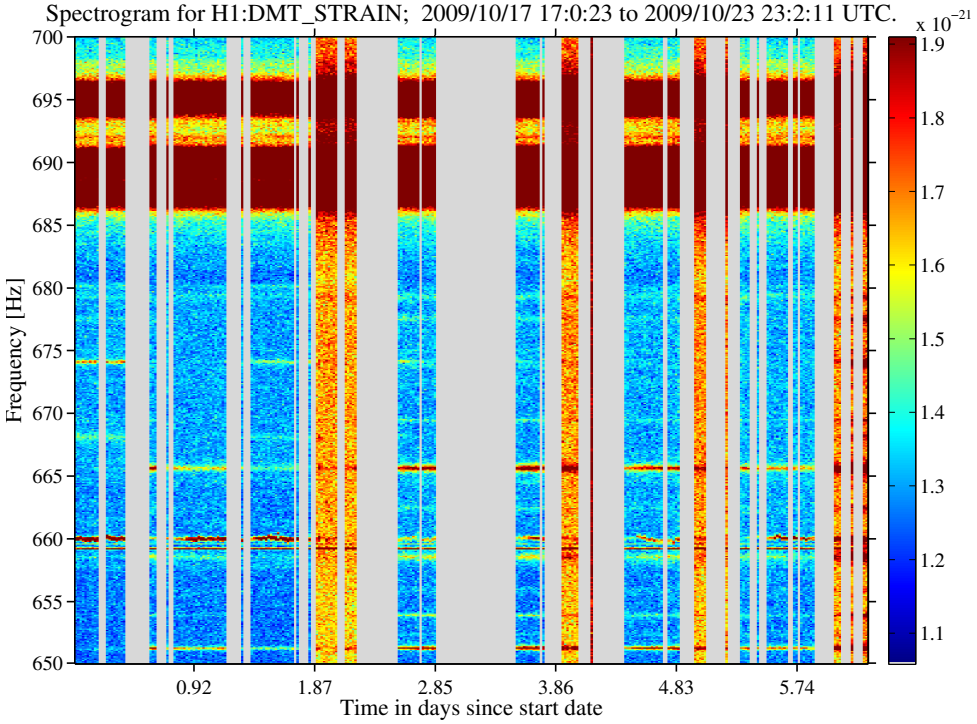

Figure 2.9: An example spectrogram from the Fscan program for the 4km interferometer at LIGO Hanford, showing two broad stationary spectral lines at ~ 690 and $\sim 695\,\mathrm{Hz}$.

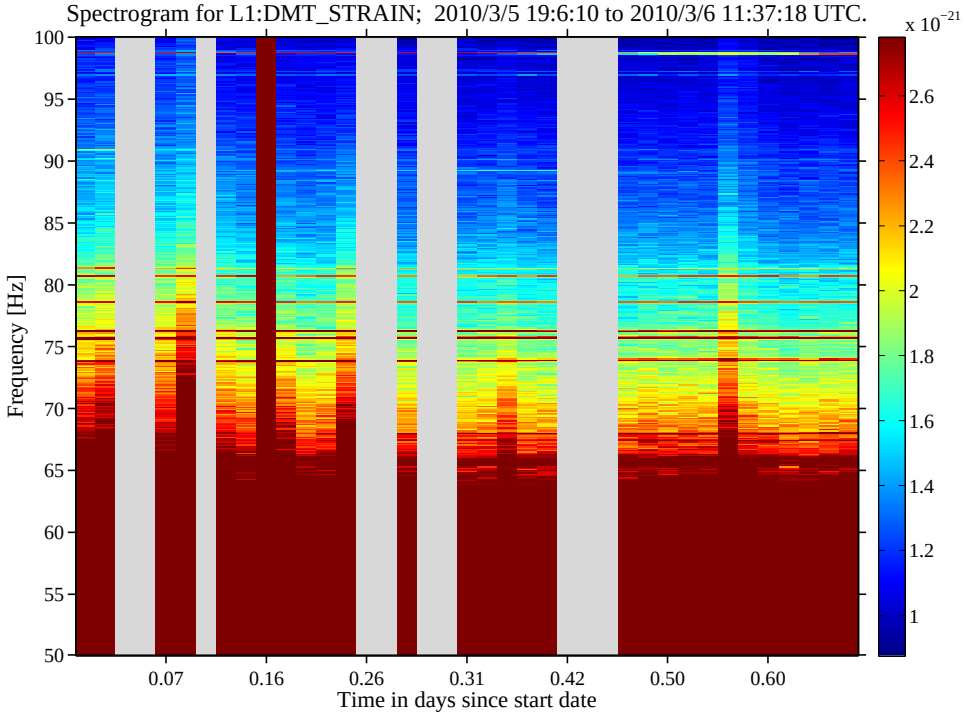

Figure 2.10: A Fscan spectrogram from 50 Hz to 100Hz showing examples of one time bin wide vertical line of increased power, possibly due to an instrument glitch. This particular "glitch" is seen across a frequency range from 50 Hz to $\sim$ 500 Hz at time $\sim$ 0.16 days.

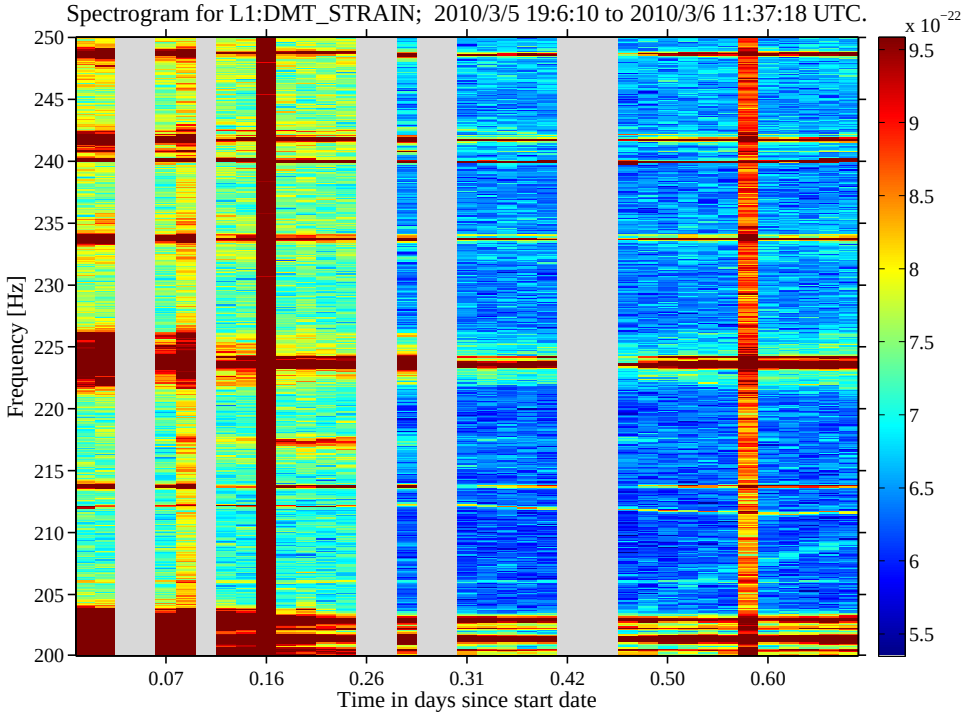

Figure 2.11: A Fscan spectrogram from 200 Hz to 250 Hz showing examples of one time bin wide vertical line of increased power, possibly due to an instrument glitch. This particular "glitch" is seen across a frequency range from 50 Hz to $\sim$ 500 Hz at time $\sim$ 0.16 days.

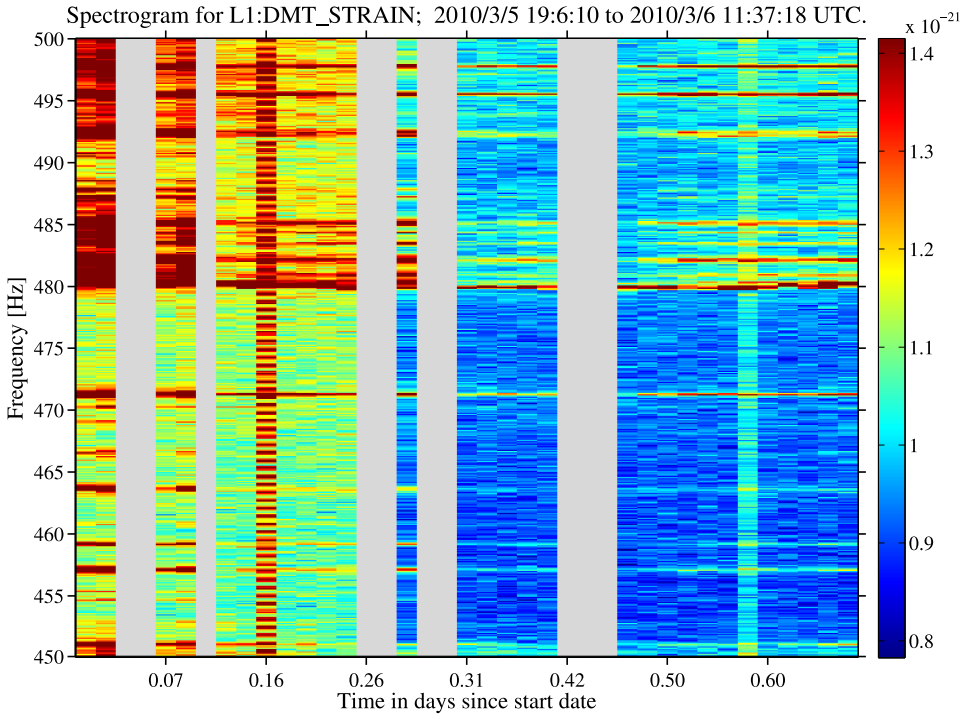

Figure 2.12: A Fscan spectrogram from 450 Hz to 500 Hz showing examples of one time bin wide vertical line of increased power, possibly due to an instrument glitch. This particular "glitch" is seen across a frequency range from 50 Hz to $\sim$ 500 Hz at time $\sim$ 0.16 days.

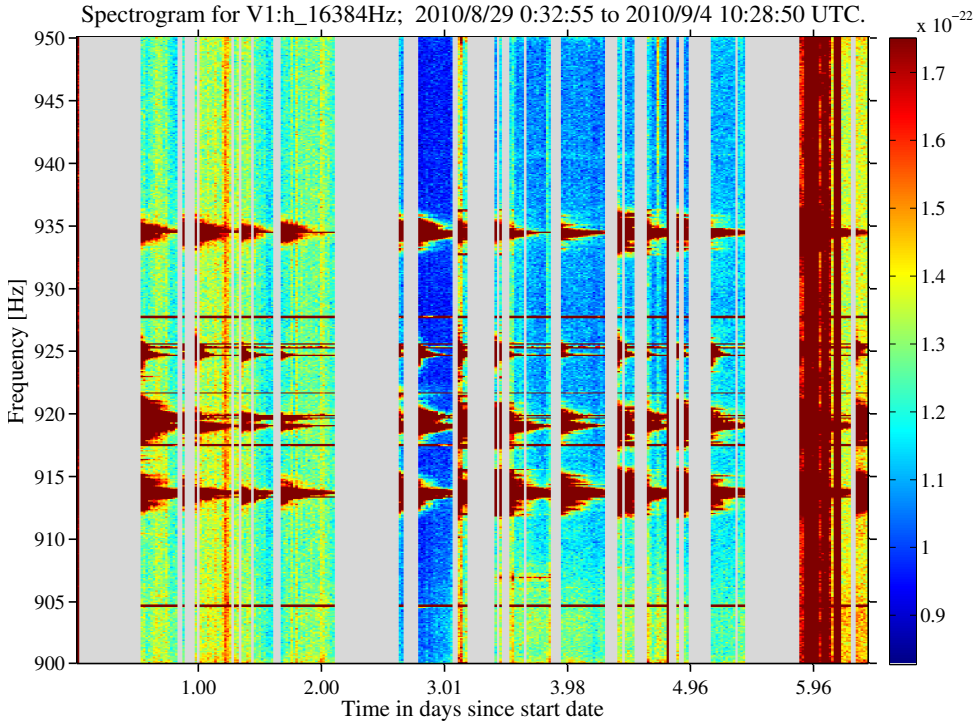

Figure 2.13: A Fscan spectrogram showing a particular noise feature in the Virgo interferometer, which appears to be linked to the loss and regain of lock. After lock is regained the noise lines at $\sim$ 915, $\sim$ 920, $\sim$ 925, and $\sim$ 935 Hz are at their broadest, but immediately decrease in width before a subsequent loss and regains of lock sees the line back at its maximum width and the pattern repeating itself.

2.4.4 Fscan monitoring results

Fscan was used on a daily basis during S6 and VSR2, VSR3 and VSR4 by Greg Mendell for a number of interferometer channels for the LIGO and Virgo respectively. The output from these daily runs can be viewed (with the relevant username and password) for the LIGO Hanford interferometer and for the LIGO Livingston interferometer. The numerical output from these Fscans has been analysed further by others in the LSC for the purpose of line tracking and identification (Coughlin et al. 2010).

Over the duration of the S6 run I used Fscan to monitor a 1 Hz band around the Crab frequency. I set Fscan to run automatically at the start of each day on the previous days data, resulting in a webpage where a user can quickly identify obvious issues simply by examining the plots by eye. Once a potential problem has been highlighted in this way, it is then possible for others to characterise the problem noise more thoroughly with more detailed and in-depth analyses, and search for a potential source, possibly with the use of Fscans of the auxiliary channels. Over the period of S6 I twice spotted instrumental lines that were adding to the noise at the Crab frequency band, therefore degrading the sensitivity of analyses searching for GWs from the Crab pulsar. One such line is shown in Figure 2.14. This line had long been present in the data, however around the 28th of June 2010 the line started to move around in frequency and began to affect the frequency band for the GWs from the Crab pulsar. The cause of this line was found to be a water chiller pump by people working at the LIGO Hanford site. When the load to this pump was decreased the frequency of it's spectral noise line increased and once the source was found, removing its affect on the Crab frequency band was as simple as restoring the load to the pump (Coughlin et al. 2010). Fscan spectrograms of the whole S6 run for both L1 and H1 are shown in §4.4.

As well as running Fscans in a band around the Crab frequency I also ran Fscans on a band around the Vela frequency on VIRGO data (the LIGO data is not calibrated down to the Vela frequency). The Vela frequency is 22.38 Hz. I did not set up the automated generation of these Vela Fscans until the start of VSR3, but was able to run Fscans retrospectively on VSR2 data a few months before the start of VSR3. In doing so I identified a pair of lines that were very close to, and overlapped with the Vela frequency and this can be seen in Figure 2.15. These spectral lines clearly add noise to the data at the Vela frequency and hence degrade the sensitivity of any searches for GWs from Vela using this data, such as the searches presented in Chapter 3. The lines are clear to see, are present in the entire data run, and can be seen to evolve over the run. The scientists at VIRGO have their own noise monitoring software similar to Fscan, called NOEMI, that they had used to monitor

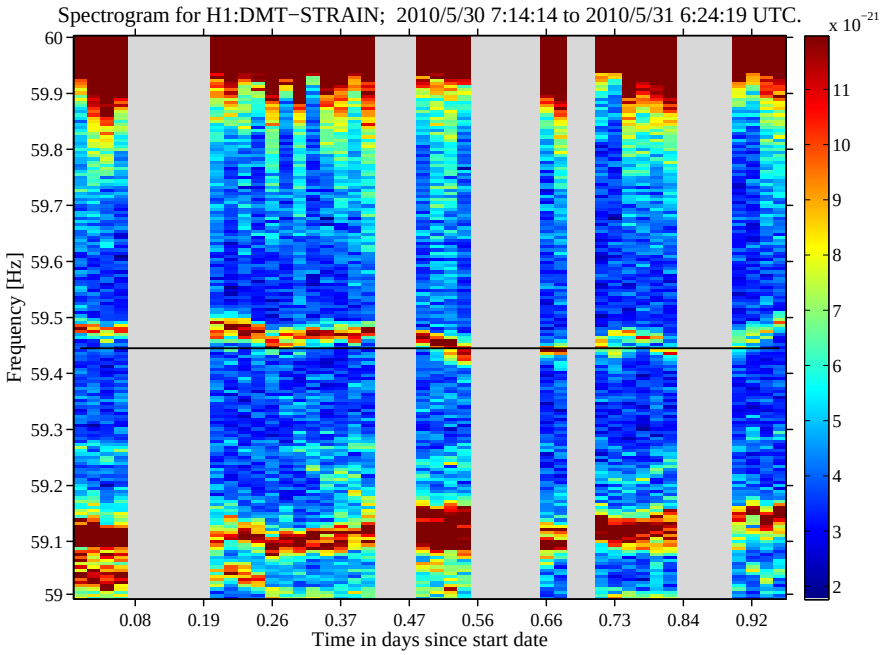

Figure 2.14: A Fscan spectrogram showing the appearance of a noise line in the data near the Crab frequency. After identifying the appearance of this line my LSC colleagues were able to track down and eliminate the source of this noise.

VSR2, but due to frequency resolution issues these noise lines remained undetected by NOEMI. After the detection of these lines by Fscan the parameters that were used to run NOEMI were changed so that these lines were visible. It was unfortunate that these lines were affecting the data in the Vela band, as Vela is a prime source for CWs at frequencies where Virgo outperforms the LIGO interferometers. It is estimated by Abadie et al. (2011a) that the chiller lines reduced the sensitivity of the search for GWs from the Vela pulsar in VSR2 data by 20% with respect to the background. Further work at VIRGO isolated the cause of the lines as a water chiller pump and the pump was subsequently modified during VSR3 to move the lines away from the Vela band.

2.5 Summary

In this chapter I have provided introductory material about pulsars as CW sources in the 10 to 100 Hz band, and also described how this region appears in the data from current ground based detectors. It is clear that this "low frequency' portion of the interferometers spectrum contains some significant noise features, notably the seismic wall and lines caused by the mains electricity in the country of operation (50 Hz and 60 Hz). I have introduced the Fscan program as a tool for finding spectral

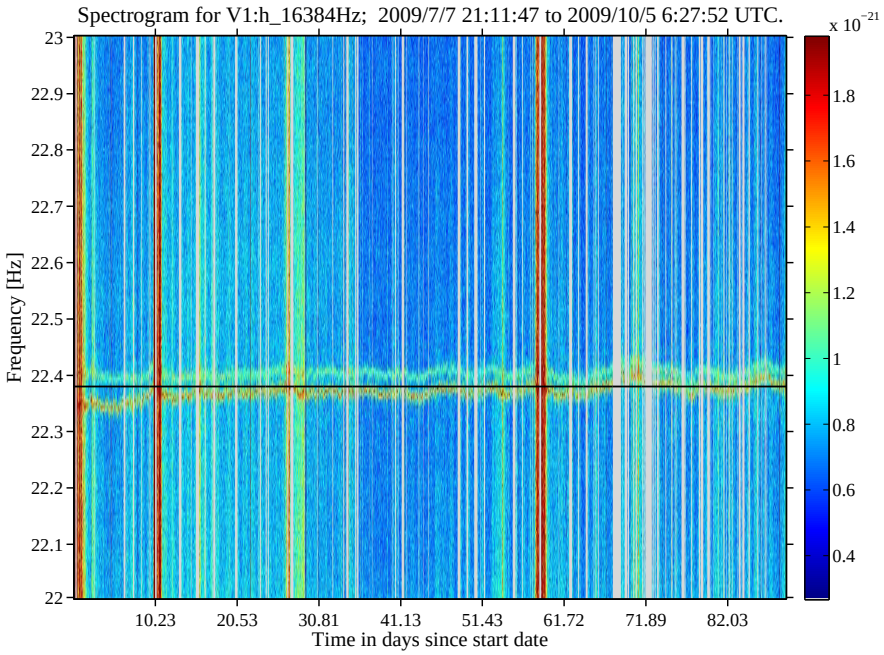

Figure 2.15: A Fscan spectrogram showing a pair of instrumental noise lines around the Vela frequency in Virgo data during the VSR2 run. The cause of the lines was found to be a water chiller and through modifications to the chiller, the lines were shifted such that they no longer made an impact on the data at the Vela frequency.

noise lines in the detector data. The importance of data quality monitoring in this unsophisticated but intuitive way, particularly around frequencies thought to be key for GW detection such as the Crab and Vela pulsars, has been demonstrated by the new noise lines discovered in S6 and VSR2 data.

Chapter 3

Searching for GWs from the Vela pulsar

3.1 Introduction

This Chapter presents the search for GWs from the Vela pulsar (PSR B0833-45, J0835-4510) using data from the Virgo Science Runs 2 and 4. The analysis method used to perform these searches is the complex heterodyne and Bayesian parameter estimation method described in §1.6.5. This chapter begins with some background introductory material about the Vela pulsar in §3.2. The data and timing models used in the analyses are discussed in §3.3 and §3.4. In the following section §3.5, results are presented and discussed from the analysis of hardware injections in the Virgo science runs, a process which provides an important check for the data and methods used for the search for GWs from Vela. The results of the searches for GWs from Vela and their discussion conclude this chapter with §3.6 and §3.7.

3.2 The Vela Pulsar

PSR B0833-45 was discovered in 1968 (Large et al. 1968), in the Vela supernova remnant, providing some of the first direct observational evidence that established pulsars are rotating NSs. Since the initial detection of radio pulses from Vela, there have been subsequent observations of pulses in the visible, X-ray and γ-ray parts of the spectrum. The γ-ray pulses from Vela are particularly strong (Razzano 2009), making it the strongest non-transient γ-ray source in the sky (see Figure 3.1), whilst it is also one of the strongest radio pulsars. As a source of GWs Vela looks appealing. It is young (with an implied age of $\sim 11000\,\mathrm{yr}$) and therefore has a high spin-down ($\dot{f} \simeq -1.56 \times 10^{-11}\,\mathrm{Hz/s}$), meaning that there is a large amount of energy lost from the system which could be powering GW emission. Vela's relative proximity

of $\sim 300\,\mathrm{pc}$ also marks it out as a prime source for GW detection as the strength of GWs falls off as $\tilde{h}_s \propto f^2/r$.

A useful a priori upper limit can be placed on the GW strain from a spinning star called the spin-down limit (Brady et al. 1998; Abbott et al. 2008b). This limit is computed by assuming that all the rotational energy lost from a source is due to GW emission, which for Vela is $h_0^{sd} = 3.3 \times 10^{-24}$. This scenario is unrealistic as we know that pulsar spin-down is due to a number of mechanisms, including magnetic dipole radiation. However the spin-down limit does provide us with a useful benchmark. If it is possible to place an upper limit on the GW emission below the spin-down limit then this can constrain the fraction of spin-down energy lost due to GWs. The spin-down limit for Vela is the highest for all known pulsars. However Vela is at a disadvantage compared to many other pulsars that are potential GW search candidates, as the rotation frequency of Vela ($\sim 11\,\mathrm{Hz}$) (Radhakrishnan et al. 1969), and hence the frequency of GWs ($\sim 22\,\mathrm{Hz}$), is near the low frequency limit of current detectors. This has meant that previous science runs of the LIGO and Virgo detectors (S5, VSR1) did not have sufficient sensitivity at $\sim 22\,\mathrm{Hz}$ for Vela to be considered a good search target. With the sensitivity achieved at low frequencies in the VSR2 run Vela has become a more appealing target. The most recent LIGO science run (S6) however does not match the sensitivity of VSR2 at lower frequencies, meaning that a search for GWs from Vela gains no advantage from including data from the LIGO detectors. Figure 3.2 shows the spin-down limit of Vela (3.3×10^{-24}) on the same axes as the noise curves for the current GW detector's science runs. It is clear from this plot, that the addition of LIGO data would bring little benefit to a search using Virgo data, where the advanced seismic isolation system of Virgo results in a significantly lower noise floor at $\sim 22\,\mathrm{Hz}$ (Acernese et al. 2008). The curves shown in Figure 3.2 are scaled to the amount of science mode data available from each run, however this scaling does not reflect the sensitivity of my search as it does not take into account the attenuation of the GW signal due to the antenna pattern.

There has been only one previous targeted search for GWs from Vela. This used 16 days of data from the Cryogenic Laser Interferometer Observatory (CLIO) detector in Japan taken in 2007 and produced an upper limit of 5.3×10^{-20}, well above the spin-down limit of 3.3×10^{-24} (Akutsu et al. 2008).

The search method used in the analyses described in this chapter, is that described in §1.6.5, and consists of performing a complex heterodyne of the data, and then applying a MCMC to the heterodyned dataset to perform a Bayesian parameter estimation analysis.

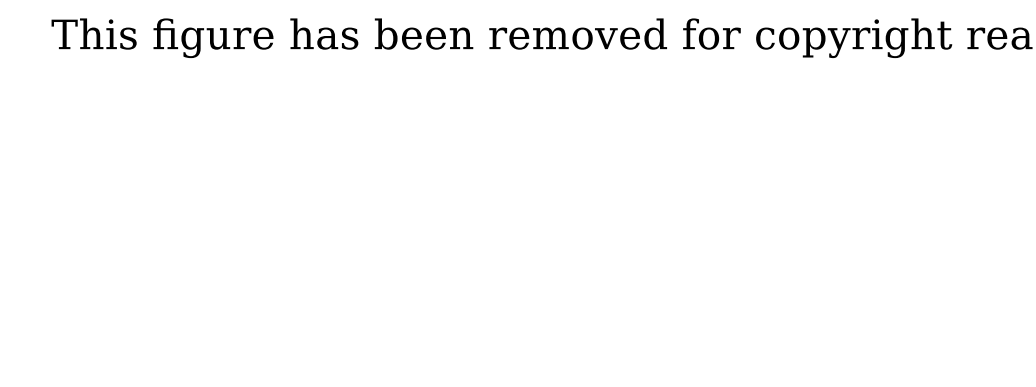

Figure 3.1: An all-sky image of the γ-ray sky showing the Vela and Crab pulsars as some of the brightest γ-ray sources, from GLAST (NASA/DOE/International LAT Team 2010).

3.3 The Data used in the Search

The VIRGO science run 2 (VSR2) started on Jul 07 2009 21:00:00 UTC and finished on Jan 08 2010 22:00:01 UTC. The noise curve for this run is shown in Figure 3.2. Segments of data from a LIGO/Virgo collaboration science run have various flags assigned to them which indicate the state of the interferometer during that time. The flag that indicates the best possible quality data is known as "science mode", and the segments of data assigned as science mode data are known as science segments. To perform the search for a GW signal from Vela, I used all the available science mode data. The data presented from VSR2 in this chapter has been calibrated using a particular calibration that has been named *HrecV3*. There are also *HrecOnline* and *HrecV2* calibrations, although it was found that these calibrations were inaccurate at lower frequencies, and therefore would have had an impact on an analysis for Vela. The difference between the VSR2 data generated using these different calibrations is shown in Figure 3.3, which shows the real and imaginary parts of data which has been heterodyned for the Vela pulsar. It is clear that for the earlier part of the VSR2 run, the different calibrations result in significantly different data.

Analysis of the VSR2 data post-run using the Fscan program found a previously

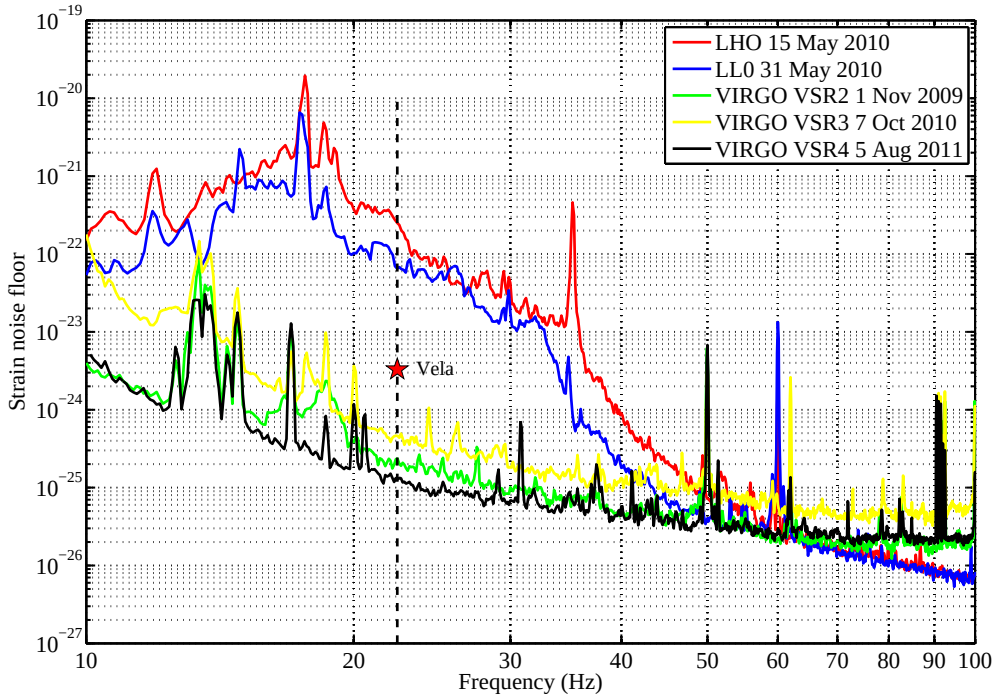

Figure 3.2: The RMS strain sensitivity noise curves for the LIGO and Virgo interferometers during S6, VSR2, VSR3 and VSR4. Each sensitivity curve is scaled to the length of its run by dividing the strain/$\sqrt{\text{Hz}}$ by $\sqrt{T}$, where T is the time in seconds of science mode data for each run. The spin-down limit is plotted for the Vela pulsar as a star at twice Vela's spin frequency. The points at which the dashed line intersects the noise curves shows the noise floor in Virgo data at twice the spin frequency of the Vela pulsar is more than 100 times lower than in LIGO data. (The Virgo Collaboration 2010; The LIGO Scientific Collaboration 2010).

unknown noise artefact in the frequency band at which we expect GWs from Vela. The noise presented itself in the form of a pair of "lines" that wandered in frequency about the Vela frequency. Analysis of these lines is presented in Section 2.15, and they are clearly visible in the Fscan of the whole of the VSR2 run in Figure 3.4. Although these lines appear as multiple lines they move in the frequency space together indicating that they are likely to share the same source. The discovery of these lines in VSR2 data led to considerable analysis by VIRGO staff and subsequent successful efforts to isolate the source of the noise and to mitigate its affect on the data. To see some of the analysis of these noise lines carried out by the Virgo staff see Accadia et al. (2012). The source of these lines was found to be a chilled water pump. By making modifications to the pump the noise lines were moved to a frequency at which they do not elevate the noise floor for the data used in Vela searches. It is estimated that the effect of the noise lines has decreased the sensitivity of the searches by 16%.

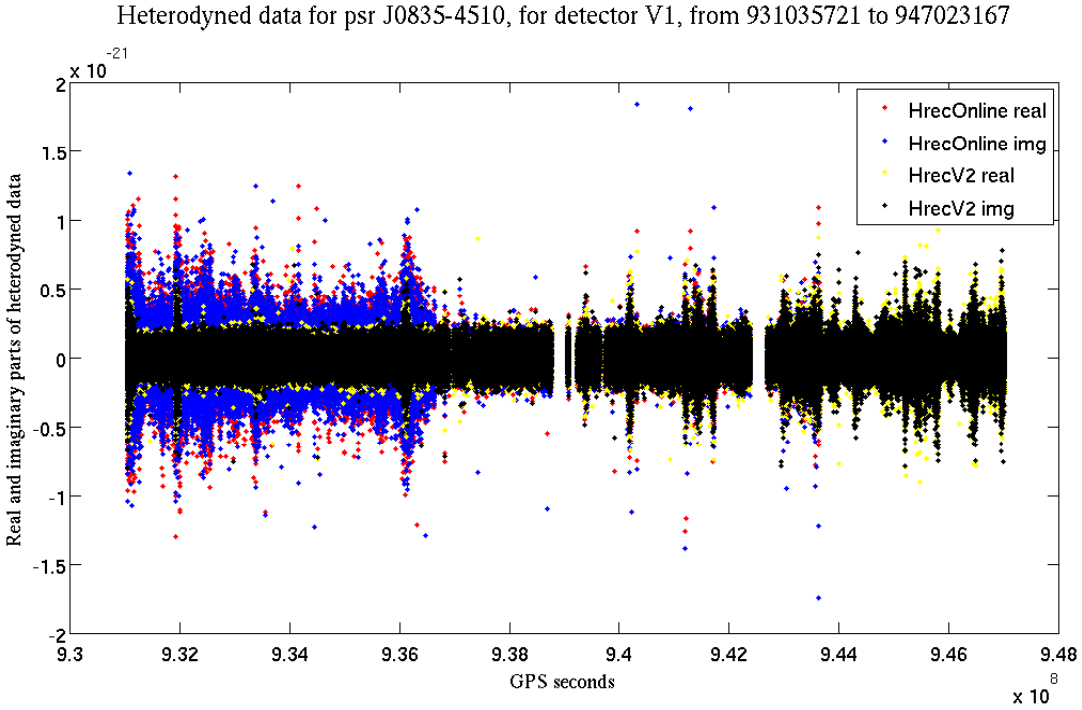

Figure 3.3: A plot of the heterodyned data for Vela using the HrecOnline and HrecV2 calibrations. The difference between the two calibrations is clear to see in the early part of VSR2.

The heterodyned VSR2 data for Vela are shown in Figure 3.5, from which it is possible to see the evolution of the noise floor over the run. It is possible to see a large number of sudden increases in the data in Figure 3.5. These spikes are seen to be more prevalent in the latter half of VSR2, where the noise floor appears in general much less stable than in the first half. This plot is also used to check that no extreme outliers have been missed by the data cleaning process that forms part of the search code. Although there are some clear outliers in this plot, these are not sufficiently extreme to significantly alter the result obtained with this data.

The data cleaning process is included in the heterodyning part of the code, and aims to remove any outliers that may be due to instrumental effects. This is done by removing any data-points that lie outside a specified limit defined as a $n\sigma$, set to 5σ as standard. To investigate the effect of this process on the analysis we have repeated the VSR2 Vela analysis using two different outlier removal methods and also a control where no outliers are removed.

The standard 5σ outlier removal rejected 100 data-points out of 205641. The first alternative method of outlier removal is manual removal of outliers, this is done by simply looking at a plot of the fine heterodyned data (without the 5σ), and choosing a cut-off where data greater than this distance from zero are removed. This cut-off value was chosen as 1×10^{-20} for the VSR2 Vela data, and this removed 22 outlying

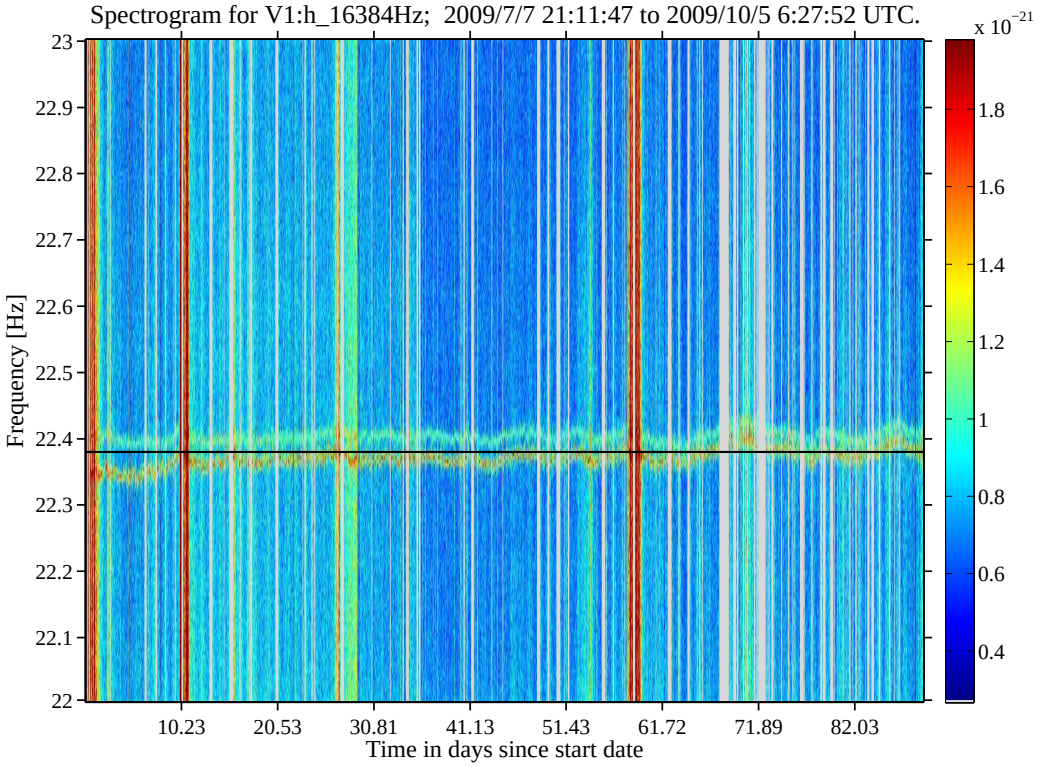

Figure 3.4: A Fscan plot of the whole of VSR2. The expected frequency of GWs from Vela is plotted in black at $\sim 22.4\,\mathrm{Hz}$. The chiller lines are clear to see at $\sim 22.4\,\mathrm{Hz}$ and $\sim 22.35\,\mathrm{Hz}$. It is also clear to see the variation in the detector noise over time.

data-points. The second alternative outlier removal method is by using the Grubbs test. The Grubbs test works by assuming that the data is accurately described by a Gaussian distribution, the data-point that is the farthest from the mean is examined and if it falls above a critical value it is considered to be an outlier and is removed (Grubbs 1969). This process is repeated iteratively until no more outliers are found. The Grubbs test is the preferred method used in the $\mathcal{F}$-statistic and $\mathcal{G}$-statistic Jaranowski & Królak (2010) analyses described in Abadie et al. (2011a). This test is applied to the coarse heterodyned data and at this stage in the heterodyne process the data is sampled at 1 Hz and the final fine heterodyne the data is sampled at 1/60 Hz. When the coarse heterodyned data has had the Grubbs test applied, and is then put through the fine heterodyne process, the resulting fine heterodyned data has 3184 less points than the un-cleaned fine heterodyned data which has 205641 data-points, a removal of $\sim 1.5\,\%$ of the data. The heterodyned datasets with outliers removed were then run through the MCMC parameter estimation code 20 times each. The MCMC was repeated in order to to account for the variability in results obtained using this method. As a check the parameter estimation was also

repeated using a grid based Bayesian parameter estimation analysis. The resulting 95 % upper limits on h_0, referred to as $h_{0,95}$ are shown in the Table 3.1.

Outlier removal method	mean $h_{0,95}$ (MCMC)	σ on $h_{0,95}$	$h_{0,95}$ (grid)
none	2.360e-24	8.44e-26	2.367e-24
manual	2.353e-24	5.42e-27	2.367e-24
5 σ	2.354e-24	8.31e-27	2.366e-24
Grubbs test	2.390e-24	7.78e-27	2.413e-24

Table 3.1: A comparison of the upper limits determined from data which has had different outlier removal methods applied.

The differences in the upper limits on h_0 are very small between the different outlier removal methods. The difference between no outlier removal and the manual and 5σ methods in particular show very little variation. The most variation is seen between the Grubbs test method compared to the others. Typical calibration errors in the data are of the order of a few percent (Accadia et al. 2011b), and hence the answer quoted for $h_{0,95}$ is normally only to 2 significant figures, so in fact there would be no difference in the quoted value for $h_{0,95}$ for any of these methods.

The VIRGO science run 4 (VSR4) started on Jun 03 2011 21:00:00 UTC and finished on Sep 03 2011 05:00:00 UTC. The VSR4 run represents the most sensitive run for VIRGO to date at frequencies below ~ 50 Hz. For VSR4 the chiller pump that caused the noise lines in VSR2 was modified such that its frequency, and hence the frequency of the noise lines it is responsible for producing, was moved to a range where it would not degrade any searches for known GW sources, including Vela. The heterodyned VSR4 data for Vela are shown in Figure 3.6, where it is possible to see the evolution of the noise floor over the run.

3.4 The timing model used in the searches

The complex heterodyne stage of the search which removes the expected phase evolution of the GW signal from the data needs a precise model of the phase evolution of the expected signal from the pulsar in question. To determine this phase model we assume that the GWs are phase locked with electromagnetic pulses emitted from the pulsar. Detailed timing of these pulses is carried out by several radio telescopes, and it is from this data the phase model is formed Abadie et al. (2011a). The time of arrival data (TOAs) of the radio pulses were supplied by two different observatories: the Mt. Pleasant Observatory near Hobart in Tasmania (which has two antennas, the 26-m Mt Pleasant antenna and the 14-m Vela antenna built specifically for observing the Vela pulsar), and the Hartebeesthoek Radio Astronomy Observatory

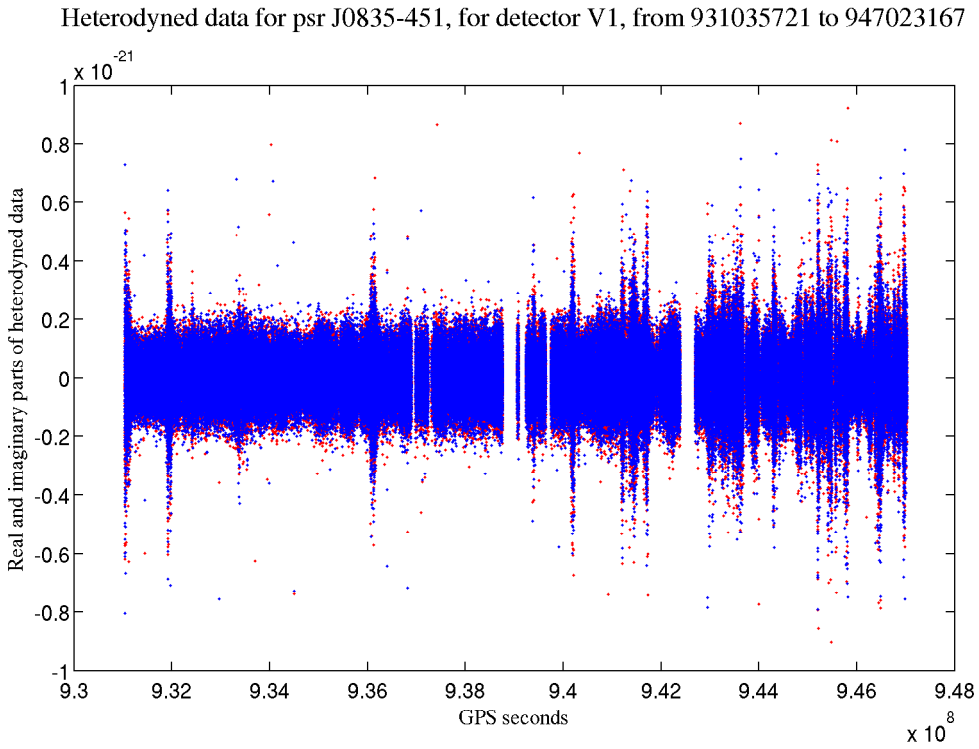

Figure 3.5: A plot of the heterodyned VSR2 data for the Vela pulsar, with the GPS seconds along the x-axis, and the strain on the y-axis. The blue and red show the real and imaginary parts of the heterodyned data respectively. The evolution of the sensitivity of the data can be seen from this figure, with the noise floor appearing to be higher in the latter half of the run. There are also many more spikes in the data during the latter half of the run.

(HartRAO) near Johannesburg in South Africa.

Tempo2 software Hobbs et al. (2006) was used to fit a modelled phase evolution to the TOAs. Best fit values for the right ascension, declination, proper motion, rotation frequency, and first and second derivatives of the rotation frequency were produced over the epoch of VSR2. TOAs were used from 1st June 2009 to 31st March 2010. By ensuring that the TOAs span VSR2, we aim to produce an accurate fit to the data and therefore an accurate model of the GW phase evolution over the same period. The timing model for VSR2 was produced by Matthew Pitkin, the parameters are shown in Table 3.2.

Right Acension	Declination	$f_{\rm rot}$ [Hz]	$\dot{f}_{\rm rot}$ [Hz/s]	$\ddot{f}_{\rm rot}$ [Hz/s^2]
$08^{\rm h}\,35^{\rm m}\,20.^{\rm s}7543822$	$-45^\circ\,10'\,32.95068''$	11.191	-1.558×10^{-11}	4.907×10^{-22}

Table 3.2: Table showing the parameters for the fitted timing model for Vela TOAs from 1st June 2009 to 31st March 2010.

Vela is known as a particularly glitchy pulsar, with a glitch rate of $\sim 1/3\,{\rm yr}^{-1}$, and as the GW phase evolution is uncertain during a glitch, it was important to ensure

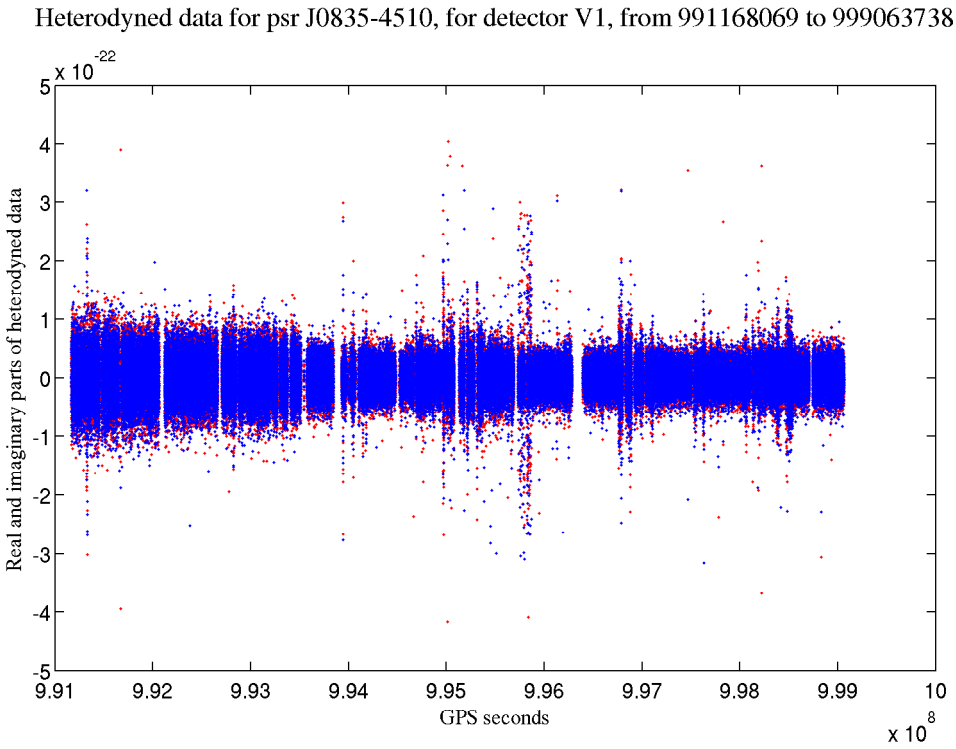

Figure 3.6: A plot of the heterodyned VSR4 data for the Vela pulsar, with the GPS seconds along the x-axis, and the strain on the y-axis. The blue and red show the real and imaginary parts of the heterodyned data respectively. This figure shows a steady reduction in the magnitude of the data, corresponding to an increase in sensitivity, during approximately the first third of the run, with the final third of the run in particular showing a comparatively low and stable noise floor.

that Vela did not glitch during VSR2. The observations of Vela by Hartesbessthoek and Mt. Pleasant radio antennas show no evidence for a glitch during VSR2.

The ephemeris for Vela during the VSR4, which ran from 28th of July 2010 21:00 UTC through to 20th of October 2010 05:00 UTC, was obtained from Sarah Bruckner from the Hartesbessthoek Radio Astronomy Observatory. The fitted parameters are shown in table 3.3. As with VSR2 the timing of Vela during this time showed no evidence of a glitch.

The timing solutions for VSR2 and VSR4 show some differences in the position and in $\ddot{f}_{\rm rot}$. However both solutions present a best fit to the TOA data used for each timing model, what is important for our search is that the models accurately describe the phase of the GW signal as observed at Earth rather than the absolute values of these parameters of the timing model.

Right Ascension	Declination	$f_{\rm rot}$ [Hz]	$\dot{f}_{\rm rot}$ [Hz/s]	$\ddot{f}_{\rm rot}$ [Hz/s^2]
$08^{\rm h}\,35^{\rm m}\,20.^{\rm s}61149$	$-45^\circ\,10'\,34.8751''$	11.192	-1.573×10^{-11}	6.423×10^{-22}

Table 3.3: Table showing the parameters for the fitted timing model for Vela TOAs from 3rd July - 5th September 2011.

3.5 Hardware injections

An important test for current search algorithms, particularly at a time where no detections are being made, is to see if they can recover artificial signals injected into the detector data. Where the search code has already been tested with hardware injections in this way, and has been found to recover them well, hardware injection recovery can be used with a new dataset to verify that the calibration of the interferometer data is consistent over the run. The search codes here have undergone a lengthy review process as part of the LSC approval for publication and as such the use of hardware injections here is primarily as a sanity check of the calibration, but also still serves as a check on the search code. Hardware injections are created by moving one of the interferometer mirrors to simulate a GW signal. For CW analyses there are ten pulsar like signals injected into the data over the entire length of a science run and each hardware injection pulsar has its own set of parameters. This enables testing of a CW search pipeline's ability to recover a GW signal from pulsars with a range of different parameters. Here I present results from analyses aiming to find the hardware injection pulsars and their parameters in data from VSR2 and VSR4.

The hardware injection analyses use the search method described in §1.6.5, as this is the method used for the search for a GW signal from Vela in the Virgo science runs. The output of this search method are probability density functions (PDFs) for each of the signal parameters. These PDFs give the most amount of information about the search results, and are shown in Figures 3.7 to 3.8 for VSR2, and in Figures 3.9 to 3.10 for VSR4. These are summarised in tables 3.4 and 3.5 for VSR2 and VSR4 respectively, where the most probable values from the PDFs are quoted for each recovered parameter's value. It should be noted that the use of the most probable value here is only as it is an easy way to summarise the results in table form. For a full picture of the results the PDFs should be consulted.

For the most part the parameters of the hardware injection pulsars in both VSR2 and VSR4 are seen to be recovered well, particularly the parameter h_0. The parameters of the stronger pulsar hardware injections, which are psr 03, psr 04,and psr 08, are very well recovered. The PDFs for these stronger pulsar hardware injections confine the possible values of each parameter to very small ranges about, or very close to, the actual injected values. Where these PDFs do not overlap with the

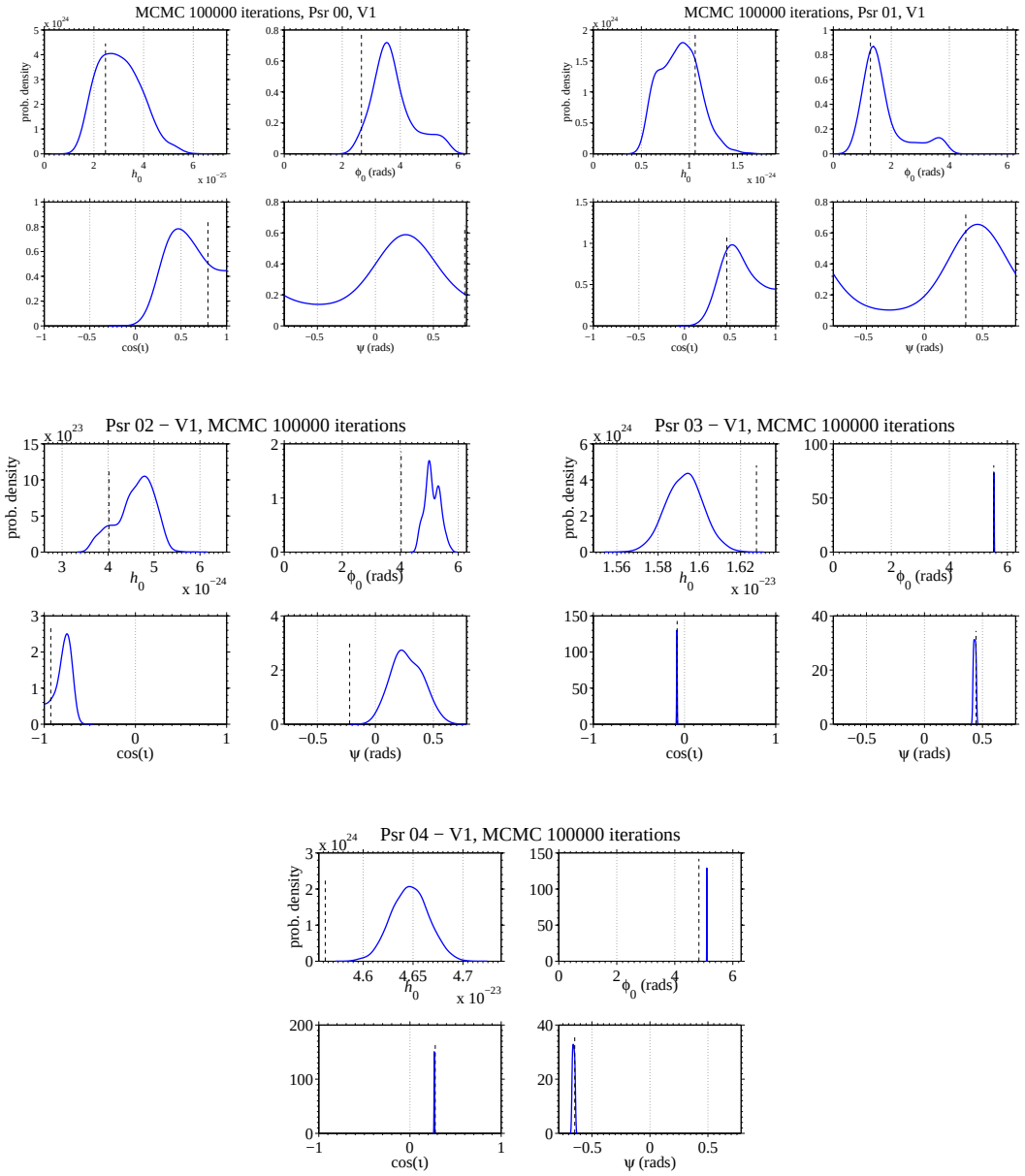

Figure 3.7: Probability density functions (PDFs) for the recovery of pulsar hardware injections psr00 to psr04 in VSR2 data. The PDFs are shown in blue, and the injected parameters are shown by dashed black vertical lines.

injected values of certain parameters, for example for the h_0 parameter for psr 03 and psr 08, the amount of this mismatch is typically around a few percent. This is of the order of errors in the calibration of the data (Accadia et al. 2011b).

There are some obvious cases where the orientation parameters are not recovered well. For example the PDFs for psr 00 for both VSR2 and VSR4 data, as seen in Figures 3.7 and 3.9, show that large regions of the parameter space are not able to be ruled out for the parameters ϕ_0, ψ, and $\cos(\iota)$, and that the regions of high probability do not match well with the injected values, particularly for the

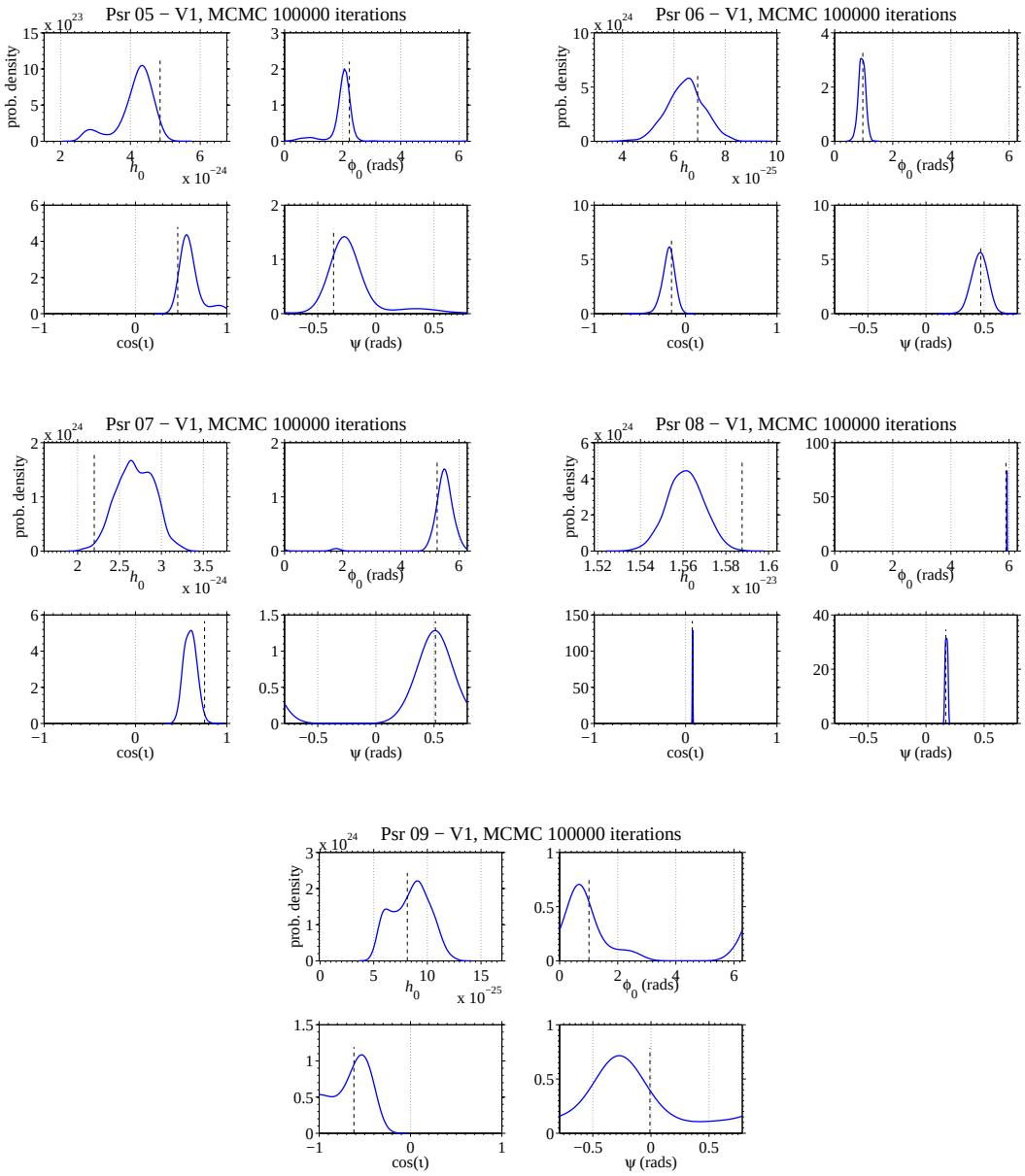

Figure 3.8: Probability density functions (PDFs) for the recovery of pulsar hardware injections psr05 to psr09 in VSR2 data. The PDFs are shown in blue, and the injected parameters are shown by dashed black vertical lines.

parameters ψ and ϕ_0. To investigate this further I look more closely at these PDFs, where I can see that the reason for this poor recovery of the parameters is linked to the parameter space that the value of $\cos(\iota)$ has been able to be confined to by the analysis. The possible parameter space for $\cos(\iota)$ from this analysis includes where $\cos(\iota) = 1$. Where the value of $\cos(\iota) = 1, -1$ the spin axis of the pulsar is directly along our line of sight to it, this means that the angle ψ, which together with ι describes the orientation of the pulsar's spin axis, and the initial phase ϕ_0, become degenerate and can therefore no longer be individually well confined by our

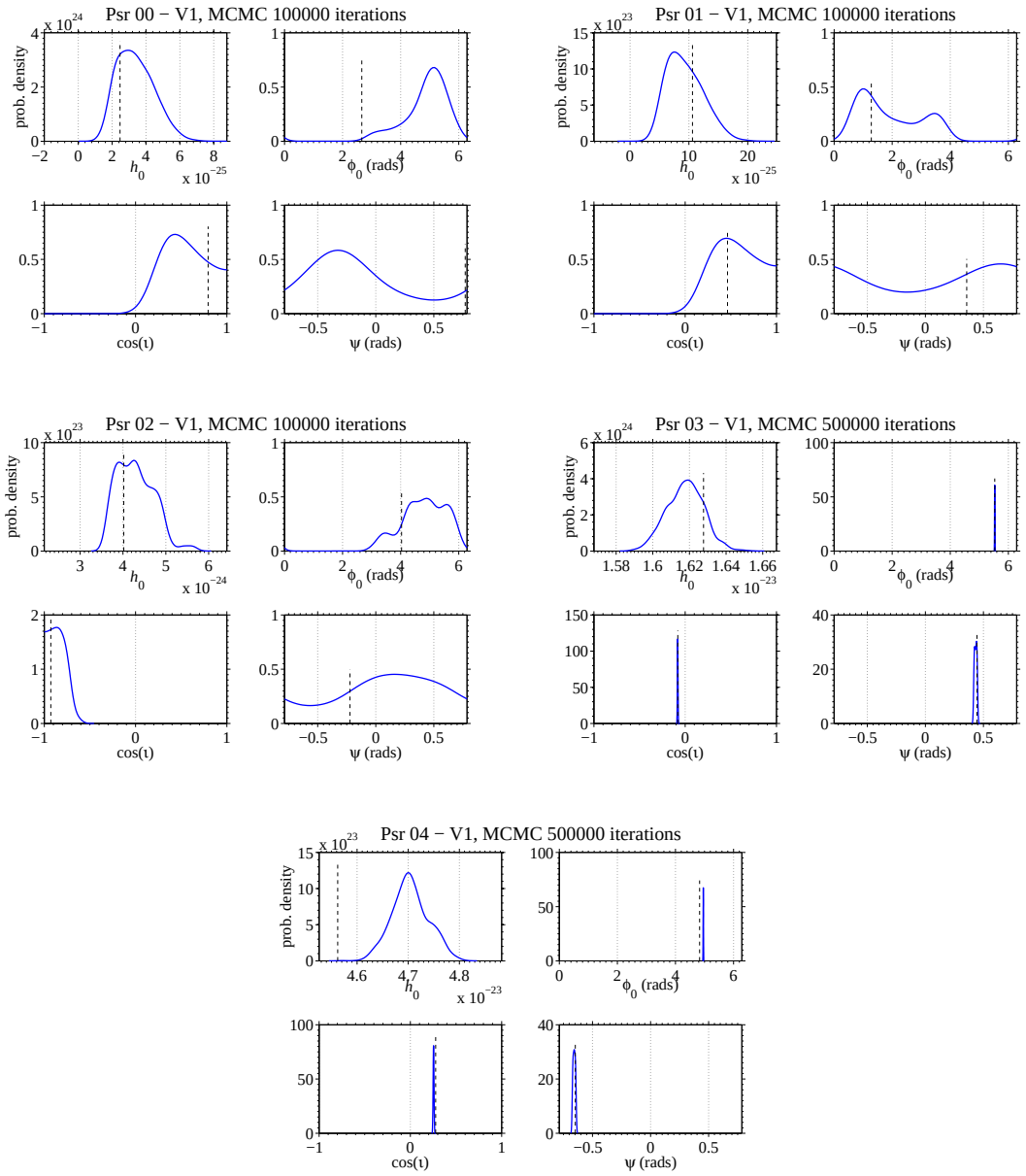

Figure 3.9: PDFs of VSR4 hardware injection pulsar for pulsars psr00 to psr04. The PDFs are shown in blue, and the injected parameters are shown by dashed black vertical lines.

analysis. Although the injected value of $\cos(\iota)$ is not one or minus one, or even very close in this case, because the analysis can not be sure that $\cos(\iota) \neq 1$ the ψ and ϕ_0 degeneracy still impacts on the analysi s. This effect can be seen in Figure 3.11, which shows the Markov Chain Monte Carlo output for psr 00 for VSR4 data, for h_0 and $\cos(\iota)$ against each other, and ϕ_0 and ψ against each other. The effect of not being able rule out $\cos(\iota) = 1$, and the associated degeneracy in ψ and ϕ_0 can be seen as a strong correlation between MCMC chains between ψ and ϕ_0.

The test of recovering the pulsar hardware injections has shown that where the

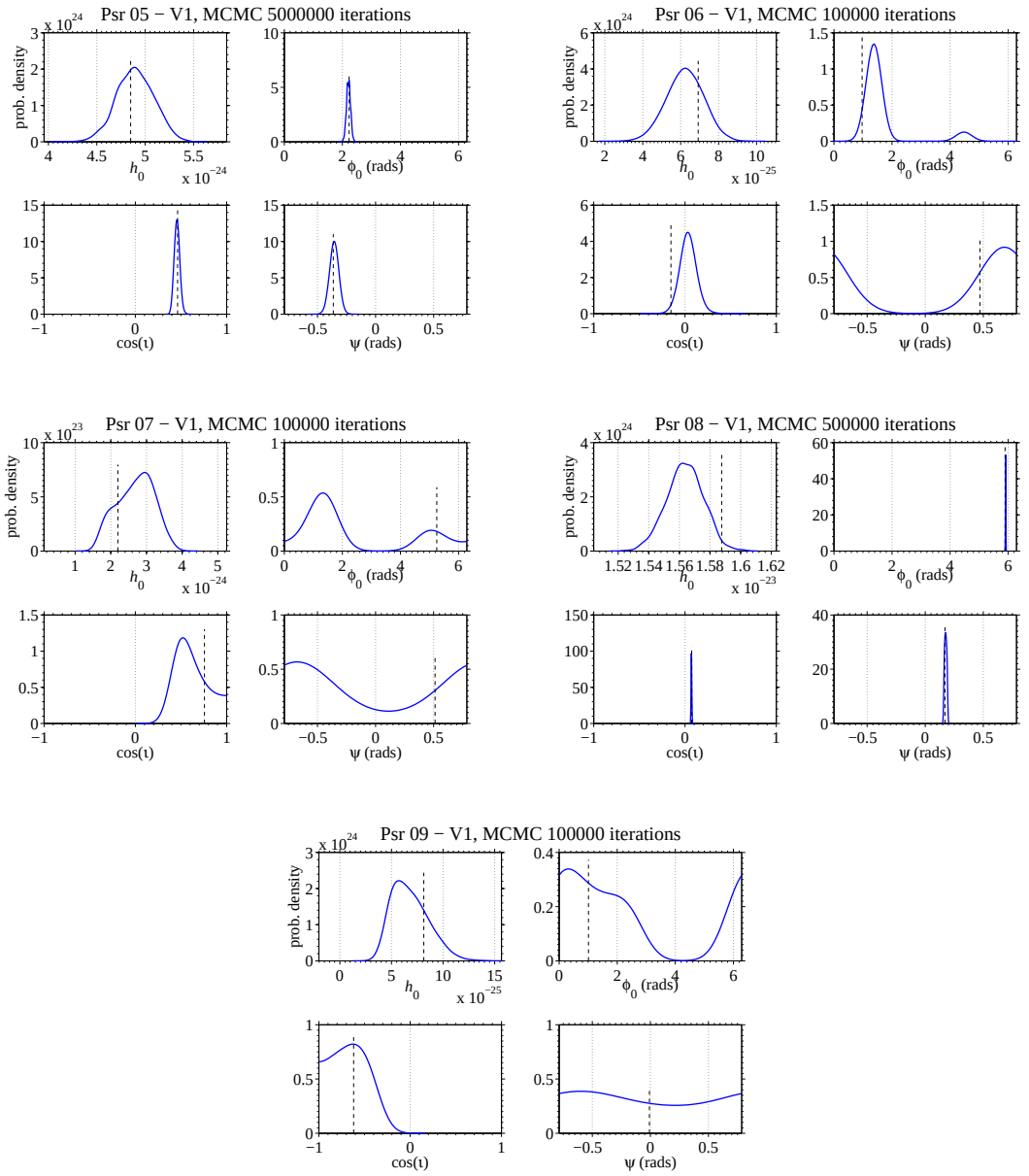

Figure 3.10: PDFs of VSR4 hardware injection pulsars psr05 to psr09. The PDFs are shown in blue, and the injected parameters are shown by dashed black vertical lines.

signal is sufficiently strong our analysis is capable of recovering the injected signal, as well as highlighting cases where our analysis is unable to confine the values of the orientation parameters well. The ideal test of course would be actually recovering a real signal, but whilst this is not possible the hardware injections have been important in verifying our search codes and the calibration of the data. These analyses highlight no major issues, beyond expected error budgets, with the calibration of the data from VSR2 or VSR3, although as discussed in §3.3, the initial calibrations of VSR2 data were found to be incorrect and these did produce notable errors in

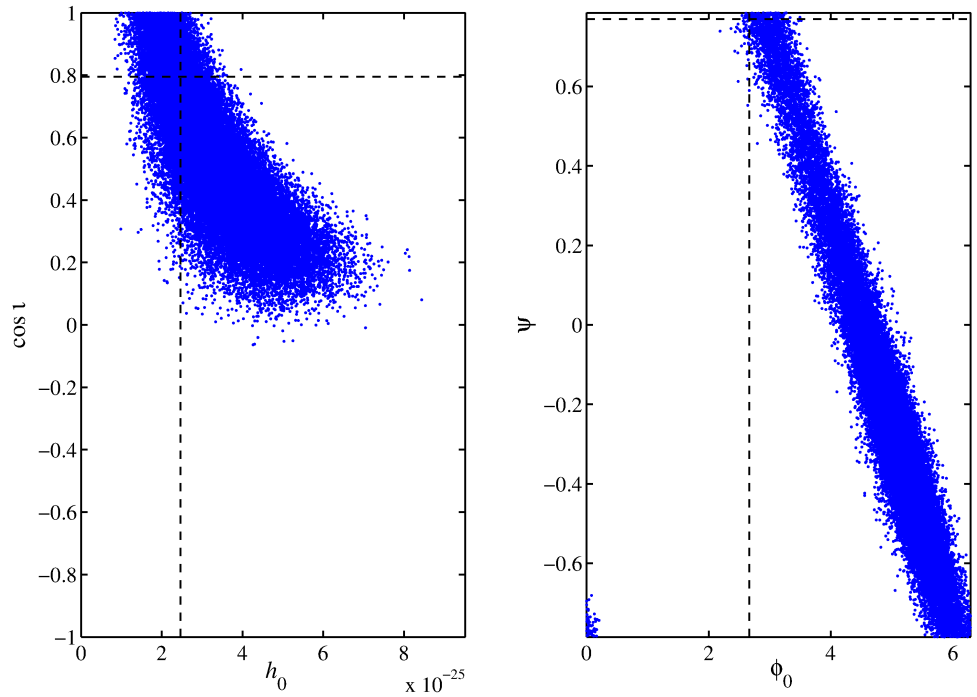

Figure 3.11: MCMC chains for psr00, showing the degeneracy in the parameters ψ and ϕ_0 for the case when $\cos(\iota)$ is at, or close to, 1 or -1. It is also possible to see the correlation between h_0 and $\cos(\iota)$.

the hardware injection recovery using that data.

3.6 Results

For both VSR2 and VSR4 I have performed two Bayesian parameter estimation runs. The first run assumed flat priors on all parameters, whilst the second run assumed Gaussian priors on the orientation parameters $\cos(\iota)$ and ψ. The first run's flat priors represent complete ignorance of the parameters prior to the analysis. The second run assumes flat priors on the parameters h_0 and ϕ_0, but with Gaussian priors on $\cos(\iota)$ and ψ. The motivation for using Gaussian priors on $\cos(\iota)$ and ψ comes from observations of Vela's wind tori, as described by Ng & Romani (2008), and the premise that the orientation of the wind tori is determined by the orientation of the pulsar spin axis. These observations inform Gaussian priors of $\psi = 130°.63 \pm 0°.086$ and $\iota = 63°.6 \pm 0°.6$, although as ψ wraps around at $\pm 45°$ I use $\psi = 40°.63$ in the analysis. These two different assumptions and their corresponding sets of priors are expected to produce different results where no signal is detected, but if the signal was sufficiently strong, the signal would dominate over any affect of the priors.

The results of the parameter estimation runs are probability density functions

	h_0	ϕ_0	$\cos\iota$	ψ	f (Hz)
Psr 00 inj	2.47e-25	2.66	0.79	0.77	265.58
Psr 00 rec	2.69e-25	3.53	0.47	0.26	
Psr 01 inj	1.06e-24	1.28	0.46	0.36	849.08
Psr 01 rec	9.31e-25	1.39	0.52	0.46	
Psr 02 inj	4.02e-24	4.03	-0.93	-0.22	575.16
Psr 02 rec	4.79e-24	4.99	-0.75	0.23	
Psr 03 inj	1.63e-23	5.53	-0.08	0.44	108.86
Psr 03 rec	1.59e-23	5.54	-0.08	0.43	
Psr 04 inj	4.56e-23	4.83	0.28	-0.65	1403.16
Psr 04 rec	4.65e-23	5.10	0.27	-0.66	
Psr 05 inj	4.85e-24	2.23	0.46	-0.36	52.81
Psr 05 rec	4.33e-24	2.06	0.56	-0.27	
Psr 06 inj	6.92e-25	0.97	-0.15	0.47	148.72
Psr 06 rec	6.61e-25	0.91	-0.18	0.47	
Psr 07 inj	2.20e-24	5.25	0.76	0.51	1220.98
Psr 07 rec	2.63e-24	5.49	0.61	0.52	
Psr 08 inj	1.59e-23	5.89	0.07	0.17	194.31
Psr 08 rec	1.56e-23	5.93	0.08	0.17	
Psr 09 inj	8.13e-25	1.01	-0.62	-0.01	763.85
Psr 09 rec	9.11e-25	0.67	-0.54	-0.28	

Table 3.4: Table showing the injected and recovered parameters for pulsar hardware injections during the VSR2 run. The injected (inj), and recovered (rec) values are listed for each parameter for each hardware injection pulsar. The frequencies of each of the injections is also shown.

(PDFs) for each of the signal parameters. These PDFs show the probability density at different values of the parameters. By definition the area under a PDF is one, i.e. I have assumed that the true value for the parameter lies within the parameter range I have specified. Each PDF is calculated by marginalising over the other signal parameters. This means that at each value of the parameter for which the PDF has been calculated, the probability density is calculated considering all combinations of values for the other signal parameters. The PDF that is of most interest is the one for the signal parameter h_0, as this is the strength of the GW signal. Where the h_0 PDF peaks at zero, the data tells us that the most likely strength of the GW signal in the data is zero, i.e. there is no signal present or that if there is a signal present it is not visible above the detector noise. Where this is the case

	h_0	ϕ_0	$\cos\iota$	ψ
Psr 00 inj	2.47e-25	2.66	0.79	0.77
Psr 00 rec	2.92e-25	5.17	0.44	-0.33
Psr 01 inj	1.06e-24	1.28	0.46	0.36
Psr 01 rec	7.57e-25	1.04	0.46	0.65
Psr 02 inj	4.02e-24	4.03	-0.93	-0.22
Psr 02 rec	4.25e-24	4.89	-0.87	0.16
Psr 03 inj	1.63e-23	5.53	-0.08	0.44
Psr 03 rec	1.62e-23	5.53	-0.08	0.44
Psr 04 inj	4.56e-23	4.83	0.28	-0.65
Psr 04 rec	4.70e-23	4.96	0.25	-0.66
Psr 05 inj	4.85e-24	2.23	0.46	-0.36
Psr 05 rec	4.89e-24	2.23	0.46	-0.36
Psr 06 inj	6.92e-25	0.97	-0.15	0.47
Psr 06 rec	6.22e-25	1.39	0.03	0.69
Psr 07 inj	2.20e-24	5.25	0.76	0.51
Psr 07 rec	2.96e-24	1.30	0.52	-0.69
Psr 08 inj	1.59e-23	5.89	0.07	0.17
Psr 08 rec	1.56e-23	5.91	0.07	0.17
Psr 09 inj	8.13e-25	1.01	-0.62	-0.01
Psr 09 rec	5.67e-25	0.31	-0.63	-0.61

Table 3.5: Table showing the recovered and injected parameters for VSR4 hardware injections. The injected (inj), and recovered (rec) values are listed for each parameter for each hardware injection pulsar.

we can still extract some meaning from the results. From the PDFs we can find the value of h_0 which bounds 95% of the probability density and this corresponds to a 95% confidence upper limit on h_0. This can be used to set upper limits on the ellipticity of the pulsar. It is at this stage that the spin-down limit discussed earlier comes into play. The spin-down limit presents an absolute upper limit on the GW emission and hence the pulsars ellipticity. If our 95% upper limit is below this then we have gained some quantitative knowledge of the pulsar beyond our initial optimistic assumptions. It is also possible to infer an upper limit on the fraction of the star's spin-down luminosity that is emitted as GWs. If we are able to make a detection, then the inferred ellipticity of the star can be used as observational test for theories of NS equations of state, which make predictions about the ellipticities that a NS can maintain.

3.6.1 VSR2

The resulting PDFs from the first parameter estimation run can be seen in Figure 3.12, this is the parameter estimation run with flat priors on all the parameters. The important PDF from Figure 3.12 is the h_0 PDF, as this tells us how likely different signal strengths are. The most likely value for h_0 is at zero for this PDF, i.e. the data does not suggest that there is a signal present. However as discussed previously, where this is the case we can place a 95 % confidence upper limit on h_0, and for this run this is 2.4×10^{-24}.

The resulting PDFs from the second parameter estimation run can be seen in Figure 3.13, this parameter estimation run uses Gaussian priors on ψ and $\cos(\iota)$. Again, the important PDF is the h_0 PDF, and this indicates that there is no signal present. It should also be clear that the PDFs for ψ and $\cos(\iota)$ are strongly peaked compared with those from Figure 3.12. These PDFs, in this case where no signal is detected, simply reflect the priors used. The 95 % confidence upper limit on h_0 is 2.1×10^{-24}.

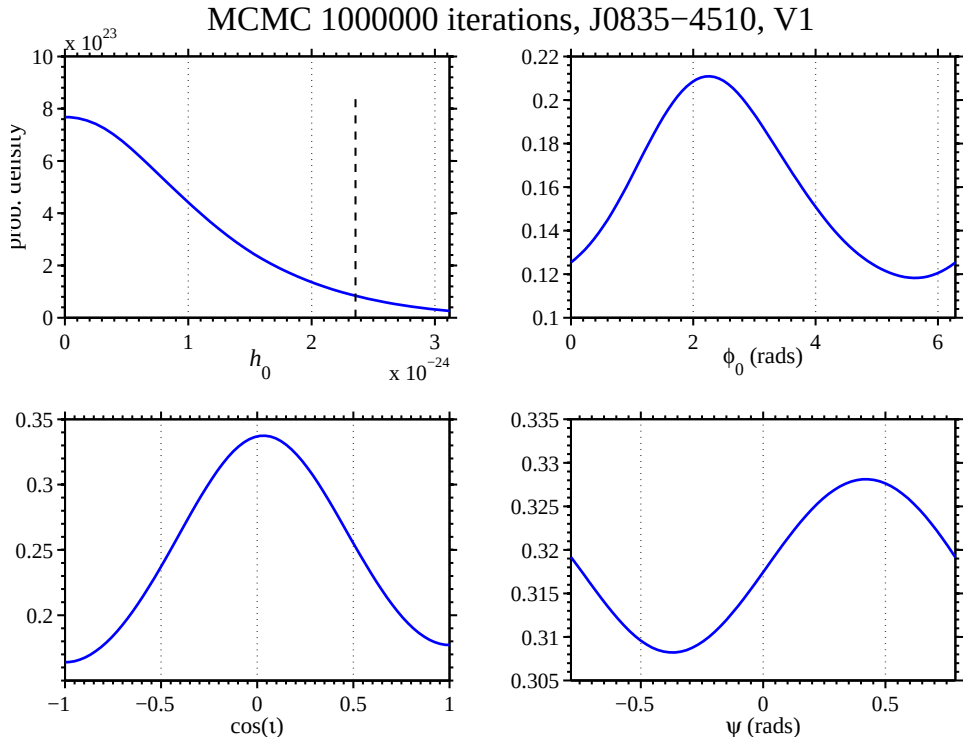

Figure 3.12: The PDF outputs from VSR2, produced by MCMC with 100 000 iterations. The MCMC was run with uniform priors on all parameters. The 95% upper limit on h_0 derived from this MCMC is 2.4×10^{-24}, and is shown as a vertical black dashed line on the h_0 PDF.

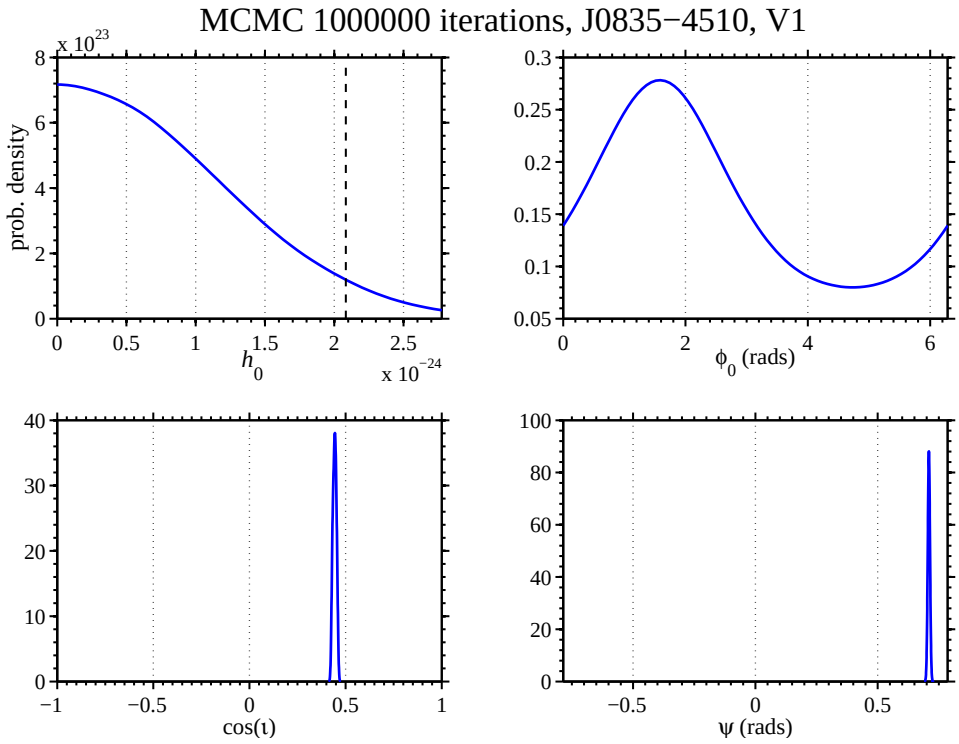

Figure 3.13: The PDF outputs from VSR2, produced by MCMC with 100 000 iterations. The MCMC was run with Gaussian priors on the orientation parameters ψ and $\cos(\iota)$. The 95% upper limit on h_0 derived from this MCMC is 2.1×10^{-24}, and is shown as a vertical black dashed line on the h_0 PDF.

3.6.2 VSR4

The PDFs from the parameter estimation run with flat priors on all parameters and with Gaussian priors on the orientation parameters can be seen in Figures 3.14 and 3.15 respectively. The h_0 PDFs from these results indicate that there is no signal present. The 95 % confidence upper limits on h_0 for the run with uniform priors on all parameters is 1.2×10^{-24}, and with Gaussian priors on the orientation parameters is $1.1 \times 10^{-24} \times 10^{-24}$. These upper limits are significant improvements on those set using VSR2 data, which was to be expected given the gains in sensitivity at low frequencies from VSR2 to VSR4, as well as the removal of the chiller pump noise lines that degraded the VSR2 search.

3.6.3 VSR2 and VSR4 combined

The data from the VSR2 and VSR4 runs can be coherently combined to form one larger dataset, with the prospect of providing a more sensitive search. As there was no glitch seen in Vela between these two runs, it is reasonable to expect the GW signal phase to remain coherent over the two runs. The PDFs from the parameter estimation run with flat priors on all parameters and with Gaussian priors on the

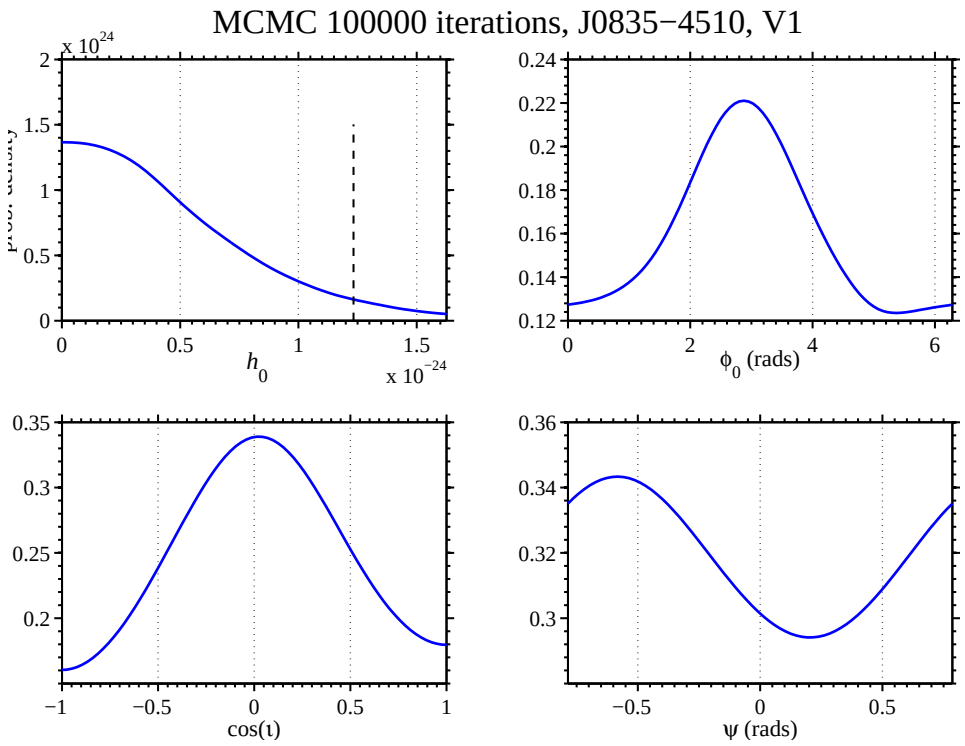

Figure 3.14: The PDF outputs from VSR4, produced by MCMC with 100 000 iterations. The MCMC was run with uniform priors on all parameters. The 95% upper limit on h_0 derived from this MCMC is 1.2×10^{-24}, and is shown as a vertical black dashed line on the h_0 PDF

orientation parameters can be seen in Figures 3.16 and 3.17 respectively. As with the previous results, these PDFs are consistent with there being no signal in the data. The 95 % confidence upper limits on h_0 for the run with uniform priors on all parameters is 1.1×10^{-24}, and with Gaussian priors on the orientation parameters is 1.0×10^{-24}, which is only a slight improvement on the upper limits derived from VSR4 data. The small amount of sensitivity gained by combining VSR4 with VSR2 is consistent with the relative sensitivities of each dataset.

3.7 Discussion

In this chapter I presented the search for GWs from the Vela pulsar over the Virgo Science Runs VSR2 and VSR4. These datasets are the most sensitive yet recorded at the frequency at which we expect CWs from Vela from the triaxial emission model. The PDFs shown in Figures 3.12 to 3.15, are consistent with both datasets containing only noise and no GW signal. Although these datasets have not provided a GW detection, I have been able to place 95 % confidence upper limits on the GW amplitude below the Vela's spin-down limit of $h_0^{sd} = 3.3 \times 10^{-24}$, making it the second pulsar after the Crab for which this milestone has been surpassed. The upper limits

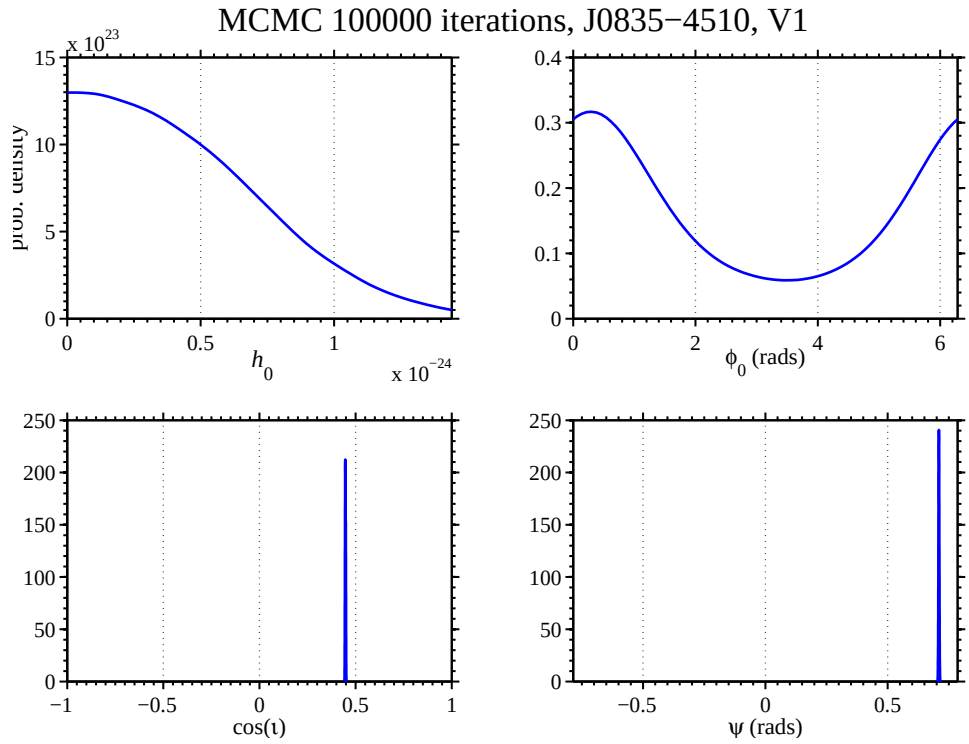

Figure 3.15: The PDF outputs from VSR4, produced by MCMC with 100 000 iterations. The MCMC was run with Gaussian priors on the orientation parameters ψ and $\cos(\iota)$. The 95% upper limit on h_0 derived from this MCMC is 1.1×10^{-24}, and is shown as a vertical black dashed line on the h_0 PDF.

on h_0 from VSR2 when assuming no prior knowledge of the spin axis, and where we assume prior knowledge of the spin axis, correspond to $\sim 73\,\%$ and $\sim 64\,\%$ of the spin-down limit respectively. Some discussion of these results, together with those obtained using two other independent search methods, is presented in Abadie et al. (2011a). The improvements to the Virgo interferometer for the VSR4 run resulted in an improvement in sensitivity at lower frequencies. This led to significantly lower upper limits on h_0 for VSR4, which correspond to $\sim 36\,\%$ of the spin-down limit for the analyses assuming no prior knowledge of the spin axis, and $\sim 34\,\%$ of the spin-down limit where we assume prior knowledge of the spin axis. When these two runs are combined and analysed coherently a slight improvement on the upper limits obtained with VSR4 only data is achieved. The upper limits produced from this combined dataset correspond to $\sim 34\,\%$ and $\sim 30\,\%$ when using uniform and Gaussian priors respectively. This improvement is so small as the VSR4 dataset is substantially more sensitive than VSR2.

It can be useful to represent these upper limits on h_0 in terms of the NS's ellipticity so that this can be directly compared against theoretically predicted values for the maximum sustainable ellipticity of a NS. Determining an upper limit on the fraction of the NS's spin-down energy lost through GWs is also useful. Although

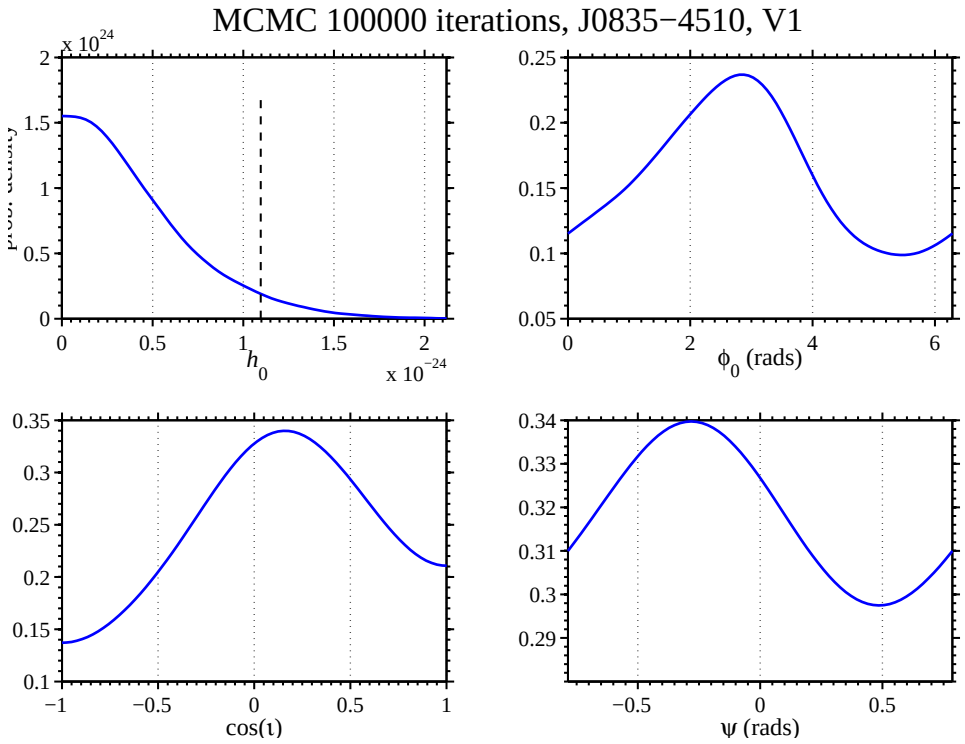

Figure 3.16: The PDF outputs from VSR2 and VSR4 combined, produced by MCMC with 100 000 iterations. The MCMC was run with uniform priors on all parameters. The 95% upper limit on h_0 derived from this MCMC is 1.1×10^{-24}, and is shown as a vertical black dashed line on the h_0 PDF

there are no predictions about the exact fraction that this could be, it is widely thought that the majority of a pulsars spin-down is due to magnetic dipole breaking, and so clearly an upper limit of a few percent of the spin-down luminosity is more likely to be closer to the true value than a much higher percentage. This quantity can be calculated by $(h_{0,95}/h_0^{sd})^2$ (Abbott et al. 2008b). The lowest upper limit on the percentage of a pulsar's spin-down power lost through GWs derived to date is for 2 %, and is for the Crab pulsar using LIGO S5 data (Abbott et al. 2010). The lowest of the upper limits on h_0 obtained here for the Vela pulsar is using the combined VSR4 and VSR2 dataset with restricted Gaussian priors on ψ and $\cos(\iota)$, which corresponds to 9 % of the spin-down energy, with the upper limit from VSR4 with uniform priors on these parameters corresponding to 11 %. The inferred upper limits on the ellipticity for Vela for the lowest upper limits, obtained using the combined VSR2 and VSR2 dataset, gives $\sim 5.7 \times 10^{-4}$ and 6.2×10^{-4} for the analysis using Gaussian priors on ψ and $\cos(\iota)$ and the analysis using uniform priors for these parameters respectively. These upper limits on Vela's ellipticity are both greater by several orders of magnitude than the maximum allowable equatorial ellipticity predicted by standard NS equations of state, as discussed in §2.2.9. The lowest such upper limit on a NSs ellipticity obtained through GW analysis is 7×10^{-8} for J2124-

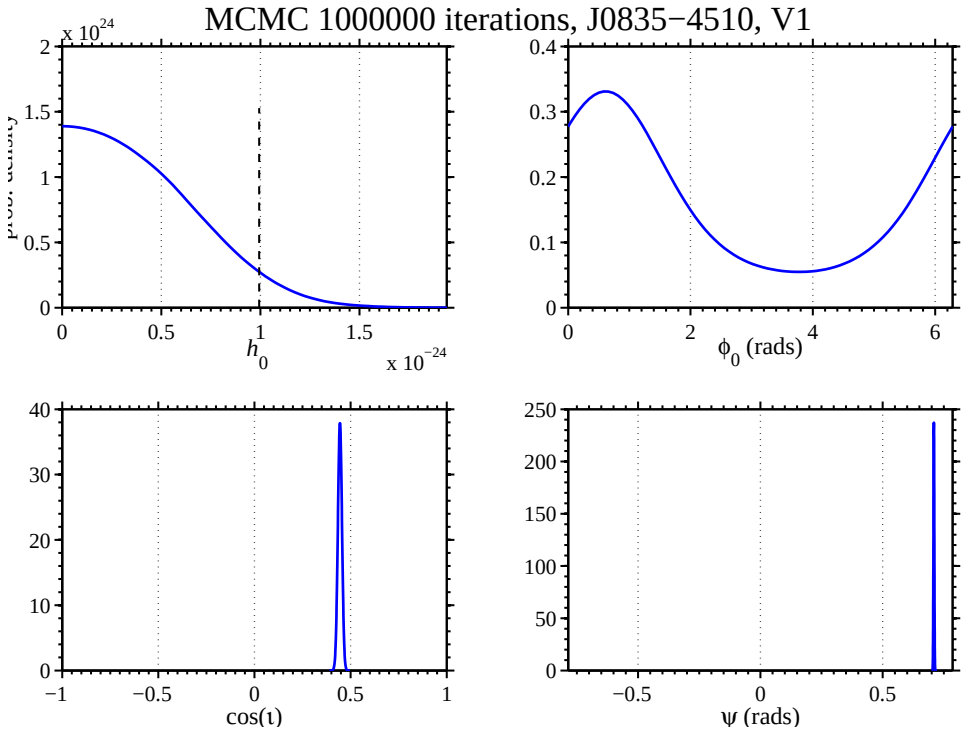

Figure 3.17: The PDF outputs from VSR2 and VSR4 combined, produced by MCMC with 100 000 iterations. The MCMC was run with Gaussian priors on the orientation parameters ψ and $\cos(\iota)$. The 95% upper limit on h_0 derived from this MCMC is 1.0×10^{-24}, and is shown as a vertical black dashed line on the h_0 PDF.

3358, which was obtained using LIGO S5 data (Abbott et al. 2010). The upper limits on Vela's ellipticity represent conservative estimates, as the theoretical predictions for I range from $\sim 1 - 3 \times 10^{38}\,\mathrm{kg\,m^2}$ Abbott et al. (2010). However the upper limits are in the range of ellipicities predicted by the more exotic NS equations of state discussed in §2.2.9, and represent the lowest upper limits determined for Vela to date. Note that a failure to detect GWs from a source can not be used to rule out a NS EOS that predicts a maximum sustainable ellipticity that is greater than implied upper limit form the non-detection. This is because the EOS predicts only the *maximum* sustainable ellipticity, there is no need for the NS in question to have this maximum ellipticity. However if a GW detection is made and the implied ellipticity is greater than the maximum sustainable ellipticity predicted by a particular NS EOS, then it can help to rule out that particular EOS.

Vela remains an interesting target for GW searches. The fact that it frequently glitches did not affect the analyses presented in this chapter, but could complicate future searches for CWs from Vela and also means that it is an interesting source of transient GWs as well as CWs (Abadie et al. 2011b). With the upgrade of the current GW detector network (Harry & the LIGO Scientific Collaboration 2010; Accadia et al. 2011a) promising improved sensitivity across the frequency range but

in particular at lower frequencies for the LIGO detectors, the next coincident science runs between the LIGO and VIRGO detectors should be able to surpass the upper limits obtained here, and hopefully make a detection of CWs from Vela.

Chapter 4

Searching for GWs from the Crab pulsar

4.1 Introduction

This Chapter reports on a number of searches for GWs from the Crab pulsar (PSR B0531+21, J0534+2200) using the complex heterodyne and Bayesian parameter estimation search codes. A short introduction to the Crab pulsar is given in §4.1, followed by details of the timing solution used in the subsequent searches in §4.3. A summary of analyses of hardware injections into the LIGO S6 and Virgo VSR3 data is given in §4.5. In §4.6 results are presented from searches for GWs from the Crab in the recent LIGO and Virgo science runs. The chapter concludes with a discussion of these search results in §4.7.

4.2 The Crab pulsar

The Crab pulsar is named after the Crab nebula in which it resides. The nebula and the pulsar are the remnants of a supernova which was observed by Chinese astronomers in 1054 AD and described as a "guest star". This "guest star" was bright enough to be visible during the day, and remained visible at night for 22 months after its first appearance. The nebula was named by William Parsons, and was established as the remnant of the 1054 AD supernova in the 1940s (Mayall & Oort 1942). It was also the first object added to the Messier catalogue. The Crab nebula has been extensively studied in its own right, as indicated by the vast wealth of publications detailing studies across the EM spectrum, with recent studies revealing new behaviour - such as the recently reported occurrence of γ-ray flares (Tavani et al. 2011; Abdo et al. 2011). A composite image of the Crab nebula in X-rays and optical light is shown in Figure 4.1.

Figure 4.1: A composite X-ray (blue) and optical (red) image of the Crab nebula taken using the Chandra satellite and the Hubble space telescope, (Hester et al. 2002).

The first observations of radio pulses linked to the Crab nebula were by Staelin & Reifenstein (1968), who reported two sources of "sporadic" radio pulses near to the Crab nebula. This was at a time when Pulsars were first being linked with spinning NSs and Supernova remnants (Large et al. 1968; Ostriker & Gunn 1969; Gold 1969), and a follow up publication quickly followed (Comella et al. 1969) where the authors examined the two sources using the Aricebo radio antenna. The weaker of the two sources was not detected, but the authors were able to establish a periodicity in the other and determined the location of the"Crab nebula pulsar" to within 5 arc-minutes from the centre of the Crab nebula. The Crab was one of the first pulsars to be discovered, and as such was integral to the early studies that formed the foundations of pulsar astronomy. Even today with hundreds of known pulsars, the Crab pulsar remains one of the most important and most studied. This is because the radio pulses from the Crab are particularly strong at Earth. The strength of its radio pulses has meant that the study of single pulses is possible, whereas for most pulsars hundreds, if not thousands, of individual pulses must be combined for them to become visible above the noise. This makes the Crab pulsar an important object for studying and understanding pulsar physics, for example in determining models that explain the pulsed emission that gives pulsars their name. Pulses from the Crab pulsar can be seen right across the EM spectrum in the radio, optical, X-ray and γ-ray, which again is useful for studying the underlying physics of pulsars (Ramanamurthy 1994). Given the importance of the Crab pulsar to pulsar astronomy it is no surprise that it has been closely monitored since its discovery.

The Crab pulsar has long been considered a prime source for GWs due to its high spin down rate ($\dot{f} \sim -3.7 \times 10^{-10}\,\mathrm{Hz\,s^{-1}}$). A number of searches have concentrated explicitly on finding GWs from the Crab pulsar, with both the current generation of GW detectors (Abbott et al. 2008b, 2010), and in the past with resonant bar

detectors (Hirakawa et al. 1978). The high spin-down rate of the Crab pulsar tells us that it is losing a lot of energy, meaning that even if only a small proportion of this energy is emitted as GWs, they could still be strong enough to be detectable at Earth. The relative close proximity of the Crab means that its GWs are more likely to be detectable when they reach Earth as the signal strength falls off as $\tilde{h}_s \propto f^2/r$ (Cutler & Thorne 2002). The Crab pulsar remains a prime target for a direct observation of GWs. But even without a direct detection recent searches are approaching astrophysical significance with non-detection (Abbott et al. 2008b, 2010) by placing upper limits on the ellipticity and moment of inertia of the Crab pulsar. The data collected in the recent science runs of the Virgo and LIGO detectors have provided the opportunity to conduct more searches for GWs from the Crab, with a sensitivity comparable to the most sensitive yet conducted. This chapter presents results from searches using these datasets.

4.3 The timing model used in the search

The timing model for the crab pulsar is more involved than the model used for Vela. This is due to the large amount of timing noise seen in the radio pulse time of arrivals (TOAs) from the Crab. Timing noise is the random variation in the TOAs in comparison to a steady spin-down, and was discussed in §2.2.4. Astronomers at Jodrell Bank radio observatory have been closely monitoring the Crab pulsar since 1982 (Lyne et al. 1993), and have built up an extensive dataset of its radio pulse TOAs. This is used to provide a public monthly ephemeris of the Crab's spin parameters from 1982 to the present day, and can be found at online (Andrew Lyne 2011). The timing model used in the Crab searches described in this chapter is taken from this monthly ephemeris. The ephemeris provides values for the Crab's spin frequency and frequency derivative $(f, \dot{f})$, from which higher derivatives that track the timing noise can be calculated. The importance of taking into account the timing noise of the Crab pulsar, and the suitability of using the Jodrell bank observatory's monthly ephemeris to do so, are discussed in detail in Pitkin & Woan (2004).

4.4 The data

The LIGO S6 run started on Jul 07 2009 21:00:00 UTC and ran until Oct 20 2010 15:04:17 UTC. The S6 run took place after an upgrade from the initial LIGO design to the enhanced LIGO design (Smith & LIGO Scientific Collaboration 2009). The Virgo science runs VSR2 and VSR4 are described briefly in §3.3. VSR3 ran from Jul 28 2010 21:00:00 UTC to Oct 20 2010 05:00:00 UTC. The sensitivity curves for

a frequency band around the Crab frequency for all of these science runs are shown in Figure 4.2. Each sensitivity curve in Figure 4.2 is taken at a point in time during the run, and therefore may not be an accurate representation of the run as a whole. Each curve has been scaled to the length of the run (determined by the total time the interferometer was in science mode during a run). Also plotted in this figure is the spin-down limit for the Crab pulsar at twice its spin frequency. It should be noted that the sensitivity curves do not take into account the attenuation of the GW signal by the detectors' antenna patterns over the course of the runs, and hence the upper limit that can be set on the GW signal strength from the Crab using the data in the science runs is substantially higher than the value of these curves at the Crab frequency. What should be clear from this plot is that each of the runs are of very similar sensitivity at the Crab frequency, with the exception of VSR3 which is the least sensitive.

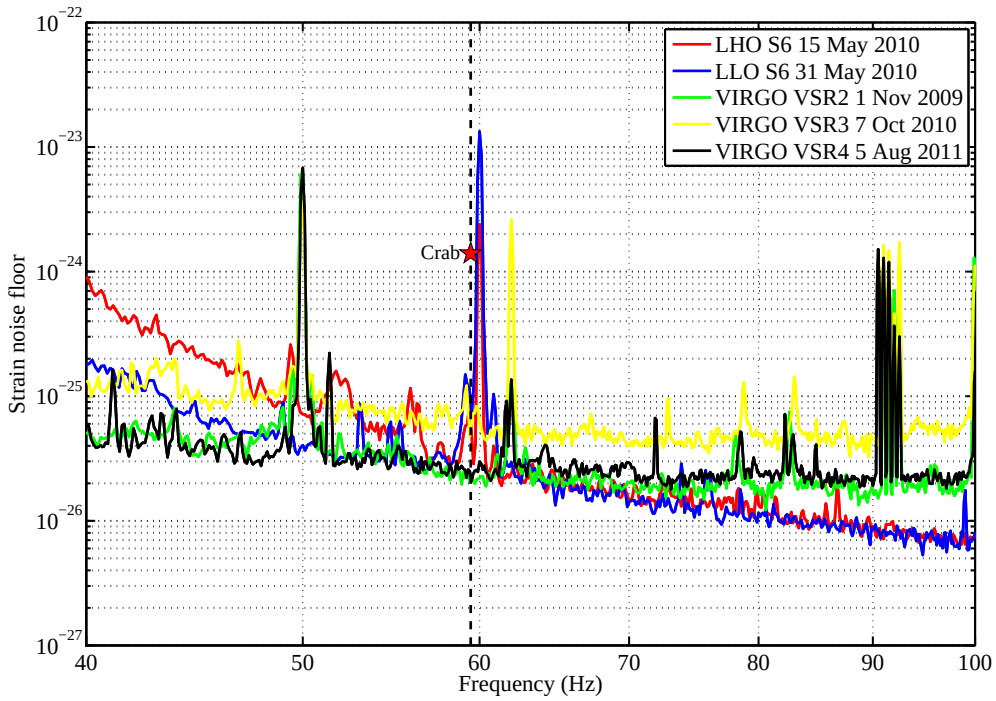

Figure 4.2: The RMS strain sensitivity noise curves for the LIGO and Virgo interferometers during S6, VSR2, VSR3 and VSR4. Each sensitivity curve is scaled to the length of its run. The spin-down limit is plotted for the Crab pulsar as the red star at twice its spin frequency (indicated by the vertical dashed black line). The values of the noise curves for S6, VSR2, VSR3 and VSR4 at this frequency are all relatively close to each other. (The Virgo Collaboration 2010; The LIGO Scientific Collaboration 2010).

The heterodyned data for the Crab pulsar from these science runs are shown in Figures 4.3 to 4.7. These plots of the heterodyned data show the evolution of the

noise at the Crab frequency over each of the runs. For example the noise floor in VSR3 can be seen to vary quite considerably over the run with a number of spikes where the noise floor is seen to suddenly increase, most notably at $\sim$ 966000000 and $\sim$ 969500000, while the noise floor during VSR4 appears to be very stable over the entire run without any such spikes. Visually checking the heterodyned data is an important step in the analysis. The analysis codes remove some outliers from the data, but if the data are particularly outlier prone, and the outliers are uncharacteristically large in comparison to the rest of the data, the automatic outlier removal method can be overwhelmed, resulting in a noisy dataset that could skew the results from the analysis.

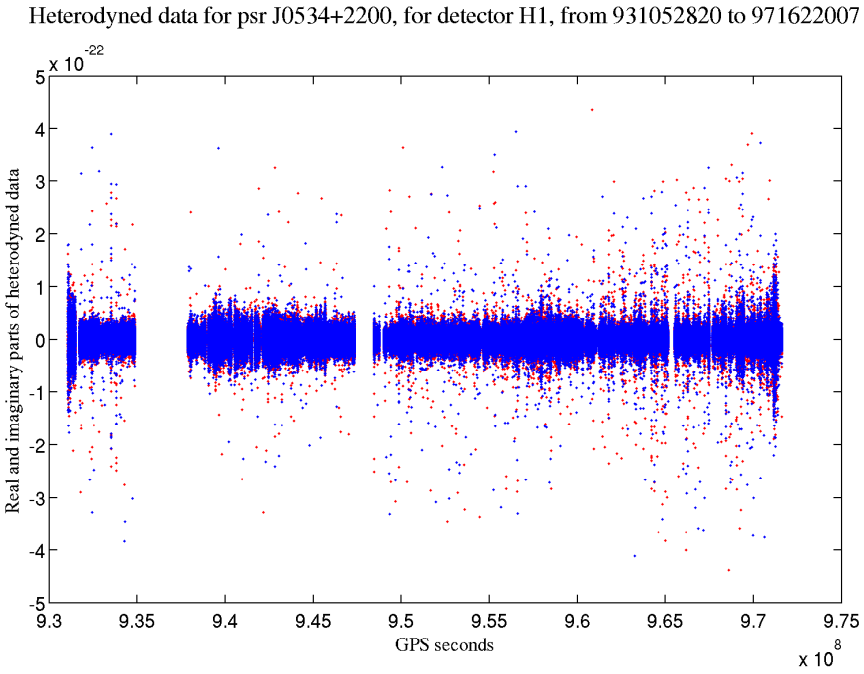

Figure 4.3: A plot of the heterodyned S6 H1 data for the Crab pulsar, with the GPS seconds along the x-axis, and the strain on the y-axis. The blue and red show the real and imaginary parts of the heterodyned data respectively.

Fscan spectrograms of the whole of S6 for 10 Hz band are shown in Figures 4.8 and 4.9 for H1 and L1 respectively. These spectrograms show the evolution of the noise in a 10 Hz frequency band around the Crab frequency over the course of the run. This wider view of the noise complements the narrower view provided by the plots of the heterodyned data. The frequency at which we expect GWs from the Crab at Earth is plotted onto the spectrograms as a black line. The 60 Hz line is clear to see in both spectrograms, but it does not appear to affect the noise floor at the Crab frequency. There are a number of other instrumental lines present in the spectrograms; for H1 there are lines at 59.1 Hz and 59.3 Hz, as well as some shorter duration noise features that are seen to increase the noise at the Crab frequency, which were discussed in more detail in §2.4.4. In Figure 4.9, there is a broad line

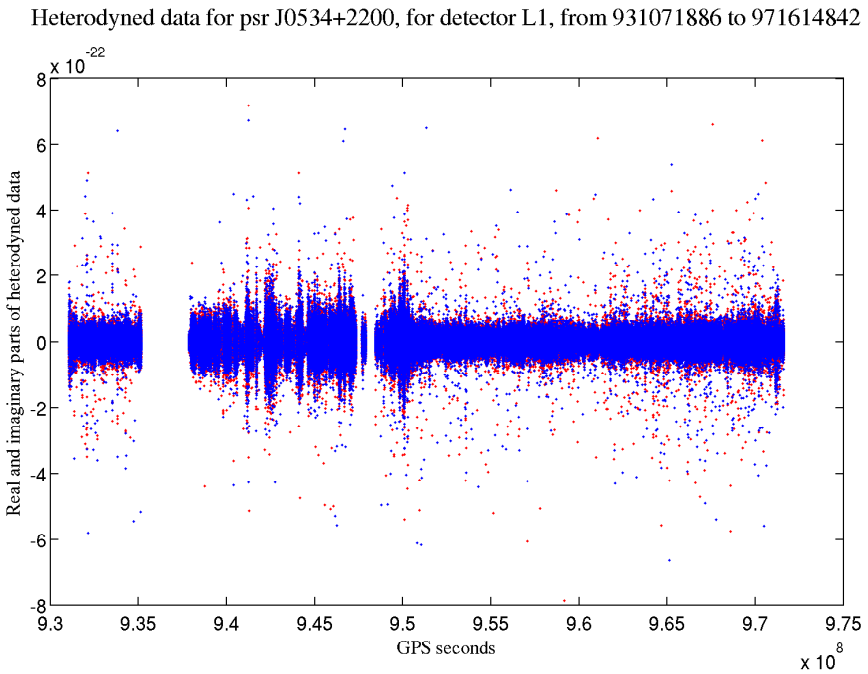

Figure 4.4: A plot of the heterodyned S6 L1 data for the Crab pulsar, with the GPS seconds along the x-axis, and the strain on the y-axis. The blue and red show the real and imaginary parts of the heterodyned data respectively.

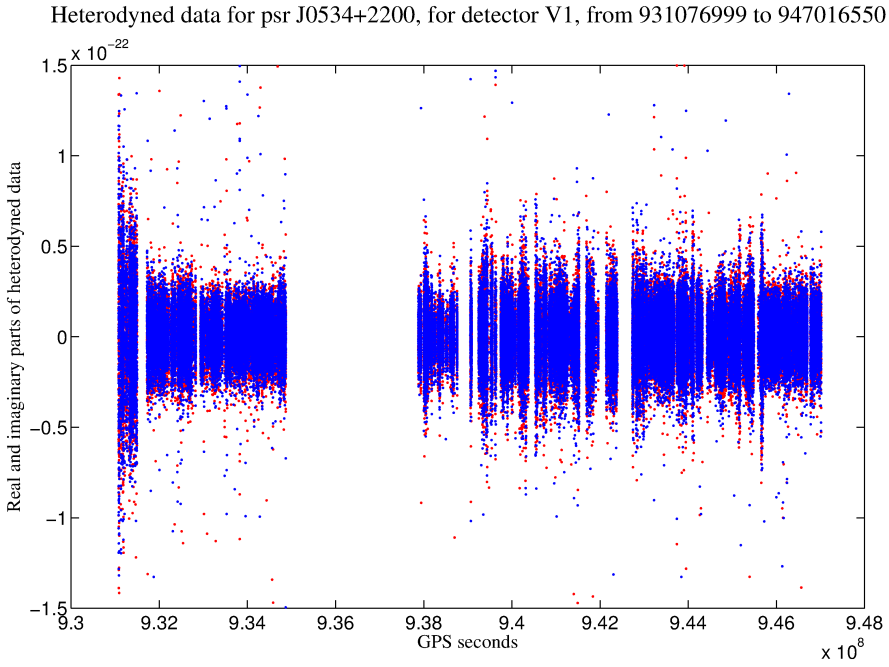

Figure 4.5: A plot of the heterodyned VSR2 data for the Crab pulsar, with the GPS seconds along the x-axis, and the strain on the y-axis. The blue and red show the real and imaginary parts of the heterodyned data respectively.

at $\sim$ 59.15 Hz, but again this does not appear to have affected the data at the Crab frequency. It appears from these Fscan spectrograms for S6, that the Crab

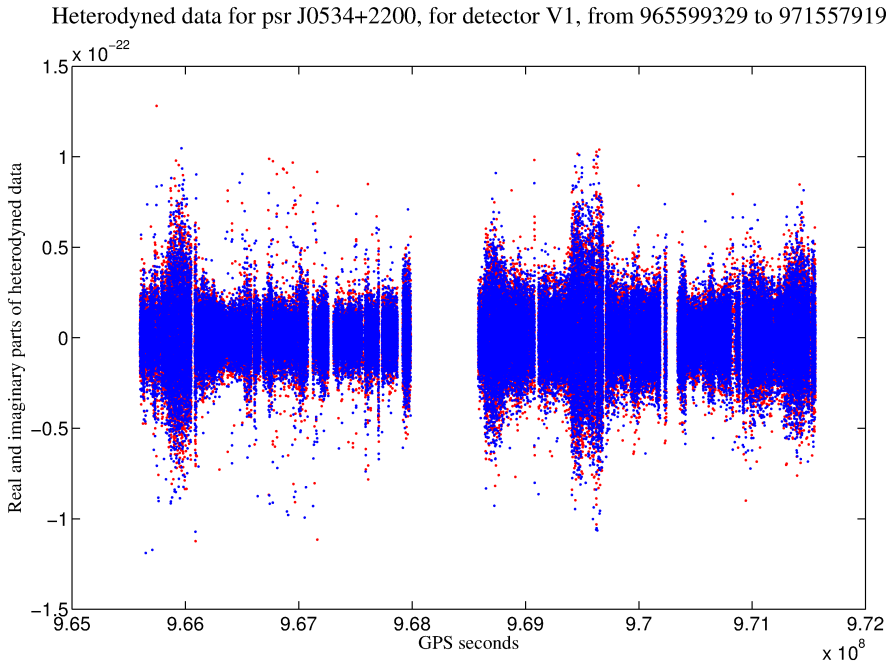

Figure 4.6: A plot of the heterodyned VSR3 data for the Crab pulsar, with the GPS seconds along the x-axis, and the strain on the y-axis. The blue and red show the real and imaginary parts of the heterodyned data respectively.

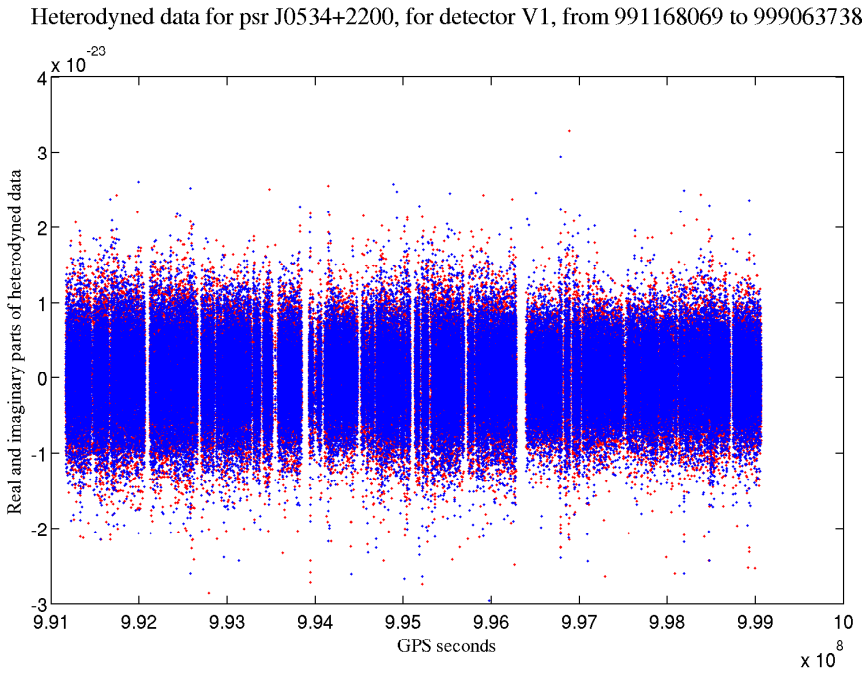

Figure 4.7: A plot of the heterodyned VSR4 data for the Crab pulsar, with the GPS seconds along the x-axis, and the strain on the y-axis. The blue and red show the real and imaginary parts of the heterodyned data respectively.

frequency was between two strong instrumental lines during the S6 run. This may not be the case with advanced LIGO. The advanced LIGO project will use entirely

new hardware, however some of the instrumental lines seen in enhanced LIGO may also be present in advanced LIGO - certainly the 60 Hz line will be. The spin-down of the Crab means that the frequency at which we expect its GWs is gradually decreasing, moving this frequency away from the 60 Hz line, but also moving it closer to the other lines described above in the band between 59.1 Hz and 59.2 Hz. If these lines are present in advanced LIGO, they could become a problem for future Crab GW searches.

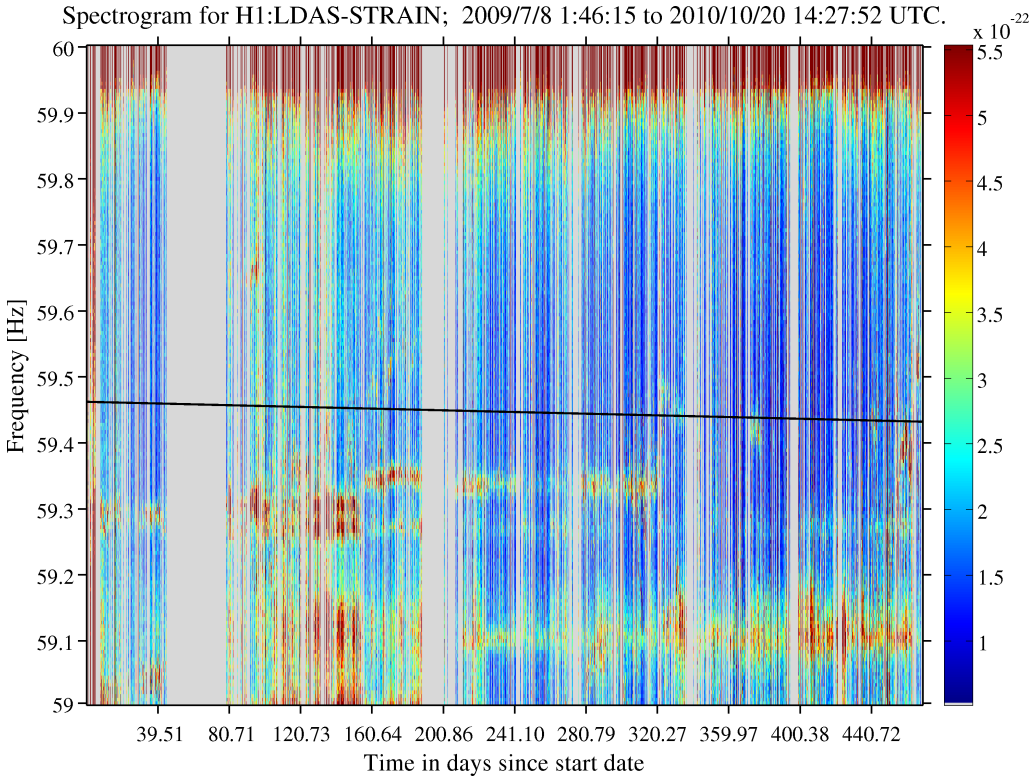

Figure 4.8: A Fscan spectrogram for a 10 Hz band over the whole of S6 with H1 data. Plotted as a black line is the frequency at which we expect GWs from the Crab pulsar. The spectrogram shows the evolution of the noise in this frequency band over the length of the run, and how it affects the data used for searches for GWs from the Crab.

4.5 Hardware injections

As previously discussed in §3.5, hardware injection pulsars provide an important test for search codes while actual detections remain elusive, as well as providing a sanity check for the detector calibration. The hardware injections in VRS2 and VSR4 data have already been presented and discussed in §3.5 and this is not repeated here. The hardware injection recovery PDFs for the LIGO S6 data are shown for the H1 detector in Figures 4.10 and 4.11, and for the L1 detector in Figures 4.12 and 4.13. The results for both detectors are summarised by the maximum likelihood values

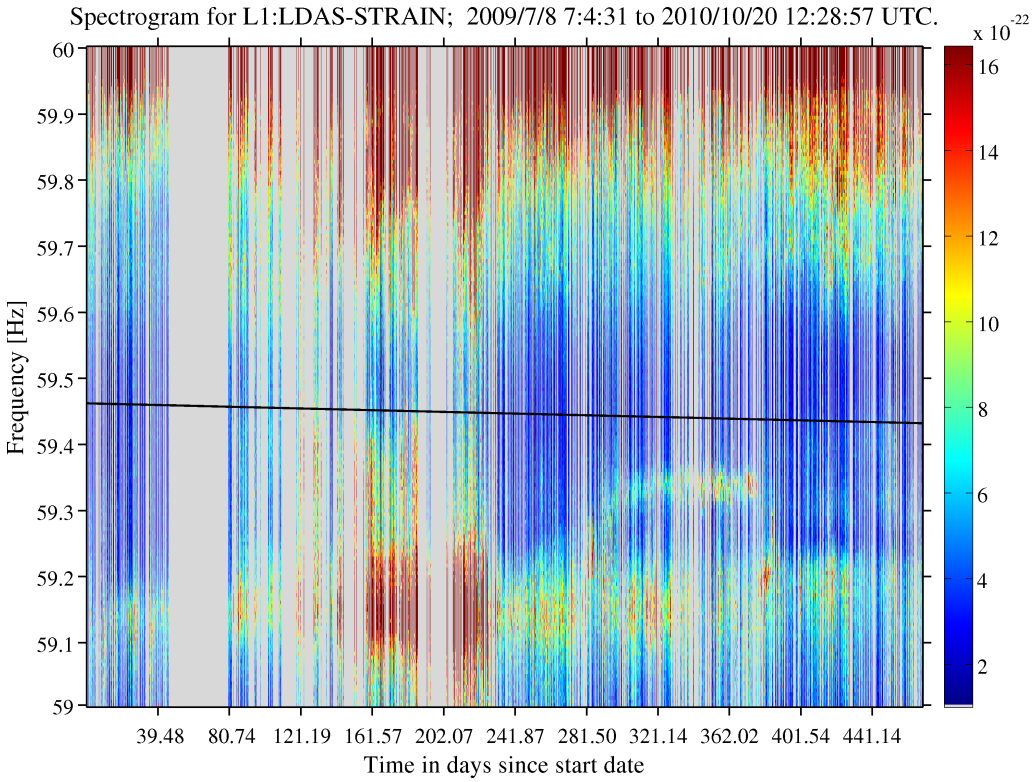

Figure 4.9: A Fscan spectrogram for a 10 Hz band over the whole of S6 with L1 data. Plotted as a black line is the frequency at which we expect GWs from the Crab pulsar. The spectrogram shows the evolution of the noise in this frequency band over the length of the run, and how it affects the data used for searches for GWs from the Crab.

of the four signal parameters in table 4.1. The table should be used for a quick summary only, if the reader wishes to fully understand the results the PDFs should be examined as they portray the full picture including the uncertainties. The data used in these hardware injections is taken from Nov 25 2009 06:25:07 UTC to Jan 28 2010 11:52:52 UTC. This is not the entire S6 dataset, but a subset of the whole. As with the Virgo hardware injection recovery results presented in §3.5, the signal parameters are generally recovered well, particularly for the stronger injections. The parameters that are not recovered so well are $\cos(\iota), \phi_0$ and ψ for hardware injection pulsars where there is a non-zero probability at $\cos(\iota) = 1, -1$. The results are consistent with what is expected given the relative strengths of the injections. The amplitude and phase errors are consistent with expected systematic errors and those reported for S5 (Abadie et al. 2010a). These results provide confidence in both the search codes and the calibration of the S6 data.

The hardware injection recovery PDFs for VSR3 data are shown in Figures 4.14 and 4.15, which are summarised in the same way as for other science runs in Table 4.2. The data used for the VSR3 hardware injections is taken from the entire run and consists of all the science data available. The results from the hardware injection

	h_0	ϕ_0	$\cos\iota$	ψ	f (Hz)
Psr 00 inj	2.47×10^{-25}	2.66	0.79	0.77	265.58
Psr 00 rec H1	2.60×10^{-25}	3.70	0.41	0.21	
Psr 00 rec L1	3.62×10^{-25}	3.87	0.51	0.18	
Psr 01 inj	1.06×10^{-24}	1.28	0.46	0.36	849.08
Psr 01 rec H1	1.27×10^{-24}	1.12	0.32	0.47	
Psr 01 rec L1	5.00×10^{-25}	0.87	0.48	0.56	
Psr 02 inj	4.02×10^{-24}	4.03	-0.93	-0.22	575.16
Psr 02 rec H1	3.73×10^{-24}	4.83	-0.94	0.16	
Psr 02 rec L1	4.15×10^{-24}	3.66	-0.90	-0.45	
Psr 03 inj	1.63×10^{-23}	5.53	-0.08	0.44	108.86
Psr 03 rec H1	1.63×10^{-23}	5.54	-0.08	0.43	
Psr 03 rec L1	1.62×10^{-23}	5.54	-0.09	0.47	
Psr 04 inj	4.56×10^{-23}	4.83	0.28	-0.65	1403.16
Psr 04 rec H1	4.34×10^{-23}	4.94	0.29	-0.63	
Psr 04 rec L1	4.31×10^{-23}	4.95	0.30	-0.62	
Psr 05 inj	4.85×10^{-24}	2.23	0.46	-0.36	52.81
Psr 05 rec H1	5.17×10^{-24}	1.96	0.37	-0.18	
Psr 05 rec L1	3.71×10^{-24}	0.46	0.59	0.67	
Psr 06 inj	6.92×10^{-25}	0.97	-0.15	0.47	148.72
Psr 06 rec H1	6.25×10^{-25}	1.08	-0.16	0.45	
Psr 06 rec L1	3.82×10^{-25}	1.02	-0.48	0.43	
Psr 07 inj	2.20×10^{-24}	5.25	0.76	0.51	1220.98
Psr 07 rec H1	2.00×10^{-24}	5.44	0.62	0.59	
Psr 07 rec L1	3.50×10^{-24}	0.24	0.40	-0.03	
Psr 08 inj	1.59×10^{-23}	5.89	0.07	0.17	194.31
Psr 08 rec H1	1.56×10^{-23}	5.90	0.07	0.17	
Psr 08 rec L1	1.56×10^{-23}	5.88	0.07	0.18	
Psr 09 inj	8.13×10^{-25}	1.01	-0.62	-0.01	763.85
Psr 09 rec H1	6.11×10^{-25}	1.93	-0.67	0.42	
Psr 09 rec L1	6.99×10^{-25}	0.37	-0.46	-0.62	

Table 4.1: Table showing the recovered and injected parameters for S6 H1 and L1 hardware injections for psr00 to psr09, with the frequency for each injection also listed.

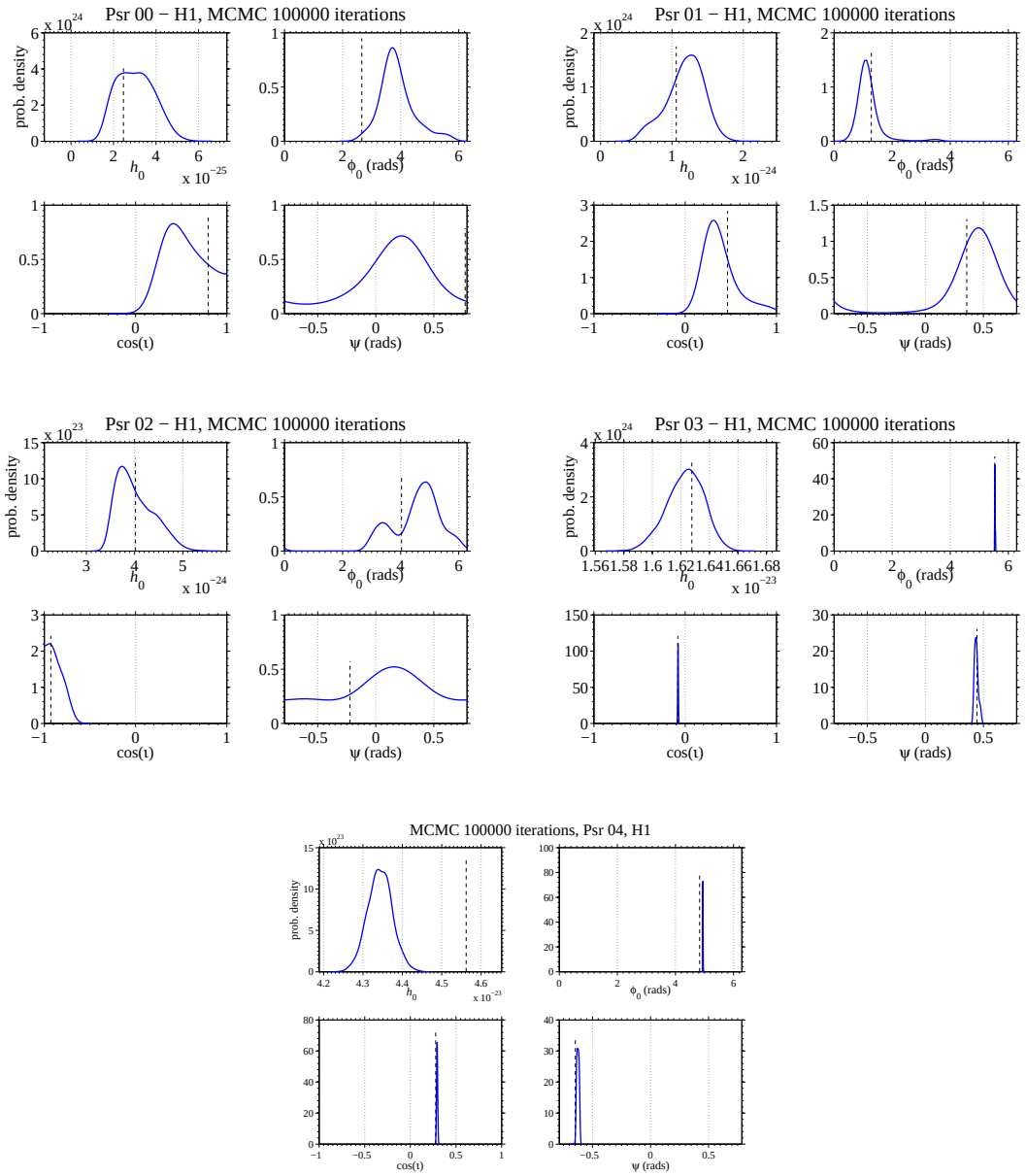

Figure 4.10: PDFs of S6 hardware injection pulsars Psr 00 to Psr 04, using H1 data

recovery from VSR3 do not show any issues with the calibration of the data or the search codes used for the analysis, and follow the general picture seen in hardware injection recovery for other science runs, i.e. the strong injections are recovered very well, with errors in the calibration taken into account, and the degeneracy between ϕ_0 and ψ showing for the injections where the probability density is non-zero at $\cos(\iota) = 1, -1$.

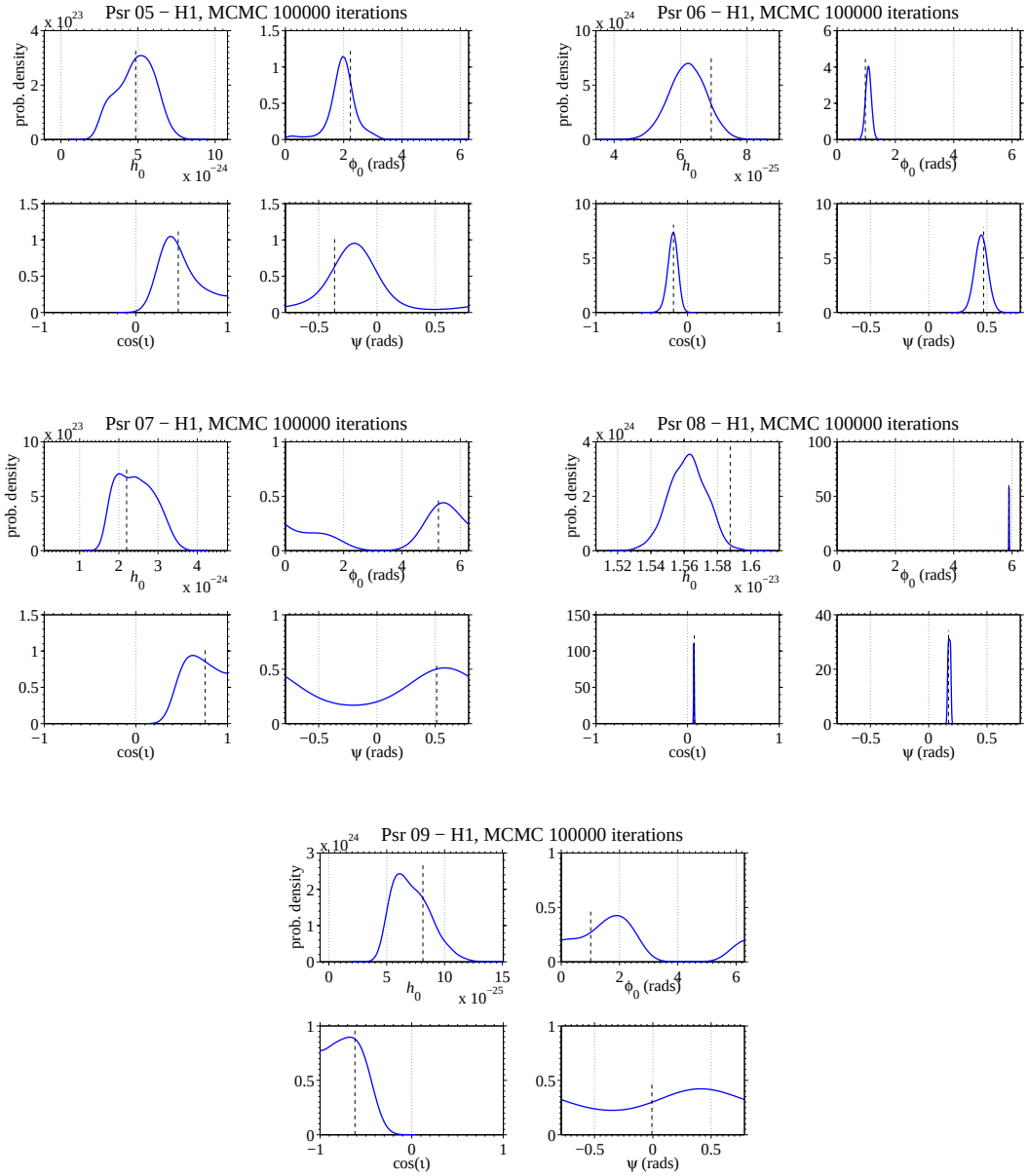

Figure 4.11: PDFs of S6 hardware injection pulsars Psr 05 to Psrt 09, using H1 data

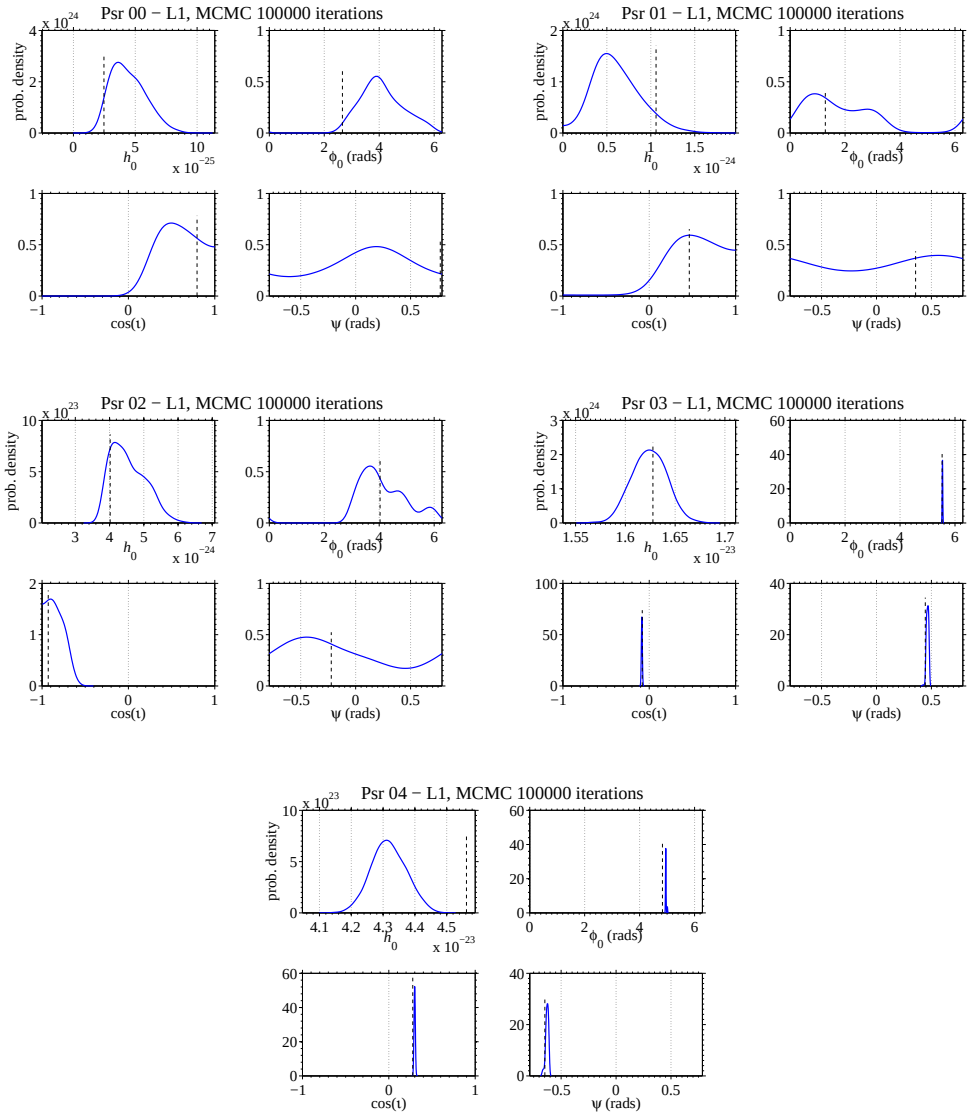

Figure 4.12: PDFs of S6 hardware injection pulsars Psr 00 to Psr 04, using L1 data

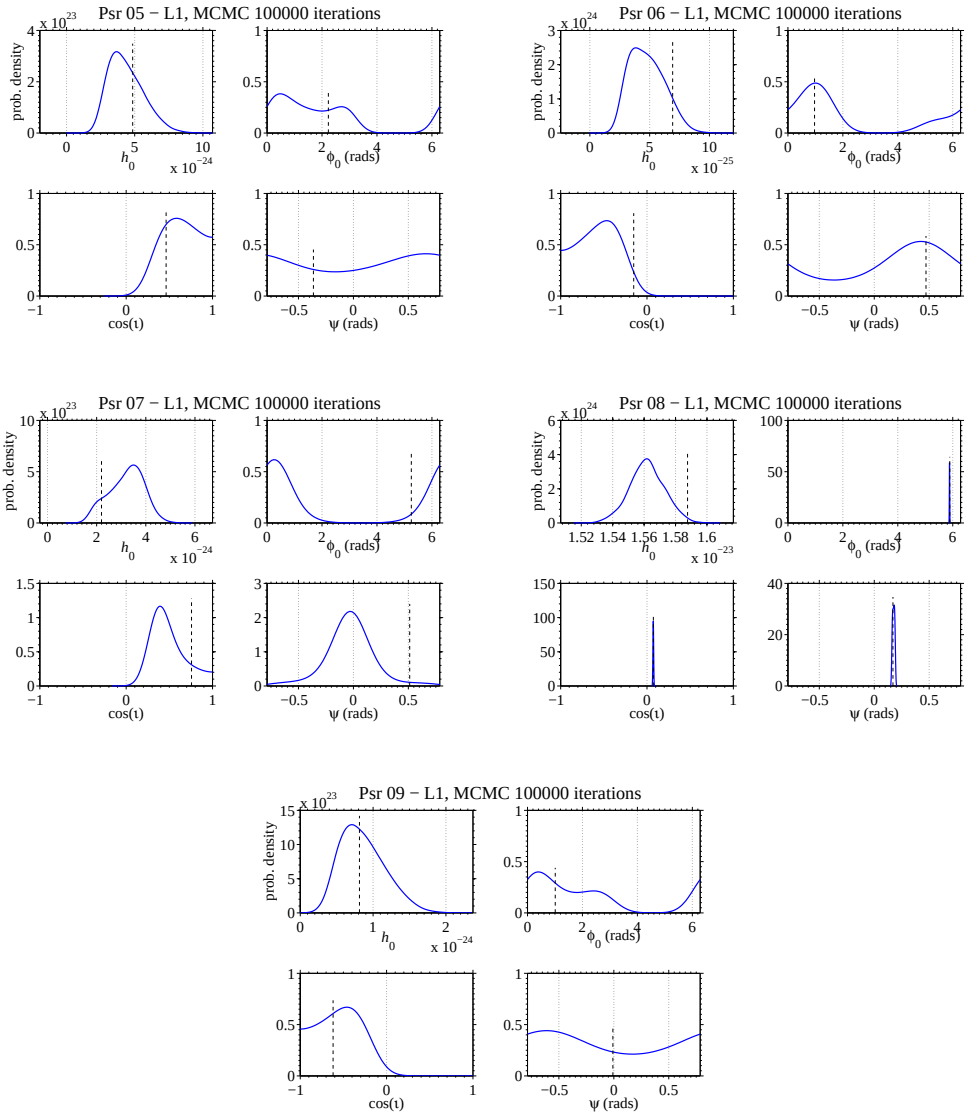

Figure 4.13: PDFs of S6 hardware injection pulsars Psr 05 Psr 09, using L1 data

	h_0	ϕ_0	$\cos\iota$	ψ
Psr 00 inj	2.47×10^{-25}	2.66	0.79	0.77
Psr 00 rec	3.60×10^{-25}	3.94	0.53	0.25
Psr 01 inj	1.06×10^{-24}	1.28	0.46	0.36
Psr 01 rec	8.08×10^{-25}	0.97	0.47	0.66
Psr 02 inj	4.02×10^{-24}	4.03	-0.93	-0.22
Psr 02 rec	4.01×10^{-24}	4.07	-0.94	-0.18
Psr 03 inj	1.63×10^{-23}	5.53	-0.08	0.44
Psr 03 rec	1.68×10^{-23}	5.53	-0.08	0.43
Psr 04 inj	4.56×10^{-23}	4.83	0.28	-0.65
Psr 04 rec	4.59×10^{-23}	4.94	0.26	-0.65
Psr 05 inj	4.85×10^{-24}	2.23	0.46	-0.36
Psr 05 rec	3.70×10^{-24}	2.46	0.69	-0.61
Psr 06 inj	6.92×10^{-25}	0.97	-0.15	0.47
Psr 06 rec	3.45×10^{-25}	1.18	-0.14	0.41
Psr 07 inj	2.20×10^{-24}	5.25	0.76	0.51
Psr 07 rec	3.85×10^{-24}	5.77	0.36	0.31
Psr 08 inj	1.59×10^{-23}	5.89	0.07	0.17
Psr 08 rec	1.58×10^{-23}	5.89	0.07	0.18
Psr 09 inj	8.13×10^{-25}	1.01	-0.62	-0.01
Psr 09 rec	7.73×10^{-25}	0.44	-0.55	-0.40

Table 4.2: Table showing the recovered and injected parameters for VSR3 hardware injections.

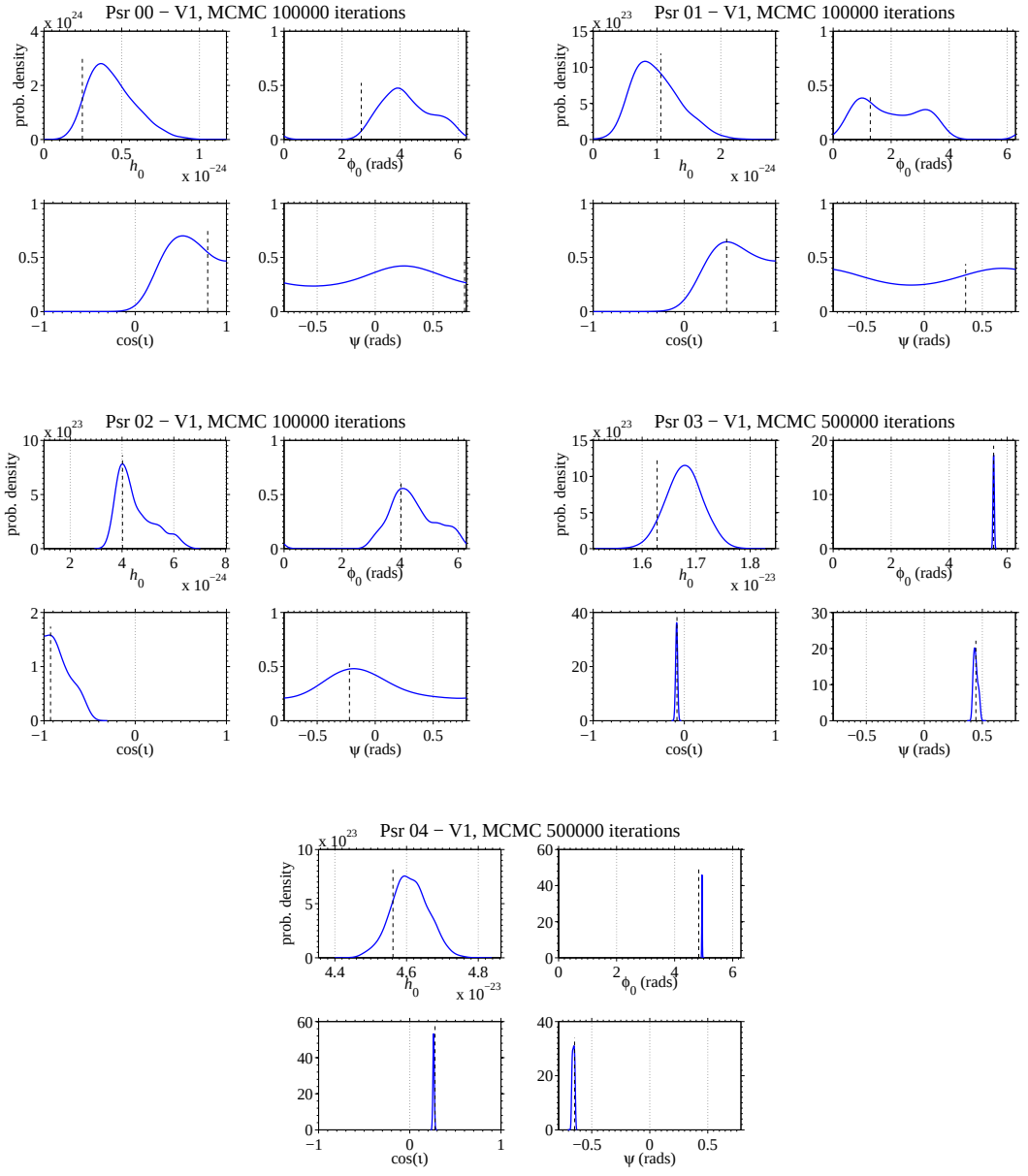

Figure 4.14: Probability density functions (PDFs) for the recovery of pulsar hardware injections psr00 to psr04 in VSR3 data.

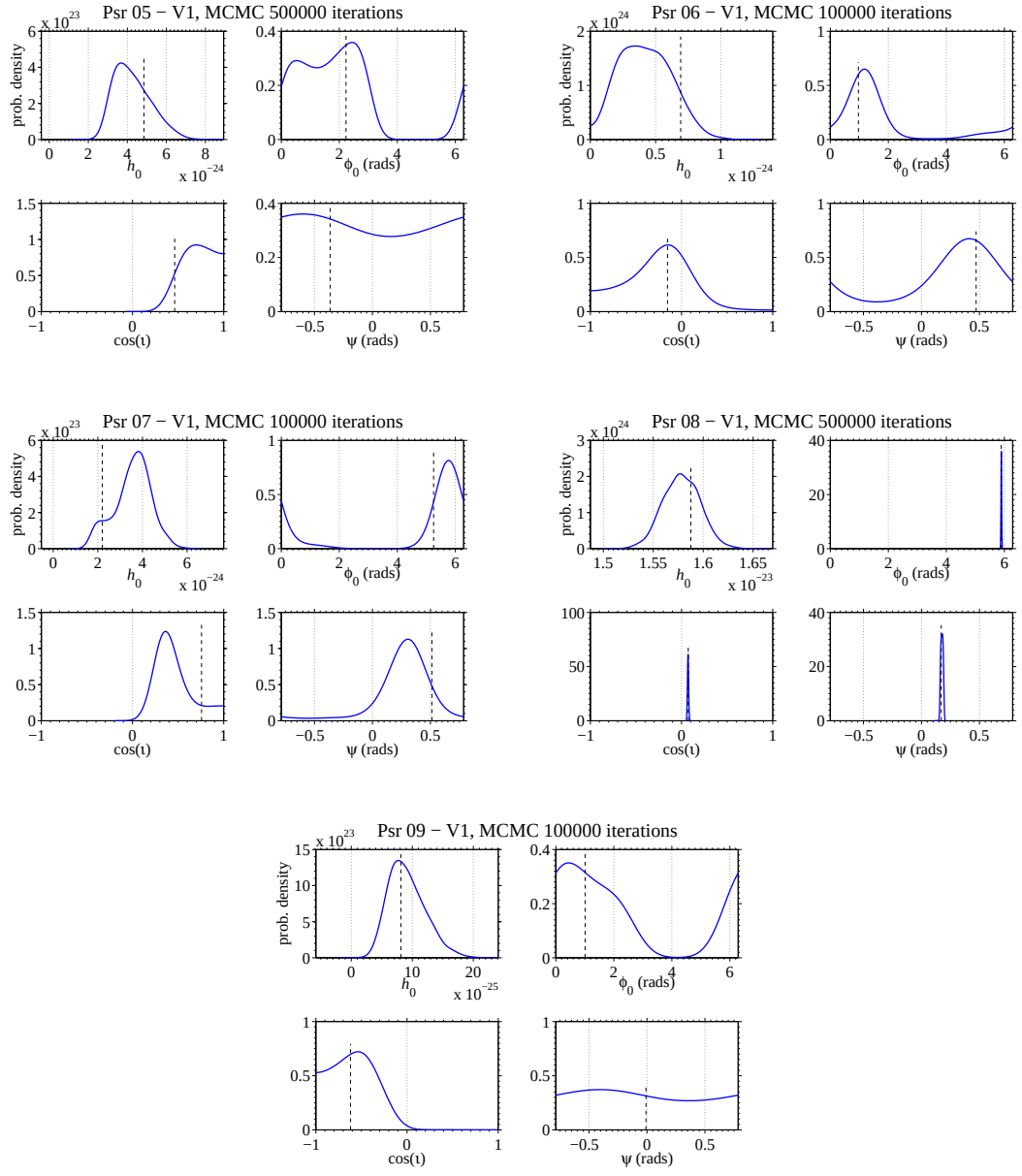

Figure 4.15: Probability density functions (PDFs) for the recovery of pulsar hardware injections psr05 to psr09 in VSR3 data.

4.6 Results

The results from analyses looking for GWs from the Crab pulsar, using the datasets described in §4.4, are presented in this section. The main results from these analyses are PDFs for each of the unknown signal parameters. Exactly what the PDFs represent is discussed in detail §3.6, but as a quick reminder - they show the marginalised probability density across a range of values for each of the unknown signal parameters. For all the datasets, I present results from two different parameter estimation runs. One run assumes no prior knowledge of the orientation of the Crab pulsar, and the other run uses observations of the Crab pulsar's wind tori by Ng & Romani (2008) to place Gaussian priors on the parameters $\cos(\iota)$ and ψ. These two different assumptions are expected to produce different results where no signal is detected, but if a signal was present and sufficiently strong, the signal would dominate over any affect of the priors.

Again, as discussed in §3.6, the most important PDF in these results is the h_0 PDF, as this will tell us the most likely value for the signal amplitude. Where there is no signal present in the data then one would expect this PDF to peak at zero, i.e. to show that the most likely situation is where there is no signal. However, there may also be cases where the peak in the h_0 PDF is non-zero. This does not necessarily mean that a detection has been made. In tests where multiple sets of simulated data containing only Gaussian noise are analysed a small proportion of the analyses return PDFs for h_0 which do not peak at zero. In this case the rest of the h_0 PDF can tell us something interesting, particularly what is the probability of $h_0 = 0$. Where there is a strong signal present the probability density at $h_0 = 0$ can be expected to be zero, or close to zero. The PDFs for the other parameters are also able to help, where there is a strong signal present - it is reasonable to expect the PDFs of these parameters to show a strong peak. Where this is not the case, i.e the probability density at $h_0 = 0$ is high and the other PDFs show no strong peaks, the PDFs are consistent with no signal being present in the data. This way of determining whether a signal is present in the data is far from ideal, Chapter 6 details a development of the search code to deal with this question in a more robust way through the process of model selection.

4.6.1 S6

The analyses using S6 data to search for GWs from the Crab pulsar shows no evidence of a signal. The resulting PDFs for the signal parameters where uniform priors are placed on all the parameters are shown for H1 only, L1 only and a combination of H1 and L1 data in Figure 4.16. The 95% upper limits obtained from these results with data from H1 is 4.5×10^{-25}, for L1 is 5.8×10^{-25}, and for H1 and L1 combined

is 3.1×10^{-25}. The PDF for h_0 for H1 data can be seen to peak at a non-zero value. The fact that a similar peak does not appear in the L1 h_0 PDF would suggest that this is not due to a GW. That the probability density at $h_0 = 0$ for the H1 PDF is relatively high and the other PDFs for H1 are not strongly peaked, suggests that this is not due to a GW, but rather is a function of the noise in the H1 data.

The resulting PDFs from the analyses with Gaussian priors on ψ and $\cos(\iota)$, are shown for H1 only, L1 only and a combination of H2 and L1 data in Figure 4.17. The 95 % confidence upper limits on h_0 obtained for H1 is 3.9×10^{-25}, for L1 is 5.0×10^{-25} and for H1 and L1 joint is 2.8×10^{-25}.

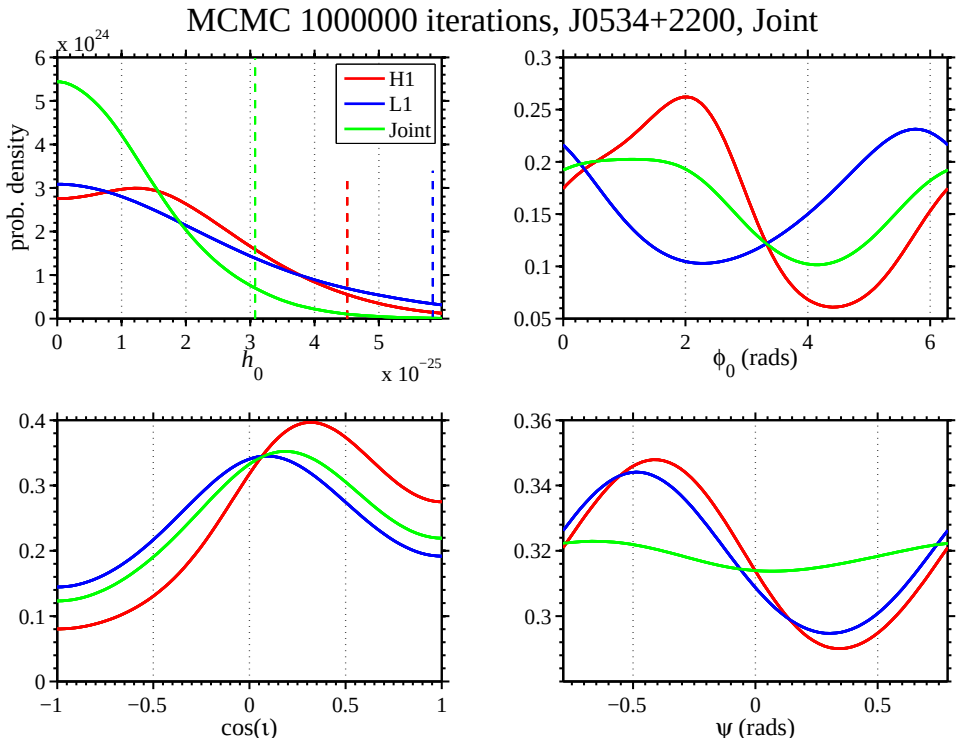

Figure 4.16: The PDFs from S6, data from H1, L1, and H1 and L1 combined, produced by MCMCs with 100 000 iterations. The MCMCs were run with uniform priors on all parameters.

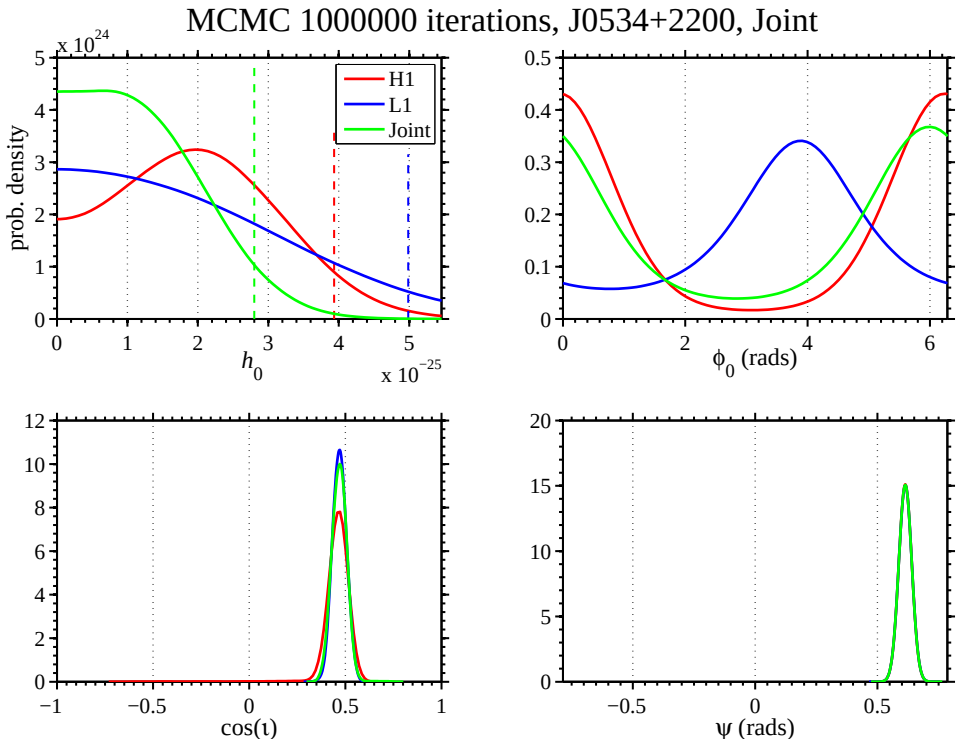

Figure 4.17: The PDFs from S6, data from H1, L1, and H1 and L1 combined, produced by MCMCs with 100 000 iterations. The MCMCs were run with Gaussian priors on ψ and $\cos(\iota)$.

4.6.2 VSR2

The PDFs for VSR2 from the parameter estimation run using uniform priors on ψ and $\cos(\iota)$ can be seen in Figure 4.18, and for the parameter estimation run using Gaussian priors on ψ and $\cos(\iota)$ in Figure 4.19. For both sets of PDFS, the h_0 PDF peaks at zero, i.e. the data does not suggest that there is a signal present. The 95 % confidence upper limit on h_0 for these runs are 2.8×10^{-24} and 2.6×10^{-24}, for the run with uniform priors and the run with Gaussian priors respectively.

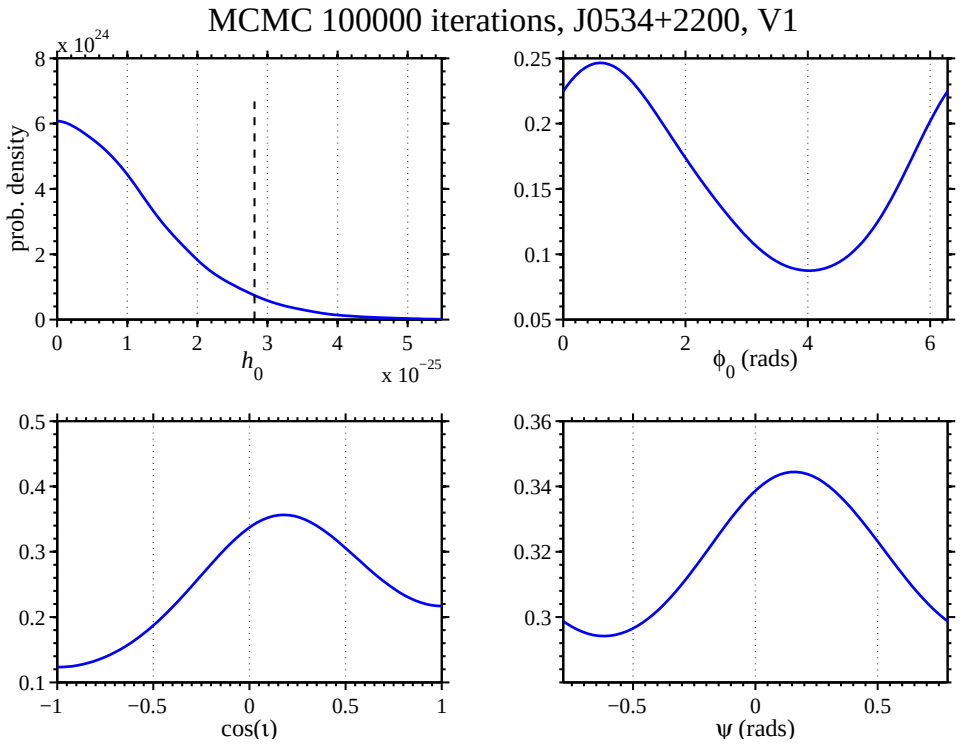

Figure 4.18: The PDFs from VSR2 for the Crab pulsar produced by a MCMC with 100 000 iterations. The MCMC was run with uniform priors on all parameters. The 95% upper limit on h_0 derived from this MCMC is 2.8×10^{-25}.

4.6.3 VSR3

The PDFs resulting from the run using uniform priors on ψ and $\cos(\iota)$ can be seen in Figure 4.20, and in Figure 4.21 for the run with Gaussian priors on ψ and $\cos(\iota)$. Both of these runs have produced PDFs consistent with no GW signal present in the data, so are used to place 95 % confidence upper limits on h_0. These upper limits are 1.0×10^{-24} for the run with uniform priors, and 8.5×10^{-25} for the run with Gaussian priors.

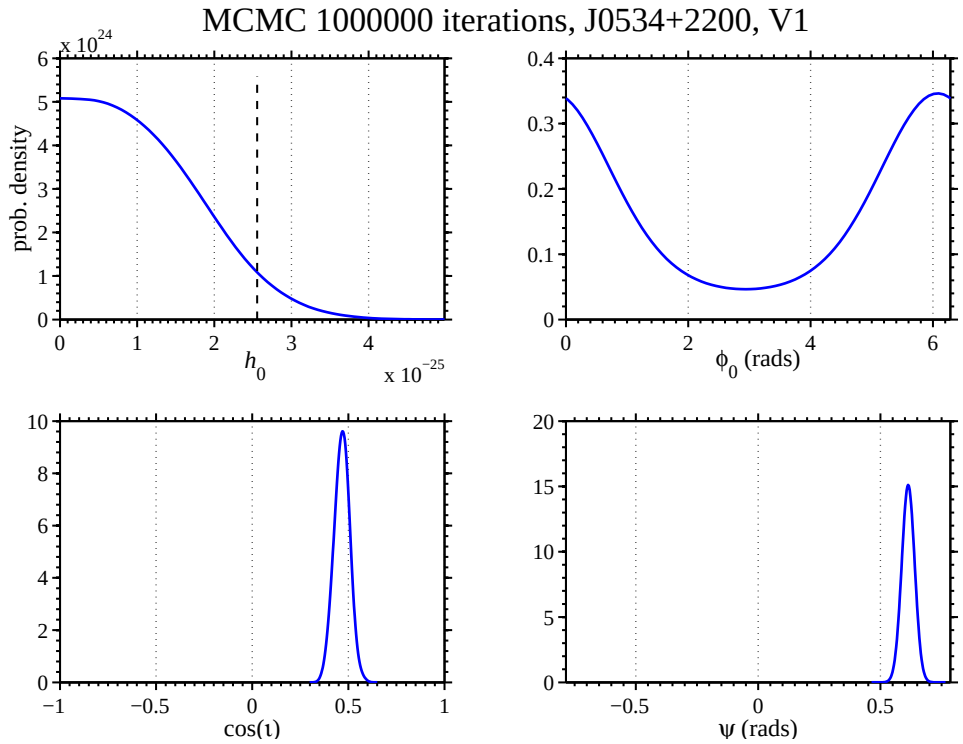

Figure 4.19: The PDFs from VSR2, produced by a MCMC with 100 000 iterations. The MCMC was run with Gaussian priors on the orientation parameters ψ and $\cos(\iota)$. The 95% upper limit on h_0 derived from this MCMC is 2.6×10^{-25}.

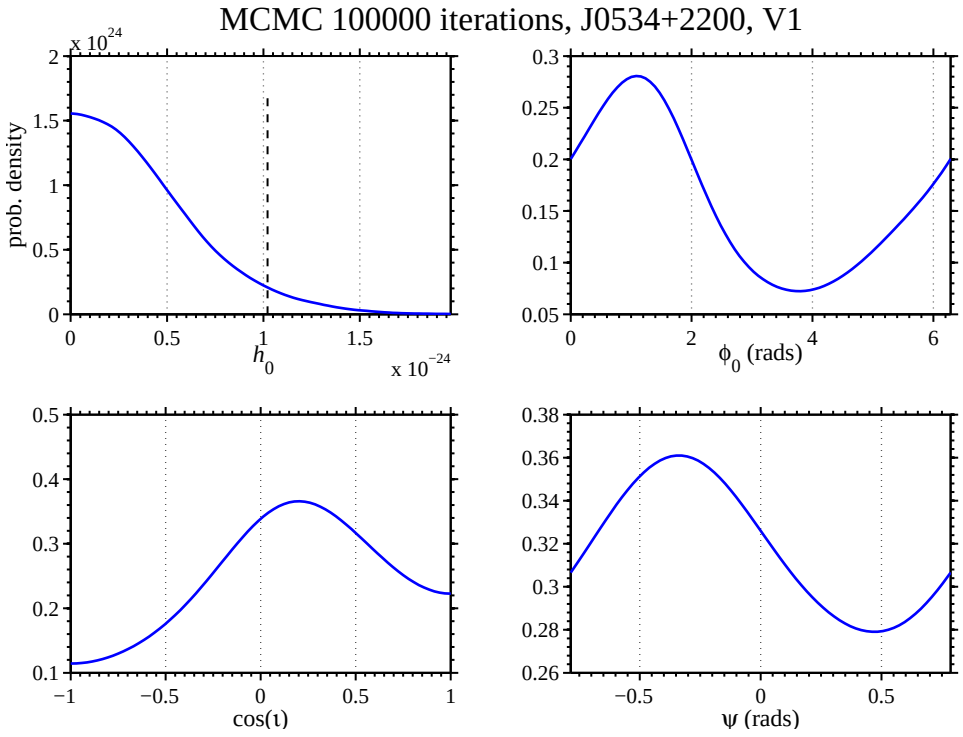

Figure 4.20: The PDFs from VSR3 for the Crab pulsar produced by a MCMC with 100 000 iterations. The MCMC was run with uniform priors on all parameters. The 95% upper limit on h_0 derived from this MCMC is 1.0×10^{-24}.

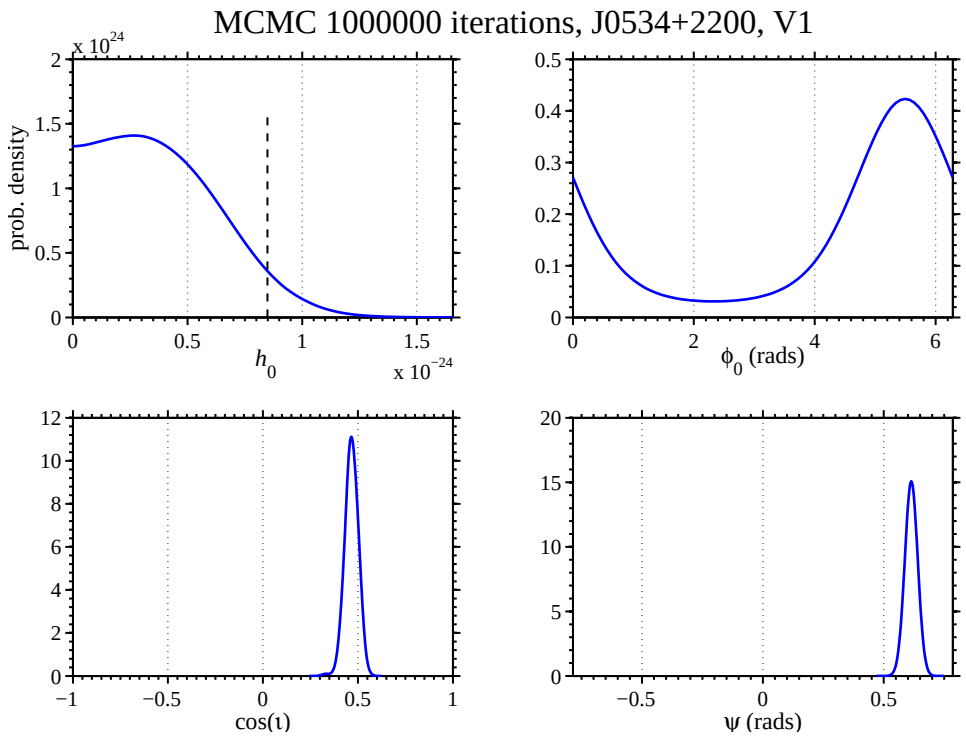

Figure 4.21: The PDFs from VSR3, produced by a MCMC with 100 000 iterations. The MCMC was run with gaussian priors on the orientation parameters ψ and $\cos(\iota)$. The 95% upper limit on h_0 derived from this MCMC is 8.5×10^{-25}.

4.6.4 VSR4

The PDFs from the parameter estimation run with flat priors on all parameters and with Gaussian priors on the orientation parameters can be seen in Figures 4.22 and 4.23 respectively. The h_0 PDFs from these results indicate that there is no signal present. The 95 % confidence upper limits on h_0 for the run with uniform priors on all parameters is 3.1×10^{-24}, and with Gaussian priors on the orientation parameters is 2.3×10^{-24}.

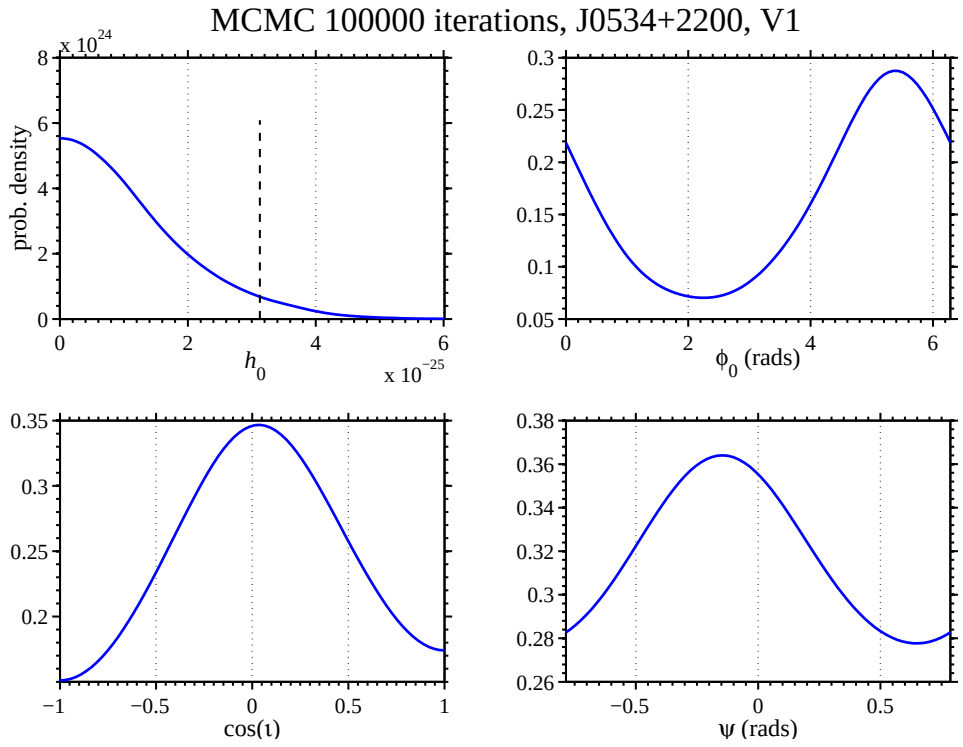

Figure 4.22: The PDFs from VSR4, produced by a MCMC with 100 000 iterations. The MCMC was run with uniform priors on all parameters. The 95% upper limit on h_0 derived from this MCMC is 3.1×10^{-25}.

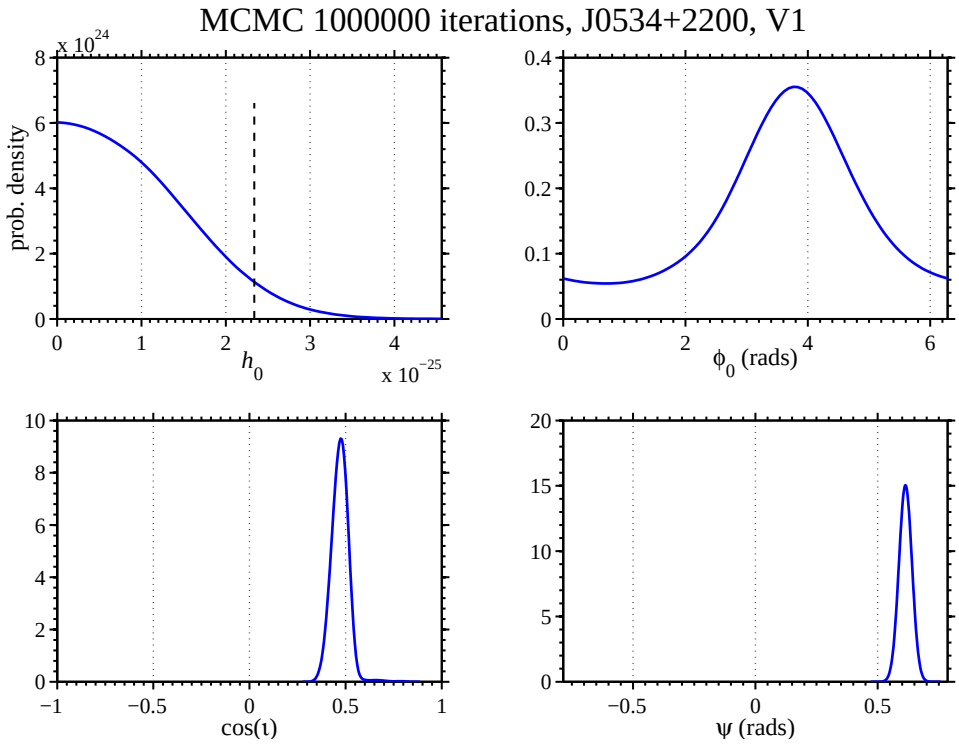

Figure 4.23: The PDFs from VSR4, produced by a MCMC with 100 000 iterations. The MCMC was run with Gaussian priors on the orientation parameters ψ and $\cos(\iota)$. The 95% upper limit on h_0 derived from this MCMC is 2.3×10^{-25}.

4.6.5 S5, S6, VSR2, VSR3, VSR4

By combining the datasets from S5, S6, VSR2, VSR3 and VSR4 I can create a large dataset that spans years and provides the data for the most sensitive search for GWs from the Crab pulsar to date. Unfortunately the occurrence of two glitches during this period complicates the search slightly.

Despite these glitches I have performed a simplistic naive search where the effect of the glitches is simply ignored and the whole dataset is treated as one coherent dataset. Whilst this is a naive view to take, our ignorance of the effect of glitches on GW emission from pulsars means that it is not necessarily an incorrect one.

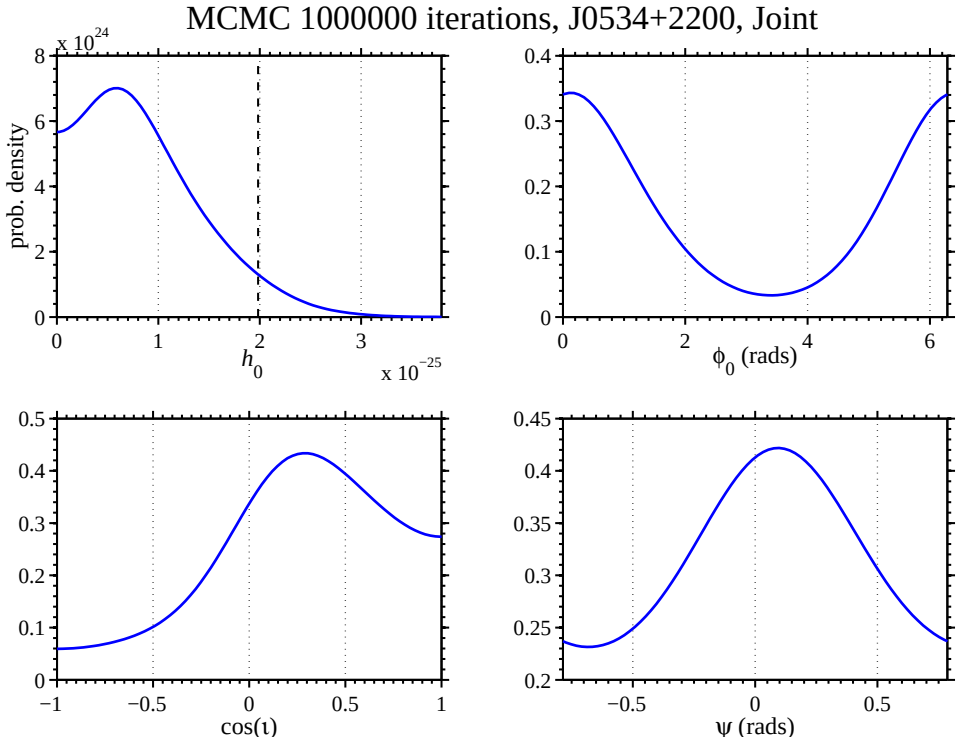

Figure 4.24: The PDFs from S5, S6, VSR2,VSR3 and VSR4 combined, produced by a MCMC with 100 000 iterations. The MCMC was run with Gaussian priors on the orientation parameters ψ and $\cos(\iota)$. The 95% upper limit on h_0 derived from this MCMC is 2.8×10^{25}. This result assumes no change in GW emission as a result of glitches.

A pulsar glitch is where there is a non-steady change in the spin frequency of the pulsar (a more detailed description of glitches was included in §2.2). The results shown in Figures 4.24 to 4.25 were obtained by assuming no change in the GW emission as a result of two glitches in the Crab pulsar which occurred at 53970.1900 MJD (23 Aug 2006 04:33:36, 840342830 UTC) and 54580.38 MJD (24 April 2008 09:07:12 UTC, 893063246) (Espinoza et al. 2011). This places one glitch in the middle of the S5 run, and one glitch between the S5 and S6 runs, before VSR2. To make use of all the available data but not ignore the fact that the glitches may have caused some

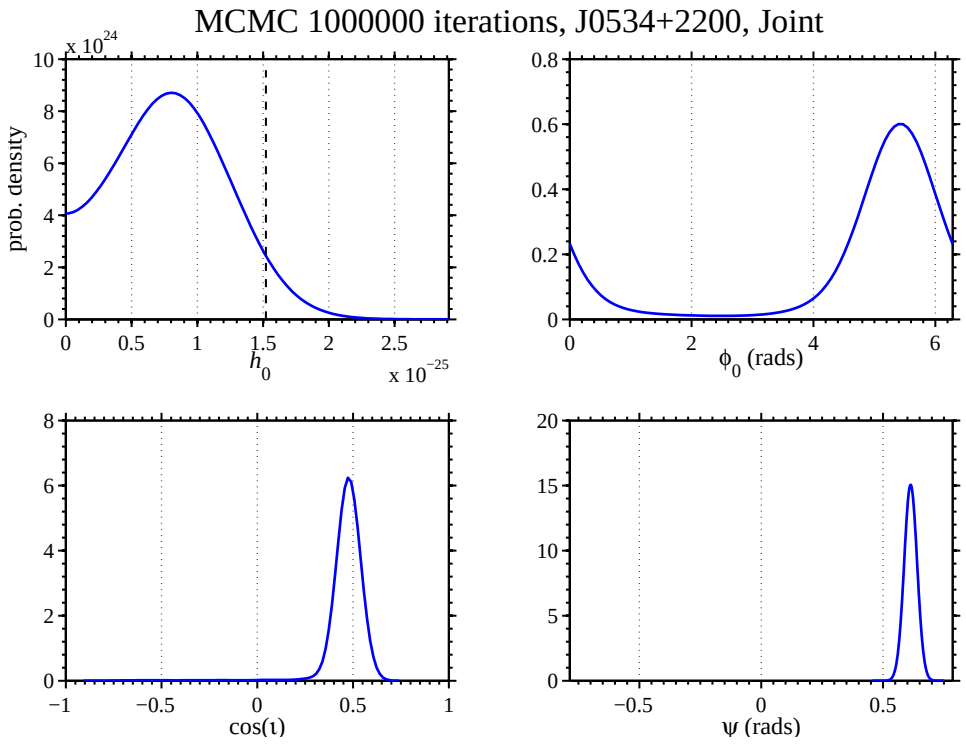

Figure 4.25: The PDFs from S5, S6, VSR2,VSR3 and VSR4 combined, produced by a MCMC with 100 000 iterations. The MCMC was run with uniform priors on all parameters. The 95% upper limit on h_0 derived from this MCMC is 3.2×10^{25}. This result assumes there is no change in GW emission as a result of glitches.

change in the GW emission, I have run the parameter estimation part of the search with two extra phase parameters, so instead of the normal ϕ_0 parameter there are now three phase parameters $\phi_{0,1}, \phi_{0,2}, \phi_{0,3}$. Any data that lies within 86400 seconds (1 day) of a glitch is removed from the dataset as it is unclear what happens to the GW signal before and after the glitch. 86400 seconds is chosen, as typical glitch related changes in the EM signal from the pulsar occur over much shorter timescales, so this cut is conservatively chosen as one that would exclude such changes in the GW signal. The remaining data either side of the glitches are then treated as separate chunks of data, so if there is one glitch in a dataset then that dataset is separated into two distinct chunks of data and the signal is assumed to not be coherent between them. The initial phase of the GW signal is determined for each of these newly defined chunks of data separately, however the other GW signal parameters $(h_0, \psi, \cos(\iota))$ are assumed to stay the same over both chunks of data. The reasoning behind this approach is that the energy involved in a glitch is unlikely to change the shape of the NS significantly, yet the evolution of the GW signal immediately around the time of the glitch is not understood or even well hypothesised. The PDFs from these analyses with the datasets from each detector combined are shown in Figures 4.26 and 4.27. Each of the three ϕ_0 parameters has an associated

PDF, which are shown as three different coloured PDFs for ϕ_0 in these figures. The upper limits on h_0 derived from these analyses are 1.3×10^{-25} when uniform priors are used on all parameters, and 1.0×10^{-25} when Gaussian priors are used for ψ and $\cos(\iota)$. The upper limits derived from the PDFs for each of the detector's datasets individually, and combined, are shown in Table 4.3, the PDFs for each of these is not shown for reasons of saving space.

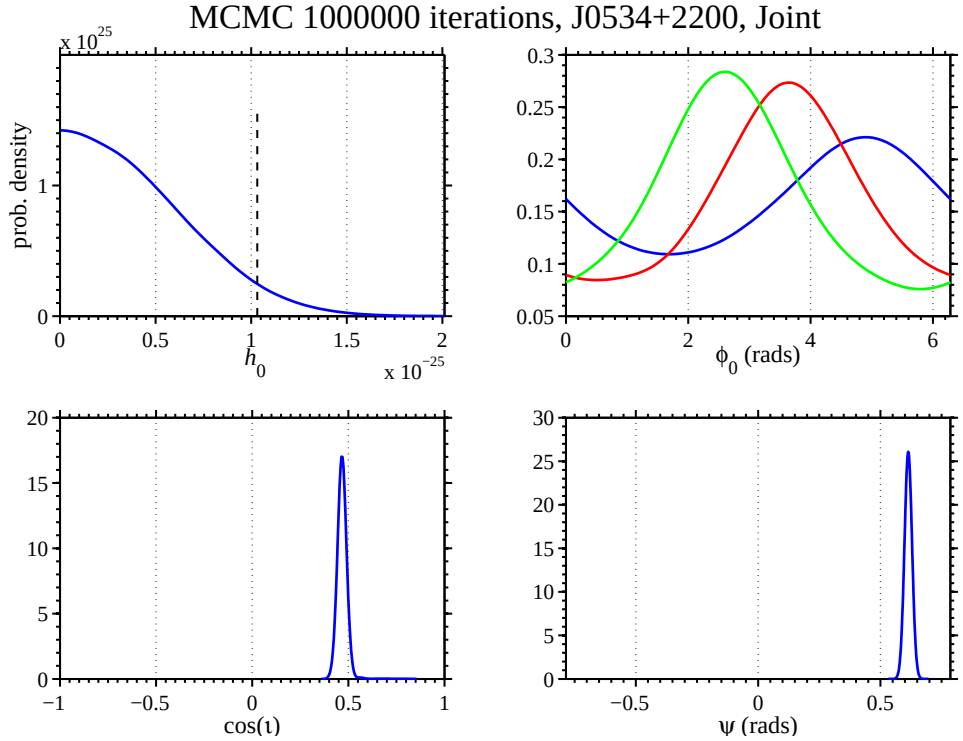

Figure 4.26: The PDFs from S5, S6, VSR2, VSR3 and VSR4 combined, produced by a MCMC with 100 000 iterations, using data from V1, H1 and L1. The MCMC was run with Gaussian priors on the orientation parameters ψ and $\cos(\iota)$. Due to the Crab pulsar glitching twice during the data runs, the data were separated into three sections and the ϕ_0 parameter is allowed to take a different value in each of these sections. Hence the three PDFs, coloured green, red and blue, for the ϕ_0 parameter shown here. The 95% upper limit on h_0 derived from this MCMC is 1.0×10^{25}.

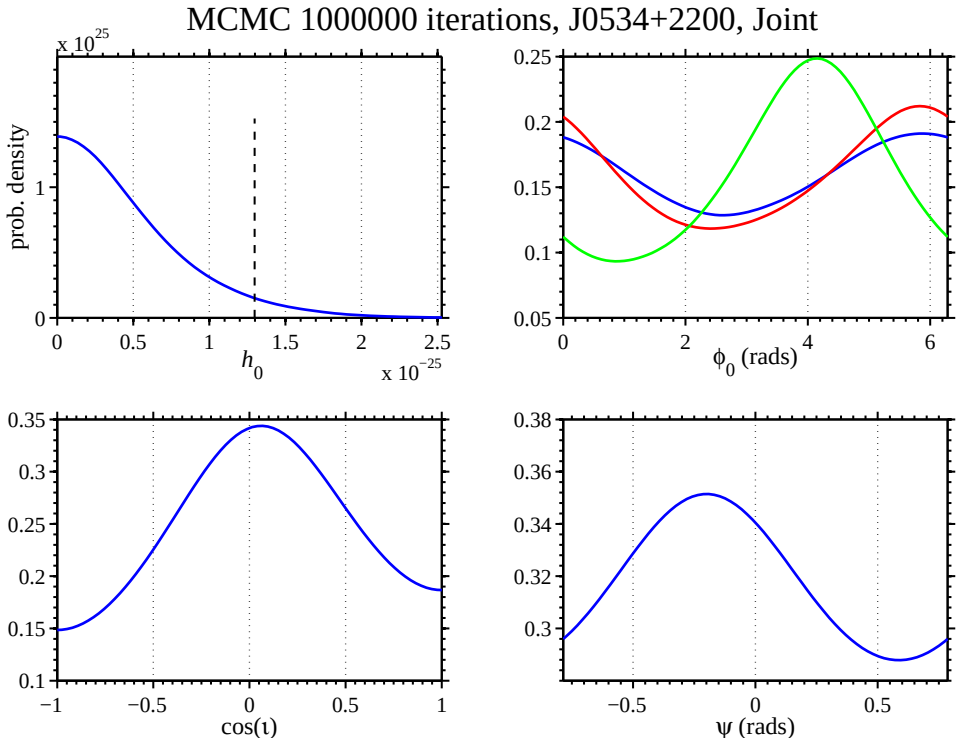

Figure 4.27: The PDFs from S5, S6, VSR2, VSR3 and VSR4 combined, produced by a MCMC with 100 000 iterations, using data from V1, H1 and L1. The MCMC was run with uniform priors on all parameters. Due to the Crab pulsar glitching twice during the data runs, the data were separated into three sections and the ϕ_0 parameter is allowed to take a different value in each of these sections. Hence the three PDFs, coloured green, red and blue, for the ϕ_0 parameter shown here. The 95% upper limit on h_0 derived from this MCMC is 1.3×10^{-25}.

Dataset	$h_{0,95}$	h_0^{95}/h_0^{sd}	Ellipticity	Priors on ψ and $\cos(\iota)$
S5, S6 (H1)	2.3×10^{-25}	0.16	1.2×10^{-4}	uniform
S5, S6 (L1)	3.7×10^{-25}	0.26	2.0×10^{-4}	uniform
VSR2, VSR3, VSR4	2.0×10^{-25}	0.14	1.1×10^{-4}	uniform
VSR2, VSR3, VSR4, S5, S6 (H1,L1)	2.0×10^{-25}	0.14	1.1×10^{-4}	uniform
S5, S6 (H1)	2.0×10^{-25}	0.14	1.1×10^{-4}	Gaussian
S5, S6 (L1)	2.8×10^{-25}	0.20	1.5×10^{-4}	Gaussian
VSR2, VSR3, VSR4	1.6×10^{-25}	0.11	8.6×10^{-5}	Gaussian
VSR2, VSR3, VSR4, S5, S6 (H1,L1)	1.5×10^{-25}	0.11	8.0×10^{-5}	Gaussian
S5, S6 (H1)	2.9×10^{-25}	0.21	1.6×10^{-4}	uniform
S5, S6 (L1)	3.5×10^{-25}	0.25	1.9×10^{-4}	uniform
VSR2, VSR3, VSR4	2.4×10^{-25}	0.17	1.3×10^{-4}	uniform
VSR2, VSR3, VSR4, S5, S6 (H1,L1)	1.3×10^{-25}	0.09	7.0×10^{-5}	uniform
S5, S6 (H1)	2.5×10^{-25}	0.18	1.3×10^{-4}	Gaussian
S5, S6 (L1)	2.8×10^{-25}	0.20	1.5×10^{-4}	Gaussian
VSR2, VSR3, VSR4	1.8×10^{-25}	0.13	9.6×10^{-5}	Gaussian
VSR2, VSR3, VSR4, S5, S6 (H1,L1)	1.0×10^{-25}	0.07	5.4×10^{-5}	Gaussian

Table 4.3: Table showing the 95% upper limits placed on h_0 from each analysis on the different datasets, with analyses assuming the GW signal remains coherent between times before and after a glitch shown in the top half of the table, and analyses with separate ϕ_0 parameters for the periods between the glitches shown in the bottom half of the table.

4.7 Discussion

Unfortunately there is no clear cut evidence of the existence of a GW signal in the results described in §4.6. In a few of the PDFs (see Figures 4.25 and 4.24), the h_0 PDF peaks at a non-zero value. Strictly speaking this is saying that the most probable value for h_0, if it is assumed that there is a GW present, is a non-zero value. However, such non-zero peaks occur in simulations using purely white noise and no-signal, and so too much weight should not be applied to such a result. Indeed, part of the advantage of using a Bayesian parameter estimation method comes from the resulting PDF and the ability to assign a probability to any range of values for that parameter; simply taking the "maximum likelihood" result from the PDF and ignoring the rest of the information it holds negates this. The PDFs from these runs, where the maximum likelihood value of h_0 is non-zero are, as the rest of the PDFs, consistent with the data containing no GW signal. As will be seen in Chapter 6, Bayesian inference has a methodology for better asking the question - "does this data contain a GW signal", in the process of model selection through calculating Bayesian evidence values of competing models. In this rest of this section I discuss individual results, however it should be noted that each of the analyses and their associated results are valid for the stated assumptions. For example - I present results where the GW signal is assumed to be coherent throughout the time spanned by the data, despite the presence of two glitches seen in the Crab during this time, I also present results where the signal is not assumed to be coherent because of the observed glitches. Each of these results is equally valid given their assumptions and whilst we remain ignorant of which assumption is in fact correct.

Because my results in this section have been consistent with no GW signal being present in the data, I have been able to place upper limits on h_0. Some of these upper limits are lower than the previously lowest set using S5 data (Abbott et al. 2010), and some are not. The lowest of these for an individual dataset for the analyses using uniform priors on all parameters is from VSR2, with an upper limit of 2.8×10^{-25}. For the analyses using Gaussian priors on the ψ and $\cos(\iota)$ parameters, the lowest upper limit from an individual dataset is 2.3×10^{-25} using VSR4 data. These upper limits are lower than those obtained using the first part of the S5 run and presented in Abbott et al. (2008b) and the Crab's spin-down limit of 1.4×10^{-24}, but the upper limits using the whole of the S5 run are lower still (Abbott et al. 2010).

The results obtained using all of the S5 data use the same two methods for dealing with the glitch that occurred during this run as I have used in §4.6.5, and so a direct comparison between the results can be made. Given that the data used in my final analysis includes H1 and L1 data from S5, only omitting the H2 S5 data, but includes data from H1 and L1 from S6, and from Virgo from VSR2, VSR3

and VSR4, I expect that the upper limits from the analyses using all these datasets to be lower than those using S5 only. The upper limits using the fully coherent method, which essentially ignores the glitches from the analysis, are 2.8×10^{-25} and 3.2×10^{-25} for the uniform priors and Gaussian priors runs respectively. These compare to the similar results reported in Abbott et al. (2010) of 2.6×10^{-25} and 2.0×10^{-25}. That the addition of the extra data results in a higher upper limit is somewhat surprising. A possible explanation for this could be the addition of noisy datasets such as VSR3. However additional noisy data should be effectively down-weighted and therefore should not degrade the result in this way. This could be verified by repeating the analysis without VSR3 data. In fact the most sensitive dataset would possibly be formed by combining the latter half of S5 with VSR2 and VSR4.

The incoherent analyses, where each data segment between the glitches is assigned a independent initial phase, gives upper limits of 1.0×10^{-25} when using uniform priors, and 1.3×10^{-25} when using Gaussian priors, which compares to the S5 upper limits of 2.4×10^{-25} and 1.9×10^{-25}. These upper limits correspond to 7 % and 9% of the spin-down limit of 1.4×10^{-24}. For this analysis method, the additional data does improve the sensitivity significantly, with the results presented here representing the lowest observational upper limits on h_0 for the Crab pulsar to date. As a fraction of the spin-down energy these upper limits correspond to 0.9% and 0.5%, which compares to the best S5 result for the Crab of 2 %. These upper limits correspond to ellipticities of 5.4×10^{-5} and 7.0×10^{-5} with the assumption of $I = 10^{38}\,\mathrm{kg\,m^2}$. These figures are an improvement on those previously set for the Crab, but still significantly higher than the lowest set for any pulsar of 6.96×10^{-8}, which was for J2124-3358 using S5 data. They are also orders of magnitudes greater than the more conservative estimates of the maximum sustainable ellipticity for NSs that were discussed in §2.2.9. However, they are within the range of the maximum sustainable ellipticities that are predicted by the more exotic theories of NS matter. It is important to bear in mind that even if the more exotic theories are correct, and NSs are capable of sustaining ellipticities of up to 10^{-4}, this does not mean that every NS will have an ellipticity this large. Indeed the ellipticity may still be much smaller or even zero. Hence, setting an upper limit on the ellipticity of a pulsar that is below the maximum sustainable ellipticity predicted by a theory of NS matter does not disprove that theory. It is useful to compare observationally derived upper limits to these predictions purely because they are an indication of the strongest GW emission we can realistically expect. Therefore, given these predictions, if the more exotic theories are to be believed, and the Crab's ellipticity is close to maximum sustainable by a NS, we are close to the sensitivities needed to detect GWs from the Crab. If the more conservative theories are to be believed, even if the Crab's

ellipticity is near to the maximum NSs are capable of sustaining, we are orders of magnitude off the sensitivities needed to detect GWs from the Crab.

4.8 Summary

In this chapter I have introduced the Crab pulsar as an astrophysical object and as a potential source of GWs. I have analysed hardware injections in S6 and VSR3 data to demonstrate the validity of the detector calibrations and the search codes used. The timing solution used for GWs searches from the Crab pulsar and the results obtained by using this timing solution to search for GWs in LIGO S6 data, and Virgo VSR2, VSR3, and VSR4 data have also been shown. All of these results are consistent with no GW signal being present in the data analysed, but have been used to infer upper limits on the GW emission comparable to the lowest yet achieved for the Crab pulsar which used LIGO S5 data. Results obtained using a master dataset combining the LIGO S5 data with data from the aforementioned runs have also been presented, and these were able to set upper limits on the GW emission from the Crab which are lower than the previous best. Although this combined dataset search was able to make use of much more data to improve the sensitivity of the search, that the Crab was seen to glitch twice during the time period spanned by this combined dataset complicated the search, and therefore its interpretation. The best of the upper limits obtained from the combined dataset places a 95 % confidence upper limit on h_0 of 1.0×10^{-25}, which corresponds to just 0.5 % of the Crab's spin-down energy and an ellipticity of 5.4×10^{-5}. These upper limits are in the region of ellipticities predicted by more exotic NS EOS, but are still far from the more conservative predictions based on the more widely accepted EOS. Whilst GW detection remains elusive, the advanced detector network will present significant increases in sensitivity, particularly at low frequencies for the LIGO detectors, and using this data the Crab will remain a prime target for GWs from rotating NS.

These results remain preliminary pending a review by the LIGO Virgo collaboration.

Chapter 5

S6 search, all known pulsars

5.1 Introduction

In this chapter I present results from a search for GWs from 110 known pulsars. The ephemerides for 105 of these pulsars are those that were used to analyse LIGO S5 data (Abbott et al. 2010), and so these results should be considered provisional and only as a guide as to what can be expected with updated ephemerides. For these pulsars the LIGO S6 data has been analysed. For five pulsars analyses have been carried out using up to date ephemerides obtained from the Fermi LAT team. These analyses were carried out using VIRGO VSR4 data, as the Virgo detector is much more sensitive than the LIGO detectors at the frequencies that these sources are expected to emit GWs at ($\lesssim 40$ Hz). The LIGO detectors' data is also not calibrated below 40 Hz. The analyses of both sets of pulsars was carried out using the complex heterodyne and MCMC parameter estimation method used in the previous chapters of this thesis. The analyses are discussed briefly in §5.2, the results from the analyses are presented in §5.3 and accompanied by a brief discussion.

5.2 The analyses

To perform the search for GWs from the 110 known pulsars I have used the complex heterodyne and MCMC parameter estimation codes, as with the searches for GWs from the Crab and Vela pulsars described in previous chapters. However, as information on the orientation of these pulsars is not available as it is for the Crab and Vela pulsars, there is no motivation for performing analyses using restricted priors on any of the parameters. Hence all the results presented here are from searches where uniform priors are used for all of the signal parameters. The pulsars for which results are presented in this chapter are split into two groups: those that were used in the S5 search, and those whose ephemerides were provided by the Fermi LAT

team.

5.2.1 S5 pulsars

The most comprehensive search for GWs from pulsars to date was performed with LIGO S5 data, and searched for GWs from 116 pulsars. To encompass so many pulsars in the search required the collaboration of a number of pulsar astronomers from different radio telescopes to provide an ephemeris for each pulsar over the period of S5. The radio telescopes used to provide this data were the Green Bank Telescope (GBT), the Jodrell Bank Observatory (GBO) and the Parkes Radio Telescope (PRT). Efforts to collect the ephemerides for all known pulsars for times covering the LIGO S6 and the Virgo VSR2, VSR3 and VSR4 runs, is currently under way. Given that there are new pulsars being discovered all the time, the list of pulsars for which we can obtain valid ephemerides, and that lie in the frequency band the LIGO and Virgo detectors are sensitive to, can be expected to be greater than the equivalent list for S5. In the mean time, I have used the S5 list of pulsars and the S5 ephemerides to perform a search using LIGO S6 data. The search uses all science mode data from both LIGO detectors. Validation of the data through the recovery of hardware injections was reported in §4.5, and will not be repeated here. The sensitivity curves for the LIGO detectors in S5 and S6 are shown in Figure 5.1, and can give us an idea of how sensitive the two runs should be compared to each other. From this comparison it can be seen that both runs are very similar in sensitivity, with S6 showing a slight advantage over S5 at higher frequencies. However it should be noted that S5 includes the H2 detector that was decommissioned before the start of S6, and whilst H2 was the least sensitive of the detectors during S5, having an extra detector in comparison to S6 may make a difference in their combined overall sensitivity.

5.2.2 Fermi pulsars

The Fermi γ-ray space telescope was successfully launched in 2008, and consists of two instruments; the Large Area Telescope (LAT) and the Gamma-ray Burst Monitor (GBM). The LAT is Fermi's main instrument. It has a wide field of view that covers approximately 20% of the sky, and images gamma-rays in a range between approximately 20 Mev and 300 Gev (201 2012). The LAT has proven to be a useful tool for observing pulsars. It has provided new observations of known pulsars (Razzano 2009), as well as enabling the discovery of a number of new pulsars (Abdo et al. 2010; Saz Parkinson et al. 2010). The Fermi LAT team have provided the ephemerides for 5 γ-ray pulsars that they have been monitoring. These are J0106+4855, J0205+6449, J1747-2958, J1813-1246, and J1954+2836. There

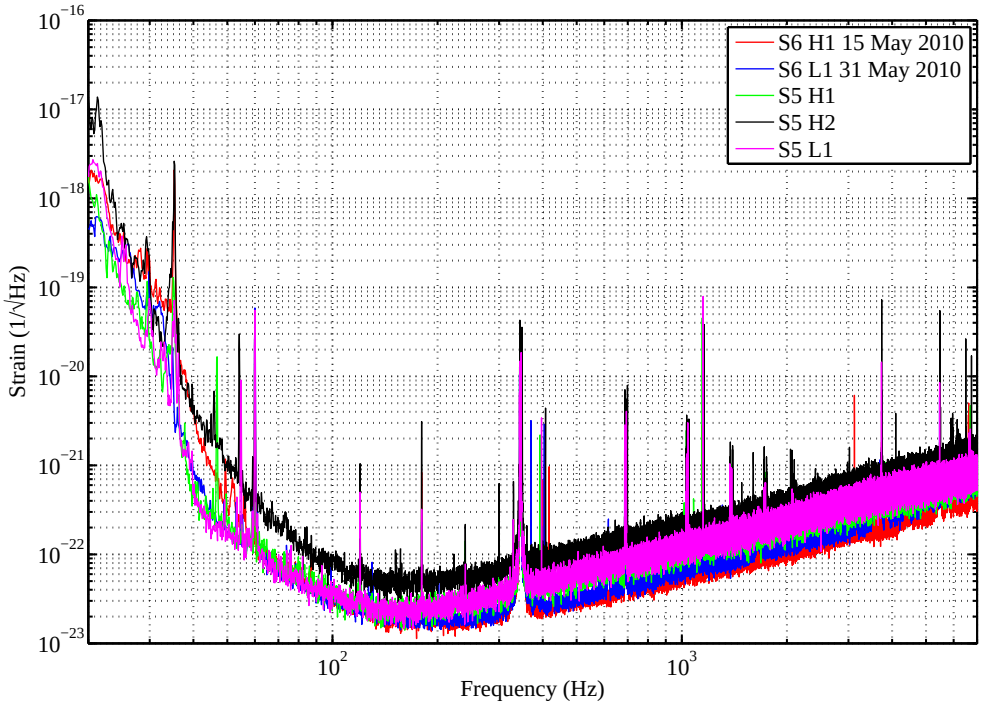

Figure 5.1: A comparison of the S5 and S6 sensitivity curves

have beem no searches for GWs from these pulsars previously. I have used these ephemerides to perform GW searches for these pulsars using Virgo VSR4 data. The reason for using VSR4 data is due to the low spin frequencies of these pulsars. These pulsars have spin frequencies in the range of 10 - 20 Hz, meaning that the VSR4 dataset represents the most sensitive one available for these pulsars. The calibration of VSR4 data has been verified using hardware injections, the results from which are reported in §3.5.

5.3 Results

5.3.1 Fermi results

Of the five fermi pulsars analysed, none showed evidence of GWs in the results from this search. The implied upper limits on the GW emission are reported in Table 5.1. In order to calculate the spin-down limit for a pulsar its distance from Earth must be known. For some of these Fermi pulsars the distances are not necessarily known with a high degree of confidence. Some estimates place the distance within a very large range, and some pulsars have distances estimated from two different methods that do not agree. For pulsars where the distance is not well constrained, the spin-down limits shown in Table 5.1 are derived from the maximum and minimum

distance estimates found in the literature. For some the maximum and minimum distance estimates represent a range of values based on one distance estimation method in one paper and for others they represent estimates obtained using different methods entirely. The distance to J0106+4855 was taken from the ATNF catalogue (Manchester et al. 2005), as no publications with a distance estimate for this pulsar could be found. For pulsar J0205+6449 distances are taken from Ackermann et al. (2011) and Marelli et al. (2011). The distance for the pulsar J1747-2958 is taken from Abdo et al. (2010). For pulsar J1813-1246 a distance is obtained using a new method based on the γ-ray observations from Fermi LAT Wang (2011), but estimates are also reported by Saz Parkinson et al. (2010). Pulsar J1954+2836 has distances reported in Saz Parkinson et al. (2010),Ackermann et al. (2011), and Wang (2011).

Pulsar	ν (Hz)	$\dot{\nu}$ (Hz^{-1})	r (kpc)	h_{sd}	$h_{0,95}$
J0106+4855	12.025	-6.189×10^{-14}	7.33	7.9×10^{-27}	1.2×10^{-24}
J0205+6449	15.214	-4.001×10^{-11}	2.6-3.2	$4.1 - 5.0 \times 10^{-25}$	5.5×10^{-25}
J1747-2958	10.119	-6.278×10^{-12}	2-5	$1.3 - 3.2 \times 10^{-25}$	2.2×10^{-24}
J1813-1246	20.802	-7.560×10^{-12}	0.88-3.52	$1.4 - 5.5 \times 10^{-25}$	6.3×10^{-25}
J1954+2836	10.786	-2.462×10^{-12}	1.7	2.3×10^{-25}	1.8×10^{-24}

Table 5.1: Table showing the 95% upper limits placed on h_0 for pulsars timed by the Fermi satellite.

Whilst the calculation of the spin-down limits for these Fermi pulsars has a large amount of uncertainty attached to them, the h_0^{95} values computed from the analyses are not below even the largest possible spin-down limits based on the closest distance estimates. However, for pulsars J0205+6449 and J1813-1246 h_0^{95} is close to the higher estimates of their spin-down limits, for J0205+6449 the ratio of h_0^{95}/h_0^{sd} is just 1.1, and for J1813-1246 this value is 1.2. It may be possible to beat these higher spin-down limits with the inclusion of VSR2 data. This is of course a very optimistic estimate of the spin-down limits.

5.3.2 S6 analyses of S5 pulsars

The analysis of the "S5 pulsars" uses the data presented by Abbott et al. (2010), including the distances. The results from the analyses of these pulsars showed no evidence for GWs. The upper limits calculated for these pulsars are shown in Table 5.2, alongside the upper limits that were calculated using the S5 data. It should be noted that for pulsars that are in a globular cluster, the observed spin-down is expected to be in error due to accelerations within the cluster. Therefore I follow the example of Abbott et al. (2010) and use a conservative spin-down limit for these pulsars calculated by assuming a characteristic age of $\tau = \nu/2 = 109$ years. The exception to this is J18242452A, whose spin-down is sufficiently large to stand out over any such errors. For the majority of pulsars the S5 upper limit is below the S6 upper limit, however there are a small number for which the S6 upper limit is lower than the S5 upper limit and the two are generally very close. The h_0^{95}/h_0^{sd} value for the majority of these pulsars shows that the data are not yet sensitive enough for analyses to beat the spin-down limits for any but a few special cases, such as the Crab and Vela pulsars. The pulsars that come closest to surpassing the spin-down limits are J1913+1011 and J2124-3358 and for both of these pulsars the S5 upper limits are lower than that obtained with S6 data. It should also be remembered at this point, that the ephemerides used for this analysis are not known to be valid for S6. When the updated ephemerides are obtained for S6 and VSR2 and VSR4, then it is not unreasonable to expect that the combination of these datasets with S5 would enable analyses for these pulsars to beat their spin-down limits, particularly for J1913+1011 for which the h_0^{95} is the closest to its spin-down limit and with $\nu = 27.85\,\mathrm{Hz}$ VSR2 and VSR4 are likely to offer significant improvement in sensitivity compared to S5.

Pulsar	Start-End (MJD)	ν(Hz)	$\dot{\nu}$(Hz s^{-1})	r,(kpc)	h_0^{sd}	S5 Joint h_0^{95}	S6 Joint h_0^{95}	S6 ellipticity	S6 h_0^{95}/S5h$_0$	S6 h_0^{95}/h_0^{sd}
J0024−7204C	48383 – 54261	173.71	1.5×10^{-15}	4.9	6.55×10^{-28}	5.88×10^{-25}	9.88×10^{-25}	3.80×10^{-5}	1.7	1509
J0024−7204D	48465 – 54261	186.65	1.2×10^{-16}	4.9	6.55×10^{-28}	4.45×10^{-26}	4.78×10^{-26}	1.59×10^{-6}	1.1	73
J0024−7204E	48465 – 54261	282.78	-7.9×10^{-15}	4.9	6.55×10^{-28}	9.99×10^{-26}	6.80×10^{-26}	9.88×10^{-7}	0.7	104
J0024−7204F	48465 – 54261	381.16	-9.4×10^{-15}	4.9	6.55×10^{-28}	8.76×10^{-26}	6.57×10^{-26}	5.25×10^{-7}	0.7	100
J0024−7204G	48600 – 54261	247.50	2.6×10^{-15}	4.9	6.55×10^{-28}	1.00×10^{-25}	1.19×10^{-25}	2.26×10^{-6}	1.2	182
J0024−7204H	48518 – 54261	311.49	1.8×10^{-16}	4.9	6.55×10^{-28}	6.44×10^{-26}	7.58×10^{-26}	9.07×10^{-7}	1.2	116
J0024−7204I	50684 – 54261	286.94	3.8×10^{-15}	4.9	6.55×10^{-28}	5.19×10^{-26}	8.93×10^{-26}	1.26×10^{-6}	1.7	136
J0024−7204J	48383 – 54261	476.05	2.2×10^{-15}	4.9	6.55×10^{-28}	1.04×10^{-25}	1.26×10^{-25}	6.46×10^{-7}	1.2	192
J0024−7204L	50687 – 54261	230.09	6.5×10^{-15}	4.9	6.55×10^{-28}	5.82×10^{-26}	7.99×10^{-26}	1.75×10^{-6}	1.4	122
J0024−7204M	48495 – 54261	271.99	2.8×10^{-15}	4.9	6.55×10^{-28}	6.14×10^{-26}	7.49×10^{-26}	1.18×10^{-6}	1.2	114
J0024−7204N	48516 – 54261	327.44	2.4×10^{-15}	4.9	6.55×10^{-28}	8.35×10^{-26}	9.07×10^{-26}	9.82×10^{-7}	1.1	139
J0024−7204Q	50690 – 54261	247.94	-2.1×10^{-15}	4.9	6.55×10^{-28}	5.74×10^{-26}	6.43×10^{-26}	1.21×10^{-6}	1.1	98
J0024−7204R	50743 – 54261	287.32	-1.2×10^{-14}	4.9	6.55×10^{-28}	5.53×10^{-26}	1.04×10^{-25}	1.46×10^{-6}	1.9	159
J0024−7204S	50687 – 54241	353.31	1.5×10^{-14}	4.9	6.55×10^{-28}	6.82×10^{-26}	5.77×10^{-26}	5.37×10^{-7}	0.8	88
J0024−7204T	50684 – 54261	131.78	-5.1×10^{-15}	4.9	6.55×10^{-28}	3.34×10^{-26}	3.54×10^{-26}	2.37×10^{-6}	1.1	54
J0024−7204U	48516 – 54261	230.26	-5.0×10^{-15}	4.9	6.55×10^{-28}	5.63×10^{-26}	4.45×10^{-26}	9.75×10^{-7}	0.8	68
J0024−7204Y	51504 – 54261	455.24	7.3×10^{-15}	4.9	6.55×10^{-28}	9.42×10^{-26}	1.01×10^{-25}	5.66×10^{-7}	1.1	154
J0218+4232	49092 – 54520	430.46	-1.4×10^{-14}	5.8	7.91×10^{-28}	1.47×10^{-25}	1.03×10^{-25}	7.71×10^{-7}	0.7	130
J0407+1607	52719 – 54512	38.91	-1.2×10^{-16}	4.1	3.48×10^{-28}	6.18×10^{-26}	1.12×10^{-25}	7.14×10^{-5}	1.8	322
J0437−4715	53683 – 54388	173.69	-4.7×10^{-16}	0.1	8.82×10^{-27}	5.73×10^{-25}	9.31×10^{-25}	1.10×10^{-6}	1.6	106
J0613−0200	53406 – 54520	326.60	-9.8×10^{-16}	0.5	2.91×10^{-27}	1.11×10^{-25}	7.57×10^{-26}	8.07×10^{-8}	0.7	26
J0621+1002	52571 – 54516	34.66	-5.5×10^{-17}	1.9	5.40×10^{-28}	1.53×10^{-25}	1.21×10^{-25}	4.49×10^{-5}	0.8	224
J0711−6830	53687 – 54388	182.12	-2.7×10^{-16}	1.0	9.52×10^{-28}	5.00×10^{-26}	4.32×10^{-26}	3.21×10^{-7}	0.9	45
J0737−3039A	53595 – 54515	44.05	-3.4×10^{-15}	1.1	6.17×10^{-27}	7.87×10^{-26}	6.48×10^{-26}	9.10×10^{-6}	0.8	11
J0751+1807	53405 – 54529	287.46	-6.3×10^{-16}	0.6	1.92×10^{-27}	1.64×10^{-25}	9.83×10^{-26}	1.75×10^{-7}	0.6	51
J1012+5307	53403 – 54523	190.27	-4.7×10^{-16}	0.5	2.43×10^{-27}	6.94×10^{-26}	4.34×10^{-26}	1.48×10^{-7}	0.6	18
J1022+1001	53403 – 54521	60.78	-1.6×10^{-16}	0.4	3.27×10^{-27}	4.44×10^{-26}	8.97×10^{-26}	2.30×10^{-6}	2.0	27
J1024−0719	53403 – 54501	193.72	-6.9×10^{-16}	0.5	2.88×10^{-27}	5.01×10^{-26}	4.83×10^{-26}	1.62×10^{-7}	1.0	17
J1045−4509	53688 – 54386	133.79	-2.0×10^{-16}	3.2	3.00×10^{-28}	4.37×10^{-26}	2.78×10^{-26}	1.19×10^{-6}	0.6	93
J1455−3330	52688 – 54524	125.20	-2.5×10^{-16}	0.7	1.53×10^{-27}	5.15×10^{-26}	3.69×10^{-26}	4.13×10^{-7}	0.7	24

Pulsar	Start-End (MJD)	ν (Hz)	$\dot{\nu}$ (Hz s^{-1})	r, (kpc)	h_0^{sd}	S5 Joint h_0^{95}	S6 Joint h_0^{95}	S6 ellipticity	S6 h_0^{95}/S5h$_0$	S6 h_0^{95}/h_0^{sd}
J1600−3053	53688 – 54386	277.94	-6.5×10^{-16}	2.7	4.62×10^{-28}	5.57×10^{-26}	7.23×10^{-26}	5.92×10^{-7}	1.3	156
J1603−7202	53688 – 54385	67.38	-5.9×10^{-17}	1.6	4.62×10^{-28}	2.32×10^{-26}	3.46×10^{-26}	2.96×10^{-6}	1.5	75
J1623−2631	53403 – 54517	90.29	-5.5×10^{-15}	2.2	1.46×10^{-27}	5.81×10^{-26}	4.20×10^{-26}	2.69×10^{-6}	0.7	29
J1640+2224	53410 – 54506	316.12	-1.6×10^{-16}	1.2	4.86×10^{-28}	6.65×10^{-26}	8.54×10^{-26}	2.41×10^{-7}	1.3	176
J1643−1224	52570 – 54517	216.37	-6.8×10^{-16}	4.9	2.94×10^{-28}	4.35×10^{-26}	5.24×10^{-26}	1.29×10^{-6}	1.2	178
J1701−3006A	53590 – 54391	190.78	4.8×10^{-15}	6.9	4.65×10^{-28}	5.82×10^{-26}	8.62×10^{-26}	3.87×10^{-6}	1.5	185
J1701−3006B	53650 – 54391	278.25	2.7×10^{-14}	6.9	4.65×10^{-28}	7.63×10^{-26}	7.18×10^{-26}	1.52×10^{-6}	0.9	154
J1701−3006C	53590 – 54396	131.36	1.1×10^{-15}	6.9	4.65×10^{-28}	3.52×10^{-6}	3.75×10^{-26}	3.55×10^{-6}	1.0	81
J1713+0747	53406 – 54509	218.81	-3.8×10^{-16}	1.1	9.54×10^{-28}	4.44×10^{-26}	5.36×10^{-26}	2.97×10^{-7}	1.2	56
J1730−2304	52571 – 54519	123.11	-3.1×10^{-16}	0.5	2.49×10^{-27}	5.93×10^{-26}	5.00×10^{-26}	3.99×10^{-7}	0.8	20
J1732−5049	53725 – 54386	188.23	-4.9×10^{-16}	1.8	7.18×10^{-28}	5.25×10^{-26}	5.77×10^{-26}	6.99×10^{-7}	1.1	80
J1744−1134	52604 – 54519	245.43	-4.1×10^{-16}	0.5	2.18×10^{-27}	1.10×10^{-25}	5.85×10^{-26}	1.10×10^{-7}	0.5	27
J1748−2446A	52320 – 54453	86.48	2.2×10^{-16}	5.5	5.83×10^{-28}	3.89×10^{-26}	4.13×10^{-26}	7.20×10^{-6}	1.1	71
J1748−2446C	53403 – 54516	118.54	8.5×10^{-15}	5.5	5.83×10^{-28}	5.00×10^{-26}	3.78×10^{-26}	3.51×10^{-6}	0.8	65
J1748−2446D	50851 – 53820	212.13	-5.7×10^{-15}	5.5	5.83×10^{-28}	6.78×10^{-26}	5.68×10^{-26}	1.65×10^{-6}	0.8	97
J1748−2446E	53193 – 53820	455.00	3.8×10^{-15}	5.5	5.83×10^{-28}	8.95×10^{-26}	1.20×10^{-25}	7.56×10^{-7}	1.3	206
J1748−2446F	53193 – 53820	180.50	-1.3×10^{-16}	5.5	5.83×10^{-28}	8.37×10^{-26}	7.90×10^{-26}	3.16×10^{-6}	0.9	135
J1748−2446G	51884 – 53820	46.14	-8.4×10^{-16}	5.5	5.83×10^{-28}	5.82×10^{-26}	6.98×10^{-26}	4.27×10^{-5}	1.2	120
J1748−2446H	51884 – 53820	203.01	3.4×10^{-15}	5.5	5.83×10^{-28}	7.81×10^{-26}	6.64×10^{-26}	2.10×10^{-6}	0.9	114
J1748−2446I	50851 – 54195	104.49	7.3×10^{-16}	5.5	5.83×10^{-28}	3.54×10^{-26}	4.44×10^{-26}	5.30×10^{-6}	1.3	76
J1748−2446K	51884 – 53820	336.74	1.1×10^{-14}	5.5	5.83×10^{-28}	6.67×10^{-26}	1.06×10^{-25}	1.22×10^{-6}	1.6	182
J1748−2446L	51884 – 53820	445.49	3.4×10^{-15}	5.5	5.83×10^{-28}	1.39×10^{-25}	1.02×10^{-25}	6.70×10^{-7}	0.7	175
J1748−2446M	51884 – 53820	280.15	-3.9×10^{-14}	5.5	5.83×10^{-28}	1.01×10^{-25}	6.65×10^{-26}	1.10×10^{-6}	0.7	114
J1748−2446N	53193 – 54195	115.38	-7.4×10^{-15}	5.5	5.83×10^{-28}	5.83×10^{-26}	3.27×10^{-26}	3.20×10^{-6}	0.6	56
J1748−2446O	52500 – 53957	596.43	2.5×10^{-14}	5.5	5.83×10^{-28}	2.65×10^{-25}	1.61×10^{-25}	5.90×10^{-7}	0.6	276
J1748−2446P	53193 – 54557	578.50	-8.7×10^{-14}	5.5	5.83×10^{-28}	1.75×10^{-25}	1.54×10^{-25}	6.00×10^{-7}	0.9	264
J1748−2446Q	53193 – 54139	355.62	4.6×10^{-15}	5.5	5.83×10^{-28}	8.80×10^{-26}	1.08×10^{-25}	1.11×10^{-6}	1.2	185
J1748−2446R	52500 – 53820	198.86	-1.9×10^{-14}	5.5	5.83×10^{-28}	8.23×10^{-26}	5.54×10^{-26}	1.83×10^{-6}	0.7	95
J1748−2446S	53193 – 53820	163.49	-1.7×10^{-15}	5.5	5.83×10^{-28}	4.46×10^{-26}	1.20×10^{-25}	5.85×10^{-6}	2.7	206
J1748−2446T	51884 – 53819	141.15	-6.1×10^{-15}	5.5	5.83×10^{-28}	5.12×10^{-26}	3.21×10^{-26}	2.10×10^{-6}	0.6	55

Pulsar	Start-End (MJD)	ν (Hz)	$\dot{\nu}$ (Hz s^{-1})	r,(kpc)	h_0^{sd}	S5 Joint h_0^{95}	S6 Joint h_0^{95}	S6 ellipticity	S6 h_0^{95}/S5h$_0$	S6 h_0^{95}/h_0^{sd}
J1748−2446V	53193 – 53820	482.51	2.2×10^{-14}	5.5	5.83×10^{-28}	1.26×10^{-25}	1.15×10^{-25}	6.44×10^{-7}	0.9	197
J1748−2446W	52500 – 53820	237.80	-7.1×10^{-15}	5.5	5.83×10^{-28}	9.57×10^{-26}	4.31×10^{-26}	9.93×10^{-7}	0.5	74
J1748−2446X	51884 – 54139	333.44	-6.5×10^{-15}	5.5	5.83×10^{-28}	8.18×10^{-26}	5.75×10^{-26}	6.74×10^{-7}	0.7	99
J1748−2446Y	53193 – 53820	488.24	-4.0×10^{-14}	5.5	5.83×10^{-28}	2.10×10^{-25}	1.01×10^{-25}	5.52×10^{-7}	0.5	173
J1748−2446Z	53193 – 54139	406.08	1.4×10^{-14}	5.5	5.83×10^{-28}	8.43×10^{-26}	7.00×10^{-26}	5.53×10^{-7}	0.8	120
J1756−2251	53403 – 54530	35.14	-1.3×10^{-15}	2.9	1.65×10^{-27}	9.70×10^{-26}	1.47×10^{-25}	8.24×10^{-5}	1.5	89
J1801−1417	53405 – 54505	275.85	-4.0×10^{-16}	1.8	5.42×10^{-28}	6.15×10^{-26}	6.23×10^{-26}	3.49×10^{-7}	1.0	115
J1803−30	53654 – 54379	140.83	-1.0×10^{-15}	7.8	4.11×10^{-28}	5.51×10^{-26}	4.33×10^{-26}	4.04×10^{-6}	0.8	105
J1804−0735	52573 – 54518	43.29	-8.8×10^{-16}	8.4	3.82×10^{-28}	8.44×10^{-26}	1.21×10^{-25}	1.29×10^{-4}	1.4	317
J1804−2717	52574 – 54453	107.03	-4.7×10^{-16}	1.2	1.44×10^{-27}	2.40×10^{-26}	3.83×10^{-26}	9.27×10^{-7}	1.6	27
J1807−2459A	53621 – 54462	326.86	4.8×10^{-16}	2.7	1.19×10^{-27}	1.53×10^{-25}	5.68×10^{-26}	3.40×10^{-7}	0.4	48
J1810−2005	53406 – 54508	30.47	-1.4×10^{-16}	4.0	4.28×10^{-28}	2.22×10^{-25}	3.20×10^{-25}	3.30×10^{-4}	1.4	748
J1823−3021A	53403 – 54530	183.82	-1.1×10^{-13}	7.9	4.06×10^{-28}	3.93×10^{-26}	5.00×10^{-26}	2.77×10^{-6}	1.3	123
J1824−2452A	53403 – 54509	327.41	-1.7×10^{-13}	4.9	3.79×10^{-27}	7.80×10^{-26}	8.27×10^{-26}	8.96×10^{-7}	1.1	22
J1824−2452B	53629 – 54201	152.75	5.6×10^{-15}	4.9	6.55×10^{-28}	4.26×10^{-26}	4.56×10^{-26}	2.27×10^{-6}	1.1	70
J1824−2452C	52335 – 54202	240.48	-9.8×10^{-15}	4.9	6.55×10^{-28}	6.48×10^{-26}	4.59×10^{-26}	9.22×10^{-7}	0.7	70
J1824−2452E	53629 – 54201	184.53	3.7×10^{-15}	4.9	6.55×10^{-28}	7.51×10^{-26}	5.57×10^{-26}	1.90×10^{-6}	0.7	85
J1824−2452F	52497 – 54114	407.97	-1.6×10^{-15}	4.9	6.55×10^{-28}	9.74×10^{-26}	1.11×10^{-25}	7.74×10^{-7}	1.1	170
J1824−2452G	53629 – 54202	169.23	-5.2×10^{-15}	4.9	6.55×10^{-28}	7.23×10^{-26}	1.04×10^{-25}	4.22×10^{-6}	1.4	159
J1824−2452H	53629 – 54202	216.01	-3.6×10^{-15}	4.9	6.55×10^{-28}	8.76×10^{-26}	1.08×10^{-25}	2.69×10^{-6}	1.2	165
J1824−2452J	53629 – 54201	247.54	4.7×10^{-15}	4.9	6.55×10^{-28}	1.07×10^{-25}	6.36×10^{-26}	1.21×10^{-6}	0.6	97
J1841+0130	53405 – 54513	33.59	-9.2×10^{-15}	3.2	4.19×10^{-27}	1.65×10^{-25}	1.65×10^{-25}	1.11×10^{-4}	1.0	39
J1843−1113	53353 – 54508	541.81	-2.8×10^{-15}	2.0	9.33×10^{-28}	1.64×10^{-25}	1.18×10^{-25}	1.88×10^{-7}	0.7	126
J1857+0943	53409 – 54517	186.49	-6.0×10^{-16}	0.9	1.59×10^{-27}	7.27×10^{-26}	5.47×10^{-26}	3.39×10^{-7}	0.8	34
J1905+0400	53407 – 54512	264.24	-3.4×10^{-16}	1.3	6.81×10^{-28}	7.40×10^{-26}	6.23×10^{-26}	2.83×10^{-7}	0.8	91
J1909−3744	53687 – 54388	339.32	-3.1×10^{-16}	1.1	6.78×10^{-28}	8.09×10^{-26}	6.67×10^{-26}	1.57×10^{-7}	0.8	98
J1910−5959A	53666 – 54380	306.17	-2.8×10^{-16}	4.5	7.13×10^{-28}	7.71×10^{-26}	7.59×10^{-26}	8.64×10^{-7}	1.0	106
J1910−5959B	53609 – 54473	119.65	1.1×10^{-14}	4.5	7.13×10^{-28}	3.81×10^{-26}	3.23×10^{-26}	2.41×10^{-6}	0.8	45
J1910−5959C	53666 – 54390	189.49	-7.8×10^{-17}	4.5	7.13×10^{-28}	4.34×10^{-26}	4.48×10^{-26}	1.33×10^{-6}	1.0	63
J1910−5959D	53621 – 54460	110.68	-1.2×10^{-14}	4.5	7.13×10^{-28}	3.03×10^{-26}	2.64×10^{-26}	2.30×10^{-6}	0.9	37

Pulsar	Start-End (MJD)	ν (Hz)	$\dot{\nu}$ (Hz s^{-1})	r,(kpc)	h_0^{sd}	S5 Joint h_0^{95}	S6 Joint h_0^{95}	S6 ellipticity	S6 h_0^{95}/S5h$_0$	S6 h_0^{95}/h_0^{sd}
J1910−5959E	53610 – 54441	218.73	2.1×10^{-14}	4.5	7.13×10^{-28}	4.77×10^{-26}	4.02×10^{-26}	8.96×10^{-7}	0.8	56
J1911+1347	53403 – 54530	216.17	-8.0×10^{-16}	1.6	9.63×10^{-28}	7.00×10^{-26}	4.93×10^{-26}	4.03×10^{-7}	0.7	51
J1911−1114	53407 – 54512	275.81	-4.8×10^{-16}	1.6	6.66×10^{-28}	5.62×10^{-26}	1.31×10^{-25}	6.49×10^{-7}	2.3	197
J1913+1011	53745 – 54911	27.85	-2.6×10^{-12}	4.5	5.51×10^{-26}	2.14×10^{-25}	2.93×10^{-25}	4.01×10^{-4}	1.4	5.3
J1939+2134	53407 – 54519	641.93	-4.3×10^{-14}	3.5	1.86×10^{-27}	1.79×10^{-25}	2.03×10^{-25}	4.14×10^{-7}	1.1	109
J1955+2908	53403 – 54524	163.05	-7.6×10^{-16}	5.4	3.23×10^{-28}	7.07×10^{-26}	5.11×10^{-26}	2.46×10^{-6}	0.7	158
J2019+2425	53599 – 54505	254.16	-1.7×10^{-16}	0.9	7.14×10^{-28}	9.23×10^{-26}	4.47×10^{-26}	1.49×10^{-7}	0.5	63
J2033+17	53702 – 54522	168.10	-3.1×10^{-16}	1.4	7.93×10^{-28}	7.49×10^{-26}	1.08×10^{-25}	1.25×10^{-6}	1.4	136
J2051−0827	53410 – 54520	221.80	-6.1×10^{-16}	1.3	1.04×10^{-27}	7.57×10^{-26}	5.07×10^{-26}	3.13×10^{-7}	0.7	49
J2124−3358	53410 – 54510	202.79	-5.1×10^{-16}	0.2	5.13×10^{-27}	4.85×10^{-26}	6.41×10^{-26}	9.24×10^{-8}	1.3	12
J2129−5721	53687 – 54388	268.36	-2.0×10^{-15}	2.5	8.71×10^{-28}	6.12×10^{-26}	5.60×10^{-26}	4.70×10^{-7}	0.9	64
J2145−0750	53409 – 54510	62.30	-1.0×10^{-16}	0.5	2.05×10^{-27}	3.83×10^{-26}	5.24×10^{-26}	1.60×10^{-6}	1.4	26
J2229+2643	53403 – 54524	335.82	-1.6×10^{-16}	1.4	3.95×10^{-28}	9.89×10^{-26}	9.31×10^{-26}	2.80×10^{-7}	0.9	236
J2317+1439	53406 – 54520	290.25	-1.3×10^{-16}	1.9	2.82×10^{-28}	8.83×10^{-26}	6.37×10^{-26}	3.39×10^{-7}	0.7	226
J2322+2057	53404 – 54519	207.97	-1.8×10^{-16}	0.8	9.55×10^{-28}	1.12×10^{-25}	3.89×10^{-26}	1.66×10^{-7}	0.3	41

Table 5.2: Table showing the 95% upper limits placed on h_0 for pulsars using S6 data. The results are shown alongside the results obtained using S5 data as presented in Abbott et al. (2010). The ephemerides used for the S6 analysis are the same used for the S5 analysis and hence may not be valid over the S6 run, therefore these results from S6 are demonstrative only.

5.4 Summary

In this chapter I have presented the search for GWs from a total of 110 pulsars. Although the vast majority of these searches have been conducted using out of date ephemerides it is likely that these results will be very similar to those obtained when updated ephemerides are available. There are also a small subset of five pulsars which have up to date ephemerides that have been observed using the Fermi space telescope, the data for which has been supplied by the Fermi LAT team. For all the pulsars analysed no evidence of GWs was found. Upper limits on h_0 were computed for all pulsars. For two of the Fermi pulsars these upper limits are close to the more optimistic estimates of their spin-down limits. For the other pulsars the upper limits derived were, in the vast majority of cases, higher than those set using S5 data. However with updated ephemerides and by performing analyses using S5, S6, VSR2 and VSR4 data there are a few pulsars for which the spin-down limit may be able to be beaten, in particular for J1913+1011.

Chapter 6

Evolving the search method

6.1 Introduction

The analyses of GW detector data to look for GWs from pulsars presented in the previous chapters of this thesis have relied on a common approach, with this same approach also having been used for previous searches (Abbott et al. 2007, 2008b, 2010). In this chapter I look at two different ways in which this search method has been evolved. The first of these replaces the MCMC code used for Bayesian parameter estimation with a code using the nested sampling algorithm of Skilling (2004). Use of the nested sampling algorithm allows for the computation of Bayesian evidence which can then be used for model selection, whilst also enabling Bayesian parameter estimation. The characterisation of this nested sampling search code for the triaxial NS model, which was developed by Pitkin et al. (2012), is detailed in §6.2. The second evolution of the search method is the inclusion of a different model for GW emission, formulated by Jones (2010). This model predicts GW emission at the rotation rate of the pulsar f_{rot} as well as at twice the rotation rate $2f_{rot}$, where as the previous search method has only assumed emission at twice the rotation rate. The development of the nested sampling code of Pitkin et al. (2012) to search for GWs produced by the model of Jones (2010) makes up the majority of this chapter in §6.3 and §6.4. In §6.3, I introduce the pinned superfluid model of Jones (2010), discuss the important points of the model and derive the equations for the heterodyned signal. In §6.3.2 I investigate a simplified analogy in order to gain some understanding of the basic problem of performing a Bayesian search for a signal over two separate data-streams. In §6.4 I detail the development of the nested sampling search code to include the pinned superfluid model, as well as presenting results test of both parameter estimation and evidence computation on simulated data. To finish off my investigation into the pinned superfluid search §6.5 presents a search for pinned superfluid GWs from the Crab pulsar in VSR4 data. The final

section of this chapter, §6.6, presents a brief look into the noise in the detector data used for the searches discussed in this thesis, the main point of which is to question whether the data is actually Gaussian.

6.2 The nested sampling pulsar search code

The analyses described in previous chapters have focussed on parameter estimation of the GW signal, the most crucial question - whether there is actually a signal present or not, has been inferred from the parameter estimation results of the signal amplitude parameter h_0. A strong signal would be obvious in the PDFs from the parameter estimation code, however whether the data contains a weak signal with a low SNR is harder to gauge from the PDFs of the parameter estimation analysis alone. This has not been an issue with recent searches, as there have not been any analyses that appear to have detected a GW signal. However with the planned upgrades in sensitivity to the current GW detectors that will take us into the "'advanced detector era", it is feasible that a first detection of GWs, and CWs in particular, will be made. At this time being able to answer the question of whether a GW signal is present becomes of great importance. Remaining in the Bayesian framework we look to Bayesian evidence to answer this question. In particular, I look to a different algorithm whose primary purpose is to compute Bayesian evidence, a result which can be used to select between competing models. This algorithm is Nested sampling (Skilling 2004, 2006), in particular a version of the algorithm developed specifically for GW data analyses (Veitch & Vecchio 2010), which has been employed in a pulsar search code (Pitkin et al. 2012).

The nested sampling algorithm was devised by Skilling (2004) as an alternative to standard MCMC algorithms based on Metropolis et al. (1953) and Hastings (1970). This traditional MCMC approach is focussed on computing the normalised posterior, with evidence calculations possible through additional computational steps. The nested sampling approach places evidence calculation at its core, with the option to extract the normalised posterior from the results.

It works by starting with a sample of N *live points* which are initially placed randomly in the parameter space. These live points are then evolved by removing the live point with the lowest likelihood and replacing it with a new live point whose likelihood exceeds that of the live point with the next lowest likelihood. The live point that was removed is recorded. In this way the set of live points shrinks around regions of high likelihood in the parameter space. Using all of the discarded live points, together the remaining live points when the algorithm stops, the evidence integral is calculated.

6.2.1 Algorithm characterisation

Before the search code can be used as the main tool for our analyses, it is important to benchmark it against the previous parameter estimation methods, the MCMC and grid based parameter estimation codes. It is clear from the Bayesian framework that we can use odds ratios to tell us which model is favoured by the data, however it is not necessarily clear how we can use the value of the odds ratio to enable us to say with a certain confidence that a signal is present if the odds ratio is not at an extreme. To do this I look to characterise the algorithm with signal injections for a given false alarm rate (FAR). I choose a 5 % FAR and then run the analysis on a large number of simulated data files that contain Gaussian noise and no signal, and from this determine the threshold that only 5 % of the resulting odds ratios exceed. This threshold value gives me the 5% FAR, and now I can continue the characterisation process further and look at ability of the algorithm to make a detection of signals with a range of SNRs. This is achieved by injecting signals into data at specific SNRs, and analysing these injected data files to determine the odds ratio. To account for statistical variation I do this for 1000 data-files at each SNR from 0.1 to 8, and determine the number of these injected data-files whose odds ratio is calculated as above the 95 % FAR threshold. The proportion at each SNR that pass this test gives an estimate of the efficiency of the algorithm for making a detection. With the efficiency calculated across a range of SNRS, I construct what is known as a ROC curve. In the wider statistics literature a ROC curve plots the efficiency against the FAR, however in CW literature this is commonly replaced by plotting the efficiency against the injected SNR. The ROC curve for the nested sampling algorithm with the triaxial NS model is shown in Figure 6.1.

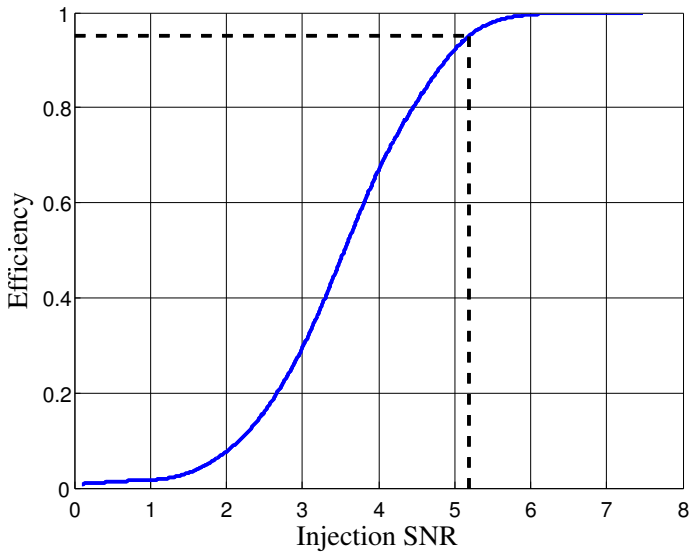

Figure 6.1: The ROC curve for the triaxial model for the nested sampling algorithm, with the 95 % confidence level shown as a dashed black line..

We can also gain some reassurance that the new algorithm is consistent with the previous methods by making a direct comparison. One important aspect of the algorithms performance is the PDFs calculated for parameter estimation when no signal has been observed, from which upper limits can be calculated on the amplitudes of GWs. This approach of setting upper limits on the amplitude of GWs from specific sources has been important for the searches for CWs to date. To test this I have reproduced Figure 1 of Dupuis & Woan (2005), which shows the 95% degree-of-belief upper limits for many realisations of pure Gaussian noise when searches are performed for sources randomly located on the sky. This is shown in Figure 6.2, where the grid result is shown in black and the nested sampling result shown in red. It is clear that there is some disagreement between the two histograms, the nested sampling histogram shows more counts at lower values for h than the grid histogram. This is a little concerning at first sight, however it is important to note that there is a difference in how the two codes handle the data, and hence in the assumptions that each analysis makes about the data. The grid code breaks contiguous data into chunks of 30 minutes, with the assumption that the data is stationary over this time period. The nested sampling code is a little more sophisticated in its handling of the data, it instead assesses the stationarity of the data and breaks it down into a minimal number of chunks such that the data is stationary in each data chunk. For our test data that is one day long, this results in the grid code breaking the data into 48 chunks and the nested sampling code handling the data in one chunk. Therefore it is perhaps not surprising that the two histograms do not agree, indeed this would suggest that where the nested sampling is able to break the data into less chunks which are longer than 30 minutes, it is able to gain some sensitivity in doing so. Because of this, we still need a check for the new nested sampling algorithm, so we perform the same test again, but this time with the nested sampling breaking the data into 30 minute chunks also, with the result shown in Figure 6.3. In this figure the grid result is again shown in black, and the nested sampling result again shown in red, the two histograms still show some small variation, but appear very similar, similar enough to claim equivalence.

6.2.2 Test on software injections

Another milestone in the testing of the Nested sampling algorithm is to recover injected pulsar signals. Signals can be injected in two ways, directly into the hardware, and at a later stage though software into the detector frame files. The injected and recovered parameters for a number of software injection pulsars can be seen in Table 6.1. These are fictional pulsars that are taken from a uniform random distribution over the sky, with the GW signals injected over all science mode frame files from

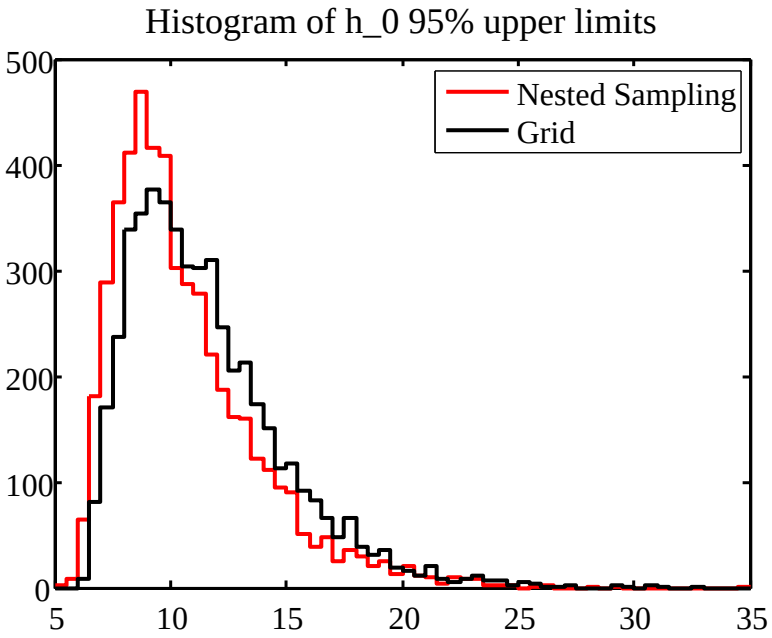

Figure 6.2: A histogram of the 95 % confidence upper limits from 5000 runs on Gaussian noise with no signal injected, with the histogram in red from the nested sampling algorithm, and the histogram in black from the grid code.

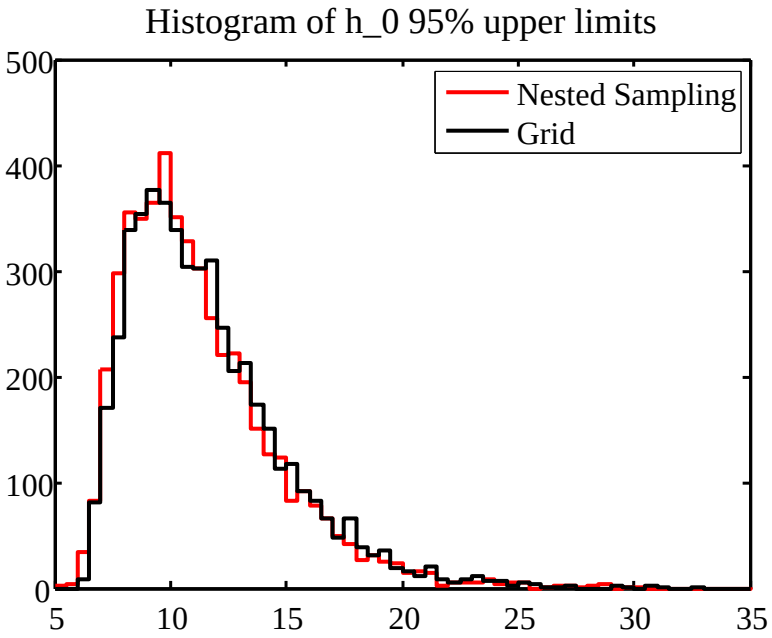

Figure 6.3: A histogram of the 95 % confidence upper limits from 5000 runs on Gaussian noise with no signal injected, with the histogram in red from the nested sampling algorithm, and the histogram in black from the grid code.

the H1 detector during S6. The PDFs for each of the software injection pulsars are shown in Figures 6.4 to 6.6. From the table of results and the PDFs it is clear to see

that the injected parameters have been recovered very well. It is also apparent from the tight PDFs that the signals have high SNRs. This is because the software injections were created primarily as a test for blind search codes, which are less sensitive than the directed search I performed due to the extra parameters they must search over, this was discussed in §1.6. There are a few software injection pulsars where the h_0 PDF shows some deviation from the injected value, such as pulsars 0850-3119 and 0738-2002, however the discrepancies are particularly small, and therefore not of concern.

Pulsar	h_0	ϕ_0	ψ	$\cos(\iota)$
J0041+6825 inj	4.69e-24	0.26	-0.02	0.42
recovered	4.69e-24	0.26	-0.01	0.42
J0108-1251 inj	4.72e-24	4.34	0.33	0.45
recovered	4.67e-24	4.36	0.34	0.45
J0407+6153 inj	3.20e-24	1.05	0.51	0.69
recovered	3.13e-24	1.06	0.49	0.71
J0450+7153 inj	2.95e-24	4.32	-0.49	0.13
recovered	2.95e-24	4.31	-0.50	0.14
J0545+8742 inj	3.76e-24	5.30	-0.50	0.43
recovered	3.74e-24	5.30	-0.50	0.43
J0602-1629 inj	7.05e-24	5.58	0.37	0.08
recovered	7.06e-24	5.58	0.36	0.08
J0710-2048 inj	1.92e-24	0.21	-0.76	0.06
recovered	1.92e-24	6.47	-0.77	0.07
J0738-2002 inj	9.03e-24	2.12	0.76	-0.23
recovered	8.95e-24	2.17	0.76	-0.24
J0810+1551 inj	5.50e-25	0.22	-0.38	0.70
recovered	6.58e-25	6.47	-0.35	0.56
J0839+5450 inj	2.56e-24	0.10	0.41	-0.75
recovered	2.59e-24	0.26	0.50	-0.74
J0850-3119 inj	9.25e-24	4.65	0.14	-0.07
recovered	9.18e-24	4.63	0.14	-0.07
J0907+3446 inj	8.23e-24	5.70	-0.05	0.38
recovered	8.22e-24	5.73	-0.06	0.37
J0928-1046 inj	5.46e-24	4.28	0.41	0.03
recovered	5.45e-24	4.31	0.41	0.03
J1125-7334 inj	9.04e-24	5.66	0.00	-0.02
recovered	8.98e-24	5.67	0.00	-0.02
J1137-2335 inj	9.42e-25	4.37	0.22	-0.67
recovered	9.94e-25	4.39	0.24	-0.64

Table 6.1: Table showing the injected and recovered parameters for a number of pulsar software injections into the S6 dataset. The recovered parameters were obtained using the nested sampling search code.

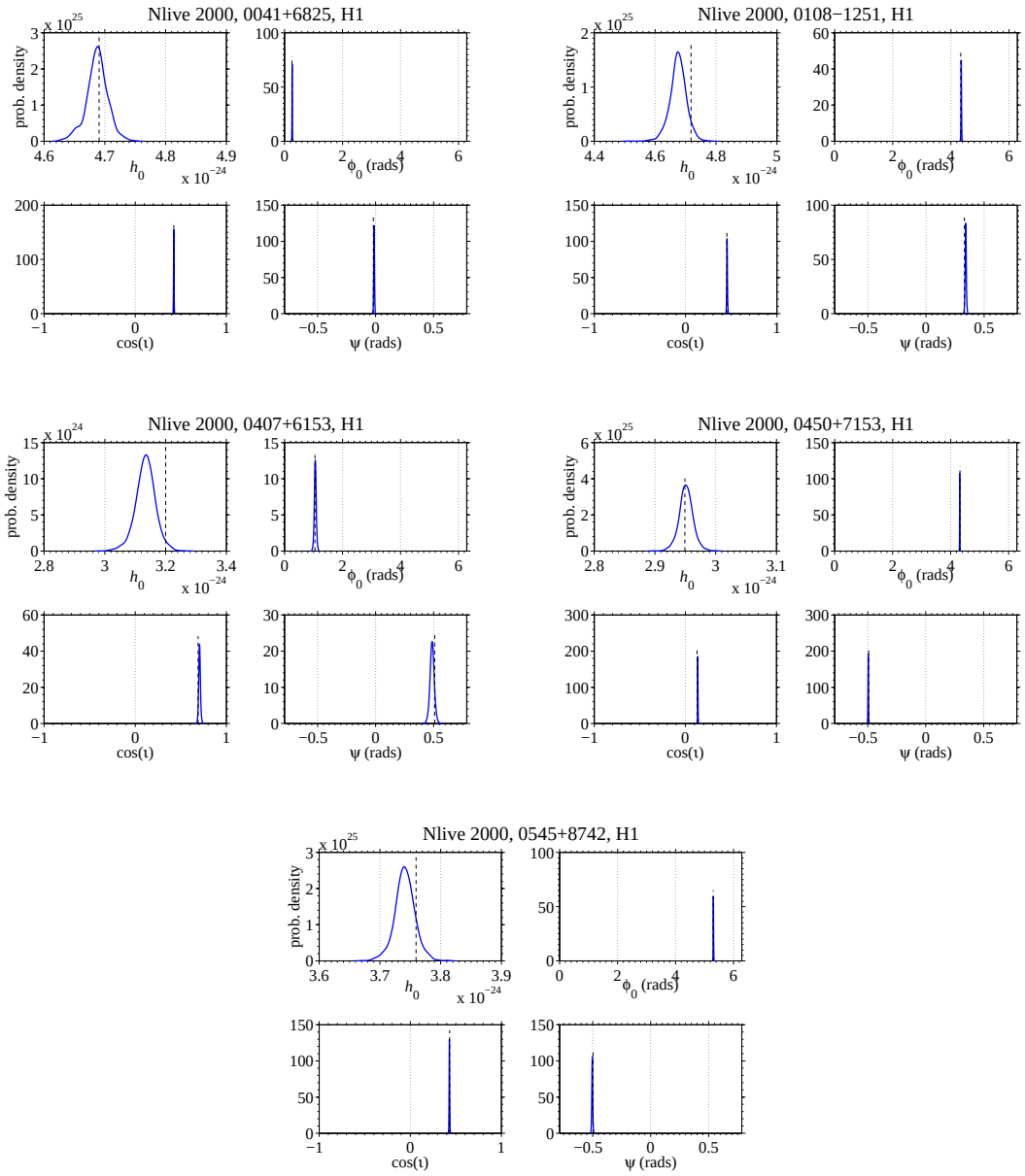

Figure 6.4: PDFs of S6 software injections using H1 data and produced by the nested sampling search code.

6.2.3 Summary

The use of the nested sampling code provides distinct advantages over the previously used MCMC parameter estimation code, and the grid based code that was employed before that, in that it computes the Bayesian evidence as well as producing marginalised PDFs for each of the signal parameters. In this section I have been able to show that the nested sampling code passes important consistency tests in terms of setting upper limits on the GW amplitude parameter h_0. I have also characterised the nested sampling search code for the triaxial NS model with the use of ROC curves and performed checks using software injections. Further tests

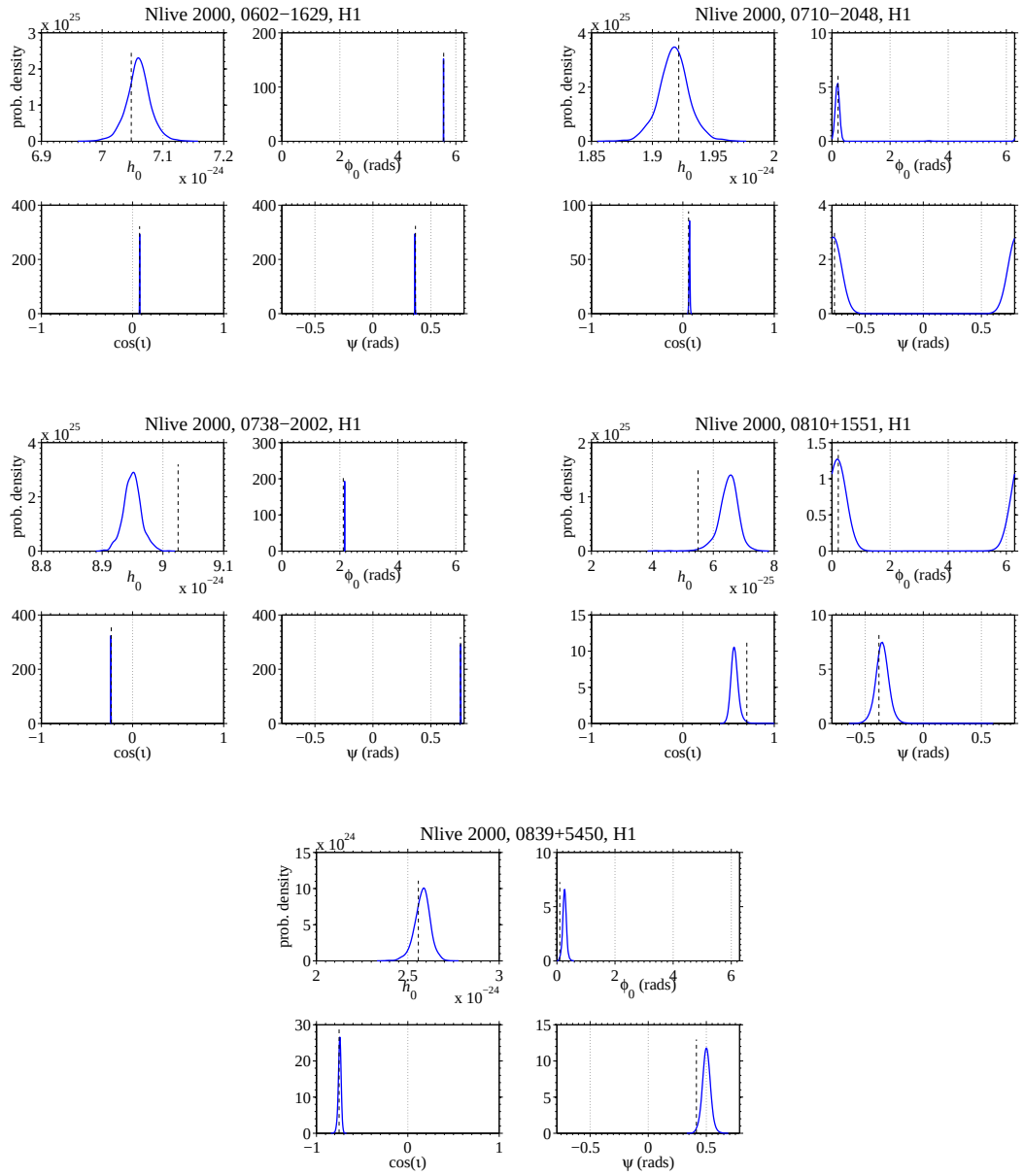

Figure 6.5: PDFs of S6 software injections using H1 data and produced by the nested sampling search code.

have been carried out by Matt Pitkin, and are presented in (Pitkin et al. 2012).

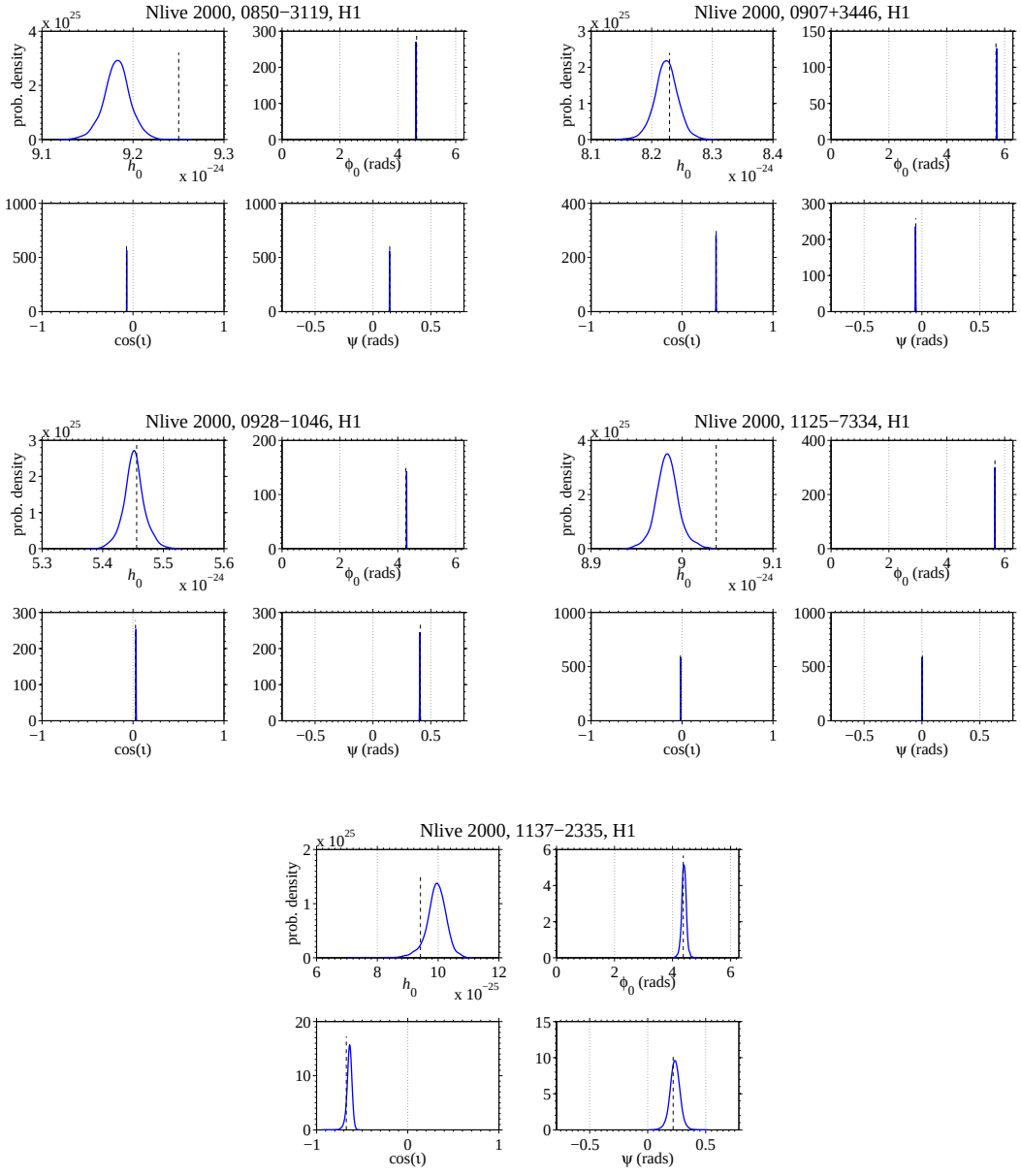

Figure 6.6: PDFs of S6 software injections using H1 data and produced by the nested sampling search code.

6.3 Searching for GWs from a pinned-superfluid NS

6.3.1 Introduction to the model

A lot of work has been invested into deciding at what frequency to search for GWs from pulsars. Early work suggested that searches at the rotation frequency f_{rot} of the pulsar were worthwhile, as the emission mechanism of a freely precessing NS is expected to emit GWs at the star's rotation frequency (Zimmermann & Szedenits 1979; Jones & Andersson 2001). However this view lost favour, as later work showed that any free precession in a NS would be strongly damped (Jones & Andersson 2002; Glampedakis et al. 2009), and therefore it would be unlikely that any NS would be freely precessing during the observation time. Since then searches have favoured looking at twice the rotation frequency, where the GW emission mechanism is the triaxial rigid rotator mechanism, and this has been the accepted wisdom for a number of the most sensitive searches for GWs from pulsars (Abbott et al. 2007, 2010). However this accepted wisdom has been called into doubt, with a new mechanism for GW emission from NSs being suggested. This is the pinned superfluid model of Jones (2010), which predicts GW emission at both the rotation frequency f_{rot} and twice the rotation frequency $2f_{rot}$ of the NS.

The details of the model can be found in Jones (2010). The basic premise of the model is that the star's superfluid interior is pinned to its crust, and the axis of this pinning is misaligned from the star's principal axes. The moment of inertia of the pinned superfluid component of the star is likely to be much greater than the differences of the principal moments of inertia, and in this case the star rotates about an axis that is very close to the pinning axis of the superfluid component. An analogy used in Jones (2010) is that the pinned superfluid component behaves like a gyroscope inside the NS forcing the NS to rotate about the pinning axis. In this way the pinned superfluid component allows the star to exist in a steady state, i.e. where it is not precessing, where its principal axes are misaligned from its rotation axis. This produces a GW signal at both f_{rot} and $2f_{rot}$ in a similar way to that of a precessing NS.

The model parameters consist of two amplitude parameters, I_{21} and I_{31}, which are the differences between the principal moments of inertia I_3, I_2 and I_1, and five angular parameters $\psi, \psi_{pol}, \theta, \phi, \iota$. The angular parameters ψ_{pol}, ϕ and ι are the same angles used to describe the triaxial rotator model which was discussed in §2.2.9, except that for the triaxial rotator model ψ_{pol} is simply referred to as ψ. The three angles θ, ϕ, ψ of the pinned superfluid model are the Euler angles that fix the orientation of the body with respect to the inertial frame, see Figure 6.7 for a

pictorial representation, with the angle ϕ describing the spin of the star about its rotation axis.

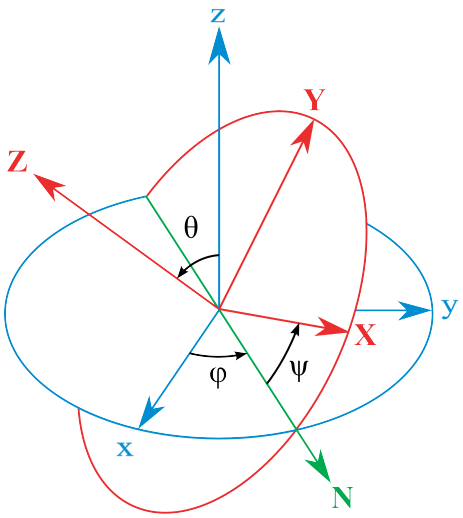

Figure 6.7: A pictorial representation of the Euler angles, for the pinned superfluid model these angles describe the configuration of the triaxial crust with respect to the pinned superfluid core of the NS. Where x, y, z are the inertial frame, and X, Y, Z are the axes of the pinned superfluid core. The green line labelled N, is the line of the nodes, and lies on the intersection of the XY plane with the xy plane.

This parameter ψ should not be confused with the GW polarisation angle described in Jaranowski et al. (1998) and given in Jones (2010) as ψ_{pol}, and hence I will refer to the ψ parameter of the pinned super-fluid model as λ, and to ψ_{pol} as ψ from here on. The parameters θ and λ are constants, whilst ϕ increases linearly with time - it is the angle that describes the rotation of the NS. On average the $2f_{rot}$ emission will be stronger than the f_{rot} emission, although there are particular combinations of parameters where the f_{rot} emission will dominate. The emission at f_{rot} is zero in the direction of the rotation axis, i.e. where $\iota = 0$, and is at its strongest in the direction of the rotational equator, i.e. $\iota = \pi/2$. The $2f_{rot}$ emission is strongest in the direction of the axis of rotation and is non-zero in all directions. It is of course worth remembering that the relative strengths of the observed signal by a detector will depend on the noise floor at the two frequencies as well as the inherent strength of the signals.

In order to get the signal equations for the heterodyned signal, which are the equations that will be used to perform an analysis for GW signals of this type, equations 42 to 45 of Jones (2010) are multiplied by $e^{-i\phi(t)}$ and $e^{-i2\phi(t)}$ for the f_{rot} and $2f_{rot}$ signals respectively. This removes the phase evolution from the signal. I go through the algebra in detail to derive the heterodyned signal in Appendix A, but as it is particularly verbose I simply include the result here.

$$h_+^{2\Omega} = \frac{-\Omega^2}{r}(1+\cos^2\iota)\{A_1\cos 2\phi - A_2\sin 2\phi + i(A_2\cos 2\phi + A_1\sin 2\phi)\}, \quad (6.1)$$

$$h_\times^{2\Omega} = \frac{-2\Omega^2}{r}\cos\iota\{A_2\cos 2\phi_0 + A_1\sin 2\phi_0 - i(A_1\cos 2\phi_0 + A_2\sin 2\phi_0)\}, \quad (6.2)$$

$$h_+^{\Omega} = \frac{-\Omega^2}{2r}\sin\iota\cos\iota\{A_1\cos\phi_0 - A_2\sin\phi_0 + i(A_2\cos\phi_0 + A_1\sin\phi_0)\}, \quad (6.3)$$

$$h_\times^{\Omega} = \frac{-\Omega^2}{2r}\sin\iota\{A_2\cos\phi_0 + A_1\sin\phi_0 + i(A_2\sin\phi_0 - A_1\cos\phi_0)\}. \quad (6.4)$$

Where $A_1 = (I_{21}\cos^2\lambda - I_{31})\sin 2\theta$, and $A_2 = I_{21}\sin 2\lambda\sin\theta$, and $B_1 = I_{21}(\cos^2\lambda\cos^2\theta - \sin\lambda) + I_{31}\sin^2\theta$, $B_2 = I_{21}\sin 2\lambda\cos\theta$.

Before using these equations to develop a search code for the pinned superfluid signal, I will look at a simpler analogy to provide some insight into the basic problem and guide the development of the actual search method. This investigation with a simple analogy is presented in the next section.

6.3.2 A simple analogy

In order to aid my understanding of the basic problem, but with a much simpler model I use a simple test case analogy. In this simple test case the data consists of two input streams, A and B. The model is a simplistic one, the signal has a magnitude h, the amount of the signal that is in each of the two data-streams depends on the angle θ. The data consists of the signal plus noise $H = h + n$. A schematic diagram of this can be seen in Figure 6.8.

So from this model I have expressions for the data A and B in terms of h and n, these are $A = h\cos(\theta) + n_1$ and $B = h\sin(\theta) + n_2$.

I want to find the posterior probability distribution functions (PDFs) for h and θ given a set of data A and B. I can write this as $prob(h, \theta|A, B)$, the probability of h and θ given A and B. However this is not something that is directly calculable, so we use Bayes theorem. Bayes theorem lets us re-write this in terms of quantities

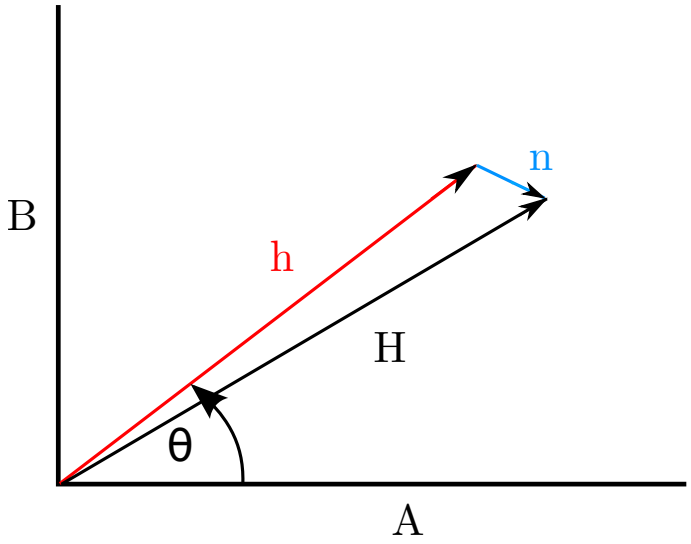

Figure 6.8: A schematic of the simple test case model, showing the two data-streams A and B, the signal of amplitude h, the noise n, and the observed signal $H = h + n$.

we can directly calculate

$$prob(h, \theta|A, B) = \frac{prob(A, B|h, \theta)prob(h, \theta)}{prob(A, B)}. \tag{6.5}$$

Where $prob(A, B|h, \theta)$ is the likelihood function, it calculates the probability of getting the data A and B given values of h and θ.

$prob(h, \theta)$ is the prior, it calculates how probable the values of h and θ irrespective of the data.

$prob(A, B)$ is the evidence, also known as the marginal likelihood. If the RHS of Bayes theorem is not divided by this then the equality becomes an proportionality.

I will now look at three different test case scenarios for this given model. Case one is where θ is known a priori and is zero, and h is unknown. Case two is where θ is known but is non-zero and again h is unknown. Case three is where both θ and h are unknown. To keep things simple I will assume that σ, the standard deviation of the noise is one for all three cases.

Model one

For this case $\theta = 0$, so $\cos(\theta) = 1$ and $\sin(\theta) = 0$, so the expression for the posterior probability is written as:

$$prob(h|A,B) \propto \frac{1}{2\pi} \exp\Big[-\Big(\frac{(A-h)^2}{2} + \frac{B^2}{2}\Big)\Big]\Big(\frac{1}{h_{max} - h_{min}}\Big) \tag{6.6}$$

Note that the expression for the posterior probability does not show any dependance on θ, but also note that despite the data B containing no signal, but instead only noise, the posterior probability is still dependent on this data stream. The reason for this is that the model where $\theta = 0$ still has something to say about the data B, it says that there should be no signal, just noise, so if B is not consistent with just noise then the model is unlikely and the posterior probability will reflect this.

Model two

For this case θ is known, and $\theta \neq 0$, so the expression for the posterior probability of h is written as:

$$prob(h|A,B) \propto \frac{1}{2\pi} \exp\Big[-\Big(\frac{(A-h\cos\theta)^2}{2} + \frac{(B-h\sin\theta)^2}{2}\Big)\Big]\Big(\frac{1}{h_{max} - h_{min}}\Big) \tag{6.7}$$

Note that unlike case one, the expression for the posterior probability is dependent on θ. However, I can simplify this case further by re-defining the data, by rotating the axes in Figure 6.8 by θ I define new data-streams x and y, such that Y will now only contain noise and no signal. To redefine the data streams by the rotation I use $A = x\cos\theta + y\sin\theta$ and $B = -x\sin\theta + y\cos\theta$, and substitute these formulae in place of A and B. To simplify things slightly I will take the factor of $1/2$ outside the brackets with the factor of -1, and just show workings on the part $(A - h\cos\theta)^2 + (B - h\sin\theta)^2$, looking at the two parts of this in turn.

$$\begin{aligned}&(A - h\cos\theta)^2 + (B - h\sin\theta)^2 = \\ &(x\cos\theta + y\sin\theta - h\cos\theta)^2 + (-x\sin\theta + y\cos\theta - h\sin\theta)^2\end{aligned}$$

Taking the first part and working through this first...

$$(x\cos\theta + y\sin\theta - h\cos\theta)^2 =$$
$$(x\cos\theta + y\sin\theta)^2 - 2h\cos(x\cos\theta + y\sin\theta) + h^2\cos^2\theta$$

$$= x^2\cos^2\theta + 2xy\sin\theta\cos\theta + y^2\sin^2\theta - 2h\cos(x\cos\theta + y\sin\theta) + h^2\cos^2\theta$$
$$= x^2\cos^2\theta + 2xy\sin\theta\cos\theta + y^2\sin^2\theta - 2h\cos^2\theta - 2hy\sin\theta\cos\theta + h^2\cos^2\theta$$

Now taking the second part and working through...

$$(-x\sin\theta + y\cos\theta - h\sin\theta)^2 =$$
$$(y\cos\theta - x\sin\theta)^2 - 2h\sin\theta(y\cos\theta - x\sin\theta) + h^2\sin^2\theta$$
$$= y^2\cos^2\theta - 2xy\sin\theta\cos\theta x^2\sin^2\theta - 2h\sin\theta(y\cos\theta - x\sin\theta) + h^2\sin^2\theta$$
$$= y^2\cos^2\theta - 2xy\sin\theta\cos\theta x^2\sin^2\theta - 2hy\cos\theta\sin\theta - 2hx\cos\theta\sin\theta + h^2\sin^2\theta$$

Now adding together parts one and two gives

$$= x^2\cos^2\theta + 2xy\sin\theta\cos\theta + y^2\sin^2\theta - 2h\cos^2\theta - 2hy\sin\theta\cos\theta$$
$$+ h^2\cos^2\theta + y^2\cos^2\theta - 2xy\sin\theta\cos\theta x^2\sin^2\theta - 2hy\cos\theta\sin\theta$$
$$- 2hx\cos\theta\sin\theta + h^2\sin^2\theta$$

$$= h^2\cos^2\theta + h^2\sin^2\theta + (x^2+y^2)\cos^2\theta + (x^2+y^2)\sin^2\theta - 2hx\cos^2\theta - 2hx\sin^2\theta$$
$$= h^2(\cos^2\theta + \sin^2\theta) + (x^2+y^2)(\cos^2\theta + \sin^2\theta) - 2hx(\cos^2\theta + \sin^2\theta)$$
$$= h^2 + x" + y2 - 2hx$$
$$= (x-h)^2 + y^2$$

And now this can finally be added back into the expression for the posterior probability, to give...

$$prob(h|A,B) \propto \frac{1}{2\pi}\exp\Big[-\Big(\frac{(x-h)^2}{2} + \frac{y^2}{2}\Big)\Big]\Big(\frac{1}{h_{max} - h_{min}}\Big) \tag{6.8}$$

It can be seen that this expression is now equivalent to that of case one, where the data A and B have been replaced by the data x and y.

Model three

For case three θ is unknown, and as such the prior probability does now depend on θ. Also notice that the prior is different for this case, as the prior probability now depends on θ, we must include a prior on θ. I have chosen the prior to be uniform in the range of $0 \rightarrow 2\pi$.

$$prob(A, B|h, \theta) \propto \frac{1}{2\pi} \exp\Big[-\Big(\frac{(A - h\cos\theta)^2}{2} + \frac{(B - h\sin\theta)^2}{2}\Big)\Big]\Big(\frac{1}{2\pi(h_{max} - h_{min})}\Big) \tag{6.9}$$

Model selection

Given a set of data, it is possible to find the most likely model between case one and case three (as case two and case one are the same I don't include case 2), and the model that the data consists of only noise and no signal. To do this I use a standard Bayesian approach for model selection, the calculation of an "odds ratio". This approach uses the simple idea that the ratio of the posterior probability of one model given the data, and another model given the data, tells me which model is more likely. This is simply written, for the comparison between model 1 and model 3, with data D, as...

$$\frac{prob(m_1|D, I)}{prob(m_3|D, I)} \tag{6.10}$$

In this case I is simply anything else we know about this situation, and for brevity I will no longer write it out. The individual posterior for any model m_n can be written as:

$$prob(m_n|D) = \frac{prob(D|m_n)\ prob(m_n)}{prob(D)} \tag{6.11}$$

By combining Equations 6.10 and 6.11, we get...

$$\frac{prob(m_1|D)}{prob(m_2|D)} = \frac{prob(D|m_1)}{prob(D|m_2)} \times \frac{prob(m_1)}{prob(m_2)} \ . \tag{6.12}$$

The term $prob(m_1)/prob(m_2)$ from Equation 6.12 is called the prior odds, this reflects any prior preference we have for one model over the other, this can of course simply be unity if both models are thought to be equally likely. The term $prob(D|m_1)/prob(D|m_2)$ is known as the odds ratio or Bayes factor and is the ratio of evidence of both models. The $prob(D)$ terms from equation 6.11 cancel out as the data is the same, and so is not written here.

The odds ratio $\mathcal{O}$ is simply the evidence of one model over the evidence of another model, written out for my models m_1 and m_3 this is:

$$\frac{prob(D|m_1)}{prob(D|m_3)} = \frac{\int prob(D|m_1, h)\delta h}{\int\int prob(D|m_3, h, \theta)\delta h \delta\theta} \tag{6.13}$$

Now I investigate the use of odds ratios and evidence values for two situations. The first situation is where I perform a search using a model that predicts a signal only in A, i.e. case 1, but where the underlying mechanism produces a signal in A and B. To do this I create a set of ROC curves, which give the efficiency of producing a detection with the case 1 model. The ROC curves are generated using a series of injection signals created using the case 3 model. For each ROC curve I generated 200 injections at each specified SNR over an increasing range of SNRs. Each injection was created using a different realisation of random Gaussian noise. To calculate the detection efficiency I compute an odds ratio of the evidence for the case 1 model over the evidence for the Gaussian noise model. To calculate the evidence for each model, I integrate the likelihood function with respect to the model parameters, for case one this is h, and for the noise only model there are no model parameters so no integration is needed. We should remember that the noise in each data-stream, both A and B has $\sigma = 1$ in all cases. I computed the evidence for each model using numerical integration. To define a detection I generated 200 sets of data containing no signal and calculated the odds ratio of the case 1 model over the Gaussian noise model. I then determine a threshold odds ratio value which 99% of the odds ratio values for these 200 datasets lies below. This sets a 1% false alarm rate for my analysis. I then run the same numerical integration on each of my injection signals. I injected signals from SNR = 0.5, to SNR = 8 at 0.5 intervals in SNR. At each SNR I calculated the proportion of results where the odds ratio is above the threshold, and this gives me the proportion of the runs where I would claim a detection with a 1% false alarm rate, for ease this is labelled the efficiency. The ROC curves are simply a plot of the efficiency against the SNR of the injected signals.

ROC curves for the odds ratio of case one versus the noise only model are shown in Figure 6.9. For each ROC curve in this figure the injection signal was generated

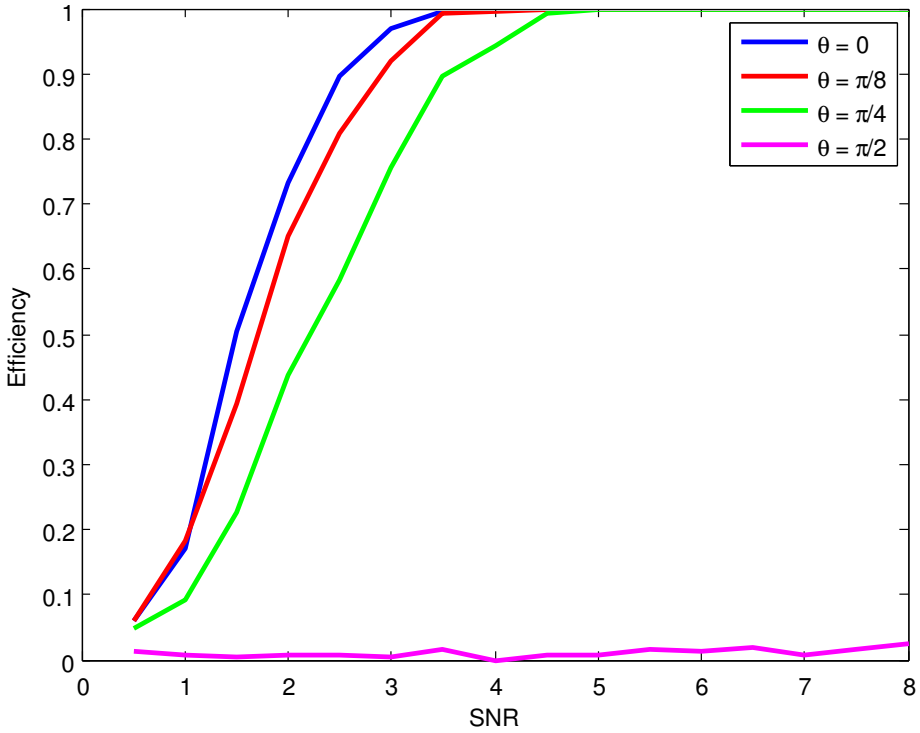

Figure 6.9: The ROC curve for odds ratio case one versus the noise only model. The value of h is scaled appropriately for the SNR, and the value for θ is set to zero for this ROC curve.

using the case 3 model and a specified value for θ. This is done on purpose to see how the efficiency is affected by searching for the incorrect signal model. If we start by looking at the $\theta = 0$ ROC curve in Figure 6.9, we can see that the signal will be very likely to be detected at all but the lowest SNRs, i.e. as soon as the signal is strong enough to stand out above the noise a detection is the most probable outcome. This should not be surprising, but it is worth mentioning that we should remember the model here, and the model assumes that all the signal is present in data A and none in data B, where $\theta = 0$. This is in fact true, so this ROC curve presents the best case scenario for the case one model.

Now if we look at all the ROC curves in Figure 6.9, we can see that as $\theta \to \pi/2$ it becomes increasingly unlikely for case one to be favoured over the noise only model at a given SNR. This is because less of the signal goes into data A, and more into data B. As $\theta \to \pi/2$, indeed at $\theta = \pi/2$ all of the signal goes into data B and none into data A. So, as soon as the signal is visible above the noise in data B case one becomes less likely, leading to a reduction in efficiency shown by these ROC curves. The ROC curve for $\theta = \pi/2$ in Figure 6.9 presents the extreme case where it is very unlikely regardless of the SNR that case one model is favoured.

The second situation I investigate is where I perform two searches, one for the case 1 model and one for the case 3 model. I investigate how well I can determine which model was used to create the signal injections. To do this I use the same

set of signal injections created with specific values of θ and over a range of SNRs. Instead of calculating ROC curves, this time I simply plot the logarithm of the odds ratio of the case 3 model over the case 1 model.

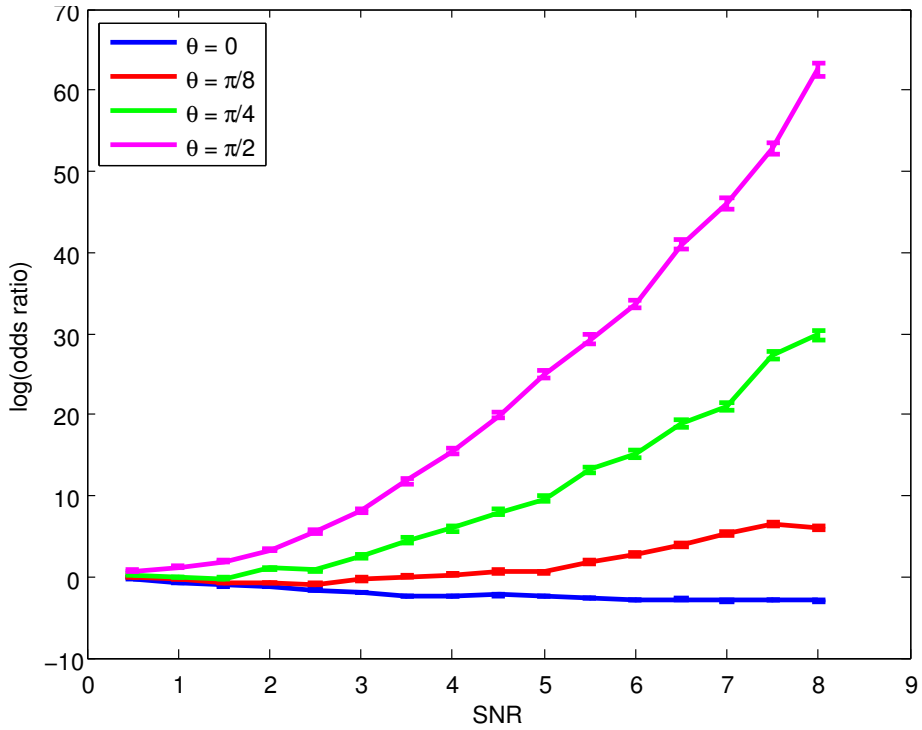

Figure 6.10: A plot of the mean odds ratio vs SNR for odds ratio case three versus case one model. The value of h is scaled appropriately for the SNR, and the value for θ is set to zero for this plot.

These results can be seen in Figure 6.10. If we start by looking at the data for $\theta = 0$ in this figure, this is the extreme case, where all of the signal goes into data A, and none into data B. This is the scenario that the case one model describes exactly, and so it should come as no surprise that the odds ratio favours case one over case three when $\theta = 0$ at all SNRs. The trend towards lower odds ratios with increasing SNR shows that as the signal is increasingly obvious, case three becomes increasingly bad at describing the data.

The remaining data for $\theta = \pi/8$ to $\theta = \pi/2$ represent a progression where more and more of the signal is fed into data B as $\theta \to \pi/2$. As the model for case one predicts no signal in data B, it is expected that the odds ratio of case three versus case one begins to stop favouring case one as it becomes increasingly obvious that there is in fact signal present in data B.

The data where $\theta = \pi/2$ in this figure represents an extreme case, as none of the signal is in data A, and all in data B. As the model for case one predicts the exact opposite of this for each data stream it should not be a surprise that as soon as the signal is strong enough to be seen over the noise, the case one model is strongly disfavoured compared to case three.

Changing the prior on θ

This section looks at the effect of changing the prior on θ on the odds ratio. Instead of applying a uniform prior to θ across its possible range, I now apply a Gaussian prior with mean zero, and with standard deviations σ ranging from 0.1 to 10, Figure 6.11 shows the odds ratio across a range of SNRs for each value of σ. The odds ratio values are the mean odds ratio from 200 different runs at each SNR. It can be seen that at low standard deviations for the prior, i.e. where the prior is very tight around $\theta = 0$, the log odds ratio is close to zero, i.e. both case 1 and case 3 are equally likely. This shows that case three is equivalent to case one where the prior on θ is restricted to very close to $\theta = 0$. As the standard deviation of the Gaussian prior on θ gets larger, the plots of odds ratio vs SNR more and more closely resemble those where a uniform prior was placed on θ.

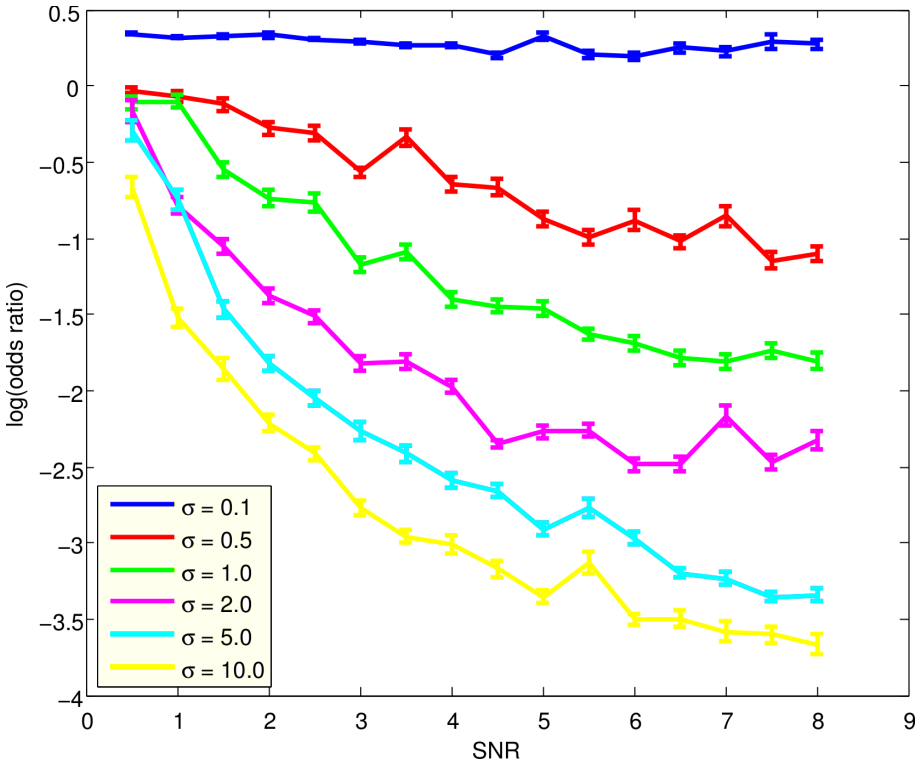

Figure 6.11: A plot of odds ratio vs SNR for odds ratio case three versus case one model. The value of h is scaled appropriately for the SNR, the value for θ is set to zero, the prior on θ is a Gaussian with mean zero and standard deviation 0.1.

Summary of the simple test case

The simple test case examined here comprises of the data split into two input streams, A and B. Where the signal has a magnitude h, the amount of the signal that is in each of the two data-streams depends on the angle θ. I examined what would happen when analysing the data using two different models given different

values of θ. With one model predicting that all the signal is in data stream A, and the other assuming that both data A and B contain the signal. The basic picture gained from this investigation shows us that in cases where there is a signal in both data-streams A and B, at some critical SNR in B the evidence for the model predicting signal only in A will begin to decrease. The data-streams A and B of the simple test case are analogous to the data-streams at f_{rot} and $2f_{rot}$ of the actual real superfluid model. Therefore this point is important for the real pinned superfluid analysis, as on average the emission at $2f_{rot}$ is stronger than that for f_{rot}, but despite this, even where the f_{rot} signal is weak, provided it can pass that critical SNR then the pinned superfluid model will be favoured by Bayesian model selection.

6.4 Developing a Bayesian search for pinned superfluid GWs

This section takes the reader through the development of the nested sampling search code to include the pinned superfluid model. This starts by considering the general Bayesian approach in §6.4.1, §6.4.2 then shows how this approach was taken to produce the actual likelihood function that has been implemented into the nested sampling search code. The next section, §6.4.3 then shows how I decided upon the principal ranges for each of the model parameters, and these represent the maximum ranges over which the code searches. The results from testing of the code are presented in §6.4.4 and 6.4.5 for parameter estimation and evidence calculation respectively. A summary of the development and testing, along with a discussion about what future work should be considered is given in §6.4.6.

6.4.1 The Bayesian approach

To consider the pinned superfluid model, I take the lead from the simple test case discussed above. The two problems bear some similarity; there are two data-streams, and the parameters of the model dictate the relative strength of the signal in each of these data-streams. The pinned superfluid model differs from the simple test case in that the relative strength of the signals at f and $2f$ depends on a complicated combination of parameters, rather than the simplistic dependence of the test case model. I start on this approach by writing out expressions for the posterior probability for the models I will consider. These will take the general form of Equation 6.5, with a greater number of model parameters, as discussed in §6.3.1. The models are; the pinned superfluid model m_{ps}, the triaxial model m_t, and the noise only model m_n. Instead of writing each of the parameters out explicitly I define the vector of parameters $\vec{\theta}$, which is different for each model. For m_n, $\vec{\theta} = (\sigma_1, \sigma_2)$,

for m_t $\vec{\theta} = (I_{21}, \psi, \iota, \phi_0, \sigma_1, \sigma_2)$, and for m_{ps}, $\vec{\theta} = (I_{31}, I_{21}, \psi, \iota, \phi_0, \lambda, \theta, \sigma_1, \sigma_2)$. The datasets are labelled d_1 and d_2, for the f and $2f$ datasets respectively, jointly they are referred to as $\vec{d}$. The posterior probability expression for each model can be derived from Bayes theorem, and is

$$prob(\vec{\theta}|\vec{d}, m) = \frac{prob(\vec{d}|\vec{\theta}, m)prob(\vec{\theta}|m)}{prob(\vec{d}|m)} \propto prob(\vec{d}|\vec{\theta}, m)prob(\vec{\theta}|m). \tag{6.14}$$

Using this one can compute how likely different values of the parameters are for a given model and the data. This is how we perform the parameter estimation stage of a CW analysis. Until recently this is where our CW analyses have ended, one of the parameters is the GW strain and if the most likely value for this parameter is zero then we conclude that there is no GW signal present in the data. However, within the Bayesian framework there is a better way of making this decision about the presence of a signal - this approach is known as model selection. Model selection enables us to select the most probable of two competing models given the data. I want to know is m_{ps} more likely than m_t, is m_{ps} more likely than m_n, and is m_t is more likely than m_n, i.e. is there evidence for a signal, and if so which signal model is the most likely. To do this I follow the same approach outlined in §6.3.2. This starts with the ratio of the posterior probability of each model,

$$\frac{prob(m_1|\vec{d})}{prob(m_2|\vec{d})}. \tag{6.15}$$

If the ratio is greater than one then the model in the numerator is favoured, less than one and the denominator is favoured. Then if the individual posterior for a model is written as

$$prob(m_n|\vec{d}) = \frac{prob(\vec{d}|m_n)\ prob(m_n)}{prob(\vec{d})}, \tag{6.16}$$

by combining Equations 6.15 and 6.16 and using Bayes theorem we arrive at Equation 6.17.

$$\frac{prob(m_1|\vec{d})}{prob(m_2|\vec{d})} = \frac{prob(\vec{d}|m_1)}{prob(\vec{d}|m_2)}\frac{prob(m_1)}{prob(m_2)} \tag{6.17}$$

Note that the term $prob(\vec{d})$ is the same for both models and so cancels out. The

prior odds is the second fraction in the right hand side of Equation 6.17, where there is no a priori reason to favour one model over the other this should be one. The other fraction on the right hand side of this equation is the odds ratio. For this situation I have no reason to believe one model over the other a priori, and as such will compute the odds ratios to determine which of the three models is more likely. To calculate the odds ratios, I can see from 6.17 that I must compute the evidence $prob(\vec{d}|m)$ for the models I am comparing. To compute the evidence I integrate the posterior probability over each of the model parameters, so

$$prob(\vec{d}|m) = \int^{\vec{\theta}} prob(\vec{d}|\vec{\theta}, m) prob(\vec{\theta}) d\vec{\theta}. \tag{6.18}$$

Now I have established the general procedure for how to select the most likely model, my next step is to write out the posterior probabilities for each of the three models explicitly, so that I can then calculate the evidence using these. I start with the noise only model m_n.

For the noise only model, $\vec{\theta} = (\sigma_1, \sigma_2)$, the posterior probability is

$$prob(\vec{d}|\vec{\theta}, m_n) prob(\vec{\theta}) = (\vec{\theta}) \frac{1}{2\pi\sigma_1^2\sigma_2^2} \exp\left(-\frac{d_1^2}{2\sigma_1^2} - \frac{d_2^2}{2\sigma_2^2}\right) \left(\prod_{i=1}^{n} \frac{1}{(\theta_{i,max} - \theta_{i,min})}\right) \tag{6.19}$$

Next I consider the triaxial model, $\vec{\theta} = (h_0, \phi_0, \psi, \cos(\iota), \sigma_1, \sigma_2)$, and the posterior probability is

$$prob(\vec{d}|\vec{\theta}, m_n) prob(\vec{\theta}) = \frac{1}{2\pi\sigma_1^2\sigma_2^2} \exp\left(-\frac{d_1^2}{2\sigma_1^2} - \frac{(d_2 - \mu_2)^2}{2\sigma_2^2}\right) \left(\prod_{i=1}^{n} \frac{1}{(\theta_{i,max} - \theta_{i,min})}\right) \tag{6.20}$$

Where μ_2 is the predicted signal in d_2 from the model m_t.
Now to look at the pinned superfluid model m_{ps}, where $\vec{\theta} = (I_{21}, I_{31}, \phi_0, \psi, \cos(\iota), \theta, \lambda, \sigma_1, \sigma_2)$, and where μ_1 and μ_2 are the predicted signal in d_1 and d_2 respectively.

$$\begin{aligned} prob(\vec{d}|\vec{\theta}, m_n) prob(\vec{\theta}) = \frac{1}{2\pi\sigma_1^2\sigma_2^2} \exp\left(-\frac{(d_1 - \mu_1)^2}{2\sigma_1^2} - \frac{(d_2 - \mu_2)^2}{2\sigma_2^2}\right) \\ \left(\prod_{i=1}^{n} \frac{1}{(\theta_{i,max} - \theta_{i,min})}\right) \end{aligned} \tag{6.21}$$

Now to stop and consider the problem I have set myself, I have written out clearly how to compute the evidence for each model, but what does this actually mean and what might we expect from this? The evidence, $prob(\vec{d}|m)$, is simply put - the probability of getting the data given the model. Looking a little deeper into the evidence, by looking at Equation 6.18, lets look first at $prob(\vec{d}|\vec{\theta}, m)$. This provides a measure of how well the data fit the chosen model. It is obvious that the model containing more parameters is more likely to fit the data better due to the increased flexibility that comes with added parameters. If this were the only contribution to the evidence it would be a cause for concern, as I do not want to simply favour the model with more parameters every time. However, if we consider the other term in the evidence $prob(\vec{\theta})$, we can see that extra parameters also bring a penalty to the evidence, as $prob(\vec{\theta}) = 1/(\vec{\theta}_{max} - \vec{\theta}_{min})$. This is commonly known as the Ockham factor, as it imposes Ockham's Razor "it is vain to do with more what can be done with fewer" on the analysis (Sivia & Skilling 2006).

6.4.2 The likelihood function

In the previous section I discussed the general approach to the parameter estimation and model selection problems with the pinned superfluid model. This has helped to provide a good picture of what it is I want to do, but does not really go into the nuts and bolts of how to actually achieve it. I will now go into these problems in more detail, starting with the parameter estimation problem. I will take my lead from Dupuis & Woan (2005), keeping much of the same notation, and also considering two cases, the special case where variance of the noise is known, and in the general case where the variance of the noise is not known. Also, it is worth a quick note to say that here I consider two data-streams for analysis, as opposed to the one data-stream considered in Dupuis & Woan (2005).

I start with the pinned superfluid model, its heterodyned signal is given in §6.3.1 Equations 6.1 to 6.4, but is again shown here in Equations 6.22 and 6.23 with the detector antenna pattern included.

$$
\begin{aligned}
&y(t_{k,f}; \vec{\theta}) = \\
&F_{+(t_k,\psi)} \frac{-\Omega^2}{2r} \sin\iota\cos\iota\{A_1\cos\phi_0 - A_2\sin\phi_0 + i(A_2\cos\phi_0 + A_1\sin\phi_0)\} + \\
&F_{\times}(t_k,\psi) \frac{-\Omega^2}{2r} \sin\iota\{A_2\cos\phi_0 + A_1\sin\phi_0 + i(A_2\sin\phi_0 - A_1\cos\phi_0)\}.
\end{aligned}
\tag{6.22}
$$

$$
\begin{aligned}
&y(t_{k,2f};\vec{\theta}) = \\
&F_{+(t_k,\psi)}\frac{-\Omega^2}{r}(1+\cos^2\iota)\{B_1\cos 2\phi - B_2\sin 2\phi + i(B_2\cos 2\phi + B_1\sin 2\phi)\} + \\
&F_{\times}(t_k,\psi)\frac{-2\Omega^2}{r}\cos\iota\{B_2\cos 2\phi_0 + B_1\sin 2\phi_0 - i(B_1\cos 2\phi_0 + B_2\sin 2\phi_0)\}
\end{aligned}
\tag{6.23}
$$

I begin by considering a simplified case, where each data stream has n samples, and consist of the complex signal defined by $y(t_{k,f})$ and $y(t_{k,2f})$, plus complex Gaussian noise with zero mean and known variance $N(0,\sigma_{k,1}), N(0,\sigma_{k,2})$. This simplified case assumes that for each sample the variance of the noise can be adequately estimated. The likelihood function can then be written as

$$
\begin{aligned}
&prob(B_{k,f,2f}|\vec{\theta},\sigma_{k,f,2f}) = \\
&\qquad (2\pi\sigma_{k,f}\sigma_{k,2f})^{-2n}\exp\left(-\sum_{\mathrm{k=1}}^{\mathrm{n}}\frac{|\mathrm{B_{k,f}}-\mathrm{y_{k,f}}|^2}{2\sigma^2_{\mathrm{k,f}}}+\frac{|\mathrm{B_{k,2f}}-\mathrm{y_{k,2f}}|^2}{2\sigma^2_{\mathrm{k,2f}}}\right).
\end{aligned}
\tag{6.24}
$$

This approach has been successfully used when applied to the triaxial NS model in a search using LIGO S1 and GEO600 data for GWs from pulsar J1939_2134 (Allen et al. 2004). However, it is not always possible to make an accurate estimate of the variance due to non-Gaussian noise artefacts present in the frequency band of a pulsar, also the practicalities of doing this for multiple pulsars becomes an issue for a large number of pulsars. Hence, an alternative approach is adopted, where the variance of the noise is treated as an extra nuisance parameter, and the likelihood function is marginalised over the variance. This approach has been adopted as the standard for known pulsar Bayesian searches. This approach has its own set of assumptions, these being that the noise is stationary (i.e. it is well described by one variance) over a period of 30 minutes. I again take the approach of Dupuis & Woan (2005). So I start by finding a general expression for the likelihood of a set of m_j data points taken from B_k which has a total number of datapoints n, and M is the number of segments which B_k is split into. This general likelihood is applicable for both data-streams $B_{k,f}$ and $B_{k,2f}$. I now write the general likelihood for a set of parameters based on the j th set of data marginalised over σ_j

$$
prob(B_{k,j}|\vec{\theta}) \propto \int_0^\infty prob(B_k,\sigma_j,|\vec{\theta})\,d\sigma_j \tag{6.25}
$$

From here, I use the product rule to express $prob(B_k,\sigma_j|\vec{\theta})$, in terms of the priors

on σ_j and the likelihood of getting the data B_k given a set of parameters $\vec{\theta}$ and σ_j.

$$prob(B_{k,j}|\vec{\theta}) \propto \int_0^\infty prob(\sigma_j|\vec{\theta}) prob(B_k|\vec{\theta})\, d\sigma_j \tag{6.26}$$

Where the likelihood function is given by equation 6.24, and for the priors $\sigma_{j,f}$ and $\sigma_{j,2f}$, I take them to be Jeffreys priors (as they are scale parameters)

$$prob(\sigma_j|\vec{\theta}) \propto \frac{1}{\sigma_j}(\sigma_j > 0). \tag{6.27}$$

The integral in Equation 6.26 is looking pretty hard, so lets take a different tack. I arrive at Equation 6.24, by the product of the two likelihoods of the f and $2f$ signal being in the two data-streams. Instead of combining these likelihoods at that stage, I can consider each separately and combine them at a later stage. So instead of Equation 6.26, I end up with something that looks much more manageable

$$\begin{aligned} prob(B_{k,f,2f,j}|\vec{\theta}) =& prob(B_{k,f,j}|\vec{\theta}) \times prob(B_{k,2f,j}|\vec{\theta}) \\ &\propto \int_0^\infty prob(\sigma_{j,f}|\vec{\theta}) prob(B_{k,f}, \sigma_{j,f}|\vec{\theta})\, d\sigma_{j,f} \\ &\quad \int_0^\infty prob(\sigma_{j,2f}|\vec{\theta}) prob(B_{k,2f}, \sigma_{j,2f}|\vec{\theta})\, d\sigma_{j,2f} \end{aligned} \tag{6.28}$$

Each of these two integrals can be solved analytically to arrive at student -t functions. The handling of the f and $2f$ data-streams in this way is directly analogous to having extra segments of data, where the overall likelihood is the product of the individual likelihoods for each segment of data. The difference simply being that a different equation is used for $y_{k,f}$ and $y_{k,2f}$. These integrals can be solved analytically to give the students -t distribution, for the f data-stream, with $m_j - 1$ degrees of freedom.

$$\int_0^\infty prob(\sigma_{j,f}|\vec{\theta}) prob(B_{k,f}, \sigma_{j,f}|\vec{\theta})\, d\sigma_{j,f} = \left(\sum_{k=k1(j)}^{k_{2(j)}} |B_k - y_k|^2 \right)^{-m_j} \tag{6.29}$$

For the entire dataset, with M segments of data, this becomes

$$\prod_j^M \left(\sum_{k=k1(j)}^{k_{2(j)}} |B_k - y_k|^2 \right)^{-m_j} \tag{6.30}$$

So, taking into account my two data-streams (f and $2f$), I can construct the joint likelihood,

$$prob(B_{k,f,2f}|\vec{\theta}) = \prod_{j_1}^{M_1}\left(\sum_{k=k1(j_1)}^{k_{2(j_1)}}|B_{k,f}-y_{k,f}|^2\right)^{-m_{j_1}}\prod_{j_2}^{M_2}\left(\sum_{k=k1(j_2)}^{k_{2(j_2)}}|B_{k,2f}-y_{k,2f}|^2\right)^{-m_{j_2}} \tag{6.31}$$

This can be worked out using the nested sampling algorithm, as described in §6.2, and for the analyses described in the sections to follow this is the algorithm used.

6.4.3 Model parameter ranges

The pinned superfluid model has seven unknown model parameters, and in order to use the nested sampling algorithm to analyse GW detector data for either parameter estimation or for model selection, the prior ranges for each of these parameters must be decided. The majority of the angular parameters will have a principal range, within which they describe unique physical configurations of the system. Outside of these principal ranges the physical configuration of the system and the signal produced, is a repetition of that produced with an angle within the principal range. The prior ranges for such parameters will span the principal range and will be circular. Some investigation of the signal is needed to determine the principal ranges for these parameters and this will be described shortly. As ι is a latitude like parameter, and I wish to have a prior that is uniform over the orientation of NS axis, it is re-parametrised as $\cos(\iota)$, which has an obvious range from -1 to 1. The ranges of the parameters r, I_{21}, I_{31} can not be determined in the same way as the angular parameters, and instead require some input from our astrophysical knowledge of the sources we are searching for. For many known pulsars there are reliable distance estimates and errors on these estimates which can be used when deciding on the prior range for r. For the parameters I_{21} and I_{31} there are no such reliable estimates, the minimum bound for these parameters could be chosen as zero, but determining the upper bounds for the prior range requires some more thought. One approach would be to use theoretical predictions for the maximum values that NS matter could sustain based on NS EOS, as discussed in §2.2.9. However, as also discussed in §2.2.9, there are a number of such models, each of which makes different predictions, choosing the most appropriate upper bound for these parameters using this approach should be undertaken with care. Another approach could be to base the upper bounds on the spin-down limit of the pulsar in question. Values for

each of these parameters could be inferred from the spin-down luminosity of the pulsar assuming that for each parameter in turn the other is zero. This would place an observationally derived upper limit on these parameters, but would require an individual estimate for each pulsar.

One way to determine the principal ranges of the parameters is by examining the heterodyned signal equations, Equations 6.1 to 6.4, and from knowledge of the trigonometric functions in which the parameters appear deduce the principal range for the parameters. For example the parameter λ appears in the heterodyned equations as $\sin(2\lambda), \sin^2(\lambda), \cos^2(\lambda)$. As $\sin(x), \sin^{2(}x), \cos^2(x)$ are all known to be unique only over the range $0 \geq x \leq \pi$, the principal range for λ should be $0 \geq \lambda \leq \pi$. For the parameter θ it is slightly more complicated, as the functions of this parameter are $\cos(\theta), \sin(\theta)$ for which the principal range of θ would be $0 \geq \theta \leq 2\pi$ and $\sin(2\theta), \cos^2(\theta), \sin^2(\theta)$ for which the principal range would be $0 \geq \theta \leq \pi$. As θ is analogous to the the latitude in a spherical coordinate system, and as I require the prior range for the orientation of the axis of pinning in the NS to be uniform I re-parametrise it as $\cos(\theta)$. The obvious principal range for $\cos(\theta)$ is from -1 to 1. For ϕ_0 the h_Ω equations have the principal range from 0 to π, and the $h_{2\Omega}$ equations have functions that have the principal range from 0 to 2π, so the combination of the two would have a principal range of 0 to 2π. The parameter ψ appears in the equations for the antenna pattern of the detector. For the triaxial case there is a degeneracy between this parameter and the ϕ_0 parameter, such that a shift of π relates to a ψ value being shifted by $\pi/2$, hence the prior range for ψ for the triaxial model is chosen between $-\pi/4$ and $\pi/4$.

A test I ran to help confirm the principal parameter ranges started with the angular model parameters selected at random over a range of 0 to 4π. This range was chosen as the principal ranges of the parameters are all expected to be less than this. From the randomly chosen parameters a signal is created and used as a reference. I then cycle through every combination of all the angular parameters in discrete steps (of $\pi/16$ for speed), and at each combination find the sum of the square of the difference in the signal produced by that particular combination of parameters and the reference signal. Where the signals match exactly the parameters are recorded and can then be examined to determine over what range each parameter produces an identical signal. The results from this test confirmed that the principal ranges that were chosen from the previous tests were correct. The only cases where exact matches for the signal were found is where certain parameters for the reference signal were at their extremes, such as $\cos(\iota) = 1, -1$ and $\cos(\theta) = 1, -1$, which are known to introduce degeneracies in the model.

Once I had decided upon these principal ranges I created a visualisation of how the signal changes over the parameter space. To do this I examined for each combi-

nation of the four circular angular parameters - $\theta, \lambda, \phi_0, \psi$, one at a time. I created a reference signal where the chosen parameter combinations were both zero and the other parameters set at random, and compared new signals generated over the principal ranges of the combination of parameters being examined. This method was used to create an image which shows the difference in the signal for combinations of two parameters. I created these images with each pixel in the image representing a value for each of the two parameters chosen, I increased their values in increments of $\pi/16$. I chose to calculate the difference in the signals as the difference between the signal where the two parameters were both zero, and taking the sum of the difference squared at each time-stamp in the signal. The timestamps for the signal were at 480 second intervals over a period of 86400 seconds (1 day). The same sky location and detector site was used for generating all of the signals. The images produced show how the signal is altered by changes in the parameters being examined, although care must be taken with this approach as the values for the other parameters which are not being varied alter the patterns seen in the images substantially. An example of one set of these images are shown in Figure 6.13.

6.4.4 Parameter estimation

Now that I have derived the principal ranges for the parameters I test the parameter estimation process using the nested sampling algorithm for the pinned superfluid case. I begin by injecting a signal with equal SNRs for f_{rot} and $2f_{rot}$ with a combined SNR of 10. The resulting PDFs are shown in Figure 6.14, in which it is immediately clear to see there are multiple peaks in the PDFs of certain parameters, and that the parameters of the signal have not been able to be recovered well. For a signal of combined SNR 10 this is perhaps not a complete surprise, however if we examine the nested samples as shown in Figures 6.15 and 6.16, it is possible to see that there are many degeneracies in the parameters, assuming that the nested samples do in fact map out the posterior probability. The degeneracies appear as lines of nested samples for parameter pairs. If there were no degeneracies the nested samples would appear clustered in distinct areas of high probability enabling the parameters to be estimated within a certain range with a certain confidence based on the tightness of the clustering. In this example the posterior probability looks particularly complex when viewing the nested samples for the pair of parameters ϕ_0 and λ in Figure 6.15, and for ϕ_0 and ψ in Figure 6.16.

In order to further investigate the parameter estimation of the pinned superfluid signal I use another example, this time with a combined SNR of 100, a far stronger signal than can be expected in GW astronomy in the forseeable future, but this extreme case is taken to provide insight into the problem only. The results from this

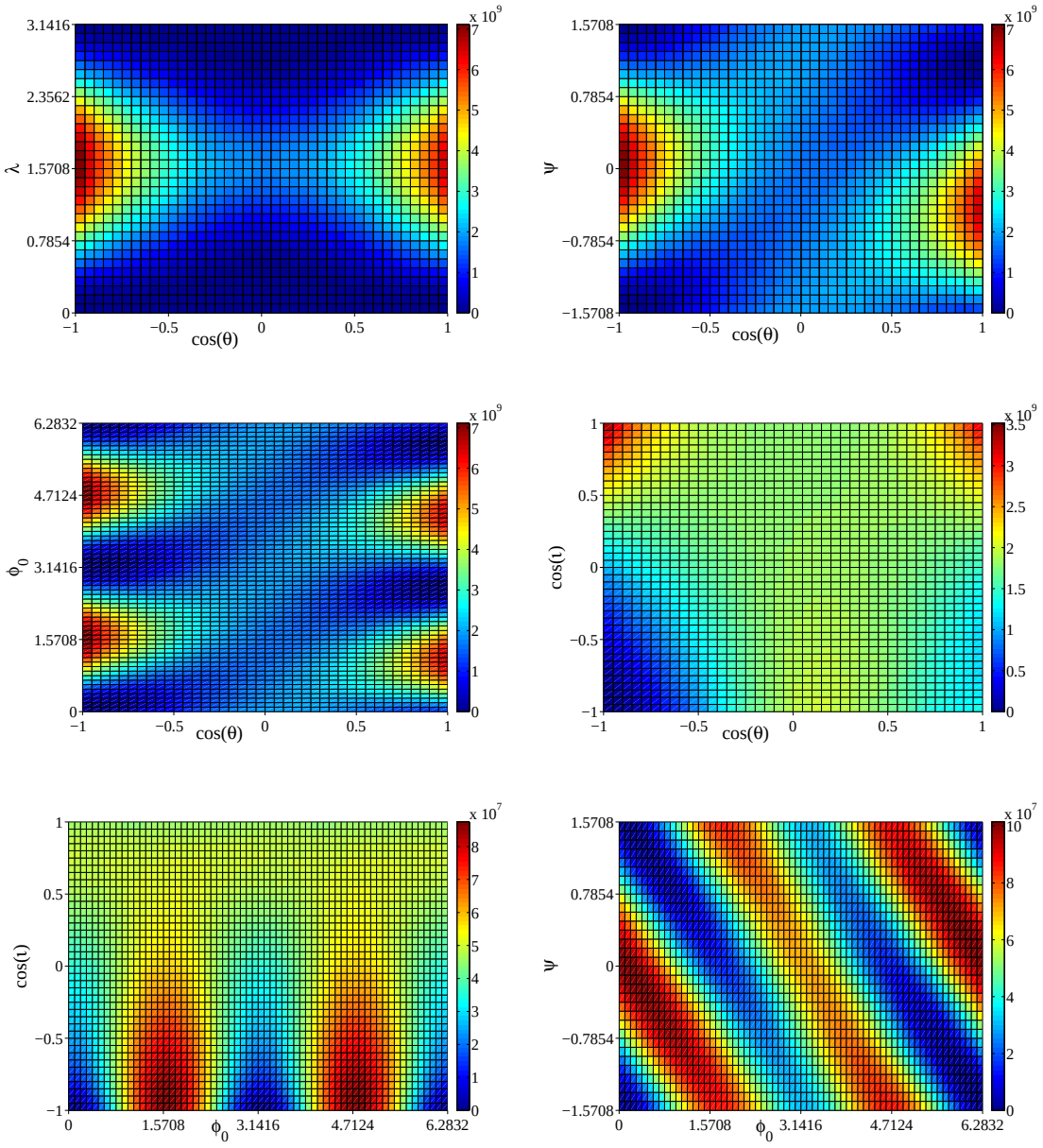

Figure 6.12: The difference in the sum of the signal squared when two of the parameters are varied throughout their principal range, for parameters $\cos(\theta), \lambda, \psi, \phi_0$ and $\cos(\iota)$.

parameter estimation run can be seen in Figures 6.17. The story with these results is much the same as those for the previous test case, the majority of parameters have not been constrained well. The exception to this is the $\cos(\iota)$, which has a tight PDF about the injected value. The I_{21} and I_{31} parameters have PDFs that peak at the injected values, however they show a non-zero probability at zero and cover a wide range in values. The ϕ_0 and ψ PDFs show multiple peaks, the $\cos(\theta)$ PDF is broad and flat, and the λ PDF has only a very weak peak. This is not what was expected for such a strong signal, and suggests that parameter estimation for this model is

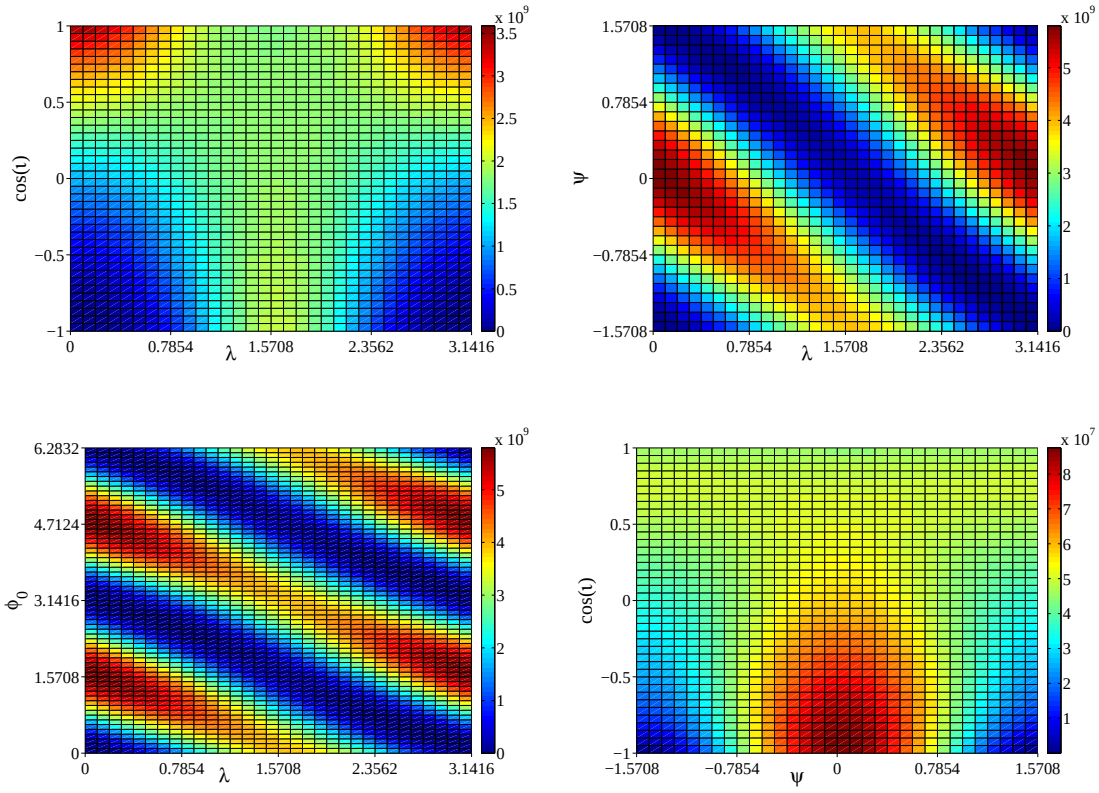

Figure 6.13: The difference in the sum of the signal squared when two of the parameters are varied throughout their principal range, for parameters λ, ψ, ϕ_0 and $\cos(\iota)$.

unlikely to yield meaningful results. Looking at the nested samples in Figures 6.18 and 6.19 the complicated patterns seen in the lower SNR test are repeated here, although with tightening of the high probability regions from the higher SNR the posterior appears even more complicated. The nested samples shown in these figures were produced from a number of nested sample runs in order to provide the fullest picture of the posterior possible. However there remain a few gaps in lines of samples seen in these plots. I believe these gaps to be due to the sampling of the algorithm rather than the true shape of the posterior. To investigate further I have taken five points selected at random from the last 5000 nested samples, these last 5000 points represent the most likely values of all the samples due to the nature of the nested sampling algorithm. These five points are highlighted with coloured squares in Figures 6.18 and 6.19. Using the parameters of these five points I have plotted the heterodyned signals that they correspond to on top of the data analysed, thus giving a visual indication of just how well they actually fit the data, this is shown in Figures 6.20 and 6.21. It was necessary to create Figure 6.21, which shows a zoomed in view of Figure 6.20 as the signals were are so similar it is not possible to tell them apart when viewing the whole signal. It is clear to see that the signals are

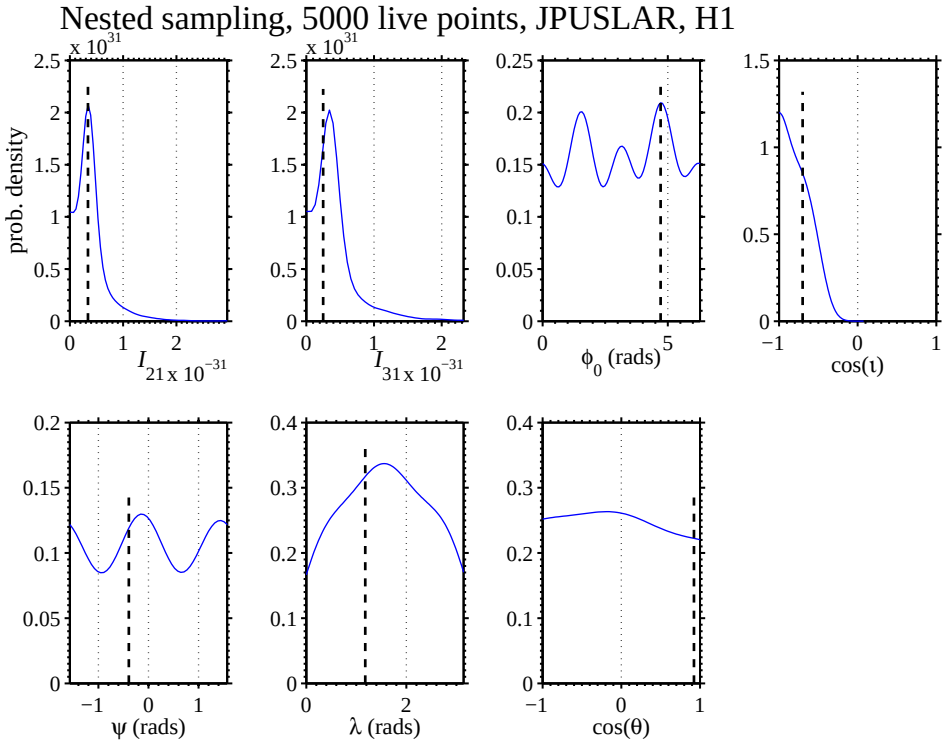

Figure 6.14: The PDFs for a injected pinned superfluid signal into Gaussian noise, with a SNR of 10. The injected values for each parameter are shown as dashed vertical black lines and the PDFs are shown in blue. The PDFs show that this analysis did not recover the injected parameters.

very similar, and that it is not possible to distinguish which of these signals is more likely to be contained in the data.

From these results it is clear that there are many degeneracies in the model which makes estimating the injected parameters impossible. I ran a number of other analyses of injected signals with SNRs of 100, where the signal parameters were chosen at random. The reason for this was to test whether the complicated patterns in the nested samples seen here where simply because I had chosen a special set of parameter values. Some of the results from this test are shown in Appendix B. The results indicate that the complex patterns seen in the nested samples here are not a special case but are the norm. One further test conducted was to see if adding an extra detector would break any of these degeneracies and enable better estimation of the model parameters. The results from this are shown in Figures 6.22 to 6.25. The data used in this test was created for the LIGO H1 and Virgo V1 interferometers for one day, with the injected signal parameters remaining the same, with the exception of the I_{21} and I_{31} which were tuned to ensure the running of the code completed in a reasonable time, as for higher combined SNRs the code takes much longer to run. These results show that an extra detector was not able

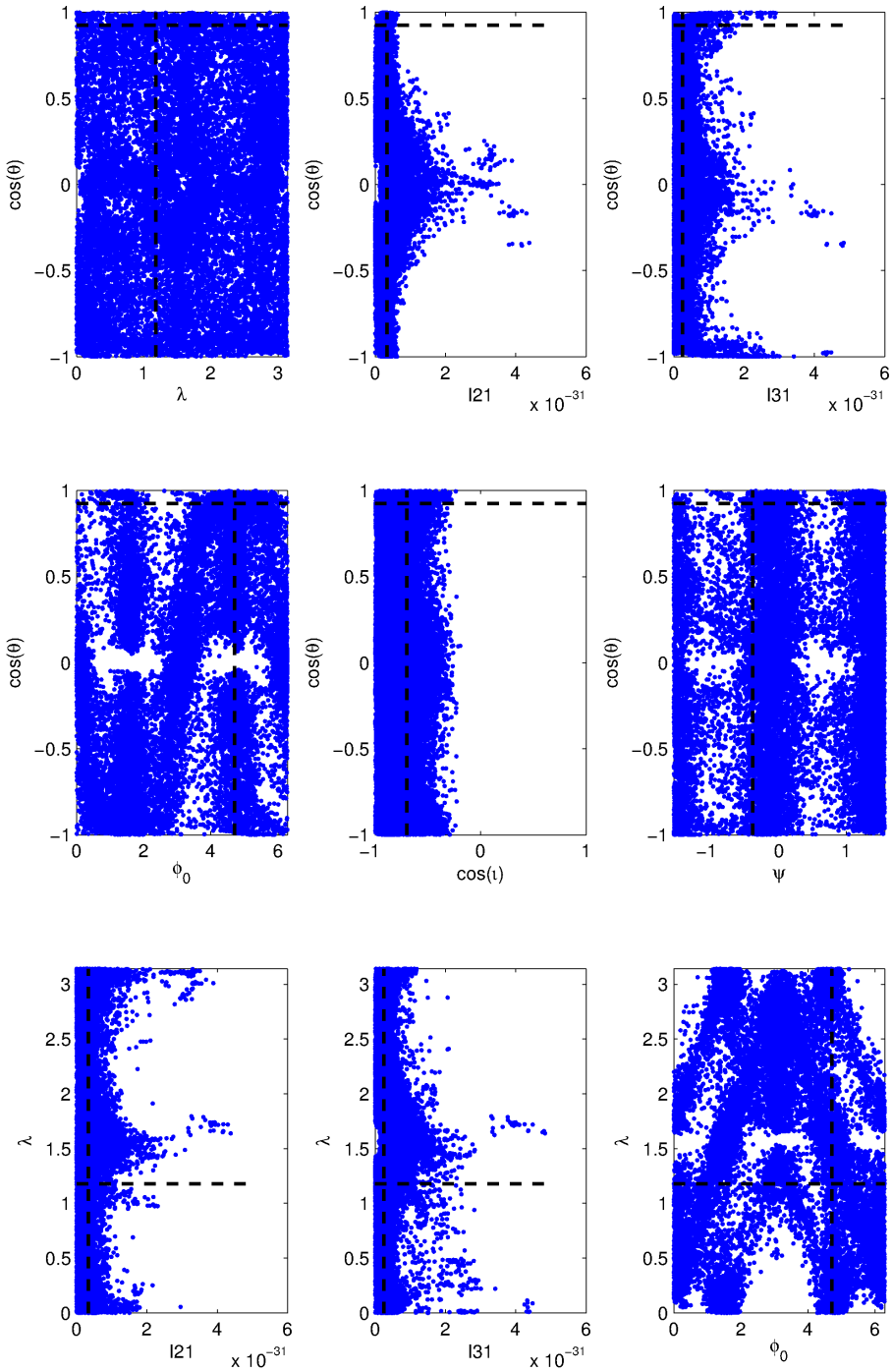

Figure 6.15: The nested samples shown for pairs of parameters, with the injected values for each parameter are shown as dashed black lines. There are some interesting patterns in these plots, particularly the plots for $\cos(\theta)$ vs ϕ_0, and for λ vs ϕ_0.

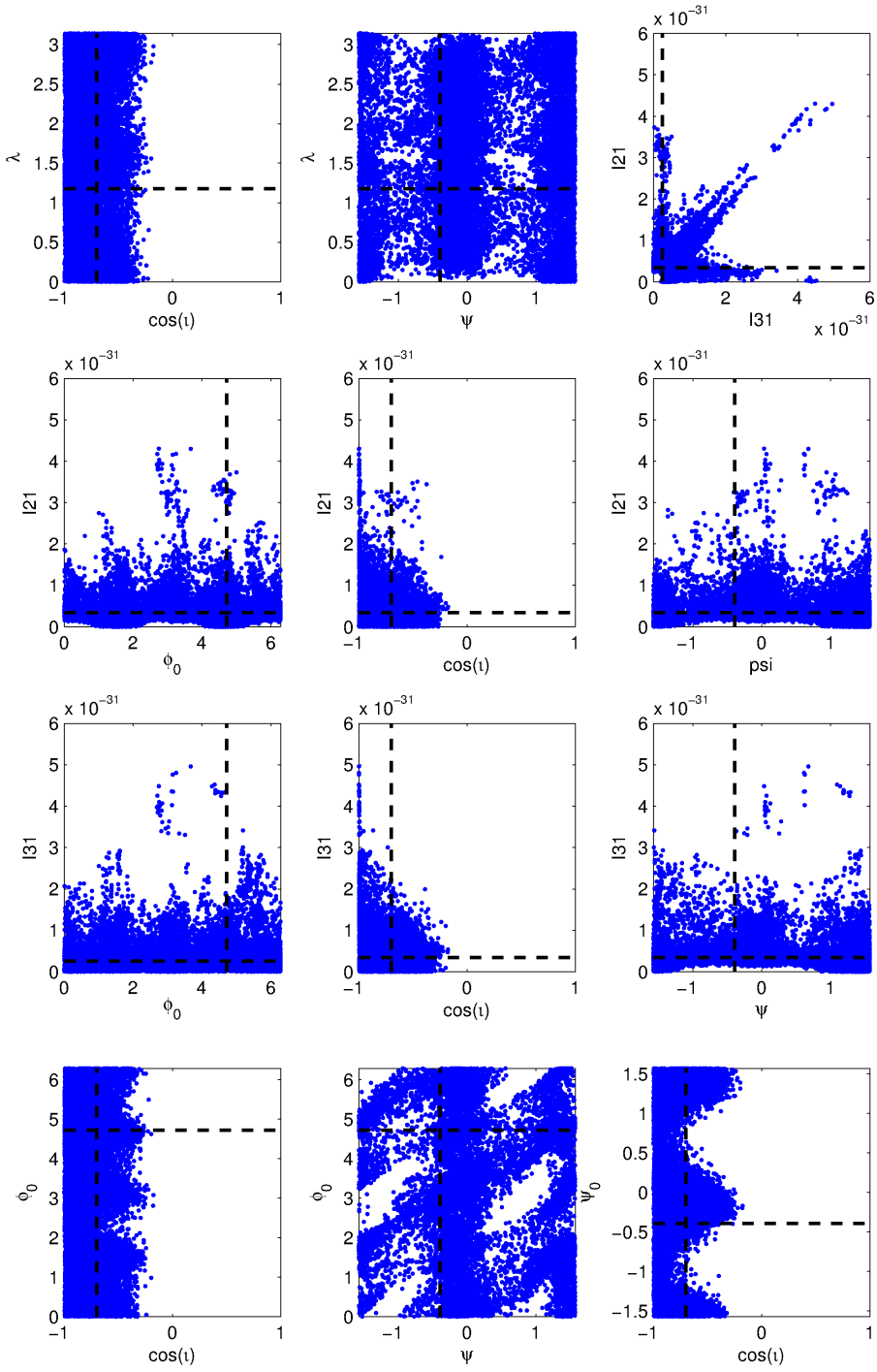

Figure 6.16: The nested samples shown for pairs of parameters, with the injected values for each parameter are shown as dashed black lines. Again there are some clear patterns in these plots.

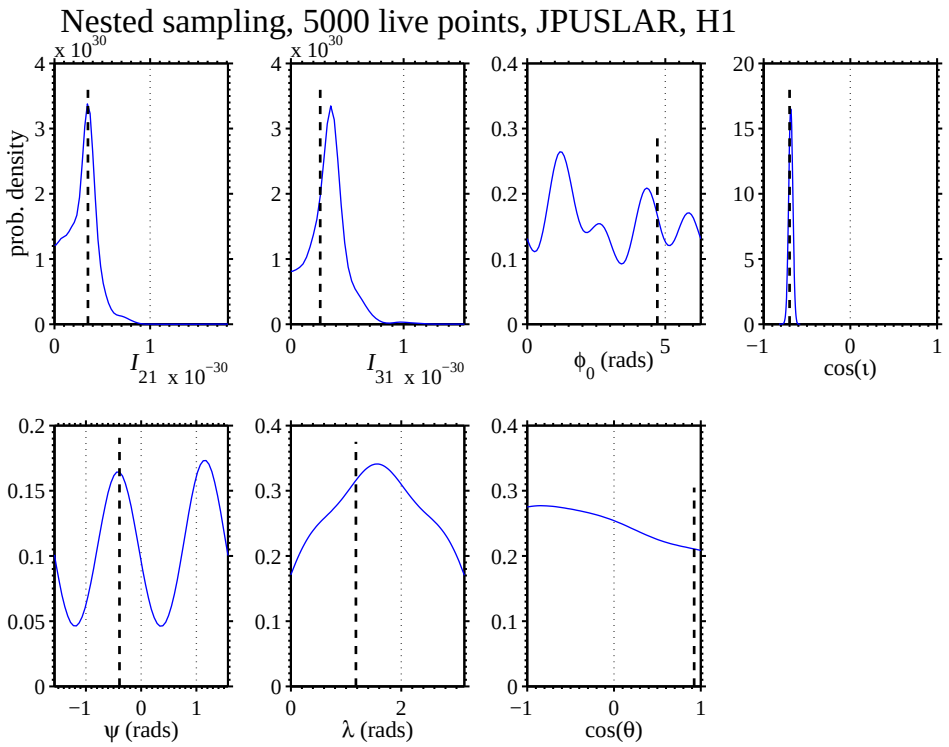

Figure 6.17: The PDFs for a injected pinned superfluid signal into Gaussian noise, with a SNR of 100. The injected values for each parameter are shown as dashed vertical black lines and the PDFs are shown in blue. For such a strong signal these PDFs show a poor recovery of the injected signal, with the exception of the $\cos(\iota)$ parameter - which is recovered well. The I_{21} and I_{31} PDFs also shown strong peaks around the injected values, however both PDFs are non-zero at zero.

to break the degeneracies seen in the previous results. Figures 6.23 and 6.24 show the samples from the nested sampling algorithm. It should be noted that these plots contain significantly fewer samples than those in Figures 6.18 and 6.19. This is because the samples are only drawn from one run of the nested sampling code for Figures 6.23 and 6.24. It is also clear that altering the values of I_{21} and I_{31} has changed the patterns seen in the samples.

From this investigation into the parameter estimation for the pinned superfluid model I can conclude that the model is very flexible, and for any given signal there will be multiple physical configurations of the NS system that could produce a similar, if not identical, signal. Even for signals at exceptionally high SNRs, a scenario very unlikely in GW astronomy, it may not be possible to estimate the true value of some the parameters of the NS system to a reasonable accuracy. This does not mean to say that analysing the data for a pinned superfluid signal is pointless, it is still worth while to consider whether the signal observed is a pinned superfluid signal or not, i.e. is there emission at f_{rot} as well as at $2f_{rot}$. This is taken up in the next section.

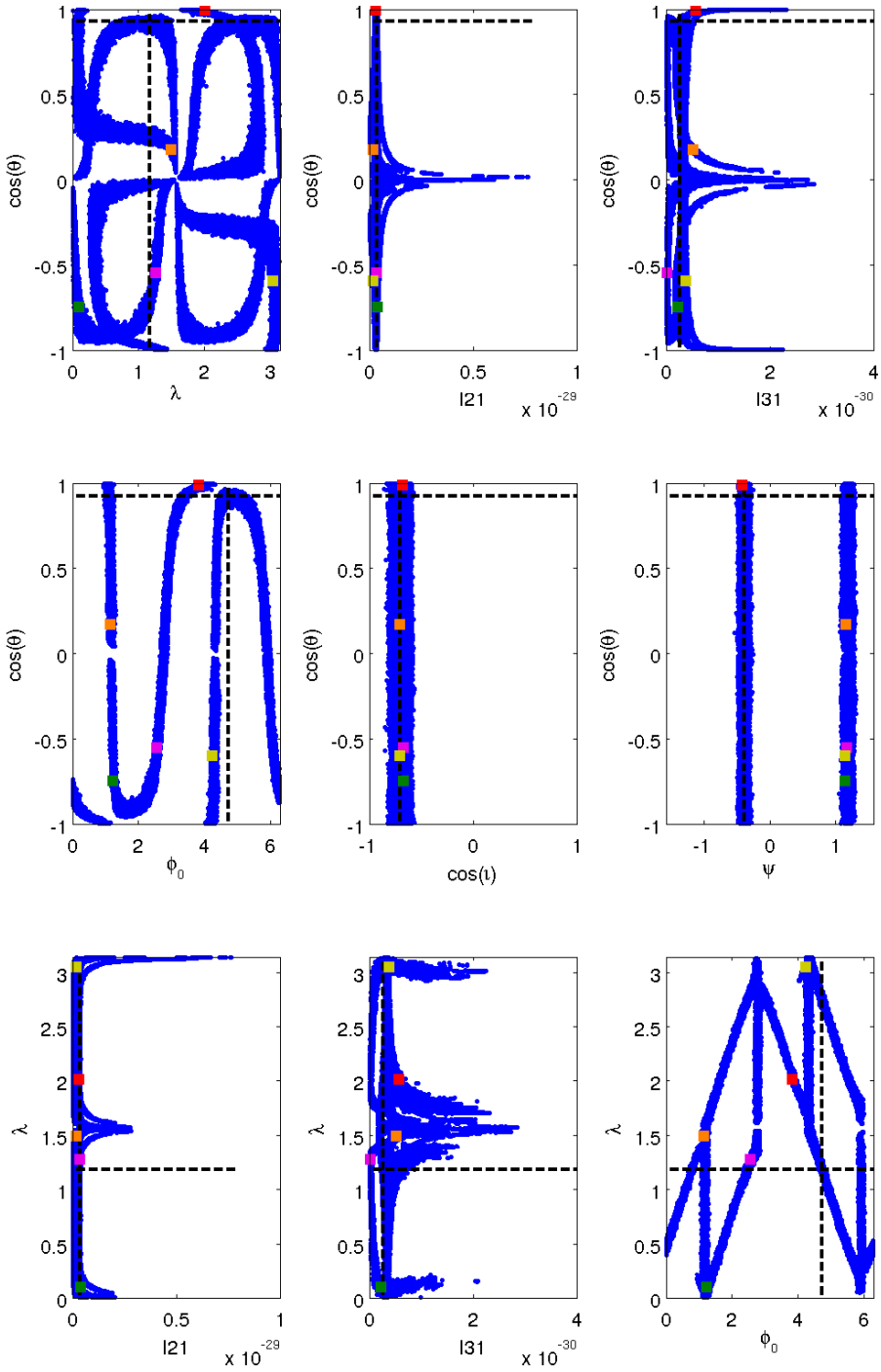

Figure 6.18: The nested samples shown for pairs of parameters from the analysis of a injected signal with SNR = 100. The injected values for each parameter are shown as dashed black lines. The patterns seen in the lower SNR plots of Figure 6.15 and 6.16 have evolved into much tighter, more complex linear patterns with this high SNR example. The coloured squares are randomly chosen points.

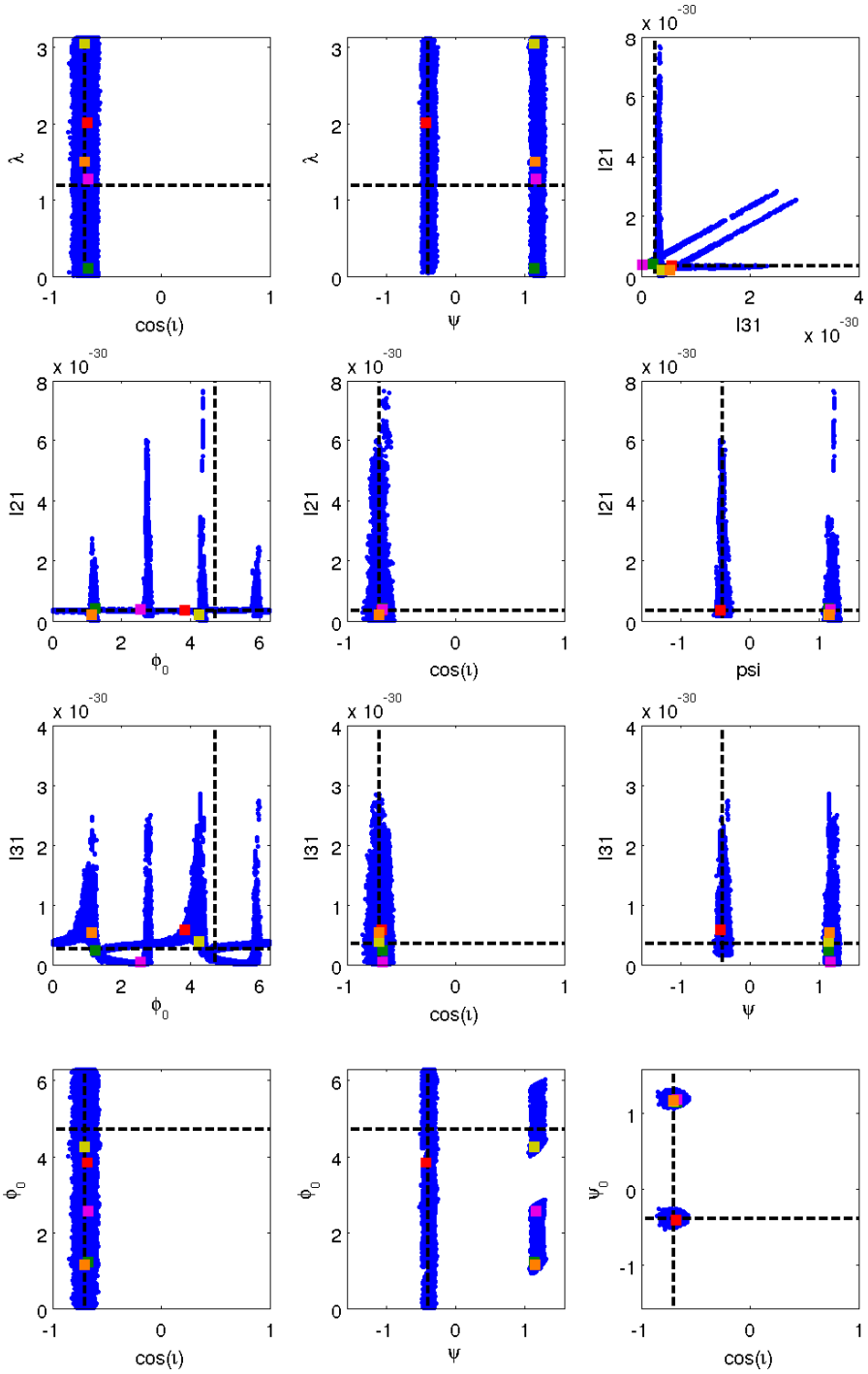

Figure 6.19: The nested samples shown for pairs of parameters for the SNR = 100 injection data, with the injected values for each parameter are shown as dashed black lines. There are many degeneracies in the model parameters, seen in these plots as lines of nested samples. The patterns of these lines are particularly complex. The coloured squares are randomly chosen points.

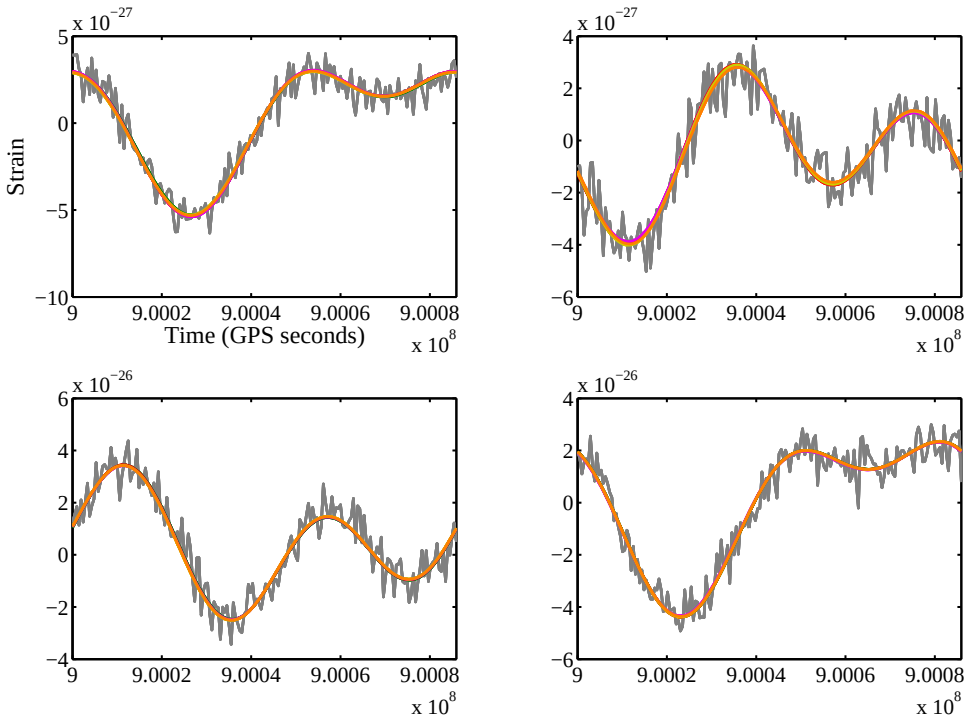

Figure 6.20: A plot showing the SNR = 100 injection data analysed in grey. The signals generated from five randomly selected nested sampling points are also shown for comparison, with the colours matching their corresponding points in Figures 6.18 and 6.18.

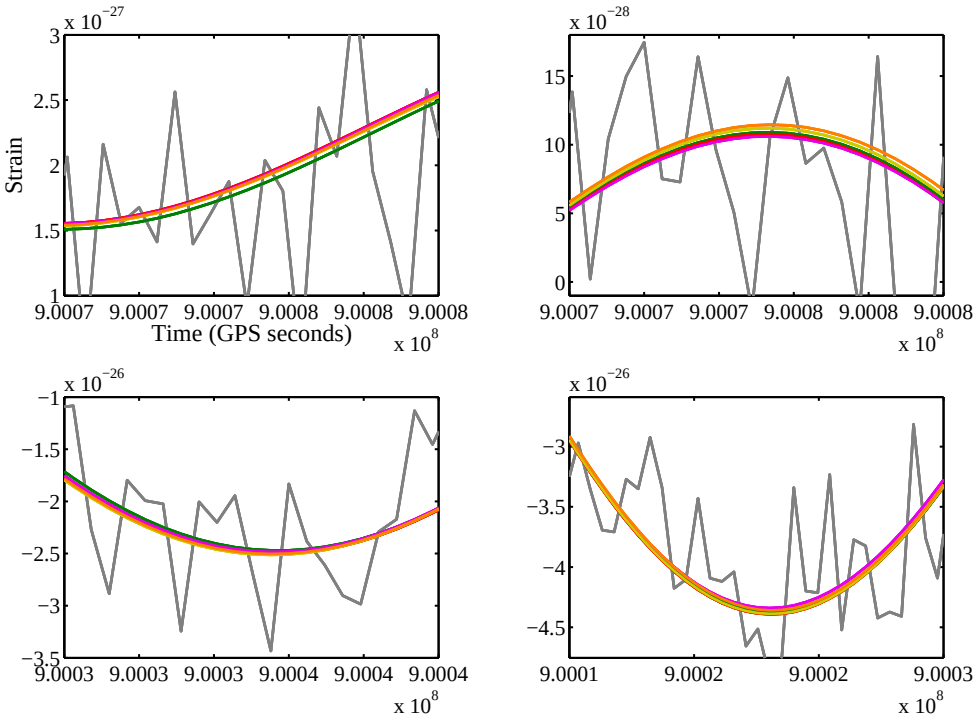

Figure 6.21: A zoomed in view of the Figure 6.20. The SNR = 100 injection data analysed is shown in grey, and the comparison signals are shown in colours matching their corresponding points in Figures 6.18 and 6.18. It is clear that the each of the signals created from the randomly selected points are undistinguishable from each other given the data.

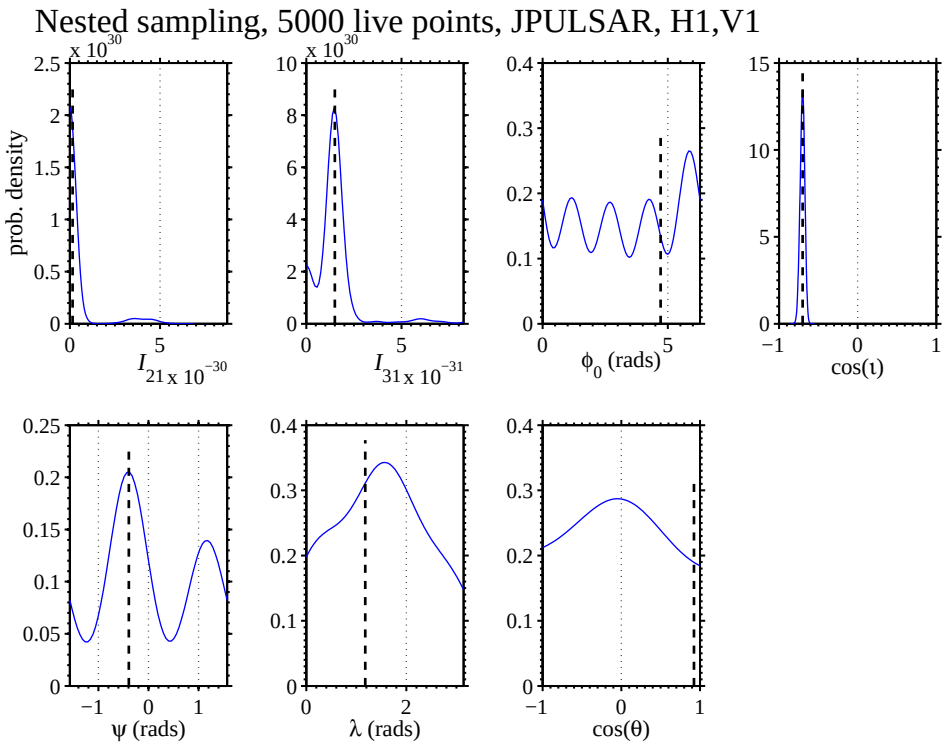

Figure 6.22: The PDFs from pinned superfluid simulation.

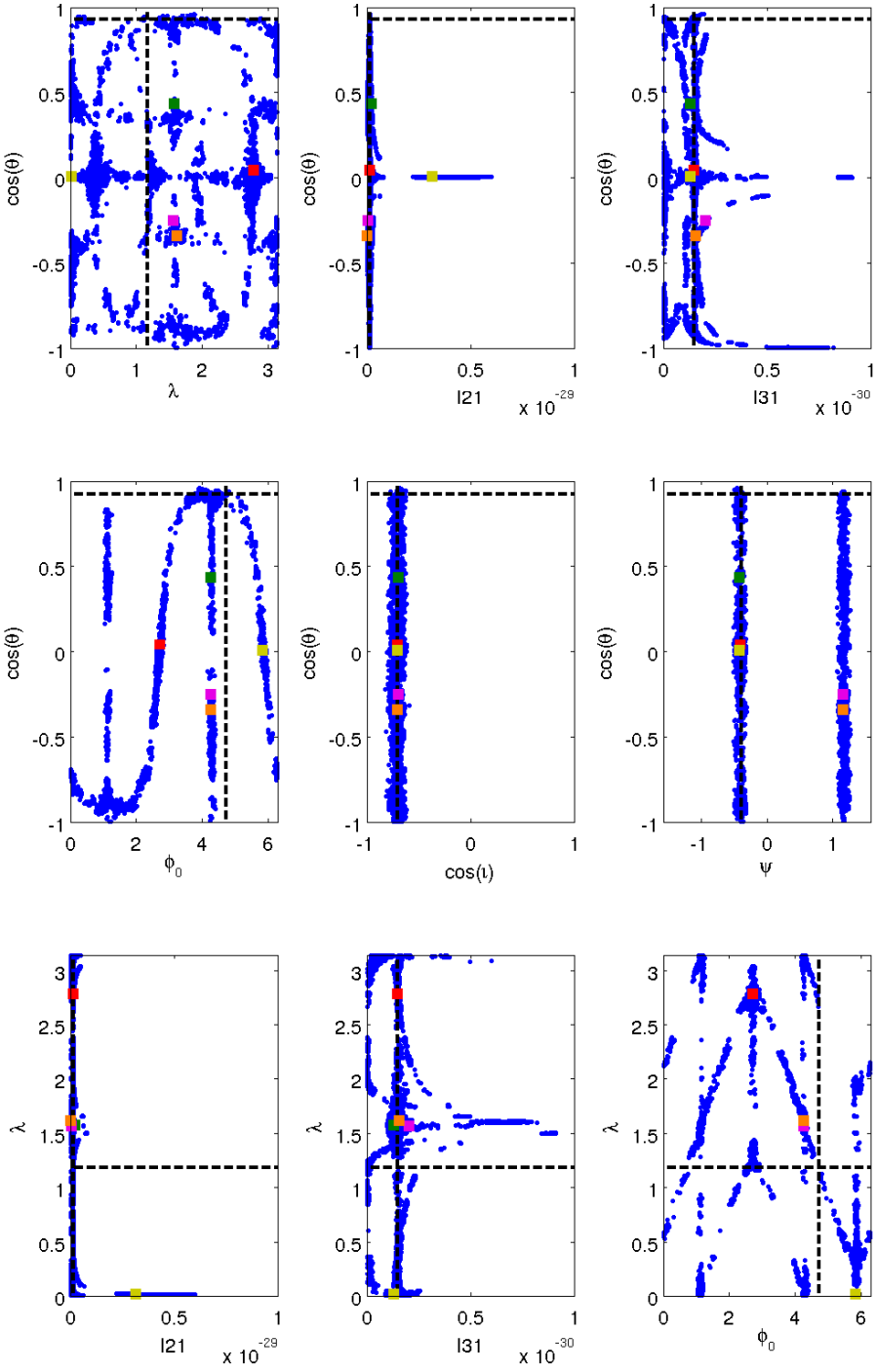

Figure 6.23: The PDFs from pinned superfluid simulation.

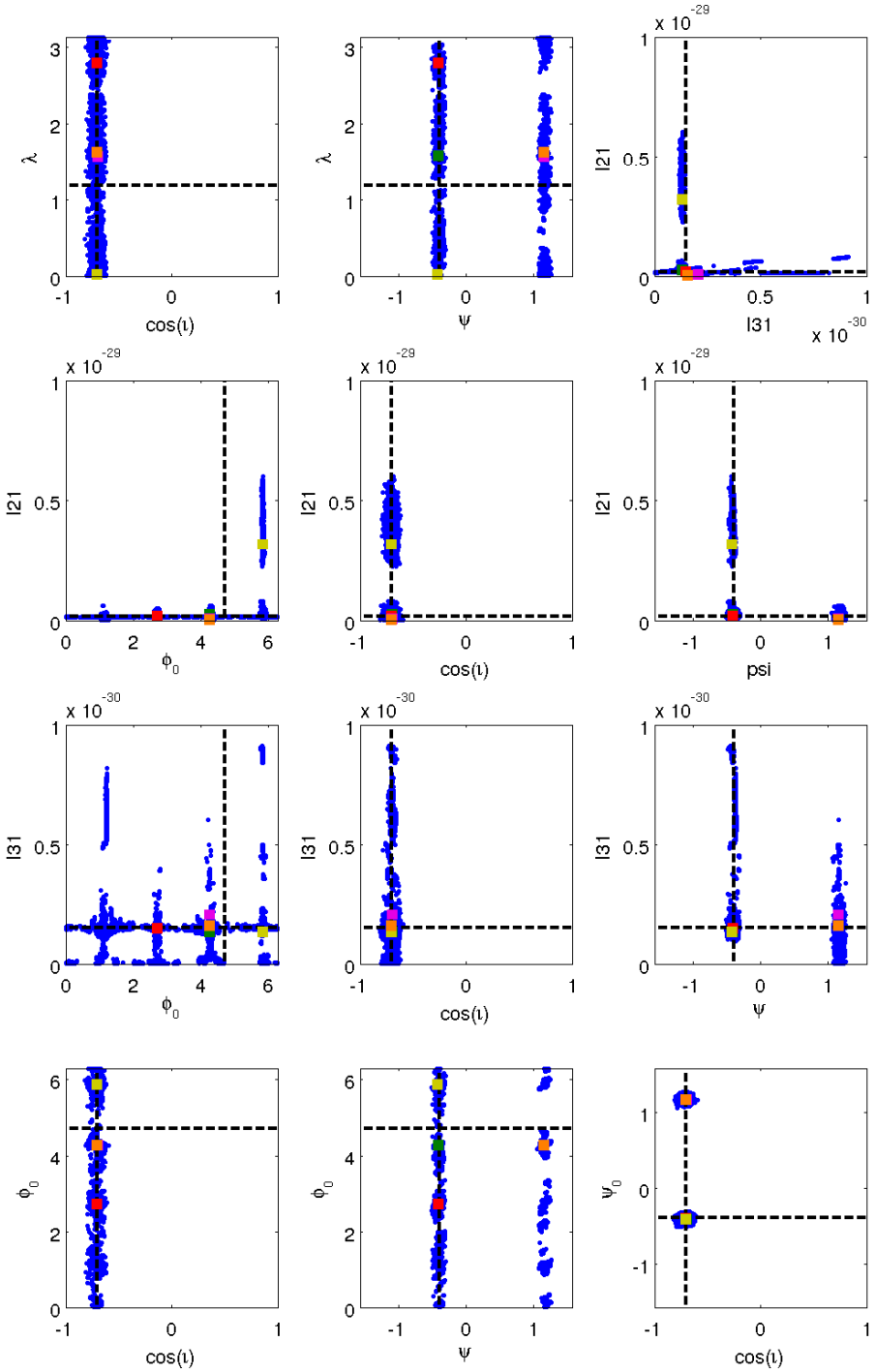

Figure 6.24: The PDFs from pinned superfluid simulation.

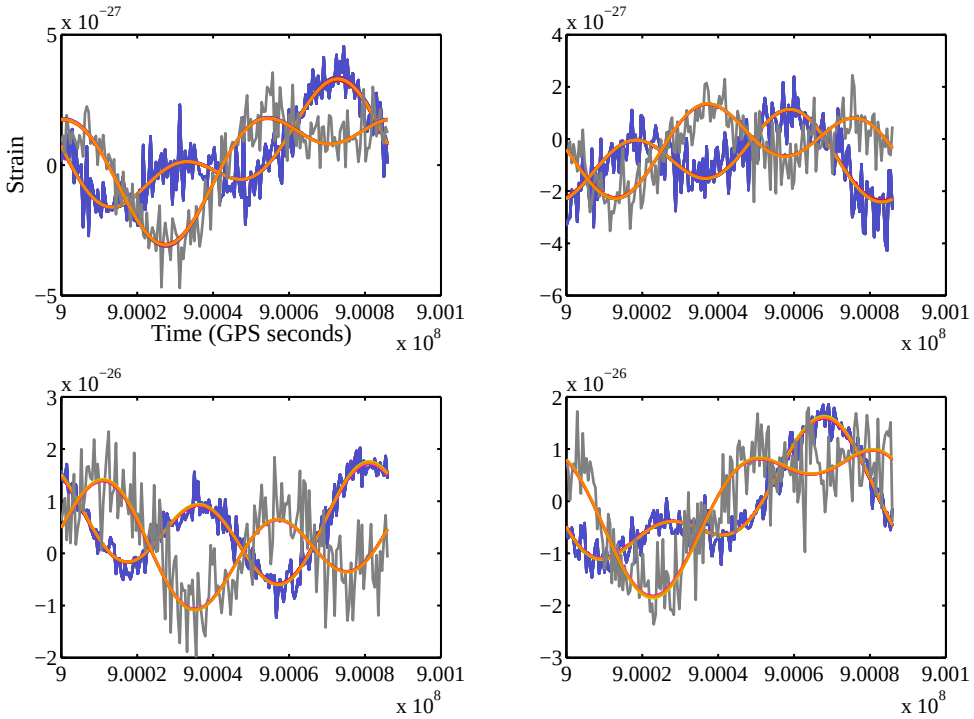

Figure 6.25: A plot showing the injection data analysed in grey for V1, and blue for H1, with the signals generated from five nested sampling points.

6.4.5 Evidence calculation and model selection

Another important aspect of using the nested sampling code to analyse GW data for a CW pulsar signal is its ability to compute the evidence of particular signal models. The computation of the Bayesian evidence allows the construction of odds ratios which can be used for model selection, i.e. to determine which of the competing models is more likely given the data and the priors. Not only is it interesting to compare the evidence for the pinned superfluid model against Gaussian noise, but also to compare its evidence against the evidence for the triaxial model given the same data. If the simple test case analogy is an accurate guide then I would expect the odds ratio of the pinned superfluid evidence over the Gaussian noise evidence to favour the pinned superfluid model as soon as the signal reaches a critical SNR. Similarly I would expect the evidence for the pinned superfluid model to outweigh the evidence of the triaxial model when the signal at f_{rot} reaches a critical SNR where the Gaussian noise model fails to describe the data at f_{rot} well.

The first set of tests I ran used the Crab pulsar as a target, I created simulated data containing a signal from the Crab pulsar with model parameters chosen by me. The data was created using the S5 LIGO H1 noise curve, so the noise at f_{rot} is about 1000 times stronger than the noise at $2f_{rot}$. The first set of data was created using a signal where the pinned superfluid parameter $\theta = 0$, which is directly equivalent to the triaxial case. Within this set of data different signals were created with different amplitudes based on different equatorial ellipticities. The I_{21} parameter is derived directly from the equatorial ellipticity parameter, and the I_{31} parameter is set as $10I_{21}$. The results from this first set of runs is shown in Figure 6.26, where the log of the odds ratios are shown for the pinned superfluid model vs Gaussian noise, the triaxial model vs Gaussian noise, and the pinned superfluid model vs the triaxial model. Each data-point is the average of 10 runs where the data is created using different realisations of random Gaussian noise. Both the triaxial and pinned superfluid vs Gaussian noise odds ratios initially favour the Gaussian noise model, until a critical SNR is reached at ellipticity 0.004, and from ellipticities greater than this both signal models are favoured over the Gaussian noise model. For all ellipticities for this plot the triaxial model is favoured over the pinned superfluid model. This is because both models describe the signal equally well - remember that the triaxial model is contained in the pinned superfluid model, but the added complexity and prior volume of the pinned superfluid model is penalised by the Ockham factor and hence the triaxial model is always favoured. In Figures 6.27 and 6.28, the same information is shown but with $\theta = \pi/4$ for the data analysed for the former, and $\theta = \pi/2$ for the data analysed for the latter, for this set of parameters the emission at f_{rot} gets stronger relative to the emission at $2f_{rot}$ from $\theta = 0 \rightarrow \pi/2$.

Figure 6.27 is much the same as Figure 6.26, as the SNR at f_{rot} is very small and this data-stream appears consistent with Gaussian noise. This means that both models describe the signal equally well, and hence the odds ratio is determined by the Ockham factor. This situation persists for all but the ellipticity of 0.064 for the case where $\theta = \pi/2$ shown in Figure 6.28. The SNRs of the signals for this case where the pinned superfluid signal is favoured over the triaxial signal at f_{rot} and $2f_{rot}$ are approximately 7×10^{-2} and 1×10^{2} respectively. This suggests that the signal at f_{rot} is still too weak to be seen, and therefore that the pinned superfluid model is favoured as it describes the signal $2f_{rot}$ better. This is supported by the fact that the triaxial odds ratio increases from an ellipticity of 0.032 to 0.064. If the data at f_{rot} were inconsistent with Gaussian noise then I would expect the evidence for the triaxial case to drop. Although it may simply be the case that a rise in the evidence for the triaxial model at $2f_{rot}$ is greater than the drop in the evidence at f_{rot}.

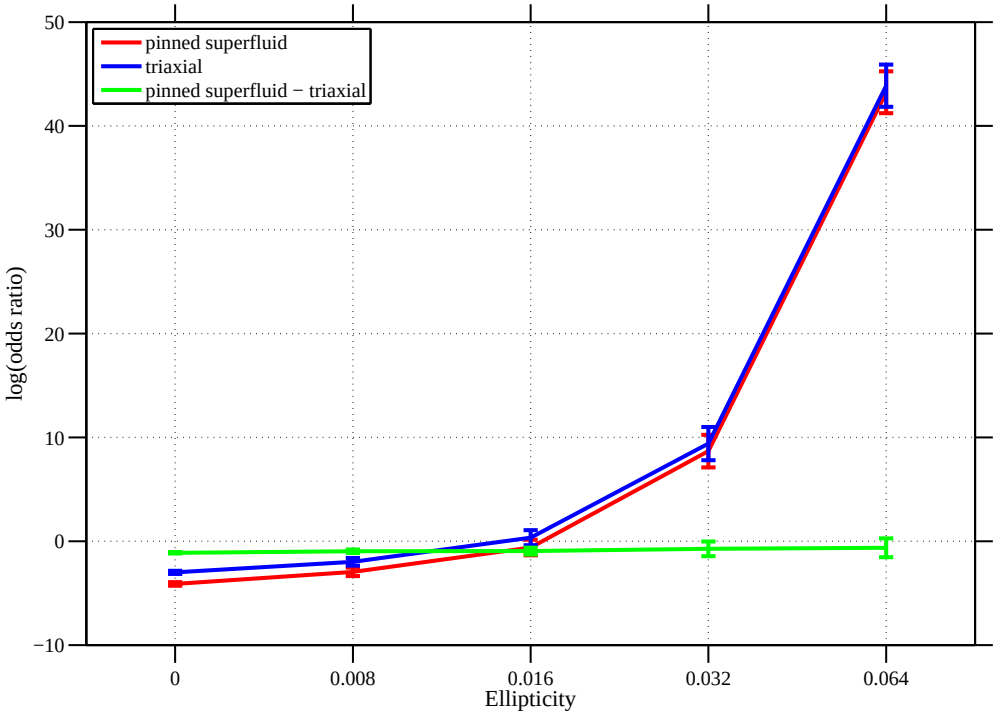

Figure 6.26: A plot of the odds ratio for the pinned superfluid model over the Gaussian noise model for data containing an injected pinned superfluid signal for a range of ellipticities. For these runs f_{rot} 29.75 Hz, and the noise at $2f_{rot}$ is about 1000 times less than the noise at f_{rot}, and the value for the model parameter θ was set to zero.

I then ran the same tests but for pulsars with different f_{rot}, and hence where the noise at f_{rot} and $2f_{rot}$ have different relative strengths. One set of runs was for

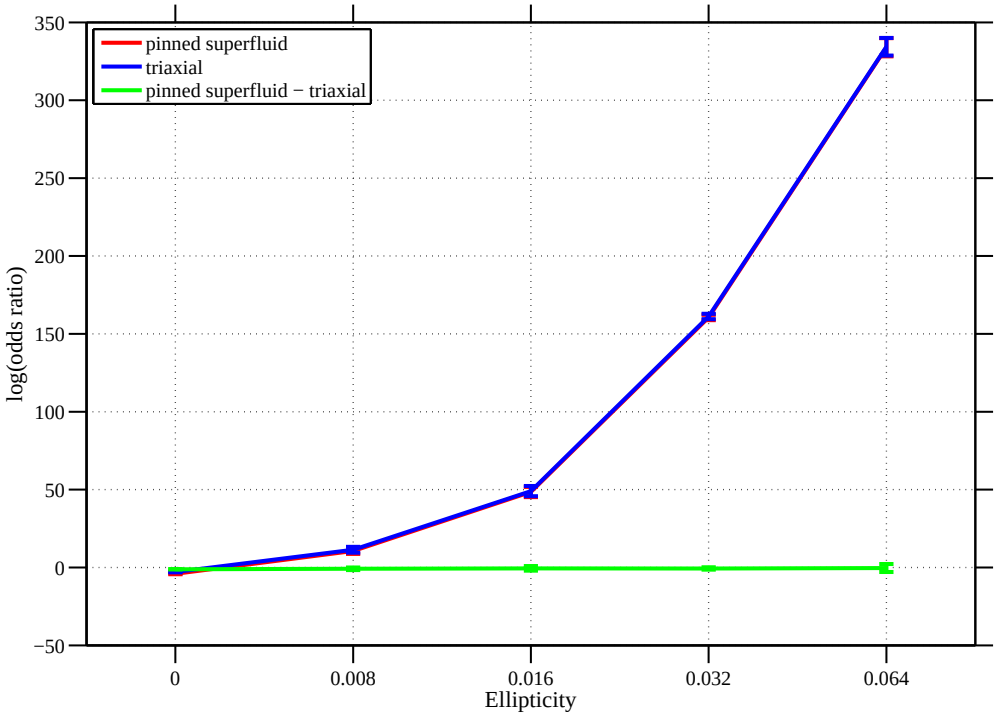

Figure 6.27: A plot of the odds ratio for the pinned superfluid model over the Gaussian noise model for data containing an injected pinned superfluid signal for a range of ellipticities. For these runs the noise at $2f_{rot}$ is about 1000 times less than the noise at f_{rot}, and the value for the model parameter θ was set to $\pi/4$.

pulsar J1804-2717, for which $f_{rot} = 110\,\text{Hz}$, so it is sitting right in the most sensitive frequencies for the LIGO detectors. At this frequency the noise at f_{rot} and $2f_{rot}$ are roughly equal. The results from this set of runs is shown in Figures 6.29 to 6.31. The pinned superfluid model is seen to be favoured from ellipticities above 0.0004 in the tests where $\theta = \pi/4$ with the noise floor lower and roughly even for both data-streams. Again the evidence for the triaxial model does not decrease, but the SNR at f_{rot} for an ellipticity of 0.0004 is approximately 10. This suggests that the fact the pinned superfluid model is favoured over the triaxial model is due to the signal being visible in the f_{rot} data-stream. For the $\theta = \pi/2$ case, the pinned superfluid is only favoured for an ellipticity of 0.0064, however at this ellipticity the odds ratio of the triaxial case vs Gaussian noise shows a marked drop when compared with the odds ratio for the ellipticity of 0.0016. This marked drop is due to the reduction in evidence at f_{rot}, as this data-stream appears very unlike only Gaussian noise.

The final set of runs simulates the case where the noise at f_{rot} is less than the noise at $2f_{rot}$, the pulsar that I chose for this set of runs was J1843-1113, which has $f_{rot} = 541\,\text{Hz}$. The results for these runs are shown in Figures 6.32 to 6.34. The case where $\theta = 0$ again shows that the triaxial model is always favoured over

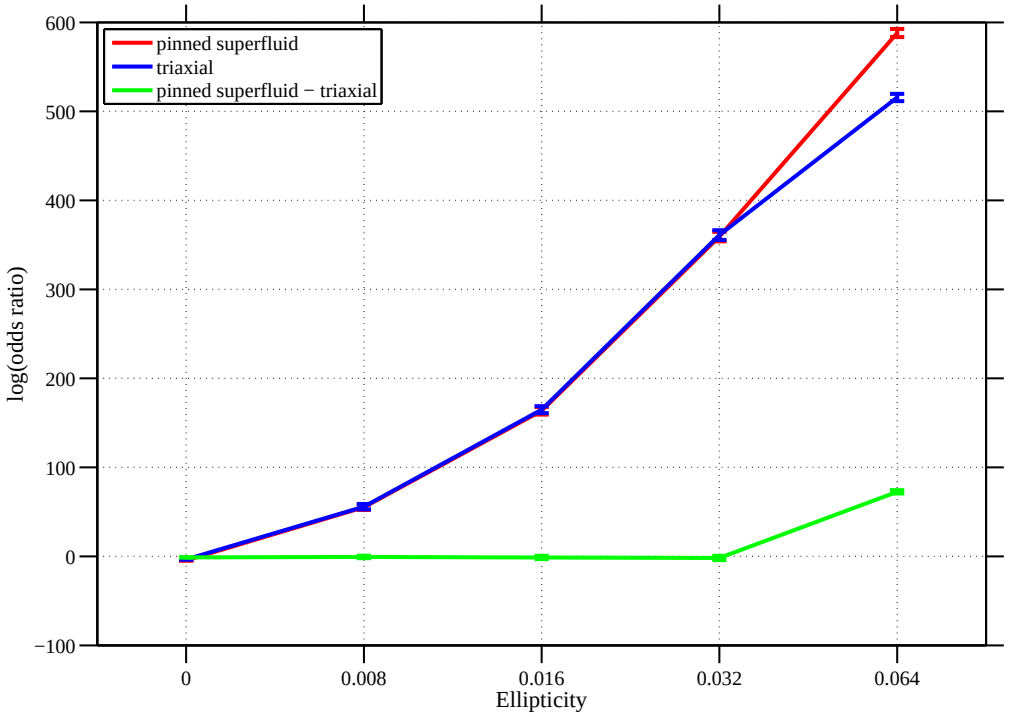

Figure 6.28: A plot of the odds ratio for the pinned superfluid model over the Gaussian noise model for data containing an injected pinned superfluid signal for a range of ellipticities. For these runs the noise at $2f_{rot}$ isabout 1000 times less than the noise at f_{rot}, and the value for the model parameter θ was set to $\pi/2$.

the pinned superfluid model, as expected. The noise at f_{rot} is now lower than the noise at $2f_{rot}$, at about 25 % of the noise at at $2f_{rot}$. For this set of tests the pinned superfluid model can be seen to be favoured over the triaxial model for the majority of ellipticities for both the $\theta = \pi/4$ and the $\theta = \pi/2$ cases. This shows that for a weaker signal, the f_{rot} signal shows above the noise sooner, and hence the model selection favours the pinned superfluid model. The reduction in the triaxial vs Gaussian noise odds ratio is seen in the $\theta = \pi/4$ case, and at lower ellipticities in the $\theta = \pi/2$ case. It is in this scenario that a search for a pinned superfluid signal is most likely to be able to add some certainty to a detection.

6.4.6 Conclusions and future work

The posterior for the pinned superfluid model is inherently complex owing to the large number of model parameters and therefore the flexibility of the model, this inhibits successful parameter estimation. Analysing the f_{rot} data stream can have some benefit for the detectability of a signal, particularly where the noise at f_{rot} is lower than the noise at $2f_{rot}$. The basic maxim derived from these odds ratio tests replicates the result from the simple test case analogy, in that when the f_{rot} SNR

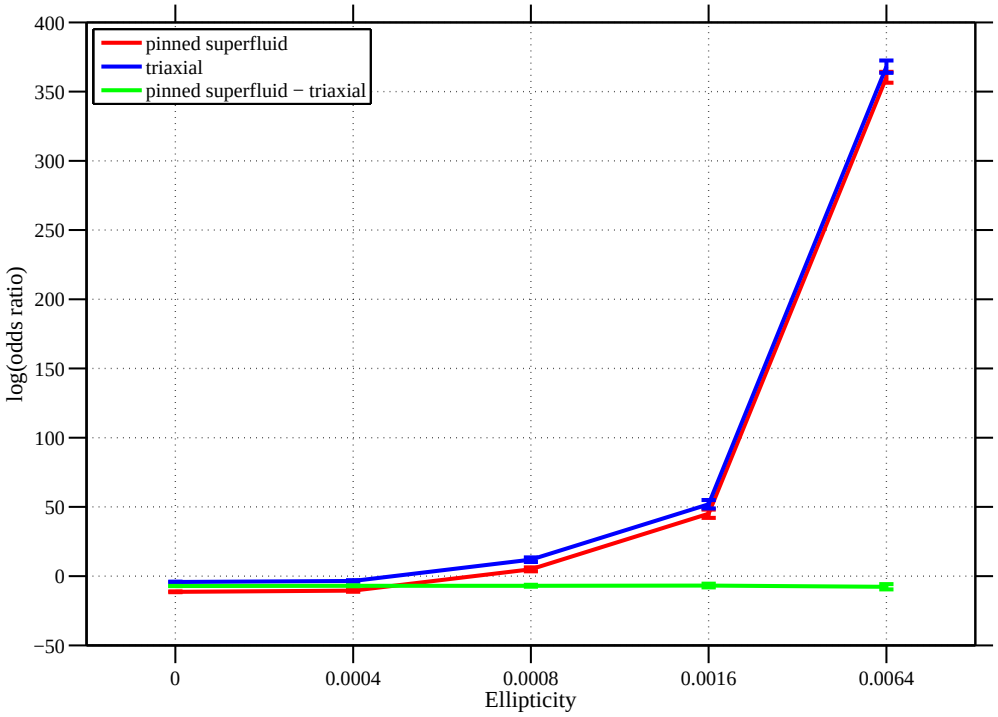

Figure 6.29: A plot of the odds ratio for the pinned superfluid model over the Gaussian noise model for data containing an injected pinned superfluid signal for a range of ellipticities. For these runs $f_{rot} = 110\,\mathrm{Hz}$, so the noise at $2f_{rot}$ is approximately equal to the noise at f_{rot}, and the value for the model parameter θ was set to zero.

passes a critical threshold the evidence for the model predicting only $2f_{rot}$ emission drops and the odds ratio starts to favour the model containing emission at f_{rot} and $2f_{rot}$. However it is important to remember that the odds ratio tests were carried out with $I_{31} = 10\,I_{21}$, more investigation into plausible ranges for these two parameters should be carried out.

6.5 Searching for the pinned superfluid signal in real data

After the initial testing of the nested sampling code to search for GWs from the pinned superfluid emission mechanism that is described above in §6.4, the next step was to use the code to search for GWs in real data. For this initial test using real data the Virgo VSR4 data was analysed for GWs from the Crab pulsar. The rotation frequency of the crab pulsar and the noise curve of VSR4 provided a suitable test as the data from Virgo is calibrated and remains of reasonable sensitivity at f_{rot} for the Crab. The data was processed using the complex heterodyne method to produce two datasets, one at f_{rot} and one at $2f_{rot}$, which were then analysed using the nested

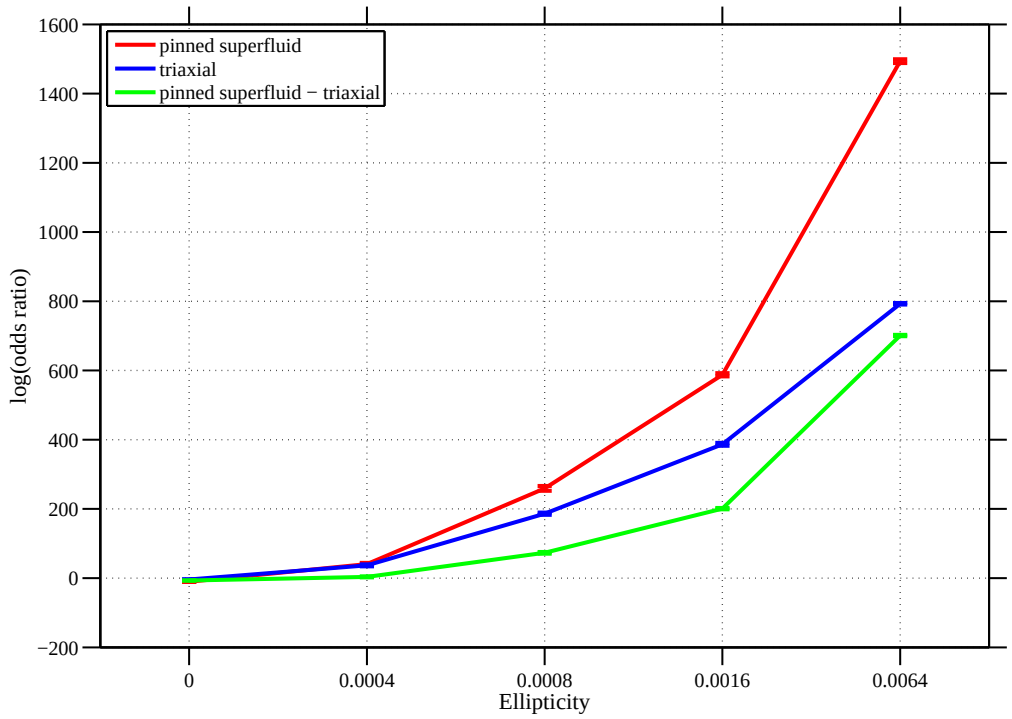

Figure 6.30: A plot of the odds ratio for the pinned superfluid model over the Gaussian noise model for data containing an injected pinned superfluid signal for a range of ellipticities. For these runs $f_{rot} = 110\,\mathrm{Hz}$, so the noise at $2f_{rot}$ is approximately equal to the noise at f_{rot}, and the value for the model parameter θ was set to $\pi/4$.

sampling code. The heterodyned data is shown in Figures 6.35 and 6.36.

The log of the odds ratio for the pinned superfluid model over the model that the data consists only on Gaussian noise, as computed by the nested sampling run, is -7.5. This tells us that the most likely model, given the data and our prior assumptions, is that the data consists only of Gaussian noise, i.e. there is no detectable GW signal present. The PDFs from this analysis are shown in Figure 6.37 and these are consistent with there being no detectable pinned superfluid GW signal in the data. With the use of the nested sampling algorithm and its ability to compute the Bayesian evidence, the PDFs are no longer the main tool for determining whether a GW signal is present or not - they are included here as supporting material. It should also be noted that this is the first run of the nested sampling code to look for a pinned superfluid signal in real data, whilst this result is consistent with expectation, more testing will be needed before this result can be completely trusted.

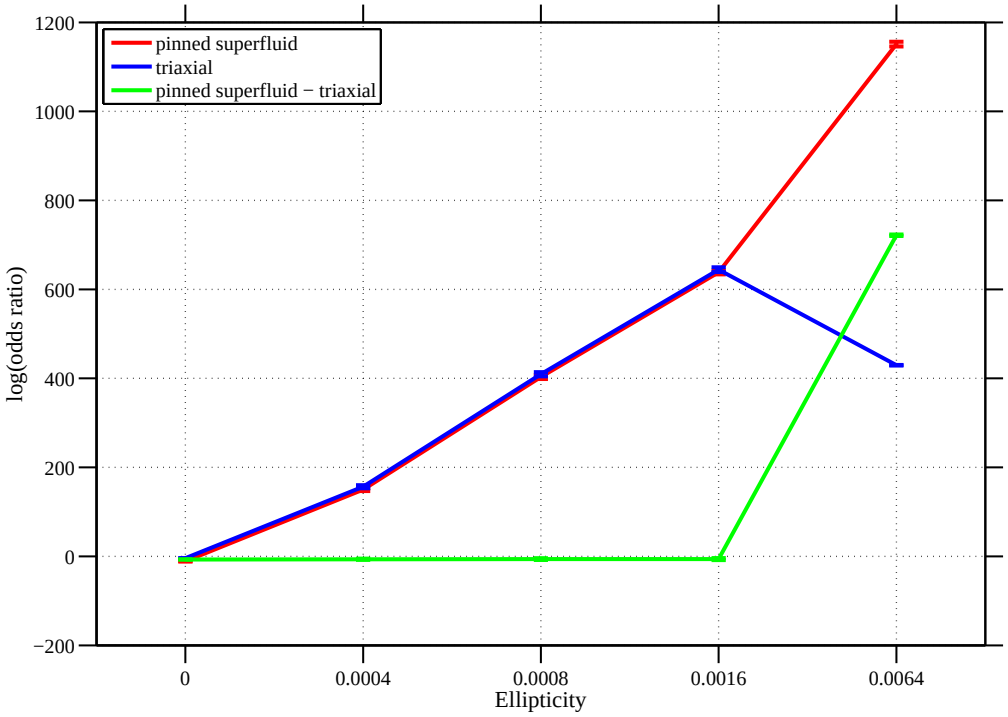

Figure 6.31: A plot of the odds ratio for the pinned superfluid model over the Gaussian noise model for data containing an injected pinned superfluid signal for a range of ellipticities. For these runs $f_{rot} = 110\,\mathrm{Hz}$, so the noise at $2f_{rot}$ is approximately equal to the noise at f_{rot}, and the value for the model parameter θ was set to $\pi/2$.

6.6 Is the noise really Gaussian?

The parameter estimation process used to obtain the results described in this chapter and the three previous uses a likelihood function which assumes that the noise in the data analysed is Gaussian. Whether this is actually the case or not could be argued irrelevant if it remains the best description of the noise we can contrive. However, there is an equally valid argument, that in our model selection, we are comparing a signal model with a Gaussian noise model, and that this will favour the signal model if the noise does not look Gaussian even where no signal is present. The conclusion to these arguments is not considered here, but instead we take a look at the noise from a number of analyses, and compare this noise to Gaussian distributions, as a means of demonstrating how well the Gaussian model describes the reality. The data I have used for this purpose is taken from the S6 for the H1 detector, a full examination of this problem would of course consider data from all the detectors used in the previous analyses presented in this thesis. The heterodyned data was produced for five pulsars using the ephemerides that were used for the S5 search and to perform the searches presented in Chapter 5. There are a number of ways in which the data can be tested in order to determine if it is Gaussian. I adopt

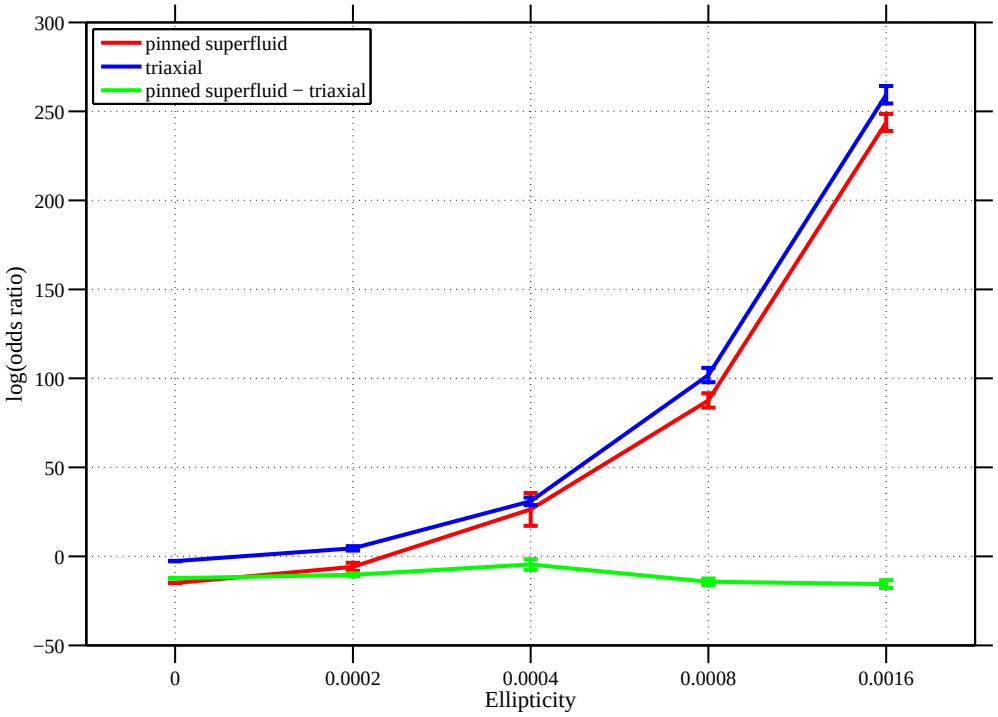

Figure 6.32: A plot of the odds ratio for the pinned superfluid model over the Gaussian noise model for data containing an injected pinned superfluid signal for a range of ellipticities. For these runs the noise at f_{rot} is approximately 25 % of the noise at f_{rot}, and the value for the model parameter θ was set to zero.

a simplistic approach of plotting a histogram of the real and imaginary data, and plotting a Gaussian curve on top of the histogram. The standard deviation used for the Gaussian curve is simply that obtained from the data using the matlab "std" routine which uses equation 6.32. The results can be seen in Figures 6.38 to 6.42. In general the data can be seen to fit the Gaussian curves very well, with a slightly stronger peak around zero than the Gaussian curve. This stronger peak feature is most noticeable for psr J2145-0750. The reason for this is not clear, although there is a strong noise line that shows up in Fscans at ~ 120 Hz that could be contributing to the noise in the heterodyned data which is also at ~ 120 Hz.

$$s = \left(\frac{1}{n-1} \sum_{i=1}^{m} (x_i - \bar{x})^2 \right)^{\frac{1}{2}} \tag{6.32}$$

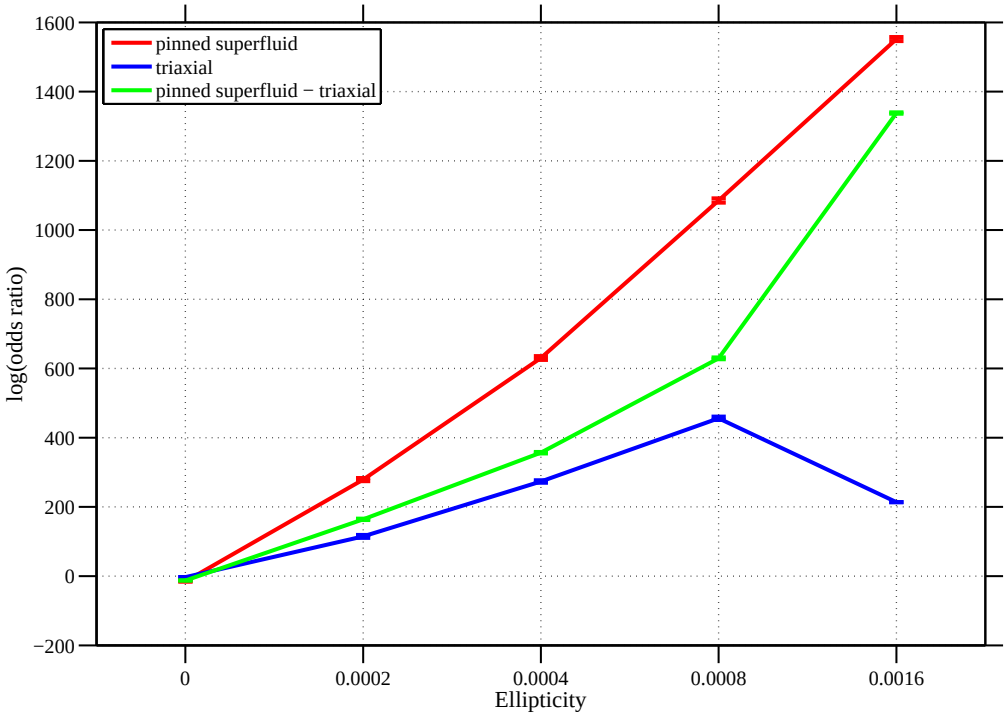

Figure 6.33: A plot of the odds ratio for the pinned superfluid model over the Gaussian noise model for data containing an injected pinned superfluid signal for a range of ellipticities. For these runs the noise at f_{rot} is approximately 25 % of the noise at f_{rot}, and the value for the model parameter θ was set to $\pi/4$.

6.7 Summary

In this chapter I have presented extensions to the approach of searching for GWs from pulsars that has been presented in previous chapters, namely using the complex heterodyne and a Bayesian parameter estimation MCMC to perform searches for signals described by the triaxial NS model. The first extension to this approach was to use a nested sampling code to analyse the heterodyned data. The nested sampling code calculates the Bayesian evidence for the data containing a GW signal described by the triaxial model and for the data consisting only of Gaussian noise, whilst its output can also be used to construct PDFs for parameter estimation. The second extension to the approach for searching for GWs from pulsars was to search for a signal produced by different mechanism to those previously considered, this being the pinned superfluid model of Jones (2010). This model bears some similarity to that of a precessing NS in that there is emission both at f_{rot} and $2f_{rot}$, where the triaxial NS model only produces GWs at $2f_{rot}$. I have presented results from parameter estimation runs on simulated data both in the low SNR regime and for a very high SNR, and have shown that it is not possible to constrain some of the model parameters, even for very high SNR signals. Despite this, analysing data

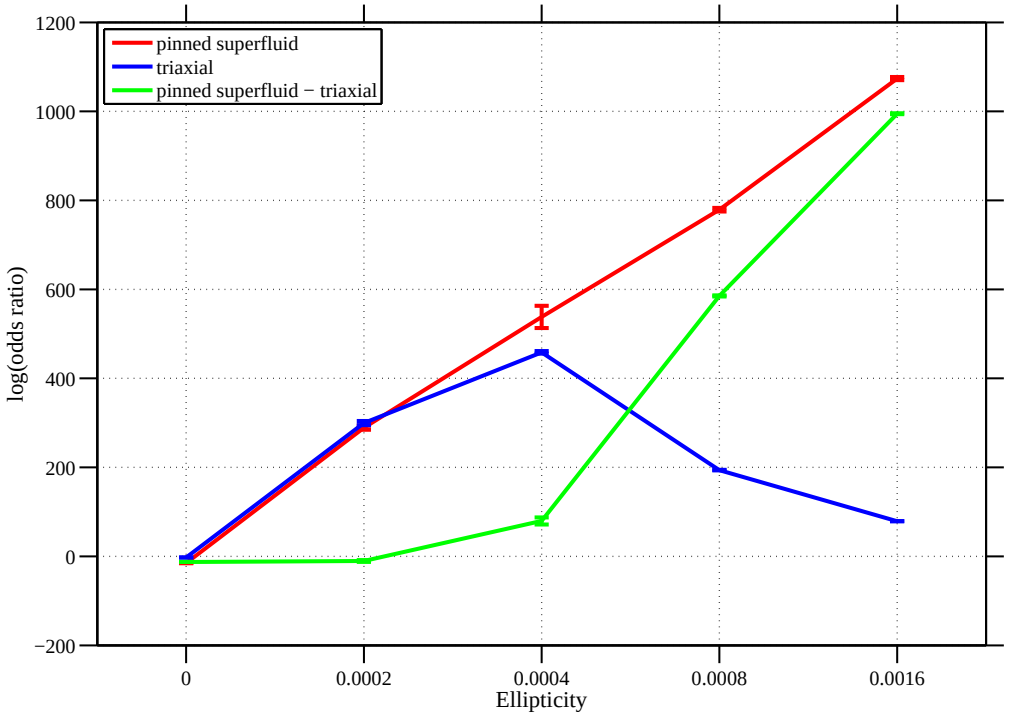

Figure 6.34: A plot of the odds ratio for the pinned superfluid model over the Gaussian noise model for data containing an injected pinned superfluid signal for a range of ellipticities. For these runs the noise at f_{rot} is approximately 25 % of the noise at f_{rot}, and the value for the model parameter θ was set to $\pi/2$.

for a pinned superfluid GW signal with the nested sampling code could be useful for certain sources given the relative strengths of the noise at f_{rot} and $2f_{rot}$. By examining the Bayesian evidence it is possible, given certain configurations of the NS, to determine whether the source is a pinned superfluid emitter or a triaxial emitter. Indeed, in certain cases performing the nested sampling analysis for a pinned superfluid signal may enable the evidence of a signal to surpass a detection threshold that would not be passed if the analysis is only performed for a triaxial signal.

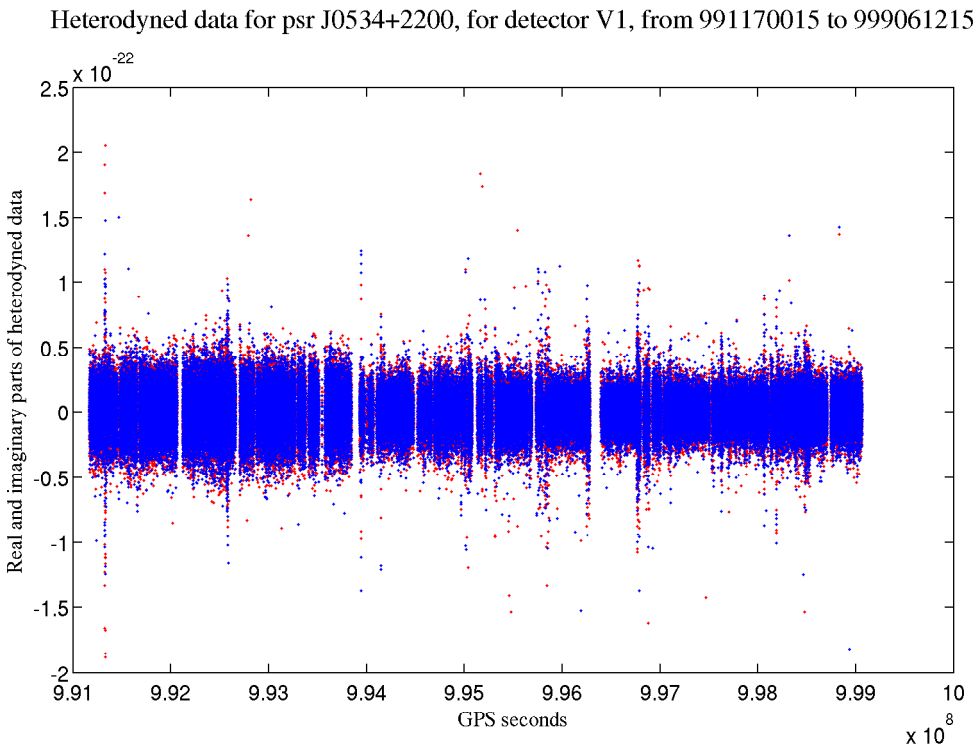

Figure 6.35: The heterodyned data for the Crab pulsar in VSR4, the data shown here is at f_{rot}.

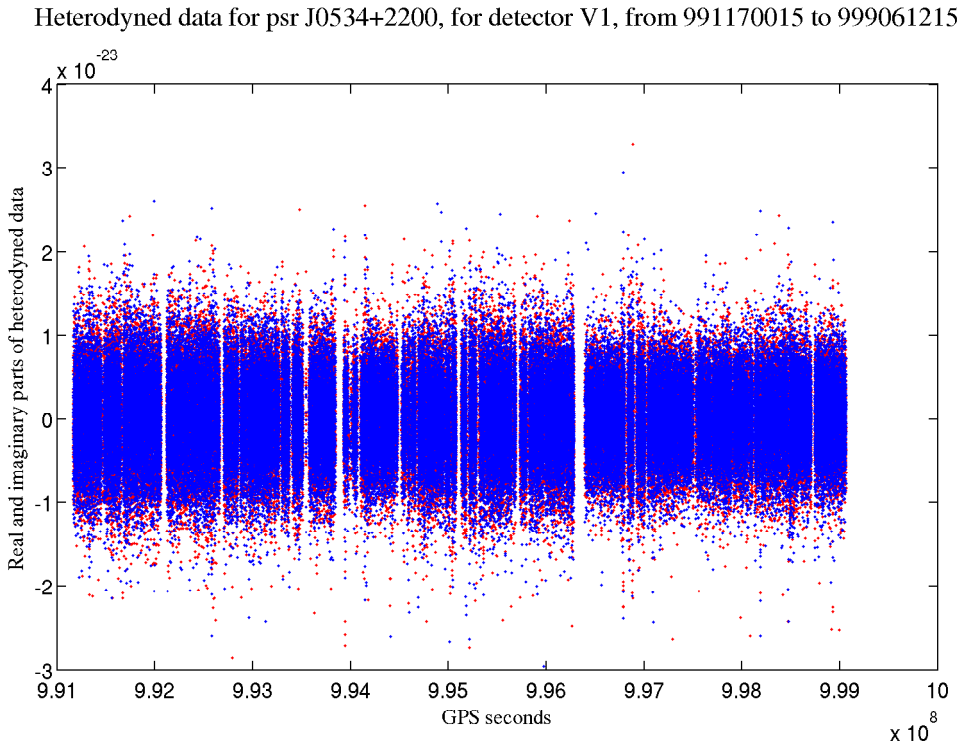

Figure 6.36: The heterodyned data for the Crab pulsar in VSR4, the data shown here is at $2f_{rot}$.

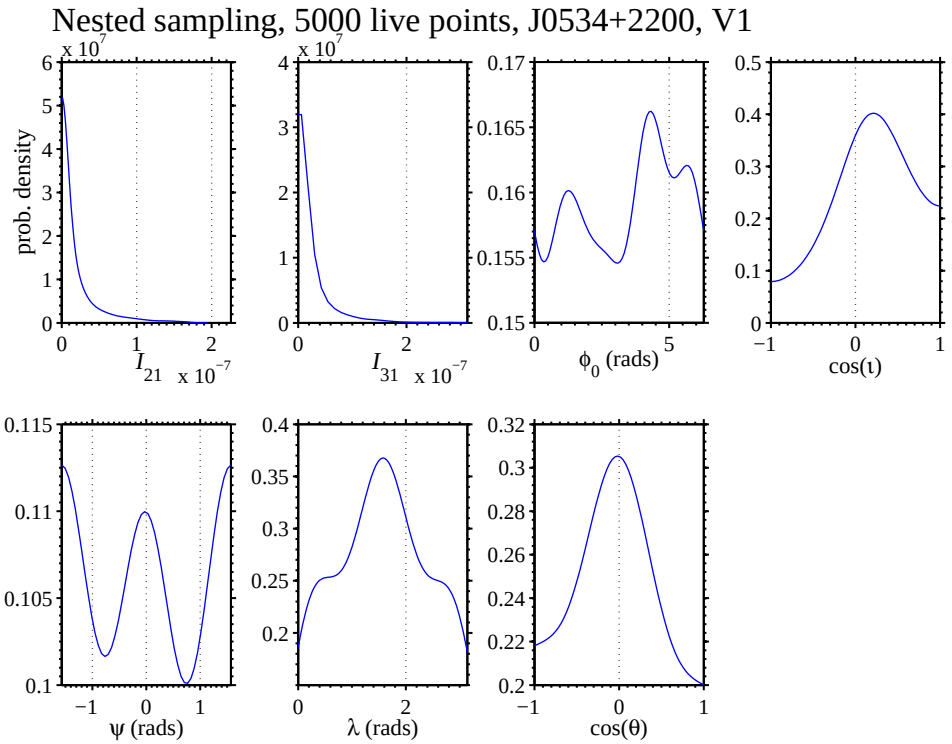

Figure 6.37: The PDFs for the pinned superfluid model's parameters, from the nested sampling analysis for the Crab pulsar in VSR4. The PDFs are consistent with there being no detectable pinned superfluid GW signal present in the data.

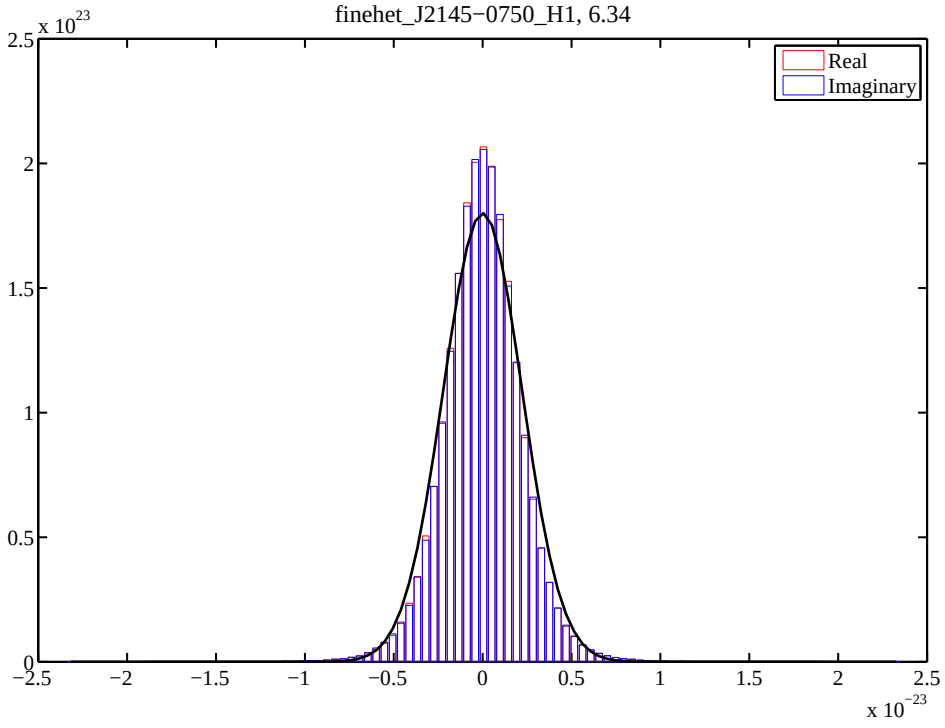

Figure 6.38: A histogram of the heterodyned data from H1 in S6, for J2145-0750.

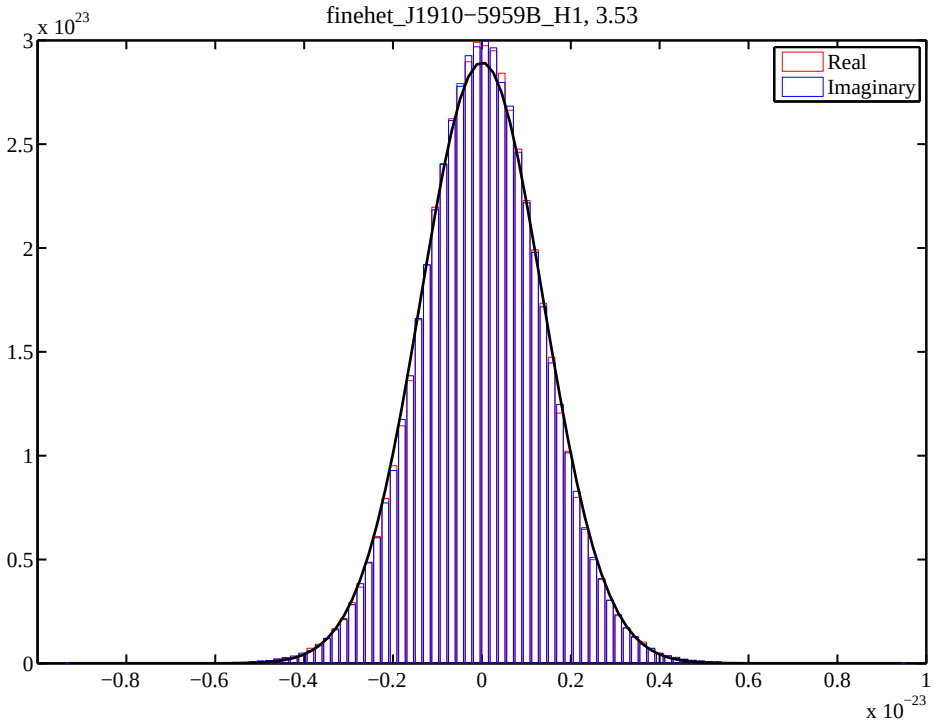

Figure 6.39: A histogram of the heterodyned data from H1 in S6, for J2145-0750.

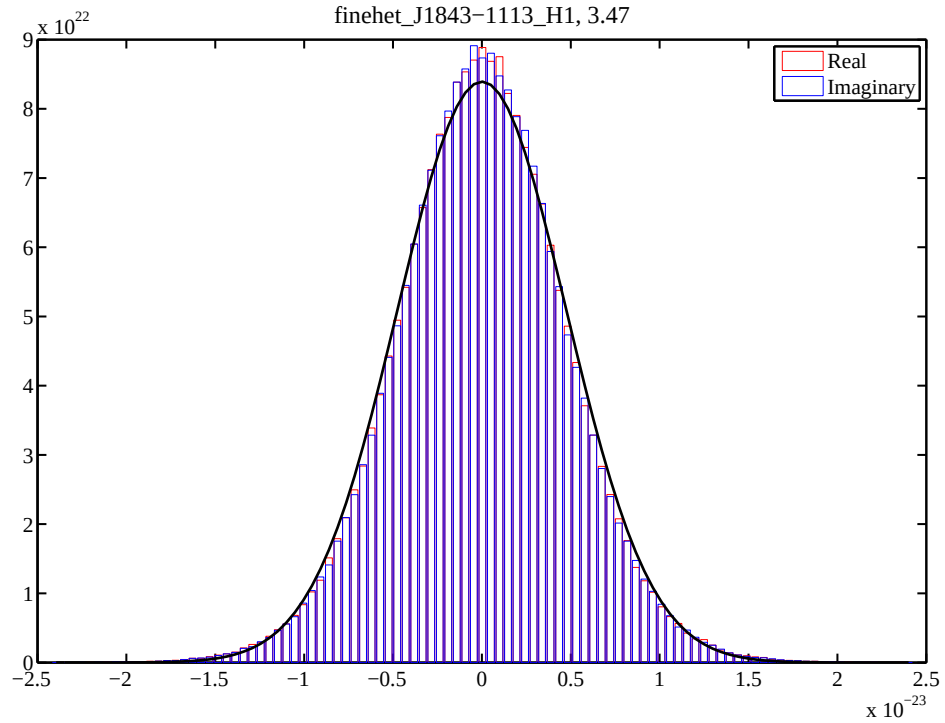

Figure 6.40: A histogram of the heterodyned data from H1 in S6, for J2145-0750.

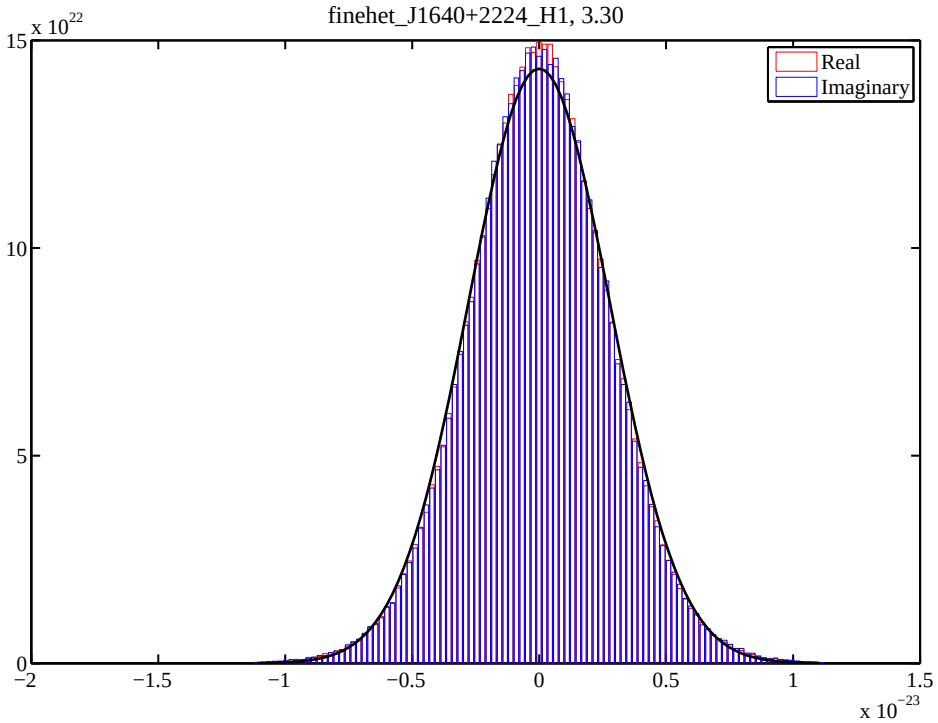

Figure 6.41: A histogram of the heterodyned data from H1 in S6, for J2145-0750.

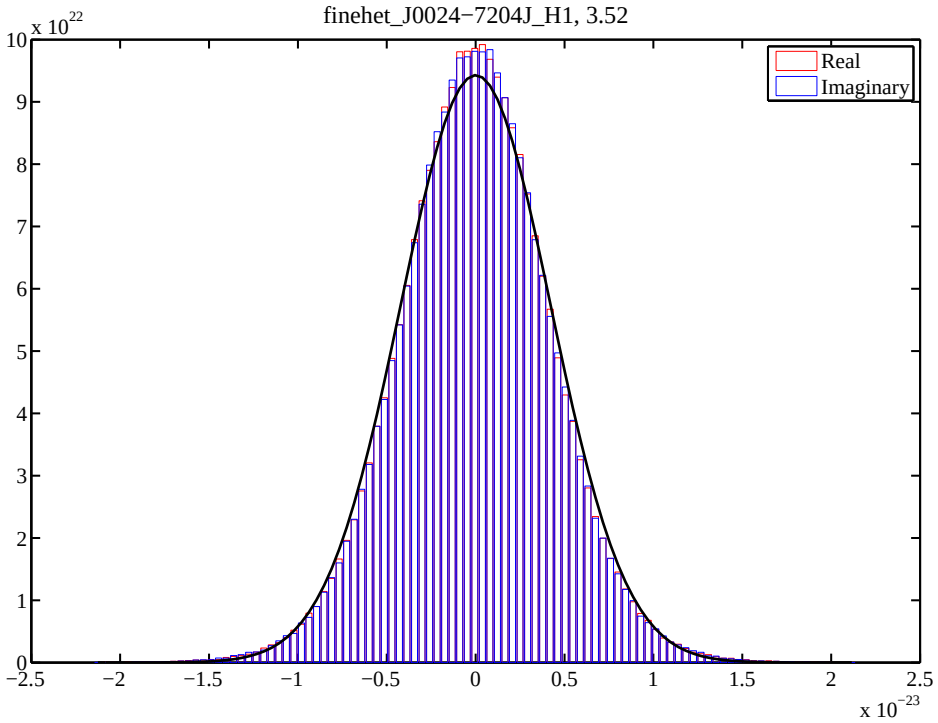

Figure 6.42: A histogram of the heterodyned data from H1 in S6, for J2145-0750.

Chapter 7

Discussion

7.1 Introduction

This chapter aims to bring together the main talking points from the previous chapters in this thesis in a short discussion. Ideas of where this work can be extended are also discussed.

7.2 Discussion and future work

In Chapter 2 I detailed the developments that I made to improve Fscan, as well as presented results from my use of Fscan to monitor the detector noise at the frequencies GWs are expected from the Crab and Vela pulsars. These results demonstrate the importance of such monitoring through the discovery of previously unknown noise lines. In particular the chiller line in VSR2, which went undiscovered by the Virgo noise monitoring program NOEMI, was shown to significantly affect the sensitivity of searches for GWs from Vela. Much work was carried out by the Virgo team after my discovery of this line, its source was identified as a chiller water pump which was subsequently modified to move the noise line out of the Vela frequency. In the case of the LIGO detectors and the Crab pulsar, I was able to identify the appearance of a noise line at the Crab frequency on two separate occasions. Fscan is currently able to be run for any pulsar given the required information, so future monitoring can easily be extended to many more pulsars. With the advent of the advanced detector era and the increased sensitivity these detectors bring, it will be important to identify a number of key CW sources and for their frequency bands to be monitored. It may also be worth while monitoring the frequency bands that relate to the rotation rate of the pulsar f_{rot}, as well as $2f_{rot}$, as the pinned superfluid emission model of Jones (2010), which was discussed in Chapter 6, predicts GW emission from pulsars at both these frequencies.

Chapters 3, 4 and 5 all report on searches for GWs from known pulsars using the search method developed by Dupuis & Woan (2005) and Pitkin & Woan (2004) to analyse data from the most recent science runs of the LIGO and Virgo detectors. None of the searches found any evidence for GWs, and so instead have been used to place upper limits on the GW amplitude parameter h_0 for each of the pulsars. For each analysis for the Vela and Crab pulsars two parameter estimation runs were performed, one that assumes the orientation of the pulsar is known and on where the orientation is assumed not to be know. Observation of the wind nebulae of these pulsars in Ng & Romani (2008), provides the information on the orientation of the Crab and Vela pulsars that is used to place restricted priors on their orientation parameters ($\cos(\iota)$ and ψ) in these searches. For both the Vela and Crab pulsars these searches have been able to beat the spin-down limit.

The search for GWs from Vela using VSR2 data was the first to place an upper limit on h_0 below Vela's spin-down limit of $h_0^{sd} = 3.3 \times 10^{-24}$. This result has been published together with results from different and independent search methods in Abadie et al. (2011a). The searches using VSR4 data, and using VSR4 and VSR2 data combined were able to place upper limits below that obtained from VSR2 only. The upper limits obtained from the analysis using VSR2 and VSR4 data combined were 1.1×10^{-24} where the orientation is assumed to be unknown, and 1.0×10^{-24} where restricted priors were placed on $\cos(\iota)$ and ψ. The upper limits relate to upper limits of 9 % and 11 % of Vela's spin-down energy. With the planned upgrades to the current GW detector network these upper limits should be able to be surpassed, in particular with the planned improved low frequency sensitivity of the LIGO detectors enabling LIGO data to be used as well as Virgo data.

The search for GWs from the Crab pulsar using S6, VSR2, VSR3 and VSR4 data were able to place an upper limit on h_0 below its spin-down limit of 1.4×10^{-24}, although this limit had been beaten already by previous searches (Abbott et al. 2008b, 2010). The upper limits obtained using the S6, VSR2, VSR3 and VSR4 datasets range from 2.3×10^{-25} from VSR4 to 1.0×10^{-24} from VSR3, which compares to the previously lowest upper limit obtained from LIGO S5 data of 1.9×10^{-25} (Abbott et al. 2010). It was expected that the enhancements made to LIGO between the S5 and S6 runs would result in an improved upper limit with the use of S6 data, this did not happen. The results from analysing the LIGO H1 data highlight a limitation of the search method used, in that the MCMC stage is only capable of performing parameter estimation and not model selection. The outputs from the MCMC are PDFs for each of the signal parameters, the h_0 parameter will normally peak at zero where there is no signal present in the data, however this is not always the case. The PDFs from both the S6 H1 MCMCs, one using restricted priors on $\cos(\iota)$ and ψ and one using uniform priors, showed a peak in the h_0 PDF at a non-zero value.

This highlights the lack of a model selection stage in the analysis method. This has been addressed with the development of a new analysis pipeline using the nested sampling algorithm, which was discussed further in Chapter 6. The final analyses for GWs from the Crab pulsar I performed combined the S5 data-set with the S6, VSR2, VSR3 and VSR4 data-sets. This analysis was complicated slightly because of the observation of timing glitches in the Crab pulsar in the middle of S5 and between S5 and S6. For the analysis I followed the example of Abbott et al. (2010), in that I performed one analysis that allowed the initial phase of the GW signal to change after each glitch, and one analysis where the GW signal is assumed to be fully coherent over the glitches. Together with the different parameter estimation runs for the different priors on $\cos(\iota)$ and ψ this creates a number of results, these are presented in Table 4.3, for brevity I recount only the lowest of these here. This was obtained with the parameter estimation run with restricted priors on the orientation parameters and allowing for a different initial phase after each glitch, and placed an upper limit on h_0 of 1.0×10^{-25}. This relates to just 0.5% of the Crab's spin-down energy. However, that is not to say that this is the most important of these results, each result should be considered as the correct answer given the stated assumptions used in the analyses to obtain them. As with the Vela pulsar, if the upgraded detectors deliver the performance improvement expected, future analyses should expect to improve on these results. However, the inferred upper limits on the equatorial ellipticity of the Crab need to improve by several orders of magnitude from the current lowest upper limit of 5.4×10^{-5} to enter the range of the more conservative predictions for the maximum sustainable ellipticity of order 1×10^{-7}.

In Chapter 5, I performed searches for GWs from a number of other known pulsars. These split into two subsets, pulsars timed with the Fermi γ-ray satellite, and those pulsars which were analysed in Abbott et al. (2010) using S5 data. There were no notable results obtained in these searches. The search for GWs from the Fermi pulsars used Virgo VSR4 data. As the GWs from these pulsars would be below ~ 40 Hz, and the LIGO detectors are not calibrated below 40 Hz, the VSR4 data-set was the most sensitive usable. The current distance estimates to the Fermi pulsars have very large errors associated with them, therefore it was not possible to get an accurate spin-down limit for the Fermi pulsars. If the lower bounds on their distance estimates are accurate, then my analyses would not beat any of these pulsar's spin-down limits. The analysis of the S5 pulsars used the LIGO S6 data, but relied on the out of date ephemerides which were used for the S5 analyses. These results are presented as an indication of what could be expected with current valid ephemerides only. The indication is that for some pulsars the S6 upper limits will be below the S5 upper limits, but for others the S5 results will remain the lower limit. Apart from the Crab, pulsar J1913+1011 was the pulsar for which the S5 analysis

came closest to surpassing its spin-down limit, with the S5 upper limit being roughly four times greater than the spin-down limit. My S6 analysis of this pulsar is unable to improve on the S5 upper limit, and is roughly five times that of its spin-down limit. An analysis, with an up to date ephemeris, and using data from S6, S5, VSR2 and VSR4 should be able to surpass its spin-down limit or at least get much closer to it. Clearly with up to date ephemerides the data should be re-analysed for all pulsars, although my preliminary results show that the likelihood of significantly improving on the S5 results of Abbott et al. (2010) with S6 data along is not very high.

In Chapter 6, I present some modifications to the search method used in the previous chapters. These modifications can be split into two parts. The first is to use the nested sampling algorithm to perform the analysis rather than an MCMC. This has the advantage of being able to compute the Bayesian evidence as well as performing parameter estimation. The development of the the nested sampling search code was carried out by Matthew Pitkin, my contribution to its development was in its characterisation. The results from this characterisation include a comparison of the new search code's results with those obtained using the old search code. I also characterise the codes ability to perform model selection through the computation of Bayesian evidence. The other modification to the search is the addition of a new GW emission model. I developed the nested sampling search code to analyse data for the signal predicted by a new model proposed by Jones (2010). The model predicts a rotating NS with a superfluid core that is pinned about an axis misaligned from the star's principal axes. The pinned superfluid core acts to force the star into rotating about an axis very close to the pinning axis, and where this is misaligned from the star's principal axis the star emits GWs at f_{rot} and $2f_{rot}$. The development of the search code necessarily considers the search range for the model parameters. In the process of testing this new search by analysing fake data-sets with injected signals, I found that the model contained degeneracies that prevented the correct estimation of individual parameters. The resulting PDFs from the parameter estimation showed that the signal model contained some degeneracies that meant the injected parameters could not be correctly identified. Future work on this problem should aim to find the degeneracies in the model causing the confusion in the parameter estimation. If the model can be re-parametrised to remove the degeneracies, then the parameter estimation process can likely be speeded up considerably owing to the less complicated parameter space being easier to explore. However, the degeneracies would remain when converting from the re-parametrised model back into the model parameters used in this thesis, so the fundamental confusion in the estimation of these parameters will remain. I have also used fake data-sets containing injected signals to test the model selection aspect of the code. The competing models exam-

ined in this way are: that the data contains no signal but just Gaussian noise, that the data contains a signal at $2f_{rot}$ only as described by the triaxial rotator model, and that the data contains a signal from the pinned superfluid model. These tests showed that it is possible to tell whether a signal is generated in the way described in Jones (2010) or the simpler triaxial rotator model. I was also able to show that the relative strengths of the detector noise floor at f_{rot} and $2f_{rot}$ are an important consideration for choosing targets for a pinned superfluid search. Where the noise at f_{rot} is roughly equal to or less than the noise floor at $2f_{rot}$, performing a search for a pinned superfluid signal can result in greater evidence for the existence of a signal compared to a search for the simple triaxial rotator model only. However, this of course depends on the parameters of the source, in particular I_{21}, I_{31}, ι, and θ. Future work into this area would do well to consider astrophysically plausible ranges for I_{21}, I_{31} and θ, as these parameters strongly affect the relative strengths of the emission at f_{rot} and $2f_{rot}$. Using this newly developed search I performed a search for GWs from pinned superfluid model for the Crab pulsar in Virgo VSR4 data. This search produced no evidence for the presence of GWs in the data, with the model selection process favouring the model that the data contained only Gaussian noise.

7.3 Summary

The work I have presented in this thesis has covered a wide range of areas concerning targeted searches for GWs from pulsars. I have shown that careful monitoring of the data at the GW frequency for a source can help improve the results of that search considerably. The searches I carried out for GWs from the Vela and Crab pulsars have improved upon the previous best upper limits obtained in the case of the Crab, and broken new ground by beating the spin-down limit for the Vela pulsar - making it only the second pulsar for which this milestone has been achieved. The nested sampling algorithm has been presented as an improvement over the existing MCMC search code, for the reason that it can compute the Bayesian evidence which can be used in model selection. This will become increasingly important as we move into the advanced detector era, where the expectations of making a detection of CWs is increased, and the community may need to present the case for a first detection. I have also developed this search code for use with a new CW emission model, and that although it will not be possible to determined the parameters for this model if a signal is seen, performing this search could provide a stronger case for a detection through a greater Bayesian evidence value than that from a search for a signal from the triaxial rotator model.

Appendix A

Heterodyning the pinned superfluid signal

Here I present the working to go from the un-heterodyned pinned superfluid signal as described in Jones (2010), to the heterodyned signal that I present in §6.3.1.

To begin with the unheterodyned signal, and the h_+^{Ω} part of the signal.

$$\begin{aligned} h_+^{\Omega} &= \frac{-\Omega^2}{r}\sin\iota\cos\iota\{[I_{21}\cos^2\lambda - I_{31}]\sin 2\theta\cos\phi \\ &\quad - I_{21}\sin 2\lambda\sin\theta\sin\phi\} \end{aligned}$$

I substitute in $\cos\phi = \frac{e^{i\phi}+e^{-i\phi}}{2}$ and $\sin\phi = \frac{e^{i\phi}-e^{-i\phi}}{2i}$.

$$\begin{aligned} h_+^{\Omega} &= \frac{-\Omega^2}{r}\sin\iota\cos\iota\{(\cos^2\lambda - h1)\sin 2\theta\Big(\frac{e^{i\phi}+e^{-i\phi}}{2}\Big) \\ &\quad - \sin 2\lambda\sin\theta\Big(\frac{e^{i\phi}-e^{-i\phi}}{2i}\Big)\} \end{aligned}$$

To simplify this a little I use $A1 = (I_{21}\cos^2\lambda - I_{31})\sin 2\theta$, and $A_2 = I_{21}\sin 2\lambda\sin\theta$. I also simplify by taking the $\frac{1}{2}$ outside the brackets and substituting $\frac{1}{i} = -i$.

$$h_+^{\Omega} = \frac{-\Omega^2}{2r}\sin\iota\cos\iota\{A_1(e^{i\phi}+e^{-i\phi}) + iA_2(e^{i\phi}-e^{-i\phi})\}$$

Substitute $\phi = \phi(t) + \phi_0$..

$$h_+^{\Omega} = \frac{-\Omega^2}{2r}\sin\iota\cos\iota\{A_1(e^{i\phi_0}e^{i\phi(t)}+e^{-i\phi}) + iA_2(e^{i\phi_0}e^{i\phi(t)}-e^{-i\phi})\}$$

Now I can perform the heterodyne step by multiplying by $e^{-i\phi(t)}$.

$$h_+^{\ \Omega} = \frac{-\Omega^2}{2r}\sin\iota\cos\iota\{A_1(e^{i\phi_0}e^{i\phi(t)}+e^{-i\phi})e^{-i\phi(t)}+iA_2(e^{i\phi_0}e^{i\phi(t)}-e^{-i\phi})e^{-i\phi(t)}\}$$

Which simplifies to.

$$h_+^{\ \Omega} = \frac{-\Omega^2}{2r}\sin\iota\cos\iota\{A_1(e^{i\phi_0}+e^{-2i\phi(t)-i\phi_0})+iA_2(e^{i\phi_0}-e^{-2i\phi(t)-i\phi_0})\}$$

The next step is to low pass filter the heterodyned data, this removes the $e^{-i2\phi(t)-i\phi_0}$ terms.

$$h_+^{\ \Omega} = \frac{-\Omega^2}{2r}\sin\iota\cos\iota\{A_1e^{i\phi_0}+iA_2e^{i\phi_0}\}$$

Now by using $e^{i\phi}=\cos(\phi)+i\sin(\phi)$, I get the following.

$$h_+^{\ \Omega} = \frac{-\Omega^2}{2r}\sin\iota\cos\iota\{A_1(\cos\phi_0+i\sin\phi_0)+iA_2(\cos\phi_0+i\sin\phi_0)\}$$

And a final rearrangement.

$$h_+^{\ \Omega} = \frac{-\Omega^2}{2r}\sin\iota\cos\iota\{A_1\cos\phi_0-A_2\sin\phi_0+i(A_2\cos\phi_0+A_1\sin\phi_0)\}$$

Now to move on to the unheterodyned signal for the $h_\times^{\ \Omega}$ part of the signal.

$$h_\times^{\ \Omega} = \frac{-\Omega^2}{r}\sin\iota\{I_{21}\sin2\lambda\sin\theta\cos\phi+(I_{21}\cos^2\lambda-I_{31})\sin2\theta\sin\phi\}$$

From here I substitute in $\cos\phi = \frac{e^{i\phi}+e^{-i\phi}}{2}$ and $\sin\phi = \frac{e^{i\phi}-e^{-i\phi}}{2i}$.

$$h_\times^{\ \Omega} = \frac{-\Omega^2}{r}\sin\iota\{\sin2\lambda\sin\theta\Big(\frac{e^{i\phi}+e^{-i\phi}}{2}\Big)+(\cos^2\lambda-h_1)\sin2\theta\Big(\frac{e^{i\phi}-e^{-i\phi}}{2i}\Big)\}$$

To simplify this a little I use $B1=(I_{21}\cos^2\lambda-I_{31})\sin2\theta$, and $B_2=I_{21}\sin2\lambda\sin\theta$. I also simplify by taking the $\frac{1}{2}$ outside the brackets and substituting $\frac{1}{i}=-i$.

$$h_{\times}^{\Omega} = \frac{-\Omega^2}{2r}\sin\iota\{A_2(e^{i\phi}+e^{-i\phi}) - iA_1(e^{i\phi}-e^{-i\phi}\}$$

Substitute $\phi = \phi(t) + \phi_0$..

$$h_{\times}^{\Omega} = \frac{-\Omega^2}{2r}\sin\iota\{A_2(e^{i\phi_0}e^{i\phi(t)}+e^{-i\phi}) - iA_1(e^{i\phi_0}e^{i\phi(t)}-e^{-i\phi})\}$$

Now I can perform the heterodyne step by multiplying by $e^{-i\phi(t)}$.

$$h_{\times}^{\Omega} = \frac{-\Omega^2}{2r}\sin\iota\{A_2(e^{i\phi_0}e^{i\phi(t)}+e^{-i\phi})e^{-i\phi(t)} - iA_1(e^{i\phi_0}e^{i\phi(t)}-e^{-i\phi})e^{-i\phi(t)}\}$$

Which simplifies to.

$$h_{\times}^{\Omega} = \frac{-\Omega^2}{2r}\sin\iota\{A_2(e^{i\phi_0}+e^{-2i\phi(t)-i\phi_0}) - iA_1(e^{i\phi_0}-e^{-2i\phi(t)-i\phi_0})\}$$

The next step is to low pass filter the heterodyned data, this removes the $e^{-i4\phi(t)-i2\phi_0}$ terms.

$$h_{\times}^{\Omega} = \frac{-\Omega^2}{2r}\sin\iota\{A_2e^{i\phi_0} - iA_1e^{i\phi_0}\}$$

Now by using $e^{i\phi_0} = \cos\phi_0 + i\sin\phi_0$, I get the following.

$$h_{\times}^{\Omega} = \frac{-\Omega^2}{2r}\sin\iota\{A_2(\cos\phi_0+i\sin\phi_0) - iA_1(\cos\phi_0+i\sin\phi_0)\}$$

And a final rearrangement.

$$h_{\times}^{\Omega} = \frac{-\Omega^2}{2r}\sin\iota\{A_2\cos\phi_0 + A_1\sin\phi_0 + i(A_2\sin\phi_0 - A_1\cos\phi_0)\}$$

Now I move onto the $2f$ data, with the unheterodyned signal, and the $h_{+}^{2\Omega}$ part of the signal.

$$h_+^{2\Omega} = \frac{-2\Omega^2}{r}(1+\cos^2\iota)\{[I_{21}(\cos^2\lambda\cos^2\theta-\sin^2\lambda)+I_{31}\sin^2\theta]\cos 2\phi - I_{21}\sin 2\lambda\cos\theta\sin 2\phi\}$$

From here I substitute in $\cos 2\phi = \frac{e^{i2\phi}+e^{-i2\phi}}{2}$ and $\sin 2\phi = \frac{e^{i2\phi}-e^{-i2\phi}}{2i}$.

$$h_+^{2\Omega} = \frac{-2\Omega^2}{r}(1+\cos^2\iota)\{[I_{21}(\cos^2\lambda\cos^2\theta-\sin^2\lambda)+I_{31}\sin^2\theta]\left(\frac{e^{i2\phi}+e^{-i2\phi}}{2}\right) - I_{21}\sin 2\lambda\cos\theta\left(\frac{e^{i2\phi}-e^{-i2\phi}}{2i}\right)\}$$

To simplify this a little I use $B1 = I_{21}(\cos^2\lambda\cos^2\theta-\sin^2\lambda)+I_{31}\sin^2\theta$, and $B_2 = I_{21}\sin 2\lambda\cos\theta$. I also simplify by taking the $\frac{1}{2}$ outside the brackets and substituting $\frac{1}{i} = -i$.

$$h_+^{2\Omega} = \frac{-\Omega^2}{r}((1+\cos^2\iota)\{B_1(e^{i2\phi}+e^{-i2\phi})+iB_2(e^{i2\phi}-e^{-i2\phi})\}$$

Substitute $\phi = \phi(t)+\phi_0$..

$$h_+^{2\Omega} = \frac{-\Omega^2}{r}(1+\cos^2\iota)\{B_1(e^{2\phi_0}e^{i2\phi(t)}+e^{-i2\phi})+iB_2(e^{2\phi_0}e^{i2\phi(t)}-e^{-i2\phi})\}$$

Now I can perform the heterodyne step by multiplying by $e^{-i\phi(t)}$.

$$h_+^{2\Omega} = \frac{-\Omega^2}{r}((1+\cos^2\iota)\{B_1(e^{2\phi_0}e^{i2\phi(t)}+e^{-i2\phi})e^{-2\phi(t)}+iB_2(e^{2\phi_0}e^{i2\phi(t)}-e^{-i2\phi})e^{-2\phi(t)}\}$$

Which simplifies to.

$$h_+^{2\Omega} = \frac{-\Omega^2}{r}((1+\cos^2\iota)\{B_1(e^{2\phi_0}+e^{-i4\phi(t)-i2\phi_0})+iB_2(e^{2\phi_0}-e^{-i4\phi(t)-i2\phi_0})\}$$

The next step is to low pass filter the heterodyned data, this removes the $e^{-i4\phi(t)-i2\phi_0}$ terms.

$$h_+^{2\Omega} = \frac{-\Omega^2}{r}(1+\cos^2\iota)\{B_1e^{2\phi_0}+iB_2e^{2\phi_0}\}$$

Now by using $e^{i\phi} = \cos(\phi) = i\sin(\phi)$, I get the following.

$$h_+^{2\Omega} = \frac{-\Omega^2}{r}(1+\cos^2\iota)\{B_1(\cos 2\phi + i\sin 2\phi) + iB_2(\cos 2\phi + i\sin 2\phi)\}$$

And a final rearranement.

$$h_+^{2\Omega} = \frac{-\Omega^2}{r}(1+\cos^2\iota)\{B_1\cos 2\phi - B_2\sin 2\phi + i(B_2\cos 2\phi + B_1\sin 2\phi)\}$$

Now to move on to the unheterodyned signal for the $h_\times^{2\Omega}$ part of the signal first.

$$h_\times^{2\Omega} = \frac{-2\Omega^2}{r}2\cos\iota$$
$$\{I_{21}\sin 2\lambda\cos\theta\cos 2\phi + [I_{21}(\cos^2\lambda\ \cos^2\theta - \sin^2\lambda) + I_{31}\sin^2\theta]\sin 2\phi\}$$

From here I substitute in $\cos 2\phi = \frac{e^{i2\phi}+e^{-i2\phi}}{2}$ and $\sin 2\phi = \frac{e^{i2\phi}-e^{-i2\phi}}{2i}$, and combine the factor of twos at the front.

$$h_\times^{2\Omega} = \frac{-4\Omega^2}{r}\cos\iota\{I_{21}\sin 2\lambda\cos\theta\Big(\frac{e^{i2\phi}+e^{-i2\phi}}{2}\Big)$$
$$+[I_{21}(\cos^2\lambda\ \cos^2\theta - \sin^2\lambda) + I_{31}\sin^2\theta]\Big(\frac{e^{i2\phi}-e^{-i2\phi}}{2i}\Big)\}$$

To simplify this a little I use $B1 = I_{21}(\cos^2\lambda\cos^2\theta - \sin^2\lambda) + I_{31}\sin^2\theta$, and $B_2 = I_{21}\sin 2\lambda\cos\theta$. I also simplify by taking the $\frac{1}{2}$ outside the brackets and substituting $\frac{1}{i} = -i$.

$$h_\times^{2\Omega} = \frac{-2\Omega^2}{r}\cos\iota\{B_2(e^{i2\phi}+e^{-i2\phi}) - iB_1(e^{i2\phi}-e^{-i2\phi})\}$$

Substitute $\phi = \phi(t) + \phi_0$..

$$h_\times^{2\Omega} = \frac{-2\Omega^2}{r}\cos\iota\{B_2(e^{i2\phi_0}e^{2\phi(t)}+e^{-i2\phi}) - iB_1(e^{i2\phi_0}e^{i2\phi(t)}-e^{-i2\phi})\}$$

Now I can perform the heterodyne step by multiplying by $e^{-i\phi(t)}$.

$$h_{\times}^{2\Omega} = \frac{-2\Omega^2}{r}\cos\iota\{B_2(e^{i2\phi_0}e^{2\phi(t)} + e^{-i2\phi})e^{-i\phi(t)} - iB_1(e^{i2\phi_0}e^{i2\phi(t)} - e^{-i2\phi})e^{-i\phi(t)}\}$$

Which simplifies to.

$$h_{\times}^{2\Omega} = \frac{-2\Omega^2}{r}\cos\iota\{B_2(e^{i2\phi_0} + e^{-i4\phi(t)-i2\phi_0}) - iB_1(e^{i2\phi_0} - e^{-i4\phi(t)-i2\phi_0})\}$$

The next step is to low pass filter the heterodyned data, this removes the $e^{-i4\phi(t)-i2\phi_0}$ terms.

$$h_{\times}^{2\Omega} = \frac{-2\Omega^2}{r}\cos\iota\{B_2e^{i2\phi_0} - iB_1e^{i2\phi_0}\}$$

Now by using $e^{i\phi} = \cos\phi + i\sin\phi$, I get the following.

$$h_{\times}^{2\Omega} = \frac{-2\Omega^2}{r}\cos\iota\{B_2(\cos 2\phi_0 + i\sin 2\phi_0) - iB_1(\cos 2\phi_0 + i\sin 2\phi_0)\}$$

And a final rearrangement.

$$h_{\times}^{2\Omega} = \frac{-2\Omega^2}{r}\cos\iota\{B_2\cos 2\phi_0 + B_1\sin 2\phi_0 + i(B_2\sin 2\phi_0 - B_1\cos 2\phi_0)\}$$

Appendix B

Examples of nested samples for pinned superfluid model

Here I include the PDFs and the associated nested samples for a three test signals. The parameters used to create the test signals are chosen from a uniform random distribution across their principle ranges, and at random from one of $7.5\times10^{-11}, 1.5\times 10^{-10}, 3\times10^{-10}, 6e\times10^{-10}, 1.2\times10^{-9}$ for I_{21} and I_{31}. The signals were all scaled such that the combined SNR was 100. Each figure shows the PDFs and the nested samples produced by analysing one signal. I ran the analysis on 100 different signals, bug only include 3 for brevity.

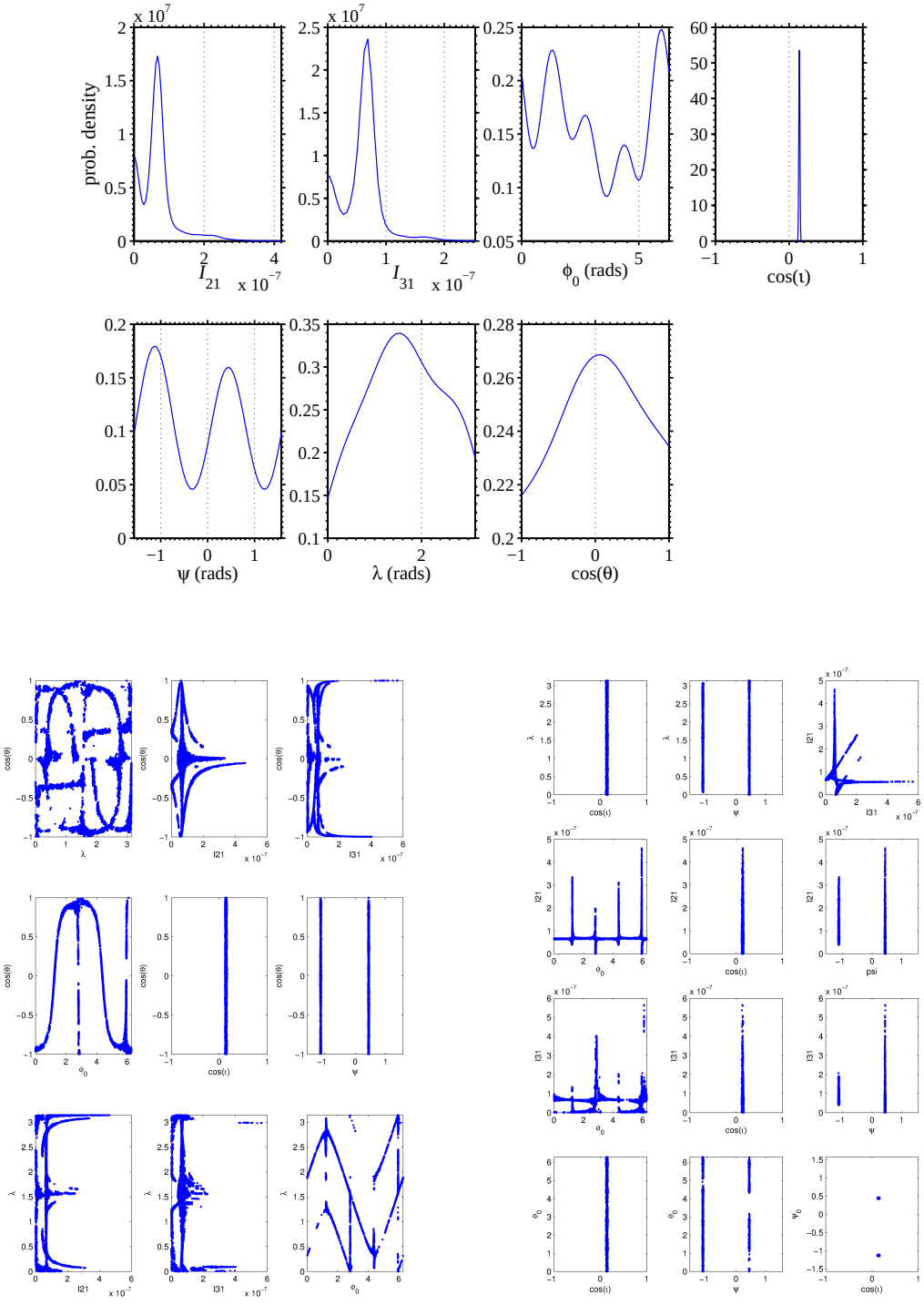

Figure B.1: PDFs and nested samples from the analysis of a randomly generated signal with SNR of 100.

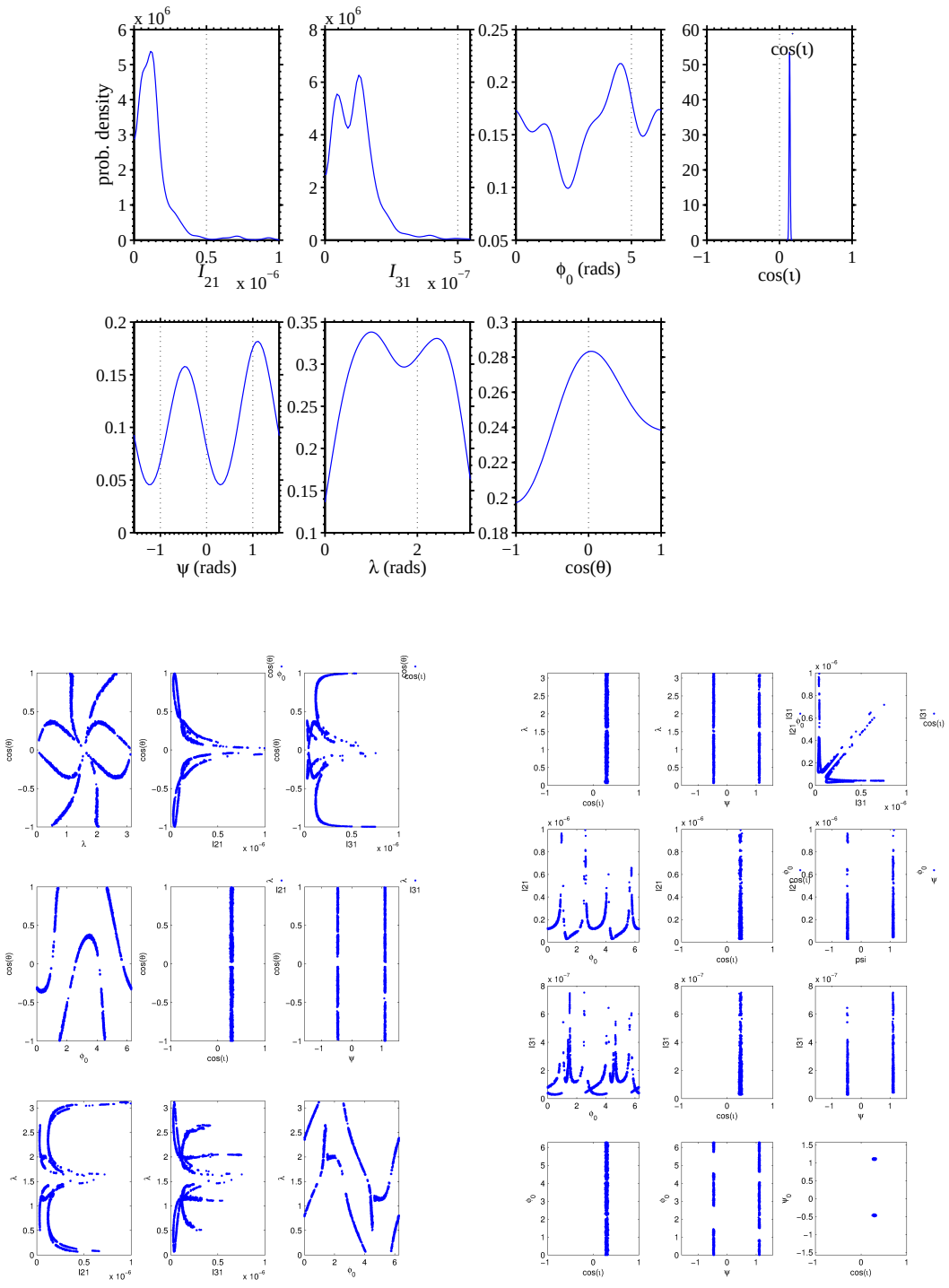

Figure B.2: PDFs and nested samples from the analysis of a randomly generated signal with SNR of 100.

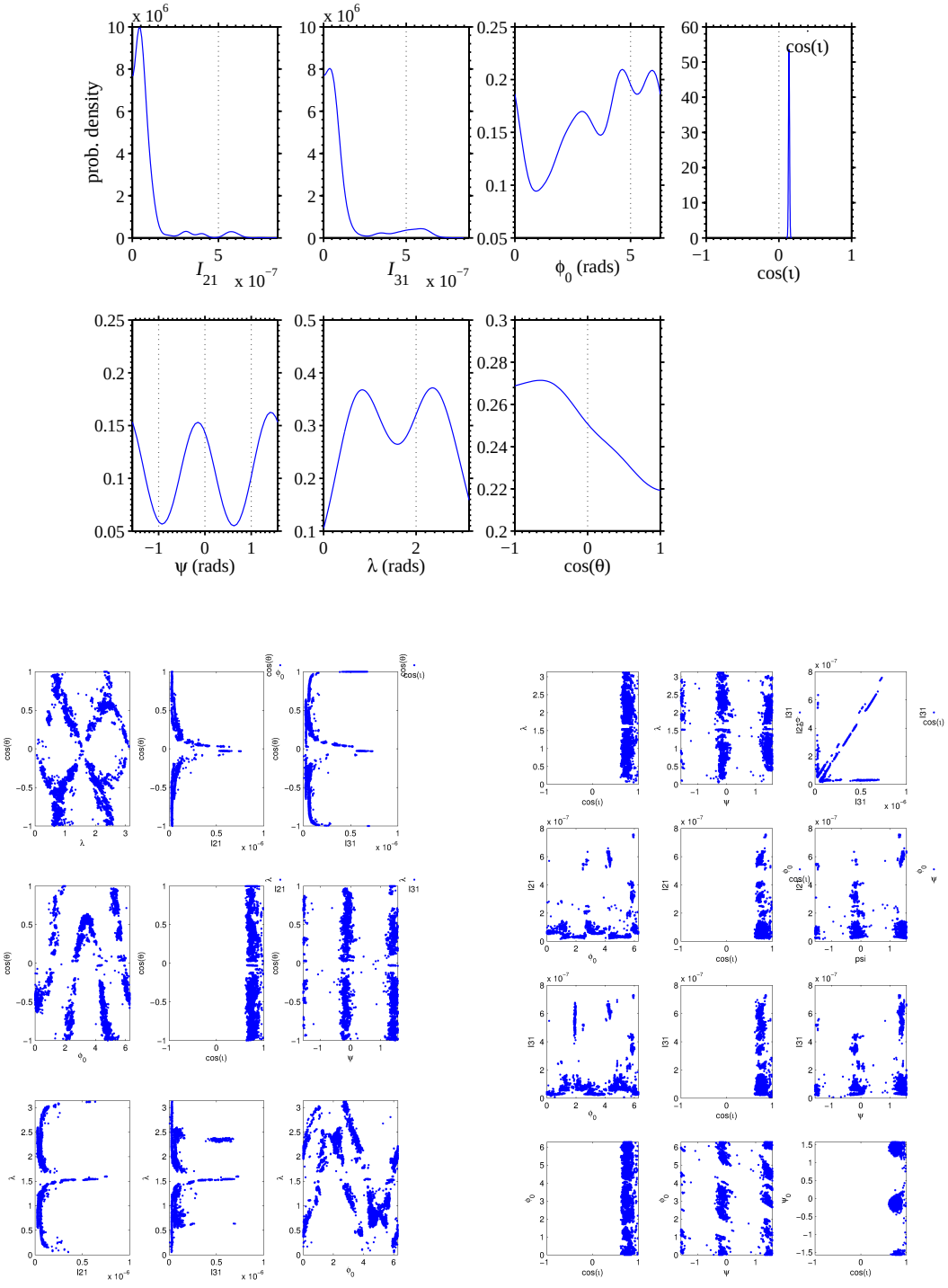

Figure B.3: PDFs and nested samples from the analysis of a randomly generated signal with SNR of 100.

Bibliography

2012, The Fermi Large Area Telescope, http://www-glast.stanford.edu/

Abadie, J., Abbott, B. P., Abbott, R., et al. 2011a, Astrophys. J. , 737, 93

Abadie, J., Abbott, B. P., Abbott, R., et al. 2010a, Nuclear Instruments and Methods in Physics Research A, 624, 223

Abadie, J., Abbott, B. P., Abbott, R., et al. 2010b, Astrophys. J. , 722, 1504

Abadie, J., Abbott, B. P., Abbott, R., et al. 2011b, Phys. Rev. D , 83, 042001

Abbott, B., Abbott, R., Adhikari, R., et al. 2004, Phys. Rev. D , 69, 122004

Abbott, B., Abbott, R., Adhikari, R., et al. 2007, Phys. Rev. D , 76, 042001

Abbott, B., Abbott, R., Adhikari, R., et al. 2008a, Phys. Rev. D , 77, 022001

Abbott, B., Abbott, R., Adhikari, R., et al. 2008b, Astrophys. J. Lett. , 683, L45

Abbott, B. P., Abbott, R., Acernese, F., et al. 2010, Astrophys. J. , 713, 671

Abbott, B. P., Abbott, R., Adhikari, R., et al. 2009a, Physical Review Letters, 102, 111102

Abbott, B. P., Abbott, R., Adhikari, R., et al. 2009b, Reports on Progress in Physics, 72, 076901

Abdo, A. A., Ackermann, M., Ajello, M., et al. 2011, Science, 331, 739

Abdo, A. A., Ackermann, M., Ajello, M., et al. 2010, Astrophys. Suppl. , 187, 460

Abramovici, A., Althouse, W., Camp, J., et al. 1996, Physics Letters A, 218, 157

Accadia, T., Acernese, F., Antonucci, F., et al. 2011a, Classical and Quantum Gravity, 28, 114002

Accadia, T., Acernese, F., Antonucci, F., et al. 2011b, Classical and Quantum Gravity, 28, 025005

Accadia, T. et al. 2012, in Proceedings from the 9th Edouardo Amaldi Meeintg, [In press]

Acernese, F., Alshourbagy, M., Amico, P., et al. 2008, Journal of Physics Conference Series, 120, 032007

Ackermann, M. et al. 2011, Astrophys. J. , 726, 35

Akutsu, T., Ando, M., Haruyama, T., et al. 2008, Classical and Quantum Gravity, 25, 184013

Allen, B., Woan, G., the LIGO Scientific Collaboration, et al. 2004, Classical and Quantum Gravity, 21, 671

Amaro-Seoane, P., Aoudia, S., Babak, S., et al. 2012, ArXiv e-prints

Anderson, P. W. & Itoh, N. 1975, Nature , 256, 25

Andersson, N. 1998, Astrophys. J. , 502, 708

Andersson, N. 2003, Classical and Quantum Gravity, 20, 105

Andersson, N., Ferrari, V., Jones, D. I., et al. 2011, General Relativity and Gravitation, 43, 409

Andrew Lyne. 2011, Jodrell bank Crab pulsar monthly ephemeris, http://www.jb.man.ac.uk/~pulsar/crab.html

Araya, A., Mio, N., Tsubono, K., et al. 1997, Applied Optics, 36, 1446

Astone, P., D'Antonio, S., Frasca, S., & Palomba, C. 2010, Classical and Quantum Gravity, 27, 194016

Aylott, B., Baker, J. G., Boggs, W. D., et al. 2009, Classical and Quantum Gravity, 26, 165008

Baade, W. & Zwicky, F. 1934a, Proc Natl Acad Sci U S A., 20, 254

Baade, W. & Zwicky, F. 1934b, Physical Review, 46, 76

Baym, G., Pethick, C., & Pines, D. 1969, Nature , 224, 872

Bignami, G. F., Caraveo, P. A., De Luca, A., & Mereghetti, S. 2003, Nature , 423, 725

Bildsten, L. 1998, in 19th Texas Symposium on Relativistic Astrophysics and Cosmology, ed. J. Paul, T. Montmerle, & E. Aubourg

Blackburn, L., Cadonati, L., Caride, S., et al. 2008, Classical and Quantum Gravity, 25, 184004

Braccini, S., Barsotti, L., Bradaschia, C., Cella, G., et al. 2005, Astroparticle Physics, 23, 557

Brady, P. R., Creighton, T., Cutler, C., & Schutz, B. F. 1998, Phys. Rev. D , 57, 2101

Buonanno, A., Cook, G. B., & Pretorius, F. 2007, Phys. Rev. D , 75, 124018

Chandrasekhar, S. 1970, Physical Review Letters, 24, 611

Chandrasekhar, S. & Fermi, E. 1953, Astrophys. J. , 118, 116

Clark, J., Heng, I. S., Pitkin, M., & Woan, G. 2007, Phys. Rev. D , 76, 043003

Comella, J. M., Craft, H. D., Lovelace, R. V. E., & Sutton, J. M. 1969, Nature , 221, 453

Coughlin, M., the Ligo Scientific Collaboration, & the Virgo Collaboration. 2010, Journal of Physics Conference Series, 243, 012010

Cutler, C. 2002, Phys. Rev. D , 66, 084025

Cutler, C. & Thorne, K. S. 2002, ArXiv General Relativity and Quantum Cosmology e-prints

Demorest, P. B., Pennucci, T., Ransom, S. M., Roberts, M. S. E., & Hessels, J. W. T. 2010, Nature , 467, 1081

Deneva, J. S., Knispel, B., Allen, B., et al. 2011, in Bulletin of the American Astronomical Society, Vol. 43, American Astronomical Society Meeting Abstracts, 217, 234.05

Detweiler, S. 1979, Astrophys. J. , 234, 1100

Dupuis, R. J. & Woan, G. 2005, Phys. Rev. D , 72, 102002

Einstein, A. 1905, Annalen der Physik, 322, 891

Einstein, A. 1915, Sitzungsberichte der Königlich Preußischen Akademie der Wissenschaften (Berlin), Seite 778-786., 778

Espinoza, C. M., Lyne, A. G., Stappers, B. W., & Kramer, M. 2011, ArXiv e-prints

Friedman, J. L. & Schutz, B. F. 1978, Astrophys. J. , 222, 281

Fritschel, P., González, G., Lantz, B., Saha, P., & Zucker, M. 1998, Physical Review Letters, 80, 3181

Gavriil, F. P. & Kaspi, V. M. 2002, Astrophys. J. , 567, 1067

Glampedakis, K., Andersson, N., & Jones, D. I. 2009, Mon. Not. Roy. Astron. Soc. , 394, 1908

Gold, T. 1969, Nature , 221, 25

Grubbs, F. 1969, Technometrics, 11, 1

Güver, T., Özel, F., Cabrera-Lavers, A., & Wroblewski, P. 2010, Astrophys. J. , 712, 964

Harry, G. M. & the LIGO Scientific Collaboration. 2010, Classical and Quantum Gravity, 27, 084006

Haskell, B., Andersson, N., Jones, D. I., & Samuelsson, L. 2007, Physical Review Letters, 99, 231101

Haskell, B., Samuelsson, L., Glampedakis, K., & Andersson, N. 2008, Mon. Not. Roy. Astron. Soc. , 385, 531

Hastings, W. K. 1970, Biometrika, 57, 97

Heinke, C. O. & Ho, W. C. G. 2010, Astrophys. J. Lett. , 719, L167

Hester, J. et al. 2002, http://hubblesite.org/newscenter/newsdesk/archive/releases/2002/24/image/a

Hild, S., Abernathy, M., Acernese, F., Amaro-Seoane, P., et al. 2011, Classical and Quantum Gravity, 28, 094013

Hirakawa, H., Tsubono, K., & Fujimoto, M.-K. 1978, Phys. Rev. D , 17, 1919

Hobbs, G., Archibald, A., Arzoumanian, Z., Backer, D., et al. 2010a, Classical and Quantum Gravity, 27, 084013

Hobbs, G., Archibald, A., Arzoumanian, Z., Backer, D., et al. 2010b, Classical and Quantum Gravity, 27, 084013

Hobbs, G., Lorimer, D. R., Lyne, A. G., & Kramer, M. 2005, Mon. Not. Roy. Astron. Soc. , 360, 974

Hobbs, G. B., Edwards, R. T., & Manchester, R. N. 2006, Mon. Not. Roy. Astron. Soc. , 369, 655

Horowitz, C. J. 2010, Phys. Rev. D , 81, 103001

Hulse, R. A. & Taylor, J. H. 1975, Astrophys. J. Lett. , 195, L51

Isogai, T., LIGO Scientific Collaboration, & Virgo Collaboration. 2010, Journal of Physics Conference Series, 243, 012005

Janssen, G. H., Stappers, B. W., Kramer, M., et al. 2008, in American Institute of Physics Conference Series, Vol. 983, 40 Years of Pulsars: Millisecond Pulsars, Magnetars and More, ed. C. Bassa, Z. Wang, A. Cumming, & V. M. Kaspi, 633–635

Jaranowski, P. & Królak, A. 2010, Classical and Quantum Gravity, 27, 194015

Jaranowski, P., Królak, A., & Schutz, B. F. 1998, Phys. Rev. D , 58, 063001

Jenet, F., Finn, L. S., Lazio, J., et al. 2009, ArXiv e-prints

Jenet, F. A., Hobbs, G. B., van Straten, W., et al. 2006, Astrophys. J. , 653, 1571

Jones, D. I. 2010, Mon. Not. Roy. Astron. Soc. , 402, 2503

Jones, D. I. 2011, ArXiv e-prints

Jones, D. I. & Andersson, N. 2001, Mon. Not. Roy. Astron. Soc. , 324, 811

Jones, D. I. & Andersson, N. 2002, Mon. Not. Roy. Astron. Soc. , 331, 203

Klähn, T., Blaschke, D., Sandin, F., et al. 2007, Physics Letters B, 654, 170

Knippel, B. & Sedrakian, A. 2009, Phys. Rev. D , 79, 083007

Large, M. I., Vaughan, A. E., & Mills, B. Y. 1968, Nature , 220, 340

Lazzarini, A., Schofield, R., & Vicere, A. 2009, 60 Hz Mains Correlations for the U.S. Power Grids, http://www.ligo.caltech.edu/docs/G/G020245-00/G020245-00.pdf

Li, B.-A. & Steiner, A. W. 2006, Physics Letters B, 642, 436

Lin, L.-M. 2007, Phys. Rev. D , 76, 081502

Lorimer, D. & Kramer, M. 2005, Handbook of Pulsar Astronomy (Cambridge University Press)

Lorimer, D. R. 2005, Living Reviews in Relativity, 8, 7

Lorimer, D. R. 2010, ArXiv e-prints

Lück, H. & the GEO600 Team. 1997, Classical and Quantum Gravity, 14, 1471

Lyne, A., Hobbs, G., Kramer, M., Stairs, I., & Stappers, B. 2010, Science, 329, 408

Lyne, A. G. & Lorimer, D. R. 1994, Nature , 369, 127

Lyne, A. G., Pritchard, R. S., & Graham-Smith, F. 1993, Mon. Not. Roy. Astron. Soc. , 265, 1003

Manchester, R. N. 2008, in American Institute of Physics Conference Series, Vol. 983, 40 Years of Pulsars: Millisecond Pulsars, Magnetars and More, ed. C. Bassa, Z. Wang, A. Cumming, & V. M. Kaspi, 584–592

Manchester, R. N., Hobbs, G. B., Teoh, A., & Hobbs, M. 2005, VizieR Online Data Catalog, 7245, 0

Marelli, M., De Luca, A., & Caraveo, P. A. 2011, Astrophys. J. , 733, 82

Mayall, N. U. & Oort, J. H. 1942, Publications of the Astronomical Society of the Pacific, 54, 95

McCulloch, P. M., Klekociuk, A. R., Hamilton, P. A., & Royle, G. W. R. 1987, Australian Journal of Physics, 40, 725

McLaughlin, M. A., Cordes, J. M., Deshpande, A. A., et al. 2001, Astrophys. J. Lett. , 547, L41

Metropolis, N., Rosenbluth, A. W., Rosenbluth, M. N., Teller, A. H., & Teller, E. 1953, Journal of Chemical Physics, 21, 1087

Mizuno, E. & et al. 1998, in Second Edoardo Amaldi Conference on Gravitational Wave Experiments, ed. E. Coccia, G. Veneziano, & G. Pizzella, 108

NASA/DOE/International LAT Team. 2010, NASA Teleconference to Announce GLAST New Name, First Light Findings, http://www.nasa.gov/mission_pages/GLAST/news/glast_findings_media.html

Ng, C. & Romani, R. W. 2008, Astrophys. J. , 673, 411

Ostriker, J. P. 1971, Scientific American, 224, 48

Ostriker, J. P. & Gunn, J. E. 1969, Astrophys. J. , 157, 1395

Owen, B. J. 2005, Physical Review Letters, 95, 211101

Owen, B. J., Lindblom, L., Cutler, C., et al. 1998, Phys. Rev. D , 58, 084020

Özel, F., Güver, T., & Psaltis, D. 2009, Astrophys. J. , 693, 1775

Pacini, F. 1968, Nature , 219, 145

Pavlov, G. G. & Luna, G. J. M. 2009, Astrophys. J. , 703, 910

Pitkin, M., Gill, C., Veitch, J., Macdonald, E., & Woan, G. 2012, Journal of Physics Conference Series, 363, 012041

Pitkin, M., Reid, S., Rowan, S., & Hough, J. 2011, Living Reviews in Relativity, 14, 5

Pitkin, M. & Woan, G. 2004, Classical and Quantum Gravity, 21, 843

Prix, R. 2006, in APS April Meeting Abstracts, C7001

Radhakrishnan, V., Cooke, D. J., Komesaroff, M. M., & Morris, D. 1969, Nature , 221, 443

Ramanamurthy, P. V. 1994, Astron. Astrophys. , 284, L13

Razzano, M. 2009, in American Institute of Physics Conference Series, Vol. 1112, American Institute of Physics Conference Series, ed. D. Bastieri & R. Rando, 89–94

Robertson, D. I., Morrison, E., Hough, J., et al. 1995, Review of Scientific Instruments, 66, 4447

Sathyaprakash, B. S. & Schutz, B. F. 2009, Living Reviews in Relativity, 12, 2

Saz Parkinson, P. M., Dormody, M., Ziegler, M., et al. 2010, Astrophys. J. , 725, 571

Sazhin, M. V. 1978, Sov. Astronom. , 22, 36

Schutz, B. 2009, A first course in general relativity, 2nd edn. (Cambridge University Press)

Shklovskii, I. S. 1970, Sov. Astronom. , 13, 562

Shoemaker, D., Schilling, R., Schnupp, L., et al. 1988, Phys. Rev. D , 38, 423

Sivia, D. S. & Skilling, J. 2006, Data Analysis, A Bayesian Tutorial, 2nd edn. (Oxford University Press)

Skilling, J. 2004, in American Institute of Physics Conference Series, Vol. 735, American Institute of Physics Conference Series, ed. R. Fischer, R. Preuss, & U. V. Toussaint, 395–405

Skilling, J. 2006, Bayesian Analysis, 1, 833

Smith, J. R. & LIGO Scientific Collaboration. 2009, Classical and Quantum Gravity, 26, 114013

Staelin, D. H. & Reifenstein, III, E. C. 1968, Science, 162, 1481

Staubert, R., Klochkov, D., Vasco, D., et al. 2011, ArXiv e-prints

Steiner, A. W., Lattimer, J. M., & Brown, E. F. 2010, Astrophys. J. , 722, 33

Stergioulas, N. 2003, Living Reviews in Relativity, 6, 3

Tavani, M., Bulgarelli, A., Vittorini, V., et al. 2011, Science, 331, 736

The Condor team. 2009, What is Condor?, http://www.cs.wisc.edu/condor/description.html

The LIGO Scientific Collaboration. 2010, Download site for archived publication-quality interferometer sensitivity curves, http://www.ligo.caltech.edu/~jzweizig/distribution/LSC_Data/

The Virgo Collaboration. 2010, Virgo Sensitivity Curves, http://wwwcascina.virgo.infn.it/DataAnalysis/Calibration/Sensitivity/

Thorsett, S. E. & Chakrabarty, D. 1999, Astrophys. J. , 512, 288

Tournefier, E. f. t. V. C. 2007, in 42nd Rencontres de Moriond Gravitational Waves and Experimental Gravity,, La Thuile : Italy(2007), 42nd Rencontres de Moriond Gravitational Waves and Experimental Gravity,, La Thuile : Italy(2007)

Ushomirsky, G., Cutler, C., & Bildsten, L. 2000, Mon. Not. Roy. Astron. Soc. , 319, 902

van Haasteren, R., Levin, Y., Janssen, G. H., et al. 2011, Mon. Not. Roy. Astron. Soc. , 414, 3117

Veitch, J. & Vecchio, A. 2010, Phys. Rev. D , 81, 062003

Wang, W. 2011, Research in Astronomy and Astrophysics, 11, 824

Weber, J. 1961, General relativity and gravitational waves

Zimmermann, M. & Szedenits, Jr., E. 1979, Phys. Rev. D , 20, 351